

Dissertation
submitted to the
Combined Faculties for the Natural Sciences and for Mathematics
of the Ruperto-Carola University of Heidelberg, Germany
for the degree of
Doctor of Natural Sciences

presented by
Dipl. Biologe Christian Peter Bacher
born in: Basel, Switzerland
Oral examination: 23rd of November 2005

Computational imaging of dynamic nuclear processes
in living somatic and germ line cells

Referees: Prof. Dr. Roland Eils
Prof. Dr. Peter Lichter

List of publications

- **C.P. Bacher**, N. Mise, M. Guggiari, B. Brors, P. LeBaccon, S. Huart, P. Avner, A. Belmont, R. Eils, E. Heard. Transient cross-talk between X-inactivation centers during the initiation of X-inactivation. (submitted)
- P. Lenart, **C.P. Bacher**, N. Daigle, A. Hand, R. Eils, M. Terasaki, J. Ellenberg. A contractile nuclear actin network drives chromosome congression in oocytes. *Nature*, 436(7052), 812-818, 2005.
- **C.P. Bacher**, M. Reichenzeller, C. Athale, H. Herrmann, and R. Eils. 4D single particle tracking of synthetic and proteinaceous microspheres reveals preferential movement of nuclear particles along chromatin-poor tracks. *BMC Cell Biology*, 5(1):45, 2004.
- S.M. Gorisch, M. Wachsmuth, C. Ittrich, **C.P. Bacher**, K. Rippe, and P. Lichter. Nuclear body movement is determined by chromatin accessibility and dynamics. *Proc Natl Acad Sci USA*, 101(36):13221-13226, 2004.
- K.F. Toth, T.A. Knoch, M. Wachsmuth, M. Frank-Stohr, M. Stohr, **C.P. Bacher**, G. Muller, and K. Rippe. Trichostatin A-induced histone acetylation causes decondensation of interphase chromatin. *J Cell Sci.*, 117(Pt 18):4277-4287, 2004.

List of presentations

- **C.P. Bacher**, N. Mise, M. Guggiari, B. Brors, P. LeBaccon, S. Huart, P. Avner, A. Belmont, R. Eils, E. Heard. Transient cross-talk between X-inactivation centers during the initiation of X-inactivation. EMBO-FEBS Conference on Nuclear Structure and Dynamics, 2005, Montpellier, France. Poster.
- **C.P. Bacher**, and R. Eils. Computational study of nuclear topology and processes. DKFZ, 2004, Heidelberg, Germany. Oral presentation.
- **C.P. Bacher**, E. Heard, and R. Eils. Spatial Aspects of Chromosomal Inactivation during Stem Cell Differentiation. ICC XV (The 15th International Chromosome Conference), 2004, London, UK. Poster.
- J. Gao, and A. Murmann. New 3D computational tools to evaluate and visualize the spatial arrangement of potential translocation partner genes in fixed nuclei (presented by **C.P. Bacher**). ICC XV (The 15th International Chromosome Conference), 2004, London, UK. Oral presentation.
- **C.P. Bacher**, M. Reichenzeller, H. Herrmann, and R. Eils. 4-D single particle tracking of synthetic and proteinaceous microspheres reveals preferential movement of nuclear particles along chromatin - poor tracks. Gordon Research Conference, Molecular Cytogenetics, The Queen's College, Oxford, UK. Poster.
- O. Masui, J. Chaumeil, P. LeBaccon, K. Ramachandran, **C.P. Bacher**, E. Bertrand, R. Eils, D. Spector, A. Belmont, N. Mise, E. Heard. 69th Cold Spring Harbor Symposium on Quantitative Biology: Epigenetics, Cold Spring Harbor, USA. Poster.
- **C.P. Bacher**, M. Reichenzeller, H. Herrmann, and R. Eils. Advanced system for 4D single particle tracking of moving subcellular particles. Annual Convention of the German Society for Cell Biology, 2004, Berlin, Germany. Poster.
- **C.P. Bacher**, J. Fieres, J. Gao, M. Gebhard, J. Mattes, and R. Eils. Image processing methods to investigate the dynamics in living cells. DKFZ, 2003, Heidelberg, Germany. Poster.

Contents

Zusammenfassung	1
Abstract	3
List of Abbreviations	5
1 Introduction	7
1.1 Nuclear architecture	7
1.1.1 Nuclear compartments	7
1.1.2 Nuclear matrix	11
1.1.3 Spatial organization of chromatin and chromosome territories	14
1.2 X-chromosomal inactivation	17
1.2.1 Introduction	17
1.2.2 X-inactivation center (Xic)	18
1.2.3 Counting	21
1.2.4 Choice	24
1.2.5 Maintenance	26
1.2.6 Developmental View	28
1.3 Biological image processing	31
1.3.1 Introduction	31
1.3.2 Workflow	31
1.3.3 Pre-processing	33
1.3.4 Segmentation	36
1.3.5 Registration	37
2 Objectives	43
3 Materials and Methods	45
3.1 Biological microscopy image processing methods	45
3.1.1 Image pre-processing	45
3.1.2 Image segmentation	50
3.1.3 Image registration	53
3.1.4 Particle tracking	57
3.2 Tikal image processing platform	62
3.2.1 Introduction	62
3.2.2 Concept of Tikal	63

3.2.3	Features of Tikal	69
3.3	Experimental procedures	73
3.3.1	ES cell lines and culture	73
3.3.2	ES cell transfections	74
3.3.3	SW13 cell culture and transfection	74
3.3.4	GFP-NLS-vimentin constructs	75
3.3.5	Microinjection of fluorescent polystyrene microspheres	75
3.3.6	3D RNA and DNA FISH	75
3.3.7	Immunofluorescence of RNA and DNA FISH	76
3.3.8	Drug treatment of SW13 cells	76
3.4	Data acquisition and analysis	76
3.4.1	4D Imaging	76
3.4.2	3D Imaging	77
3.4.3	Segmentation of cell nuclei	77
3.4.4	4D Image registration	79
3.4.5	4D Tracking of subcellular particles	80
3.4.6	Measurements of FISH signals	80
3.4.7	Correlation analysis of chromatin density and tracked nuclear particles	80
3.4.8	Calculations of MSD and diffusion coefficients	81
3.4.9	Statistical analyses, simulations and plots	81
4	Transient co-localization of Xics during the initiation of X-inactivation	83
4.1	Introduction	83
4.2	Results	85
4.2.1	Peripheral nuclear localization of the Xic in undifferentiated and differentiating male ES cells	85
4.2.2	More internal nuclear localization of the Xic in undifferentiated and differentiating female ES cells	88
4.2.3	Association of the Xic region with the nuclear periphery and constrained motion in living cells.	92
4.2.4	Spatial Xic cross-talk in female ES cells and male ES cells with multicopy transgenes	96
4.3	Discussion	102
5	4D single particle tracking of nuclear particles	107
5.1	Introduction	107
5.2	Results	108
5.2.1	An experimental system for probing particle kinetics in the cell	108
5.2.2	A computational system for tracking nuclear particles on the background of moving cells	109
5.2.3	<i>In vivo</i> observation of microspheres	112
5.2.4	Chromatin remodeling directly effects mobility of nuclear particles	114

5.2.5	Influence of inhibitors on the mobility of nuclear vimentin bodies	116
5.2.6	Particle movement in dehydrated cells	119
5.3	Discussion	120
General Conclusion & Outlook		123
A	Tikal Manual	129
A.1	General Functions	129
A.1.1	The “Canvas area”	130
A.1.2	The “Data set history” window	130
A.1.3	The “Channel selection” window	130
A.1.4	The “Colormap selection” window	130
A.1.5	The “Experiment cropping” window	131
A.1.6	The “Isosurface rendering” window	131
A.2	The “File” menu	132
A.2.1	Open 4D desktop	132
A.2.2	Save 4D desktop	132
A.2.3	Open 4D stack	132
A.2.4	Save 4D stack	132
A.2.5	Create listfile	132
A.2.6	Create listfile Leica	133
A.2.7	Create listfile DeltaVision	133
A.2.8	Open 4D Leica	134
A.2.9	Open 3D Leica	134
A.2.10	Open DeltaVision	134
A.2.11	Open Metamorph	134
A.2.12	Image properties	134
A.2.13	Batch	134
A.2.14	Quit	134
A.3	The “Filters” menu	134
A.3.1	Binarize	135
A.3.2	Pixelremove	135
A.3.3	Binarize min/max	135
A.3.4	Binning binarize	136
A.3.5	Median 3D	136
A.3.6	Median 2D	136
A.3.7	Gauss 3D	136
A.3.8	Gauss 2D	136
A.3.9	Canny 2D	136
A.3.10	Gamma	137
A.3.11	Auto Gamma	137
A.3.12	Diffusion 3D	137
A.3.13	Diffusion 2D	138
A.3.14	Dilatation	138
A.3.15	Erosion	138
A.3.16	Closing	139

A.3.17	Opening	139
A.3.18	Thinning	139
A.3.19	Thinning RG	139
A.3.20	Outline	139
A.3.21	Fill	140
A.3.22	Pyramid Segmentation	140
A.3.23	Pyramid Binarize	140
A.3.24	Inversion	140
A.3.25	Clear Border	140
A.3.26	Maximum Projection	140
A.3.27	Average Projection	141
A.4	The “ITK” menu	141
A.4.1	Binarize	141
A.4.2	Watershed	141
A.4.3	Gradient Diffusion	141
A.4.4	Bilateral Diffusion	142
A.4.5	Gradient Magnitude	142
A.4.6	Connected Thresholding	143
A.4.7	Neighborhood Thresholding	143
A.4.8	Confidence Thresholding	143
A.4.9	Distance Mapping	144
A.4.10	Otsu Thresholding	144
A.5	The “Tools” menu	145
A.5.1	Object properties	145
A.5.2	Crop	145
A.5.3	Visualization 3D	145
A.5.4	Tracking 4D	145
A.5.5	Tracking 4D Visual	146
A.5.6	Load track 4D	147
A.5.7	Enable / Disable manual tracking in image	147
A.5.8	Registration 3D	147
A.5.9	Inter Channel measurements	148
A.5.10	Border/Center pixel distances	149
A.5.11	Border/Border pixel distances	149
A.5.12	Border/Border pixel localization distances	150
A.5.13	Image calculator	151
A.5.14	Convolve image with mask	151
A.5.15	Crop with mask	152
A.6	The “3D Visualization” menu	152
A.6.1	Extract new isosurface	152
A.6.2	Load isosurface	153
A.6.3	Import old isosurface	153
A.7	The “Zoom” menu	153
A.8	The “Specials” menu	153
A.8.1	Combine Experiments	153
A.8.2	Split Experiments	154
A.8.3	Remove current time step	154

A.8.4	Add empty layers at top and bottom of Experiment . . .	154
A.8.5	Remove top layers	154
A.8.6	Remove bottom layers	154
A.8.7	Split Objects	154
A.8.8	Colormap test data	154
A.9	The “Help” menu	154
A.9.1	About Tikal	154
Acknowledgments		155
Bibliography		157

Zusammenfassung

Lichtmikroskopische Techniken können benutzt werden, um den Einfluss der räumlichen und zeitlichen Organisation von Chromatin und assoziierten nukleären Faktoren zu untersuchen. In der vorliegenden Arbeit möchte ich mit zwei biologischen Ansätzen die Bedeutung der quantitativen Extraktion von raum- und zeitabhängigen Parametern aus mikroskopischen Bildern untersuchen und deren Auswirkung auf den heutigen Wissensstand über die nukleäre Topologie zeigen. Zusätzlich soll die Software-Plattform Tikal, die ich zur Vereinfachung der quantitativen Analyse multidimensionaler mikroskopischer Bilder entwickelt habe, vorgestellt werden.

Im ersten Projekt habe ich die räumliche Position und Verteilung des X-chromosomalen Inaktivierungszentrums (Xic) während der X-chromosomalen Inaktivierung in Zellkernen weiblicher und männlicher embryonaler Mausstammzellen (ES-Zellen) mittels dreidimensionaler (3D) Fluoreszenz *in situ* Hybridisierung (FISH), sowie anhand von Lebendzellaufnahmen mittels Lac-Operator markierter Xic-Transgene untersucht. Tikal wurde zur Bildverarbeitung und zur quantitativen Bestimmung der Distanzen zwischen den Xic-Loci in weiblichen ES-Zellen, sowie zur Messung der Abstände der Xic-Signale zur nukleären Peripherie in weiblichen und männlichen ES-Zellen verwendet. In weiblichen ES-Zellen wies eine kleine Population von Zellen eine Kolo-kalisation der beiden Xic-Loci während der frühen Differenzierungsphase auf. Die funktionelle Bedeutung dieser Annäherung der Xic-Loci während der X-Inaktivierungsphase wird bestärkt durch ihr Fehlen in zwei ES-Zellmutanten, die Defizite in den X-chromosomalen Zähl- und Selektionsmechanismen aufweisen. Ausserdem konnte ich zeigen, dass der Xic-Lokus nahe der nukleären Membran lokalisiert ist. Diese periphere Lage ist am stärksten bei männlichen ES-Zellen während der frühen Differenzierung ausgeprägt. Eine solche räumliche Absonderung des Lokus könnte notwendig sein, um den aktiven Zustand des einzigen X-Chromosoms beizubehalten.

Im zweiten Projekt habe ich die Dynamik der nukleären Organisation mit Hilfe von zwei inerten nukleären Körpern, GFP-NLS-vimentin-Partikeln und mikroinjizierten Polystyren-Kügelchen, untersucht. Um die Mobilität der Partikel in sich bewegenden Zellen und in Zellkernen, die ihre Form verändern, quantitativ verfolgen zu können, verwendete ich Tikal. So konnte ich aus Serien mikroskopischer Bilder lebender Zellen die relevanten Parameter mit Hilfe von Tracking Methoden (Verfolgung von einzelnen Objekten in Raum und Zeit) und Bewegungsanalysen extrahieren. Kinetische Analysen zeigten ein Überwiegen nukleärer Partikel mit eingeschränkten Diffusionseigenschaften. Aus den vorliegenden Ergebnissen lässt sich schliessen, dass Chromatindichte und Chromatinumbau auf molekularer Ebene die Beweglichkeit von Proteinbestandteilen innerhalb des Zellkernes direkt beeinflussen.

In der vorliegenden Arbeit möchte ich zunächst die beiden biologischen Fragestellungen erklären und den aktuellen Wissensstand auf dem Gebiet der nukleären Architektur, X-chromosomalen Inaktivierung und Bildverarbeitung kurz darstellen. Anschliessend möchte ich die spezifischen Techniken der Bildverarbeitung, die ich zur Bearbeitung der mikroskopischen Aufnahmen verwendet

habe, vorstellen. Zusätzlich sollen das Konzept und die Funktionen meiner Bildverarbeitungs-Software Tikal erläutert werden. Die dann folgenden Kapitel werden sich mit den beiden Projekten über die Analyse der Xic-Lokalisation in ES-Zellen und über die räumliche und zeitliche Verfolgung nukleärer Partikel beschäftigen.

Abstract

Light microscopy techniques have been used to investigate the influence of the spatio-temporal organization of chromatin and associated nuclear factors. In this thesis I will present with two biological examples the importance of quantitative extraction of spatial and temporally dependent parameters from microscopic images and their impact on the knowledge of topological constraints in the nucleus. Additionally, I introduce a software platform, called Tikal, which I developed to facilitate the quantitative image analysis of multidimensional microscopic images.

In the first project I investigated the spatial localization and distribution of the X-chromosomal inactivation center (Xic) locus during the X-chromosomal inactivation process in female and male mouse embryonic stem (ES) cell nuclei using 3 dimensional (3D) fluorescent *in situ* hybridization (FISH) analysis, as well as live cell imaging with Lac operator-tagged Xic transgenes. I used Tikal for the image processing and the quantitative analysis of the inter Xic locus distances in female cells and the Xic signal distances to the nuclear periphery of female and male cells. In female ES cells, a small population in which the two Xics are co-localized can be detected in early differentiation. The functional importance of this apparent cross-talk between Xics during the initiation time window when X-inactivation begins is underscored by the fact that it cannot be detected in two mutant ES cell lines that are incapable of counting and choice. Further I found that the Xic locus lies very close to the nuclear envelope. This peripheral location is most pronounced in male ES cells during early differentiation. Such a sequestration of the Xic may be indicative in order to maintain the active state of the single X-chromosome.

In the second project I investigated nuclear body dynamics of two different types of inert nuclear particles, namely particles produced of GFP-NLS-vimentin and microinjected polystyrene beads in order to study the dynamics of nuclear organization. To quantitatively follow particle movement on the background of moving cells and shape changing nuclei, I used Tikal to work on images derived from live cell time-lapse microscopy and extracted relevant parameters with single particle tracking and mobility analysis. Kinetic analysis revealed predominantly obstructed diffusion for nuclear particles and I could conclude that chromatin density and thereby chromatin remodeling on the molecular level directly influences the mobility of protein components within the nucleus.

In this thesis I will first introduce the two biological questions by reviewing our knowledge about nuclear architecture, X-chromosomal inactivation and image processing. I will then introduce specific image processing techniques I used for the processing of biological microscopy images. Additionally, I present the concept and features of the software platform Tikal. The following chapters will describe the two projects on Xic localization analysis in mouse ES cells nuclei and on nuclear particle tracking, respectively.

List of Abbreviations

AIR	automated image registration
API	application programming interface
ARBP	attachment region binding protein
ATRA	<i>all-trans</i> retinoic acid
BAC	bacterial artificial chromosome
CB	cajal body
CCD	charge coupled device
COM	center-of-mass
CT	computer tomography
DAPI	4'-6-diamidino-2-phenylindole
DMEM	Dulbecco's modified eagle medium
DNA	deoxyribonucleic acid
ES	embryonic stem
FBS	fetal bovine serum
FISH	fluorescent <i>in situ</i> hybridization
FLIP	fluorescence loss in photobleaching
FRAP	fluorescence recovery after photobleaching
FRET	fluorescence resonance energy transfer
GUI	graphical user interface
HIV	human immunodeficiency virus
IC	interchromatin compartment
ICD	interchromosomal domain
ITK	insight segmentation and registration toolkit
LIF	leukemia inhibitory factor
LINE	long interspersed nuclear elements
MAR	matrix associating region
MEF	mouse embryonic fibroblast
MMSI	male meiotic sex-chromosome inactivation
MRI	magnetic resonance images
NB	nuclear body
NCTRG	neighborhood connected threshold region growing
NE	nuclear envelope
NMP	nuclear matrix protein
NUMA	nuclear mitotic apparatus protein
PET	positron emission tomography
PML	promyelocytic leukemia protein

List of Abbreviations

PMT	photo multiplier tubes
PTV	particle tracking velocimetry
OME	open microscopy environment
ORF	open reading frame
RIGS	repeat-induced gene silencing
RNA	ribonucleic acid
RNA-Pol II	ribonucleic acid polymerase II
ROI	region of interest
SAF-A/B	scaffold attachment factor A/B
SAR	scaffold associating region
SDS-PAGE	sodium-dodecyl-sulfate polyacrylamide gel electrophoresis
SINE	short interspersed nuclear elements
SNR	signal-to-noise ratio
snRNA	small nuclear ribonucleic acid
snRNP	small nuclear ribonucleoprotein
SPECT	single photon emission computed tomography
SR	serine- and arginine-rich RNA processing factors
wt	wild type
Xa	active X-chromosome
Xce	X-controlling element
Xi	inactive X-chromosome
Xic	X-inactivation center
Xist	X-inactivation specific transcript
Xm	maternal X-chromosome
XML	extensible markup language
Xp	paternal X-chromosome
YAC	yeast artificial chromosome

Chapter 1

Introduction

1.1 Nuclear architecture

The cell nucleus is not only a rudimentary object filled with deoxyribonucleic acid (DNA) that is only transcribed and replicated. It is a highly complex organelle orchestrating a high number of vital and functional processes within the cell. Therefore, especially in this context an organized structure of chromatin and proteins is essential to ensure an accurate maintenance of these cellular processes. Beside the knowledge about gene transcription and molecular mechanisms of coordinating structures it is mandatory to understand their temporal and spatial distribution within the cell nucleus. To explain functionality of cytoplasmic and nuclear proteins or RNAs only on their transcriptional or translational regulation is not appropriate and has to be revised. Epigenetic processes such as DNA methylation can not be explained by the pure quantitative regulation of responsible factors and therefore need a combination of molecular and physical properties of proteins to describe the overall physiological cell functions, e.g. the cleavage kinetics of a protein complex as well as its spatial distribution within the nucleus.

For the purpose of this thesis it is important to know how the nucleus is organized. For this reason I will give an overview on the spatial organization and compartmentalization of the nucleus.

1.1.1 Nuclear compartments

The fact, that the interior of the nucleus is not only an amorphous structure, has been widely recognized. Many discrete compartments with specific functions have been identified (see Figure 1.1) [1, 2, 3].

The most clearly distinguishable interphase subnuclear structures in mammalian cells are the nucleoli. Nucleolar compartments are the central sites of ribosomal RNA synthesis and processing and can also be seen as centers of biogenesis for the ribosomal subunits. Additionally, defined sub-compartments within nucleoli represent the centers where these different activities are performed. This has been confirmed by analysis of the kinetics of assembly and elongation of the mammalian RNA polymerase I complex on endogenous ribosomal genes in the nuclei of living cells [4].

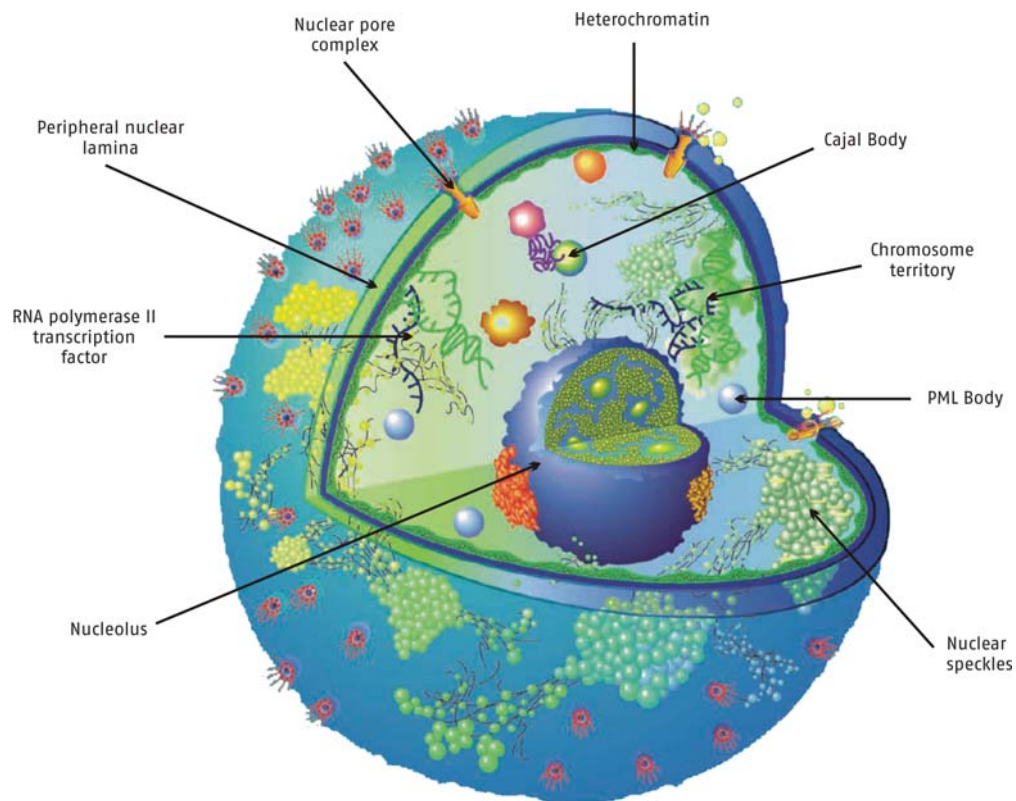


Figure 1.1: Graphical representation of a cell nucleus with its organelles and interior structures. The nucleus is surrounded by the nuclear envelope a double layer membrane coupled to a network of intermediate filaments, the lamina. Where the inner and outer nuclear membranes are fused together nuclear pores are formed that serve for the transit of materials between the nucleus and cytoplasm. The chromosomes are arranged into chromosome territories within the nucleoplasm. The most prominent structure is the nucleolus which is the site of rRNA synthesis, rRNA processing, and assembly of ribosomal subunits. Transcription is coordinated by RNA polymerase II which is abundantly found within the nucleus. Other structures such as PML and Cajal bodies are sequestered to protein complexes and can restrictively diffuse throughout the nucleus. (Image adapted from [2])

Beside the nucleoli, many other small nuclear bodies (NB) have been described. Prominent examples are the Cajal bodies (CB) (see Figures 1.1, 1.2), formerly known as coiled bodies. These subnuclear structures are generally spherical and have an approximate diameter of $0.5\text{-}1\mu\text{m}$. The composition of the CB appear in cross sections as a network of coiled fibers [5]. It has been described that CB are found in both animals and plants and are highly enriched in several classes of small nuclear ribonucleoproteins (snRNPs), nucleolar, cell-cycle control proteins and the marker protein p80 coilin, as well as several basal transcription factors. While these bodies seem not to be transcriptional active, nascent small nuclear RNAs (snRNAs) have been observed immediately next to them in mammalian cells [5]. In this context it has been found that some of the post-transcriptional modifications of the spliceosomal snRNAs take place in CBs and are guided and introduced by a recently discovered class of small CB-specific RNAs [6]. These are members of the so-called guide RNA family, which functions to align RNA modification activities with target sequences through complementary base-pairing interactions. It is likely that other guide RNAs will be discovered since the number of guide RNAs identified to date is still far less than the number of modified nucleotides found within spliceosomal snRNAs. Moreover CB proteins might be involved in the cell cycle coordination, cellular stress responses and cell aging. For the latter a putative involvement of CBs in telomerase maturation is suggested [7].

Individual CBs can show complex dynamic behavior, including translocation as well as fusion of CBs in the nucleoplasm, splitting into two daughter bodies and movements to and from nucleoli. In cases where CBs split into two smaller bodies, some components, such as fibrillarin, are seen to partition differentially between the daughter structures, whereas other components, such as coilin, are present at similar levels in both [8]. This is consistent with the view that CBs represent a heterogeneous collection of related structures that can differ in their precise molecular composition and possible biological roles. Much of the CB movement appears to occur via simple or constrained diffusion, although in some cases it is possible that more active processes are involved [9, 8]. Not all CBs are mobile at any time, and in most cases they remain tethered within a confined nuclear volume, probably through interactions with specific chromatin regions [10].

Another important nuclear structure are the promyelocytic leukemia (PML) bodies (see Figure 1.2). These bodies are defined by their content of PML protein. They are comparable in size to coiled bodies but are usually more abundant. In mammalian cells commonly 10-20 PML bodies can be found. However, the biochemical and molecular functions of PML NBs and PML proteins still seem unclear. It has been suggested that DNA and RNA viruses have a variety of effects on body morphology, whereas adenoviruses and human immunodeficiency virus (HIV) cause the PML bodies to move to the cytoplasm [11]. Another effect is observed with herpesviruses that “unwind” the PML bodies [11]. Such functional descriptions derive from earlier studies of PML bodies where they have been referred to nuclear domains that accumulate proteins that can be interferon-upregulated and thus have a vital function in nuclear defense mechanisms [12]. It was observed that herpesvirus and adenovirus genomes are

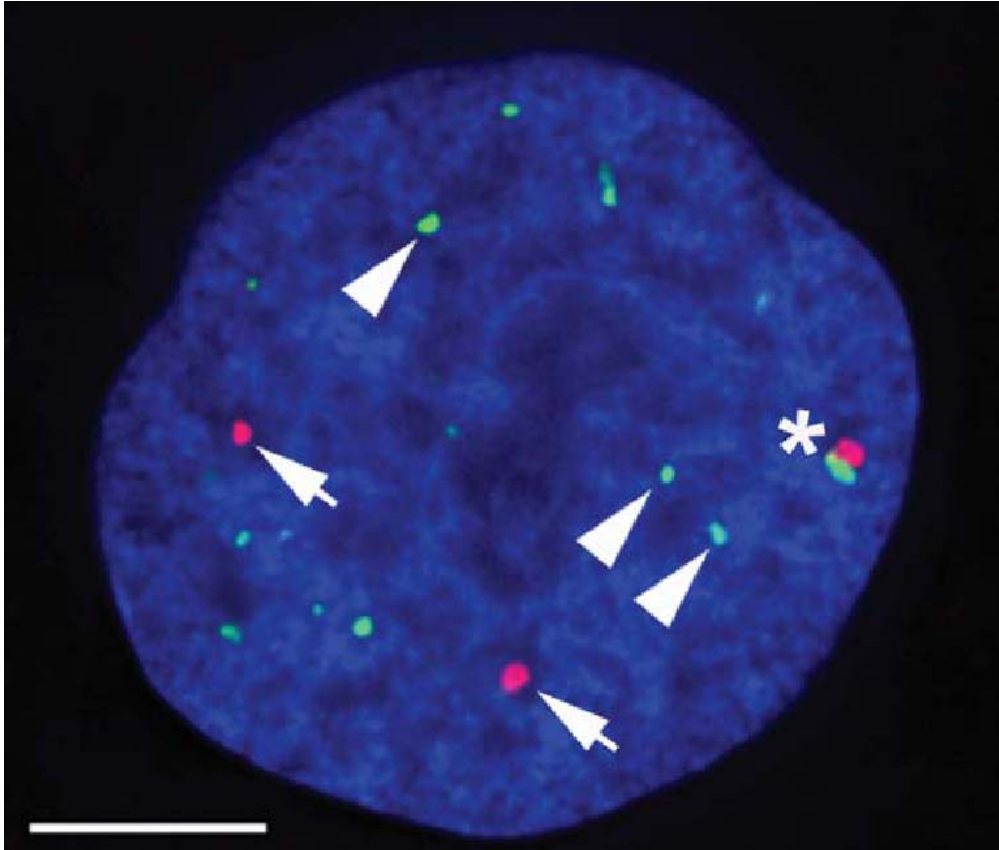


Figure 1.2: Cajal bodies (CBs) and promyelocytic leukemia protein (PML) bodies in human cells. Anti-coilin antibodies label CBs (red), which appear as spherical, bright foci distributed throughout the nucleoplasm. PML bodies are stained in green, detected here using an anti-PML antibody. Note that some PML bodies and CBs are located in close proximity (asterisk). DNA is stained with DAPI (blue). Bar: $5\mu\text{m}$. (Image from [7])

deposited at the periphery of those nuclear domains. Interestingly, it seems that DNA viruses start their transcription and consequently initiate replication at these peripheral domain sites, suggesting that viruses have evolved ways to circumvent and exploit this potential cellular defense.

PML bodies are amongst the most rapidly moving structures within the nucleoplasm with an average velocity of $4.0\text{--}7.2\mu\text{m}/\text{min}$. This mobility was not sensitive to α -amanitin and therefore not directly dependent on RNA polymerase II activity. However, an abolishment of the PML body dynamics was observed upon ATP depletion (sodium azide treatment of cells); indicating an energy-dependent movement [13]. Further it was shown that an inhibition of actin-dependent myosins I reduced the mobility of PML bodies, suggesting that nuclear motor proteins might be involved and responsible for the dynamic behavior of NBs. Interestingly, only rapidly moving PML bodies were affected by energy depletion whereas bodies with more localized movements showed no changing in dynamics [13].

A variety of other structures such as the perinucleolar compartment and gemini bodies have also been described [2]. But, while nuclear compartments and bodies have raised much interest, the extent to which they really define functional compartments remains a matter of debate. Studies by Almeida *et al.* have shown that disruption of CBs does not change cell morphology and viability [14]. Similar observations have been made in transgenic animals [15].

1.1.2 Nuclear matrix

Even though still controversially discussed, numerous experiments support the notion of a nuclear matrix that plays central roles in nuclear functional organization. The nuclear matrix is classically described as an amorphous fibrogranular structure that can be isolated from nuclei by hypertonic treatment followed by nuclease digestion [16, 17]. The nuclear matrix typically contains many hundreds of different proteins. Two-dimensional gels reveal more than 200 nuclear matrix proteins (NMPs); among the most abundant are the lamins, nuclear mitotic apparatus protein (NUMA), B23 and the hnRNP proteins [18, 19]. These findings further support the view that the internal nuclear matrix consists of a nuclear ribonucleoprotein network (see Figure 1.3).

Generally one can say that interphase chromatin is arranged into topologically distinguishable domains comprising gene expression and replication units. A possible hypothesis suggests that such a chromatin arrangement could be achieved through genomic sequence elements, so-called MAR or SAR regions (for matrix- or scaffold-associating regions). S/MAR regions are located near the boundaries of actively transcribed genes from where they can influence their activity. The nuclear matrix binds diverse nuclear proteins and might help in their assembly to functional macromolecular complexes involved in important nuclear processes, such as transcription, RNA splicing and DNA replication [20].

Many of these nuclear matrix involved proteins have been studied in detail. Amongst the best characterized are the scaffold attachment factor A (SAF-A) and the attachment region binding protein (ARBP). These proteins were discovered because they tend to associate with matrix attached DNA elements.

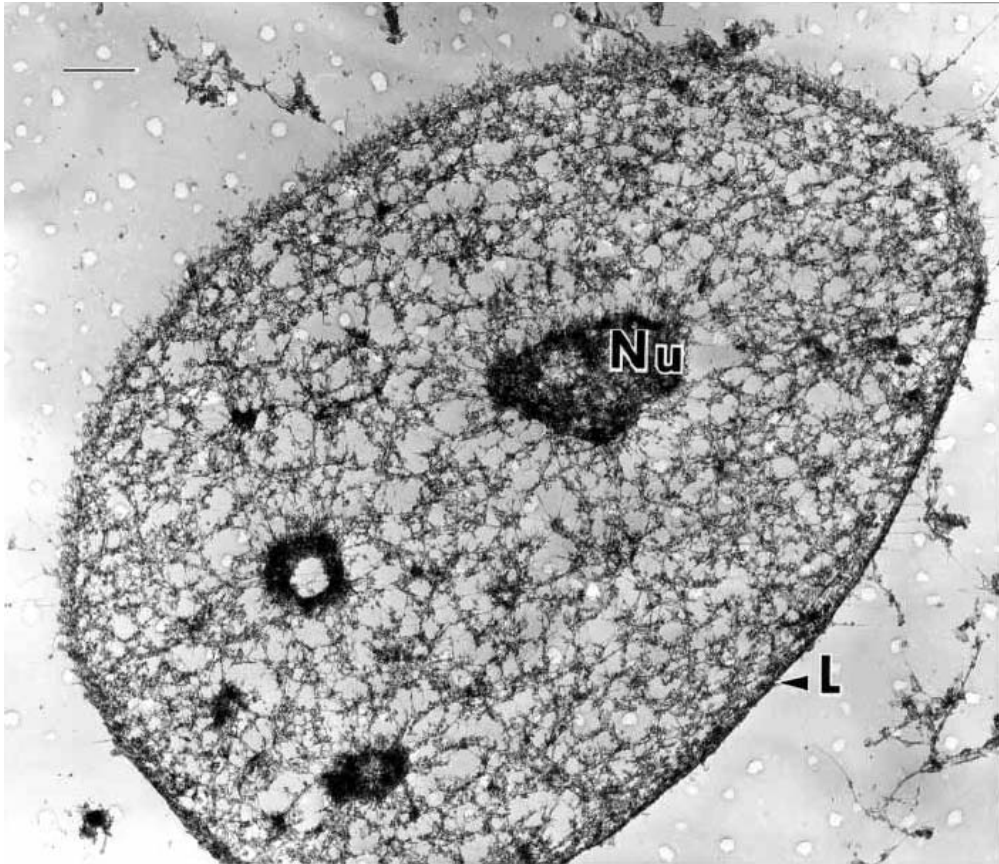


Figure 1.3: The nuclear matrix of a cell prepared by the crosslink-stabilized nuclear matrix preparation procedure and visualized by resinless section electron microscopy. The nuclear matrix consists of two parts: the nuclear lamina (L) and a network of intricately structured fibers connected to the lamina and well distributed through the nuclear volume. The matrices of nucleoli (Nu) remain and are connected to the fibers of the internal nuclear matrix. Three remnant nucleoli may be seen in this section. Bar: $1\mu\text{m}$. (Image from [20])

SAF-A was identified in nuclear extracts from HeLa cells [21]. It specifically binds to a scaffold attachment region element from the human genome. SAF-A shows the highest affinity for several homologous and heterologous scaffold attachment regions elements from vertebrate cells. SAF-A is an abundant nuclear protein and might be a constituent of the nuclear matrix and scaffold structures.

Recent results have suggested a contribution of SAF-A in the silencing of X-linked genes, maybe by inducing a local change in nuclear architecture [22]. *In vivo* mobility experiments demonstrated that SAF-A is a component of a highly stable proteinaceous structure in the territory of inactive X-chromosomes, which might act as a platform for immobilizing X-inactivation specific transcript (*Xist*) RNA during the maintenance phase of X-inactivation [23]. I will describe the possible role of SAF-A with respect to X-inactivation more thoroughly later.

It was also shown that SAF-A binds to p300, a major transcriptional co-activator [24]. The regulation of transcription occurs through scaffold/matrix attachment regions (S/MARs), the chromatin regions that bind the nuclear matrix. ARBP has been shown to interact with methylated DNA in MAR elements through interaction with mSin3A (a protein member of a chromatin remodeling complex). This interaction recruits a corepressor complex containing histone deacetylases. This in turn is thought to generate a localized silenced chromatin structure [25].

SAF-B (scaffold attachment factor B) specifically binds to S/MAR regions and interacts with RNA polymerase II (RNA pol II) and a subset of serine- and arginine-rich RNA processing factors (SR proteins). It was proposed that these interactions allow SAF-B to provide a surface for the assembly of the transcription apparatus [26].

Another interesting aspect is found where chaotic deregulation and mislocalization of genes are observed. The cause of this irregular arrangement is the loss of a single MAR-binding protein [27]. Parallels can be found in some ways in malignant dysregulation of gene expression [28].

Although strong evidence for the presence of a putative nuclear matrix was found, its meaning is still being controversially discussed since the link between the biochemical isolated structures and its *in vivo* organization is weak. However, in correlation with nuclear matrix factors such as the SAF-A complex and the later described X-chromosomal inactivation aspects SAF-A presence has shown fundamental functions. Especially in the maintenance of the inactive structures of the X-chromosomes in female cells during the cell cycles the nuclear scaffold might be, beside other epigenetic mechanisms, mandatory for the proper maintenance of function of the inactive X. For this reason it can be hypothesized that the inactive X-chromosome (also known as the Barr body), with its positioning close to nucleoli or the nuclear periphery, is connected to proteins of the nuclear matrix [29]. However, further investigations to identify nuclear matrix factors and their functions in nuclear organization in particular with *in vivo* studies have to be promoted in future.

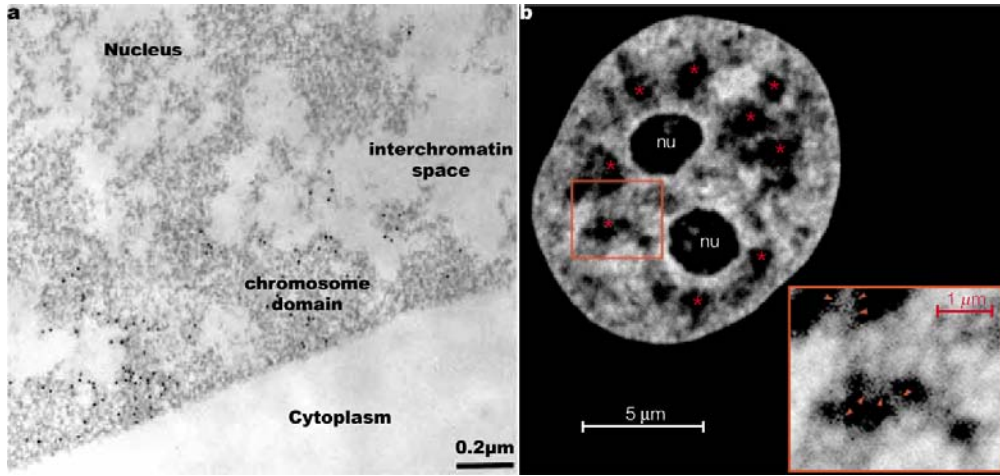


Figure 1.4: The inter-chromatin compartment. Chromosome domains and inter-chromatin space seen by a) electron microscope (Image adapted from [36]) and b) laser confocal microscope sections through a HeLa cell nucleus with green fluorescent-protein (GFP)-tagged H2B (Image from [37]). b) Section showing GFP-tagged chromatin (high density, white; low density, gray), two nucleoli (nu) and the inter-chromatin compartment (IC) space (black).

1.1.3 Spatial organization of chromatin and chromosome territories

The level of nuclear organization within interphase and metaphase cells has been studied over decades. Early hypotheses suggested that chromosomes occupy defined positions within the cell nucleus. One supporting example for this assumption included the peripheral positioning of the sex chromatin body (representing the inactive X-chromosome at interphase) in cells of eutherian females (placental mammals). This inactive chromosome (Barr body) is located at the nuclear periphery and was therefore the most convincing evidence for a non-random position of a chromosome [30]. More recent investigations are based on *in situ* hybridization techniques to identify individual chromosomes or regions in the interphase nucleus. This led to major advances in the analysis of nuclear organization. Chromosome painting and confocal microscopy of mammalian interphase cells showed that chromosomes occupy discrete territories within the nucleus. Such analyses revealed that the spatial arrangements of these territories are non-random [31, 32, 33] and in a radial configuration [34, 35] (see Figure 1.4).

The non-random arrangement of chromatin has been investigated in studies where the spatial distribution of chromosomes in the interphase nucleus was measured. The findings suggest that gene-rich chromosomes, such as human chromosome 19, locate towards the interior of the cell nucleus, whereas gene-poor chromosomes such as human chromosome 18 and the inactive X-chromosome are found towards the periphery of the cell nucleus. Generally the results suggest that the intranuclear arrangement of a human chromosome is correlated with the large-scale replication domains, even before DNA replication [38]. These findings

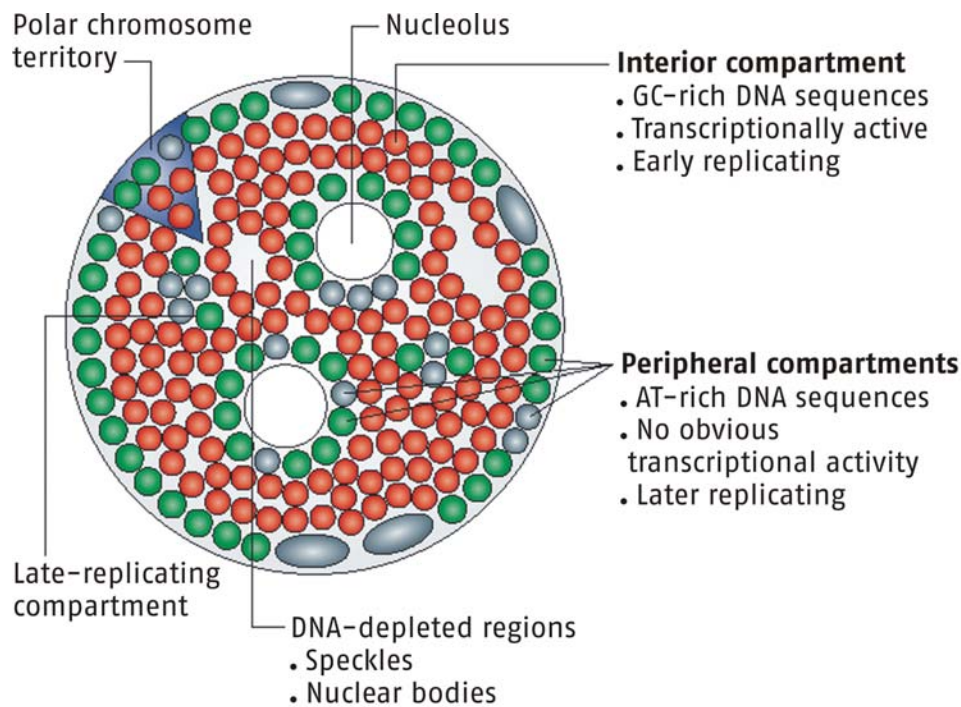


Figure 1.5: Chromosomal territories and their nuclear localization in relationship to the different chromosomal bands observed during mitosis and their functional characteristics. As the nucleus reassembles after mitosis, distinct chromosomal bands segregate into different regions, giving rise to polar chromosome territories. Alignment of polar chromosome territories results in the establishment of distinct higher-order genome compartments, with functionally distinct chromatin fractions. (Image adapted from [43])

could be validated for other cells in a cross-species study where seven different primate species were subjected to comparative analysis of the radial distribution pattern of human chromosome 18 and 19 homologs by three-dimensional fluorescence *in situ* hybridization [39]. These publications support findings where the position of actively transcribed, early-replicating DNA is located towards the center and late-replicating that correspond to inactive (low transcription rate) DNA is located to the periphery of the nucleus, respectively [40]. This higher-order organization is also seen within chromosome territories where active genes tend to locate towards the periphery and inactive genes towards the interior of the nucleus [37, 41] (see Figure 1.5). In mouse lymphocytes gene silencing that is associated with the repositioning of genes close to centromeres has been observed [42].

Recent studies suggest that the chromosomal positioning within the nucleus is dependent on its individual size. Experiments where the radial distances of chromosomes were measured showed a nonrandom distribution correlation with chromosome size. Small chromosomes were distributed significantly closer to the center of the nucleus or prometaphase rosette, while large chromosomes were located closer to the nuclear rim. This distribution is independent of the chromosomal gene density [44]. Moreover recent publications described that

chromosome positions might vary through the cell cycle [45]. However, a partial inherited chromosome arrangement can be observed over several cell proliferation cycles [46, 47].

A possible explanation why chromosomes occupy distinct nuclear domains could come from the fact that chromosomes decondense only to a limited extent after mitosis. The compaction of chromatin was measured in HeLa cells by 4D chromatin intensity measurements of H2B stained cell nuclei. It was shown that in early G1 chromatin is only four to five times less compact than in late anaphase [48]. These results might imply that the biggest part of most chromatin of a chromosome stays close together in a condensed conformation. Additionally one can hypothesize that chromosomes are rather condensed in their default state interphase. Only those loci that are transcriptional active might be more decondensed. This idea of well-defined (compact) chromosome territories has been extended. It has been observed that transcriptional active loci can be located on subchromosomal domains which loop out up to several microns away from the main body of the territory [49, 50, 51]. Such loops could probably intermingle with chromatin from other chromosomes. There is no direct data confirming this hypothesis, however, publication showed that gene loci lie far from the territory itself [52, 53].

Other interesting findings were the description of so called ridges [54, 55, 56, 57, 58]. Ridges are found to be very gene-dense domains with a high GC content, a high SINE (short interspersed nuclear element i.e. *Alu* sequences) repeat density, and a low LINE (long interspersed nuclear element) repeat density and are further characterized by high gene expression levels in a variety of cell types. In this context these domains might be an integral part of a higher order structure in the genome related to transcriptional regulation [57]. The major histocompatibility complex locus is one of these domains. Recent findings suggest that ridges coincide with large chromatin loops that extend away from the body of their chromosome territories [49]. An additional supportive feature was the discovery that transcriptional up-regulation of genes in the major histocompatibility complex by interferon-gamma led to an increase in the frequency with which this large gene cluster was found on an external chromatin loop [51]. In conjunction with this study, similar large-scale chromatin structure remodeling events induced by a strong transcriptional activator have been described in preceding studies [59].

In the next section we will look at a special case of chromosome positioning and organization. The X-inactivation process is a very complex cellular procedure to selectively inactivate a single chromosome and maintain its silenced state. Some of the described nuclear components are vital for the success of the inactivation mechanism and therefore important for the overall survival of the cell.

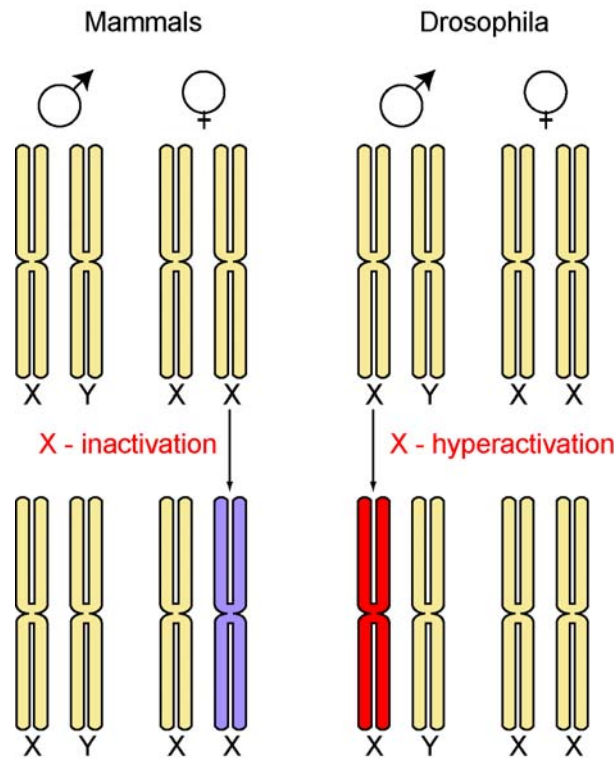


Figure 1.6: Different strategies for X-chromosomal inactivation. Dosage compensation of protein transcription in male and female animals has to be properly regulated and assured. Many animals show a specific gender determined sex chromosomal distribution. Mostly the female carries two or more X-chromosomes whereas males can carry an equal balance of X and a Y chromosomes. To ensure proper dosage compensation between the two genders the transcription rate originating from the X's has to be regulated. In female mammals and female marsupial animals all X's except one will be inactivated whereas in males the single X escapes the inactivation process. In insects i.e. *Drosophila melanogaster* a different strategy has evolved. Instead of inactivating the female X's the male organism hyperactivates the transcription rate of the single X to ensure proper dosage compensation while the female X's escape this process.

1.2 X-chromosomal inactivation

1.2.1 Introduction

In 1961 Mary Lyon suggested that the transcriptional silencing of one X-chromosome in female cells should ensure dosage compensation of X-linked genes between male and female mammals (see Figure 1.6) [60].

The silencing of one X-chromosome in mammals occurs early in development and it was shown that the process of X-inactivation occurs at random, such that the paternal or maternal X-chromosomes are silenced with the equal probability [61, 62, 63, 64]. This unique strategy has to encompass mechanisms that orchestrate the different treatment of two identical X-chromosomes in the same nucleus. Once the inactivation took place it has to be maintained throughout

countless cell divisions. Random X-inactivation is thought as a multistep process involving counting of chromosomes, choice of the active X-chromosome (Xa), initiation and spread of silencing on the inactive X-chromosome (Xi) and subsequent maintenance of the Xi's silent state. To investigate the X-inactivation processes more thoroughly mouse embryonic stem (ES) cells have become an invaluable tool. ES cells are derived from the inner cell-mass of the blastocyst, a developmental stage where random X-inactivation has not yet occurred. Thus, female ES cells undergo random X-inactivation after being induced to differentiate *in vitro* [65].

The X-inactivation is a highly complex process which follows precise and timely coordinated procedures (see Figure 1.7). At the beginning of differentiation a non-translated RNA is mandatory for the initial phases of X-inactivation. The transcription of a X-inactivation-specific RNA is upregulated on the Xi and starts to coat the chromosome in *cis* and initiates the inactivation process. The RNA transcription rate on the Xa remains low throughout the whole process and gets even downregulated at later stages. After the initial triggering phase additional coordination factors such as epigenetic histone modifications become more and more important in setting up the final inactivated state of the Xi.

In the next chapter I will describe in detail the very complex mechanism of X-chromosomal inactivation according to the coordinating elements such as the X-inactivation center (Xic) and the counting and choice regions. Finally an overview of the maintenance of the inactive X-chromosomal state over the cell cycle and the importance of X-inactivation during the developmental stages will be given.

1.2.2 X-inactivation center (Xic)

The initiation of X-inactivation is dependent on a master X-inactivation center (Xic) (see Figure 1.8) [67]. The Xic is the main control locus for X-inactivation. The most important gene within the Xic locus is the X-inactivation specific transcript (*Xist*) gene. It has been found that *Xist* is exclusively transcribed from the inactive X-chromosome [68]. The mature *Xist* molecule is a non-translated RNA, 17 kb in length and without any conserved open reading frames [69, 70]. The *Xist* sequence contains a number of regions consisting of tandem repeats. Further it has been shown that *Xist* RNA is not associated with the translational machinery of the cell and is located almost exclusively in the nucleus [70].

Xist has been shown to be the important part in choice and spreading of the future Xi [71, 72, 73]. Interestingly, even though *Xist* is present on inactive X-chromosomes throughout the life of an organism, it is only in the first phase of X-inactivation directly involved in transcriptional silencing but it is not required for its maintenance in somatic cells [74]. The first stages of inactivation are dependent on continued *Xist* expression. This expression is not accompanied by any of the later characteristics of the inactive X, such as histone hypoacetylation and late replication timing. In cells that have been induced to differentiate, *Xist* must be expressed during the first 48 hours of differentiation to initiate ectopic silencing. However, the inactivation process can be reversed

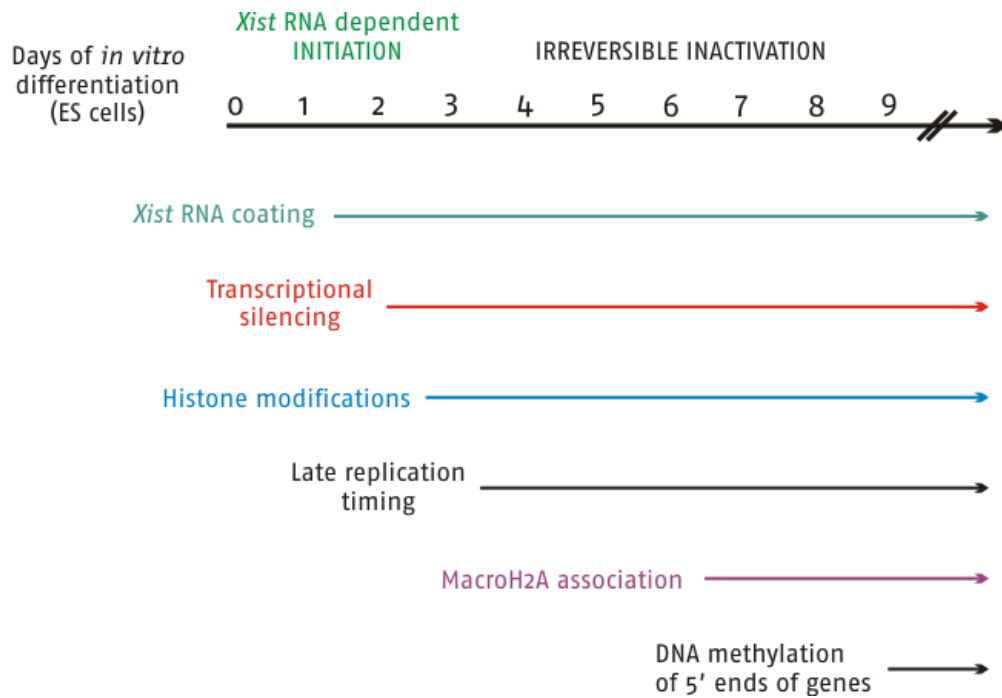


Figure 1.7: Complex timing processes during the inactivation processes. The X-inactivation process in female mouse ES cells is a highly coordinated process. Different molecular mechanisms have to be timely orchestrated to ensure the proper initiation, progression and maintenance of X-inactivation. One of the earliest visible components after initiation of the inactivation is the expression of *Xist* on the Xi. *Xist* is essential during the first hours of inactivation. At later stages other factors like histone modifications such as (de-)acetylations or (de-)methyations, later replication timings of the Xi and MacroH2A histone association support and coordinate the process. It seems interestingly that the initial inactivation phase with starting *Xist* expression is reversible within 72 hours. After this period the previously described controlling factors do not allow a reversion of the inactivation process. (Image adapted from [66])

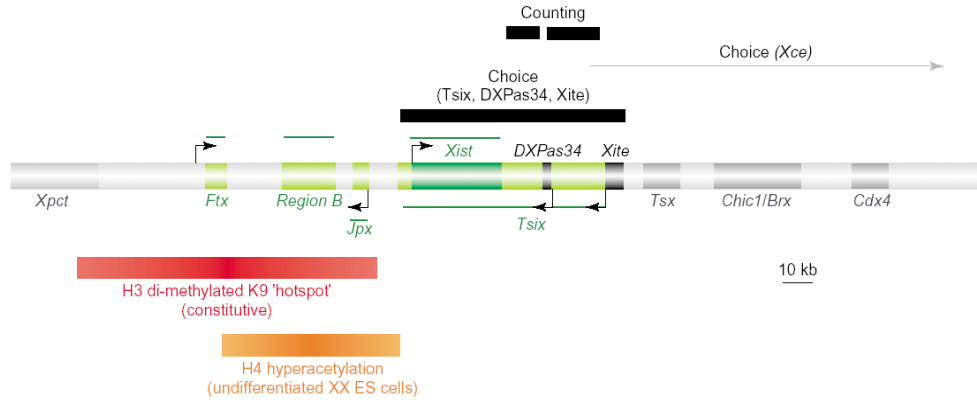


Figure 1.8: Functional elements within the X-inactivation center. The Xic region, as defined by deletion and transgenesis analyzes, is shown, together with important functional elements. Genes shown in green produce non-coding transcripts (green lines). Genes shown in gray produce protein-coding transcripts and have no known Xic related function. Above the map, regions shown in black encompass elements defined by targeted deletions involved in counting and choice. Counting is the process whereby a cell senses the number of X-chromosomes that are present and ensures that only a single X-chromosome remains active per diploid autosome set, all supernumerary X-chromosomes being inactivated; choice concerns the selection of the X-chromosome that will remain active or that will be inactivated. The candidate region for the genetically mapped Xce locus involved in choice is shown in gray. Below the map, the red bar represents a “hotspot” domain of histone H3K9 dimethylation, which is constitutively present in male and female ES cells before and after differentiation; the orange bar represents a hotspot of H4 hyperacetylation, present only in female ES cells prior to differentiation. (Image from [76])

by downregulation of *Xist* expression. Once 72 hours of differentiation have elapsed, continued silencing is no longer dependent on *Xist* expression and the full range of secondary X-inactivation characteristics are acquired [67, 75].

In all phases, the *Xist* RNA is locally constrained to the territory of the inactive X-chromosome [77, 78]. This is in contrast to almost any other RNA species that freely diffuses throughout the nucleus [79, 80]. *Xist* exclusively spreads in *cis* to neighboring regions from its site of transcription of the same chromosome until it essentially “coats” the entire inactive X-chromosome. Spreading in *trans* to other non-X-chromatin regions that may even be spatially closer has never been observed.

The molecular basis of the very low mobility of *Xist*, and the mechanism that imparts its local constraint, are currently unclear. Earlier experiments have suggested that diffusion of *Xist* is prevented by binding to components of the nuclear matrix [81]. It was recently demonstrated that SAF-A is enriched in the territories of the inactive X-chromosome and might bind *Xist* and restrain therefore its movement within the Xi territory [23, 22]. Additional analyses by fluorescence *in situ* hybridization (FISH) showed that *Xist* appears highly particulate and is located to a large nuclear domain that corresponds to the space occupied by the Xi [78]. There a three-dimensional analysis showed that *Xist* RNA is not just bound to the surface of the Xi, but seems to reside within

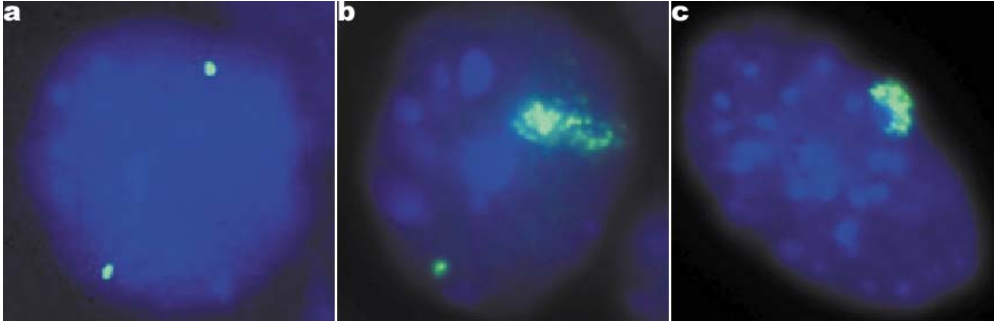


Figure 1.9: *Xist* transcription in embryonic stem cells. Patterns of *Xist* RNA expression in female ES cells undergoing differentiation using RNA fluorescence *in situ* hybridization. a) Image shows undifferentiated ES cells that have two punctuate *Xist* RNA signals, representing the presence of unstable *Xist* transcripts at the site of transcription on both (active) X-chromosomes. b) upon differentiation, *Xist* RNA from one of the two alleles becomes stabilized and coats the X-chromosome that is to be inactivated *in cis*. The X-chromosome that remains active continues to express *Xist* in its unstable form. c) *Xist* expression in fully differentiated cells. *Xist* RNA coats the inactive X-chromosome and the *Xist* gene on the active X has been silenced. (Image adapted from [67])

the entire space delineated by the Xi [78].

Prior to the X-inactivation process the *Xist* RNA can be detected as a pinpoint signal at the site of its transcription on all X-chromosomes, which are active at this point. It was shown that in undifferentiated ES cells low-level *Xist* expression was detected from the single Xa in male cells and on both Xa's in female cells. Upon differentiation *Xist* expression was detected only in female cells, in which *Xist* RNA colocalized with the entire Xi [82]. These findings were supported by the observation of differentiating female mouse ES cells that showed an increase of *Xist* expression from the Xi prior to silencing. On the contrary the Xa showed low-level transcription of *Xist*. It was suggested that the transition from low level to high level expression is regulated by the stabilization of *Xist* transcripts at the Xi [83] (see Figure 1.9).

Consistent with this role in X-inactivation, *Xist* levels increase dramatically in female but not male cells in the developmental window in which silencing of the X-chromosome occurs [84]. Additionally it was found that after the differentiation process, transcription of unstable RNA from the active X-chromosome allele continues for a period. This shows that a stabilization and accumulation of *Xist* transcript on the Xi allele is of importance for the inactivation process [85].

1.2.3 Counting

The counting process senses the X-chromosome to autosome ratio and ensures that the X-chromosome inactivation initiates in the female (XX) but not in the male (XY) mouse ES cells. Counting is regulated by the Xic locus, which contains the *Xist* gene. In earlier studies it has been shown that *Xist*, introduced onto an autosome, is sufficient by itself for inactivation *in cis*. It was observed

that *Xist* RNA becomes localized at the autosome into which the gene is integrated. This suggested that the elements required for some aspects of chromosome counting are contained within the inserted Xic construct and that the *Xist* RNA might be required for some aspects of chromosome counting [86]. For this purpose transgene mouse ES cell lines have been established because they represent an essential and stringent test tool for defining the minimal region that can carry out the functions attributed to the Xic. To detect aberrant behaviors during the inactivation process constructs containing the Xic and additional up- and downstream flanking region were introduced in mouse ES cells. In the search for a possible region responsible for the counting events these sequences were subsequently narrowed down and tested. It was found that the insertion of 450 kb of a multicopy murine Xic/*Xist* sequence onto autosomes activates female dosage compensation in male ES cells [87]. Particular in this study *Xist* was successfully induced upon differentiation and was then expressed from both endogenous and ectopic loci. This leads to successful and proper chromosomal inactivation and suggests that elements responsible for correct counting and choosing Xs are present on this particular Xic transgene sequence [87]. The ectopic multicopy Xic integration resulted in chromosome-wide changes that are characteristic for the Xi.

However, the introduction of different yeast artificial chromosomes (YACs) constructs into ES cells, it was found that single-copy transgenes, unlike multicopy arrays, can induce neither inactivation in *cis* nor counting [88]. These results demonstrate that despite their large size and the presence of *Xist*, the single copy construct lacks sequences critical for autonomous function with respect to X-inactivation. A possible conclusion might be that single-copy Xic transgenes may be lacking sufficient numbers of repeat elements, or “way stations” necessary for the nucleation and propagation of the *Xist* RNA-mediated signal along the chromosome [89]. Based on this hypothesis a recent publication suggested that LINEs (long interspersed nuclear elements) act as booster elements to promote the spread of *Xist* mRNA [67] (see Figure 1.10). From a molecular view LINEs contain a reverse-transcriptase-like gene that might be involved in the retro-transposition process in the human or mouse genome. An example is the human element LINE-1, which is 6.1 kb and has a copy number of 516'000 in the human genome.

Indeed, the X-chromosome is particularly rich in LINE sequences. Contact of the *Xist* RNA might cause the LINE elements to be sensed as repeated elements by the cell's system for repeat-induced gene silencing. This leads to the silencing of these elements and their conversion to heterochromatin [91]. Globally such a step by step reaction would eventually lead to a fully inactivated chromosome. A supportive fact in correlation with single-copy transgenic cell lines is that the LINE density in the region covered by these defined Xic/*Xist* transgene regions is not particularly high, which would correlate with the need of multiple copy inserts [89]. These multiple insertions might compensate for the missing in LINEs and override the normal but fragile *Xist* spreading pathway by brute force overexpression of the relevant transcript.

Beside the possible involvement of LINEs in the counting process, recent studies have identified a 65 kb region downstream to *Xist* that affects X-chromo-

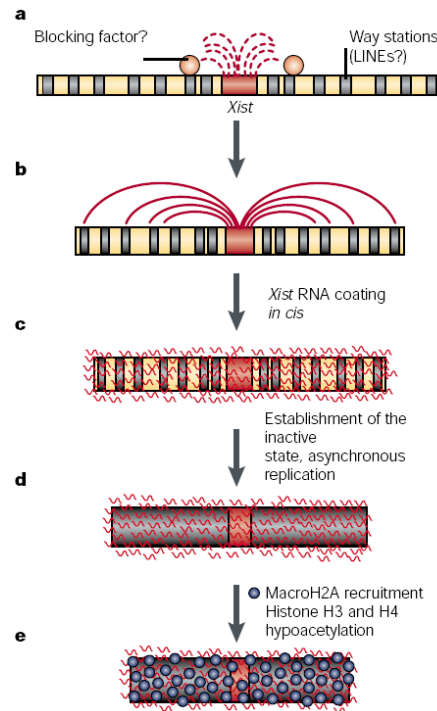


Figure 1.10: Model for X-inactivation. The model shows possible roles of some putative players in the initiation of X-inactivation. a) Before inactivation, *Xist* RNA is expressed in an unstable form (dotted red lines) and the possible blocking factor(s) (red) prevents *Xist* upregulation and/or its association with the chromosome *in cis* on the Xi. b) With ongoing inactivation *Xist* RNA becomes upregulated through stabilization, transcriptional upregulation or release of the blocking factor. LINEs might participate in the spreading process in some way. This spreading event might be either through association with nucleoprotein complexes including *Xist* or by a mechanism such as repeat-induced gene silencing (RIGS). RIGS is a mechanism observed in several organisms where transgene expression may be silenced epigenetically when repeated sequences are present. It has been proposed that interactions between homologous sequences (repeats) might lead to the formation of folded chromatin structures that attract heterochromatin-specific macromolecules [90]. c) Stabilized *Xist* RNA coats the X-chromosome before its inactivation. d) Transcriptional silencing of genes on the X-chromosome occurs as a result of *Xist* RNA coating using an unknown mechanism. The coating event is rapidly followed by a shift to asynchronous replication timing of the X-chromosome. e) Chromatin modifications, such as the histone deacetylation and methylation of promoters of X-linked genes, as well as the recruitment of the histone variant macroH2A, presumably transform the *Xist* RNA-coated chromosome into a stably inactive and condensed chromatin state. (Image from [67])

some counting by another mechanism, namely by affecting histone modifications in this sequence. It was found that deletion of the region significantly disturbed the counting process. A possible explanation is that an elementary histone H3 Lys-4 dimethylation site lies within this deleted sequence that might interact with *Xist* to coordinate the highly complex counting process [92]. Whether other up or downstream elements to *Xist* are important has to be elucidated in the future.

Another explanation for the counting process might be nuclear compartmentalization. As previously introduced an important way of regulating gene expression is the localization of genes within specific nuclear compartments [93, 94]. Subnuclear domains enriched in factors specialized in particular nuclear functions may provide a nuclear context that influences chromatin architecture and gene expression independently of their flanking sequences. Therefore the different spatial localizations of the X-chromosomes were one of the earliest models proposed to explain the differential treatment of the two X-chromosomes during X-inactivation [93]. The hypothesis for counting suggested that the Xic on the X-chromosome is sequestered to a particular nuclear region, e.g. the NE, in order to maintain its active state and to prevent it from exposure to factors involved in triggering X-inactivation. Another, not mutually exclusive hypothesis proposes transient co-localization, or “cross-talk”, between Xic’s, as reported for imprinted loci [94]. Such cross-talk might help the cell to count or “sense” the number of present X-chromosomes and ensures that only one X-chromosome remains active. This is supported by findings where cross-talk between *Xist* alleles has previously been proposed to be involved in the choice of the X-chromosome to inactivate during initiation [71].

Later in this thesis I will describe the effects of Xic localization and its implications on the counting process in mouse ES cells.

In conclusion, transgenic mouse ES cells studies have revealed that the potential for chromosome-wide gene regulation is not intrinsic to X-chromosomal DNA, but can also occur on autosomes possessing the Xic [88]. The presented data in this chapter showed that artificially integrated Xic sequences result in long-range *cis* effects on the autosome that resemble those found on an inactivated X. This implies that the Xic can both initiate X-inactivation and drive heterochromatin formation in *cis* independent of its localization.

1.2.4 Choice

During the X-chromosomal inactivation the cell has to choose which of the two apparently similar X’s is going to be inactivated. Although in mammalian cells this chromosome selection is random it is coordinated by defined factors. Again, the use of transgenic mouse cell lines has largely contributed in finding the responsible sequences of choice. Although counting and choice can be seen semantically similar, their functions and roles are different. Like the deletion of counting element sequences, deletions of a choice element disturb X-inactivation in female cells. In contrast to a counting element deletion, the lack of a choice element does not result in aberrant and lethal X-inactivation in males.

The choice function of the Xic appears to be influenced by multiple elements

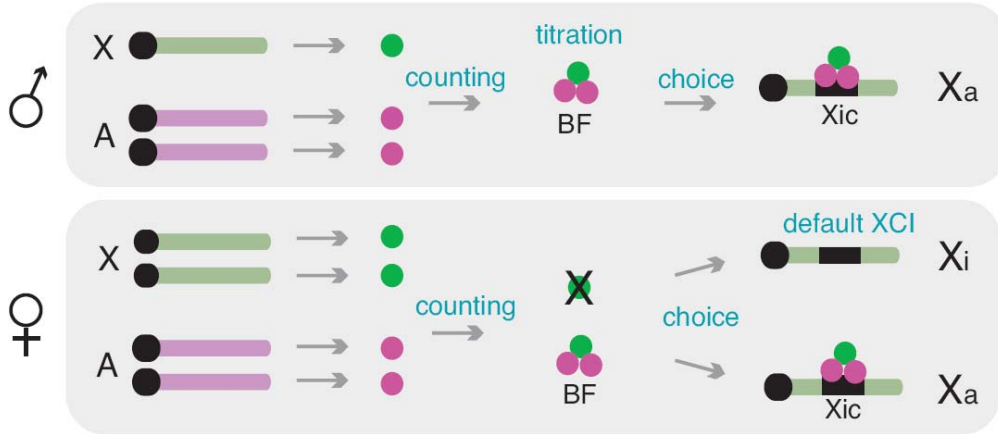


Figure 1.11: The one-factor model: “Counting” represents the titration of several factors (violet and green circles) to create a single blocking factor. The factors can originate from multiple distinct autosomes. Other options include that the blocking factors are diffusible molecules or one or several X-linked DNA sequences. “Choice” represents binding of the blocking factor to one Xic, thereby preventing the firing of *Xist*. The blocking factor designates the future Xa and the Xi forms by default. X: X-chromosome, A: autosome, XCI: X-chromosomal inactivation, BF: blocking factor. (Image adapted from [100])

spread across the Xic region. In addition to the genetically defined, but so far elusive, X-controlling element (Xce) locus, several targeted deletions lying 3' or 5' to or within *Xist* lead to a non-random X-inactivation process [95]. Deletion of the Xce locus in undifferentiated ES cells eliminates *Xist* expression and antisense transcription present in this region. Upon differentiation the deletion also led to nonrandom inactivation of the chromosome that contained the deleted transgene [63].

In 1999, several groups reported on the discovery of an antisense RNA to *Xist* (*Tsix*) which is influencing choice during the inactivation steps [96, 97]. The 40 kb RNA originates 15 kb downstream of *Xist* and is transcribed across the *Xist* locus. The *Tsix* RNA, like the *Xist* RNA, has no conserved open reading frames (ORFs). It seems to locate exclusively in the nucleus and more precisely at the Xic. Before the onset of X-inactivation, *Tsix* is expressed from both X-chromosomes. At the onset of X-inactivation, *Tsix* expression becomes monoallelic, associated with the future Xa and persists until *Xist* is turned off. *Tsix* is not found on the Xi once cells enter the X-inactivation pathway [98]. Another group reported in parallel of the correlation of Xa hypermethylation and allelism at the Xce [63]. Recently it has been shown that the duration and strength of *Tsix* transcription (*Tsix* hypertranscription) is sufficient to block *Xist* RNA accumulation in a *cis*-limited manner. It was proposed that *Tsix* transcription is necessary to decrease *Xist* activity on the future Xa. On the other hand *Tsix* repression is required for *Xist* RNA accumulation on the future Xi [99]. Interestingly, the same group found that choice is mediated by a *Tsix* promoter activity independent mechanism.

Recently a *cis* element in the mouse Xic called *Xite* was discovered. *Xite*

harbors intergenic transcription start sites and regulates *Xist*. It is suggested that *Xite* is a candidate for the Xce that can skew choice during X-inactivation [101]. Additionally other non-coding RNA transcripts have been identified in the 5' region of *Xist*. It has been shown to have high affinity to histone modification factors early after the onset of X-inactivation [102]. Other non-coding transcripts that also partially escape from X-inactivation map to an unmethylated CpG island 10 kb upstream of *Xist* [103]. Whether these represent functional RNAs, like *Xist*, or whether they are involved in regulating inactivation is not known.

Another interesting aspect is that mammalian cells have to define a single Xa, and then inactivate the remaining X-chromosome(s). Therefore the cell has to choose between two apparently identical X-chromosomes and randomly place a differentiating mark on only one of them, e.g. the future Xa. Most models propose the existence of an autosomal blocking factor. This hypothetical factor which is produced in limited quantity is responsible for setting a mark to the Xic of a single X-chromosome per diploid cell, protecting it from inactivation [104]. The amount of blocking factor activity must be determined by autosomal ploidy such that each diploid set of autosomes produces sufficient blocking factor to choose only one Xa. The interaction of the blocking factor with the counting element on the Xa finally interferes with the *Xist* RNA silencing function on this chromosome. The counting element can therefore be seen as the fundamental *cis*-element required for choosing the Xa (see Figure 1.11).

A second model proposes the presence of two factors, namely a blocking factor, that protects the future Xa and an X-linked “competence factor” that induces inactivation on the future Xi [105] (see Figure 1.12). In this respect, recent results suggest that *Tsix* and *Xite* are not only involved in choice but also play a vital part in counting supporting a two factor inactivation model [100].

1.2.5 Maintenance

Several lines of evidence indicate that after X-inactivation has been established, *Xist* is no longer required for maintenance. In studies using mouse-human somatic cell hybrids, a human Xi chromosome fragment that lacked the *XIST* gene remained transcriptional silent [74]. Similar results have been obtained with human leukemia cells where an Xi-derived isodicentric chromosome maintained its inactive state despite missing the *XIST* gene [106].

In order to understand the function of *Xist* during the inactivation but also the function of other epigenetic marks in the maintenance state it is important to characterize chromatin changes. Histone modifications like acetylations, methylations, phosphorylations and ubiquitinations represent important ways of regulating gene expression [107, 108]. Especially temporally coordinated histone modification seems to play an important role in the initiation and maintenance of the X-chromosomal inactivation [109]. In this respect, it has been reported that methylation of histone H3 at lysine 9 on the Xi occurs immediately after *Xist* RNA coating and before transcriptional inactivation of X-linked genes. This X-chromosomal H3 Lys-9 methylation occurs during the same time win-

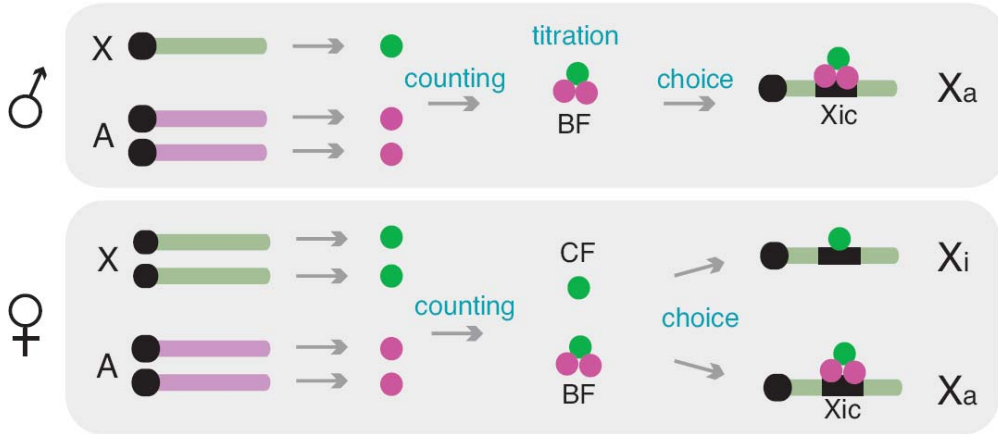


Figure 1.12: The two-factor model: “Counting” represents the titration of autosomal (violet circles) and X-linked factors (green circles) to form blocking factors. Any untitrated X-linked factor becomes a competence factor for the future Xi. This hypothetical factor can be a diffusible *trans*-acting factor or a *cis*-acting DNA element. In this context, “Choice” reflects binding of the blocking factor to *Tsix* on the future Xa and binding of the competence factor on the future Xi to elevate *Xist* expression. The mutually exclusive binding of the blocking and competence factor could be mediated by *Tsix* or *Xite*. X: X-chromosome, A: autosome, BF: blocking factor, CF: competence factor. (Image adapted from [100])

dow as H3 Lys-9 hypoacetylation and H3 Lys-4 hypomethylation. So far these Histone H3 modifications were the earliest known chromatin changes during X-inactivation [110]. A possible mechanism would identify this H3 Lys-9 methylation 5' to *Xist* as unique “hotspot” which might be a nucleation center for *Xist* RNA-dependent spread of inactivation along the X-chromosome [110]. Detailed analysis of histone tail modification states showed that the hypomethylation of Arg-17 and that of Lys-36 on histone H3 also characterize the Xi. These modifications are also found at early phases of the initiation of X-inactivation [111]. Furthermore it was found that the chromosome which is undergoing inactivation is subject to a shift in replication timing. This occurs slightly later than the *Xist* RNA coating and the chromatin modifications [111]. Recent findings showed that Histone H3K9 dimethylation and K27 trimethylation characterize the Xi in somatic cells. It is shown that the dynamic changes of H3 Lys-9 and H3 Lys-27 methylation on the inactivating X-chromosome compared to the rest of the genome are distinct. Methylation suggests that those two modifications play complementary but perhaps non-redundant roles in the establishment and maintenance of X-inactivation [112].

These findings demonstrate that the inactive X-chromosome is hypoacetylated for histone H3 in female mammalian cells and show that hypoacetylation of core histones may be a general feature of the chromatin along the Xi [113]. Especially the enrichment for H3 methylated at Lys-9 is a distinguishing mark of facultative heterochromatin on the Xi. It is interesting that also depletions of methylations at Lys-4 on the Xi can occur and influence facultative heterochromatin formation [113]. This data might demonstrate that differential

methylation marks at two distinct sites of the H3 amino terminus correlate with contrasting gene activities and may be part of a histone code involved in establishing and maintaining facultative heterochromatin. A supporting finding of this theory was that at later stages, e.g. before mitosis, characteristic histone modification patterns can be found on the Xi [111]. Despite the importance of histone modification factors it was recently demonstrated by *in vivo* mobility experiments that the previously introduced SAF-A (see nuclear matrix) is a component of a highly stable proteinaceous structure in the territory of Xi, which might act as a platform for immobilizing *Xist* RNA during the maintenance phase of X-inactivation [23].

Another interesting aspect is a possible involvement of the members of the Polycomb group PRC2 complex such as Eed and Ezh2/Enx1 in the X-inactivation process [67]. Ezh2/Enx1 is a histone methyltransferase capable of trimethylating H3 Lys-27 [114]. It was found that the Ezh2/Enx1 was recruited to the inactive X-chromosome in what appears to be a *Xist* RNA-dependent fashion [115, 116]. The dimethylation of H3 Lys-9 on the Xi may not be *Xist* RNA-dependent and may be mediated by a different HMTase and/or complex [117, 112]. Therefore the polycomb group proteins are excellent candidates for participating in the cellular memory of inactivity. This proposal is based on genetic studies in *Drosophila melanogaster* showing their role in heritability of the silent states [118]. In the case of mammalian X-inactivation, members of the PRC2 complex and H3 Lys-27 methylation are recruited to the X, potentially via *Xist*, during the early stages of X-inactivation [76]. However, recruitment to the Xi of PRC1 complex members and, in particular, of the Polycomb protein, which in *Drosophila* can bind H3 trimethyl Lys-27, has not been reported so far. It seems highly likely that at least some mouse Polycomb homologs will indeed associate with the Xi [119]. However, the understanding of the role of the Polycomb group proteins in maintaining the inactive state of the X-chromosome is still very rudimentary and their functions have to be elucidated in future studies.

1.2.6 Developmental View

X-inactivation exists in an imprinted and a random form. Based on phylogenetic analysis it has been proposed that imprinted X-inactivation may represent the ancestral state of this process, arising more than 130 million years ago in metatheria [120]. Marsupials mammals, such as the kangaroo, undergo non-random inactivation and shut off the paternal X-chromosome (Xp) (also known as imprinted X-inactivation) (see Figure 1.13) [121, 122].

In eutherians, inactivation takes place randomly in the soma so that either the paternally or maternally inherited X-chromosome can be silenced. Remains of imprinted inactivation with only the paternal X-chromosome being inactive and the maternal X remaining active can be observed in the extra-embryonic tissues of eutherian mammals [123, 124]. The mammalian imprinted inactivation only occurs between the two cell state and carries on to the blastocyst state where nearly all cells contain an inactive Xp. The inactive state of the Xp is kept in the trophectoderm and primitive endoderm over the whole development stage. In contrast, the Xp in the inner cell mass becomes reactivated again

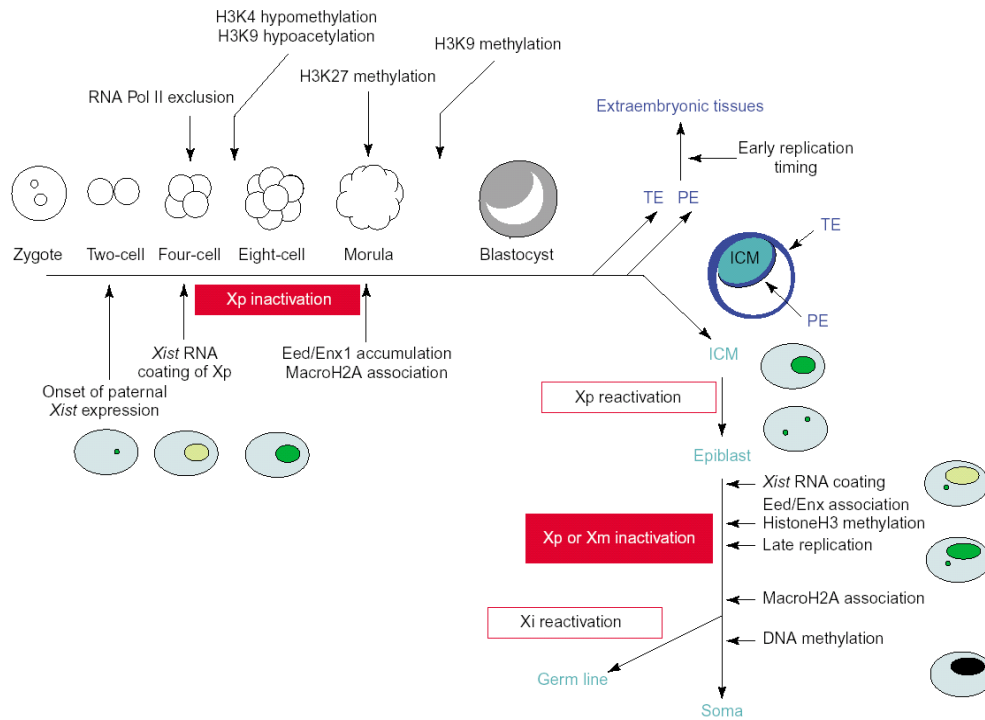


Figure 1.13: Kinetics of X-inactivation during pre-implantation mouse development. The dynamic X-inactivation events that occur in pre-implantation embryos are depicted. At the two-cell stage, *Xist* expression has just begun and is localized to its site of transcription (shown as a small spot). At the four-cell stage, *Xist* RNA is accumulated over the parental X-chromosome (shown as a domain). The initial silencing event triggered by *Xist* RNA coating occurs prior to Eed/Enx1 recruitment and H3K27 or H3K9 methylation of the X-chromosome. This event appears to be linked with H3 hypoacetylation and loss of H3K4 methylation. In the blastocyst, essentially all cells contain an inactive Xp associated with the PcG proteins Eed and Enx1. In the trophectoderm and primitive endoderm (extraembryonic lineages), this inactive state is maintained and perhaps further locked in by a shift in replication timing (early replication in this case). However in the inner cell mass the Xp becomes reactivated during the development. The Xp loses its *Xist* RNA coating and the Polycomb group proteins, and the histone methylation marks are gradually reversed. In this way, cells that will subsequently contribute to the epiblast (embryoproper) contain two active X-chromosomes, prior to the random inactivation of either the Xp or Xm. In the female germ line, which is set aside subsequently, the inactive X becomes reactivated just prior to meiosis. PE: primitive endoderm; TE: trophectoderm. (Image from [66])

during the development. The Xp loses its *Xist* RNA coating and the Polycomb group proteins, and the histone methylation marks are gradually reversed. This will subsequently lead to cells containing two active X-chromosomes in the inner cell mass. With progressing development random inactivation takes place in the embryonic cell lineages (epiblast) of these species.

In rodents, it has been proposed that the imprinted form of X-inactivation that occurs in the early embryo could represent the remains of an ancestral form of inactivation [125, 124]. However, in other placental mammals, such as humans, this form of inactivation has completely disappeared. These findings support the theory that random X-inactivation has evolved subsequently in placental mammals. This separate evolution would result in a clear selective advantage for random X-inactivation, especially in terms of controlling genetic traits.

Alternatively, the imprinting of the X-inactivation mechanism may have been exposed to selective pressures in specific mammals more than once during evolution. Evidence for such selection periods can be found in different species of mammals and their fundamental differences in their early development and extraembryonic tissue formation and their sexual differentiation and determination strategies [125, 126]. Interestingly, though the apparent similarities in imprinted X-inactivation between marsupials and the extraembryonic tissues of rodents no homolog of the *Xist* gene has been identified in marsupials to date [127]. Therefore the selection forces acting on X-linked gene expression during the development of different mammals are thus likely to be diverse. Moreover, imprinted X-inactivation may have evolved independently in marsupials and eutherians [128]. That might imply that imprinted X-inactivation may be very different between the two taxa.

As described above the paternal X is always prone to be inactivated for imprinted X-inactivation. There is clear evidence that there exists a mark on the maternal X-chromosome preventing it from inactivation. However, if there is an existing imprint on the paternal X-chromosome which might favor its inactivation is less clear [129]. One potential hypothesis suggests that preferential paternal X-inactivation could have evolved by using a form of inactivation observed in male germ cells of many species. The male meiotic sex-chromosome inactivation (MMSI) might involve the transient inactivation of the Xp and Y chromosomes [130]. The MMSI process prevents deleterious, illegitimate recombination events between the unpaired regions of the sex chromosomes and other chromosomes during meiosis [131]. One possible mechanism might be that the meiotically induced inactivity of the Xp is somehow transmitted to the female zygote and still may carry marker which predefines it for inactivation in early XX embryos [132, 129]. However, the comprehension of the causes of imprinted X-inactivation, and of the evolutionary similarities or differences between marsupial and rodent imprinted X-inactivation, can come only from the knowledge of the epigenetic marks and the early events underlying this process in different species [76].

In conclusion we have seen that inactivation is a highly complex cellular mechanism where still many detailed regulation pathways are unclear. In this context my main project will investigate the potential impact of the Xic po-

sitioning during the X-chromosomal inactivation for the counting mechanism in differentiating mouse ES cells. This is especially interesting since a recent study shows that interaction of gene loci might be involved in the coordination of complex nuclear mechanisms such as regulation of gene expression levels during T-cell development [133]. Before I present my results, I introduce general aspects important for biological microscopy image analysis. In the Material and Methods part I focus on specific image processing methods I used for my work (see Section 3.1) and the main tool, the Tikal image processing platform, that I have developed to perform successful data analysis on the later experiments (see Section 3.2).

1.3 Biological image processing

1.3.1 Introduction

The terms image processing, image analysis, machine vision and computer vision are defined very broadly. Rapidly the developments in image processing evolved from fields of active applications such as technical diagnostics, autonomous vehicle guidance, medical imaging (2D and 3D images) and automatic surveillance [134]. However, despite the fast development progresses in medical and industrial image analysis a deficit of methods for biological microscopy image analysis is noted. For this reason I will focus in this work on applicable image processing methods for mainly biological microscopy images. A variety of the presented algorithms originate from the industrial and medical image processing field but can often, with some modifications, be applied to microscopic images.

In the following chapter I will present possible data workflows and new approaches for microscopic image data analysis in biological applications in context with their underlying theoretical frameworks.

1.3.2 Workflow

Biological experiments using microscopes can provide useful quantitative information by pursuing common workflow procedures (see Figure 1.14). The images derived from this research field have to be processed after acquisition with a microscope since the raw data is commonly stored unmodified and bears lots of noise. Therefore the first step in the image processing workflow is a visual inspection of the data which gives information about the appropriate pre-processing methods needed to improve the overall image data quality, e.g. median or Gaussian filtering of the images.

After successful pre-processing the images can readily be visualized with volume rendering methods (see Figure 1.15). Volume rendering is a technique that allows displaying a complete 3D dataset at once and can be understood comparable to an X-ray image. The displayed image represents a projection through the image stacks where parts with high density appear more opaque and parts with low density are more transparent. This technique is good to obtain an overall impression of the 3D scene of microscopic images and can be

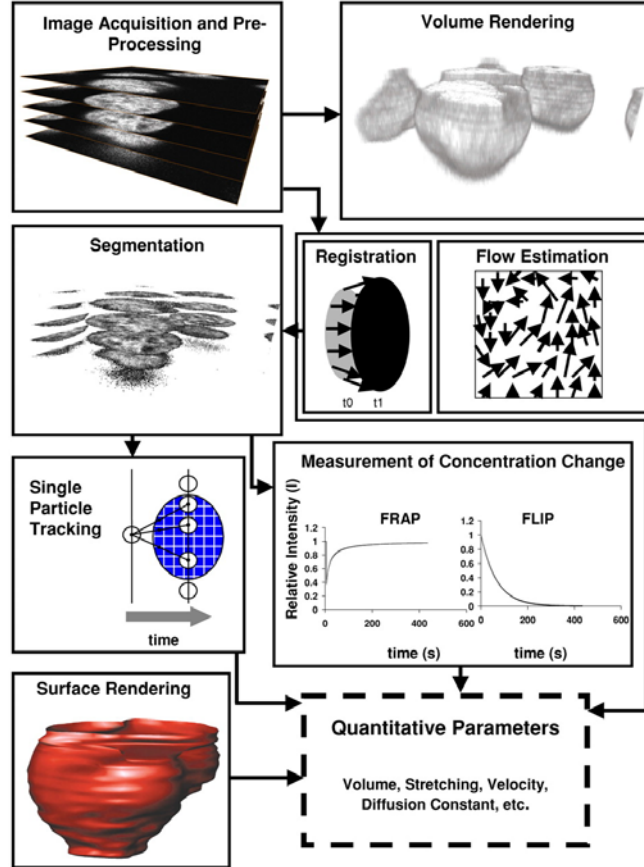


Figure 1.14: The typical workflow in computational imaging for biological microscopic 4D images. Once the images have been acquired by a microscope and pre-processed to improve the signal-to-noise ratio (SNR), they can be directly visualized by methods like volume rendering. For multiple objects in motion, single particle tracking, in which a particle is tracked over different time-steps, is the most direct method used to provide access to parameters such as velocity, acceleration, and diffusion coefficients. Segmentation is the basis for both surface rendering and kinetic measurements. Surface rendering is obtained after segmentation of contours in each individual slice and gives rise to volumetric measurements such as volume and surface area. Measurements of concentration changes for segmented areas in fluorescence recovery after photobleaching (FRAP) or fluorescence loss in photobleaching (FLIP) experiments give rise to estimates of kinetic parameters such as diffusion and binding coefficients. Image registration is used to eliminate movements of objects and can measure elastic or rigid changes of shape, i.e. comparison of cell nuclei. It is also often used to correct for global movement before further quantitative analysis. The estimation of the optical flow is an approach to quantify mobility in continuous space. All these processes lead to accurate estimates of quantitative parameters. (Image from [135])

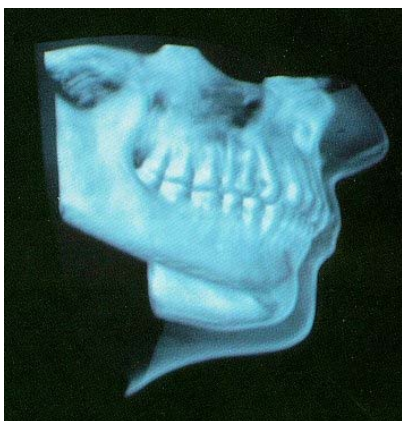


Figure 1.15: Volume rendering of a jaw overlaid by skin tissue. The technique is good to obtain an overall impression of the 3D scene of medical (and biological) images. (Image from [136])

best visualized as animated movies of the different complete scenes. However, no quantitative conclusion can be drawn from such techniques.

To allow a quantitative extraction of parameters such as volumes, surface areas but also velocities and diffusion constants of objects the images have to be segmented. Since segmentation is an essential procedure for quantification the overall approaches have to be very accurate to represent the image objects and will be explained in more detail later. Helpful tools for quantitative measurements of 3D objects and their properties in an image series are tracking algorithms or optical flow approaches. However, these are not the only applications to obtain relevant quantitative parameters and there are virtually no limitations in methods for quantifying biological processes, e.g. the measurement of gray-value recovery curves for defined regions of interest (ROI) in fluorescence recovery after photobleaching (FRAP) experiments (see Figure 1.16) or determination of protein or molecule associations and co-localizations with fluorescence resonance energy transfer (FRET) methods.

A final and important application for facilitating quantification and increasing the amount of extractable information is the use of registration algorithms. These methods can help to eliminate objects movements and deformations between two datasets by applying spatial transformations, e.g. correction of cell movements within an image series.

In conclusion, there is no strictly predefined workflow for biological image processing. Thus it is advisable to follow the roughly defined processing scaffold. This is composed of pre-processing, segmentation, registration, quantification (e.g. tracking) and visualization. This procedure is not only intuitive but, as I will show later, leads to accurate and reproducible extraction of parameters in huge datasets.

1.3.3 Pre-processing

Quantitative analysis of biological images is crucial for means of comparison of experimental data. Most of the qualitative description of processes observed in microscopic images could be explained by quantitative means by extracting the relevant features with the use of the proper tools, e.g. measurements of distances, velocities or volumes [138, 139, 134]. Especially for biological imag-

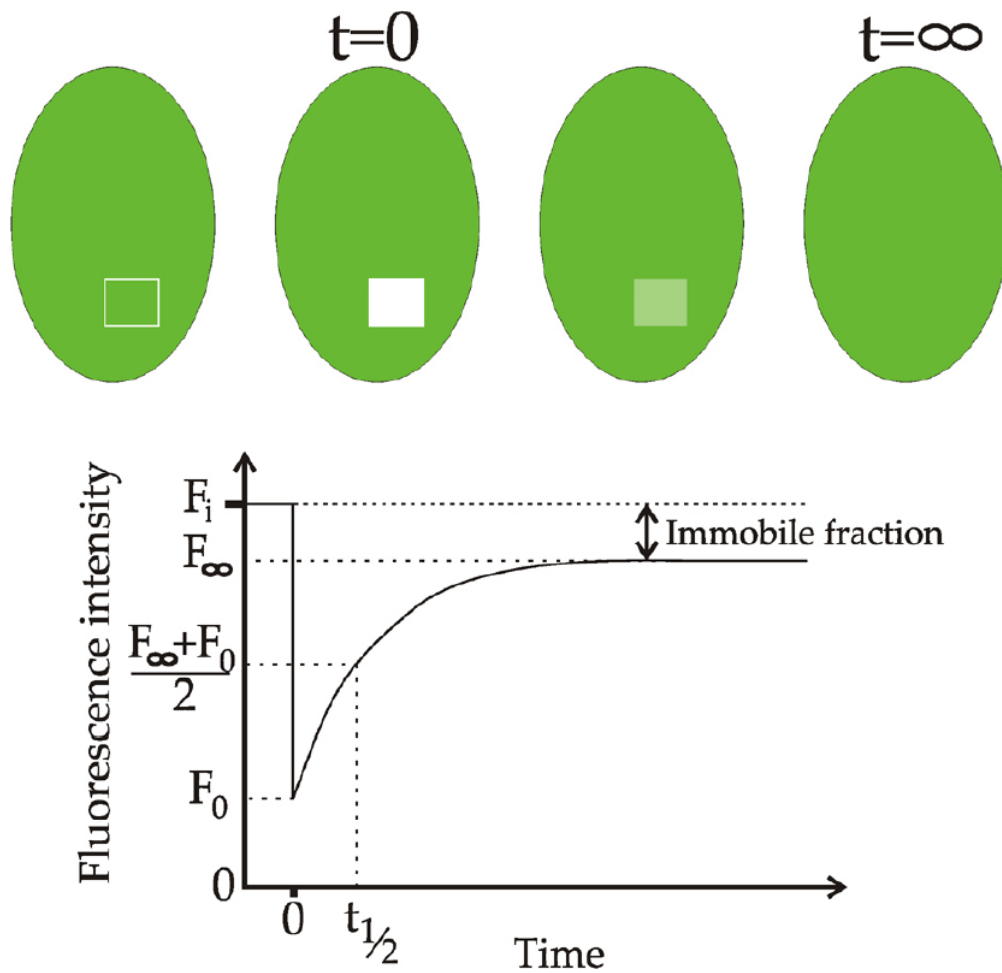


Figure 1.16: Fluorescent recovery after photobleaching (FRAP) and fluorescence recovery curve. Top) A local perturbation (white square) is introduced by photobleaching a fluorophore and the recovery of fluorescence is observed over time. Bottom) Fluorescence intensity in the bleached region of interest is measured over time and normalized to the total intensity. The immobile fraction can be measured by comparing the recovery at very long time to the initial intensity. Half time recovery is the time needed to reach half of the final recovery. (Image adapted from [137])

ing with microscopes lots of acquisition devices, such as laser scanning or wide field microscopes, are available to generate a vast amount of quantitative data. These images are often directly originating as raw data from the detectors, e.g. charge coupled device (CCD) cameras. These raw images are stored unprocessed and generally contain very noisy and blurred image features and a low signal-to-noise ratio (SNR) (see Figure 3.1). To obtain meaningful information such images have to be pre-processed prior to segmentation (e.g. binarization) and quantification (e.g. by using single particle tracking (see Section 3.1.4)). The pre-processing filtering methods can be roughly divided into distinguishable groups according to their final results; such as the linear and nonlinear smoothing noise reduction filters, gradient-based processing filters and edge preserving filters such as anisotropic diffusion filtering [140, 141].

Linear and nonlinear smoothing noise reduction filters

The first group of pre-processing filters include filters to reduce and suppress noise or other small fluctuations in the image and prepare images for further processing. Two different groups can be distinguished, namely the linear and nonlinear algorithms. The difference is that linear filters can be used for analysis in the Fourier domain whereas the latter can not [142].

For linear filters the output image is based on a local averaging of the input filter where all of the values within the filter area (filter kernel) have the same weight. This can be partially modified by implementations based on rectangular or circular filter kernels. The Gauss filter is a common implementation of a linear filter.

As already described non-linear filters do not have a frequency domain equivalent. But often images contain high frequency components, such as edges and fine details. If a linear filter would be applied to such a signal it would blur sharp edges and produce unacceptable results. To conserve edge information nonlinear filters can be used, e.g. median filter, low- or highpass filters.

Gradient-based pre-processing filters

The second class of pre-processing filters are gradient-based operators. These filters are based on local derivatives of the image function [142]. The image derivatives are bigger at locations of the image functions where they undergo rapid changes. The aim of gradient operators is to identify and to indicate such locations in the image. These operators enhance high frequencies and suppress low frequencies in the Fourier transform domain. The Fourier transform is an important image processing tool which is used to decompose an image into its sine and cosine components. The output of the transformation represents the image in the Fourier (or frequency) domain, while the original input image is equivalently represented by the spatial domain. In the Fourier domain image, each point represents a particular frequency contained in the spatial domain image. The Fourier transform can be used for gradient based operators although their major drawback is their sensibility to noise. Common examples for gradient-based pre-processing filters are Sobel, Laplace and Canny filters.

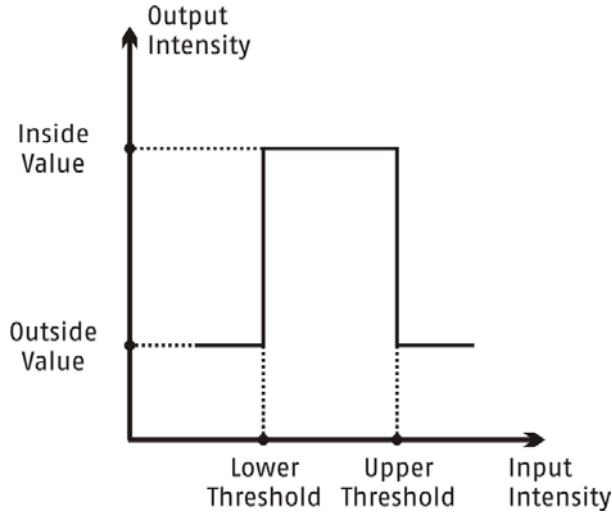


Figure 1.17: Principle of simple threshold-based segmentation. The user defines an upper and lower threshold and output values (normally 0 and 1) for pixels fulfilling the given threshold interval criteria or not. Each individual pixel is scanned resulting in a binarized image (see also Figure 3.6)

Edge preserving noise reduction with anisotropic diffusion and bilateral filtering

Anisotropic diffusion filtering [143] is closely related and partially derived from earlier results where nonlinear diffusion processes were used to model the human vision [144]. The motivation for anisotropic diffusion filtering is that a Gaussian smoothed image is a single time point of the solution to the heat equation that has the original image as its initial conditions. Anisotropic diffusion includes a variable conductance term that depends on the differential structure of the image. The variable conductance can be used to limit the smoothing at edges in images. The smoothing effect itself depends on the measured high gradient magnitude and the conductance parameter influences the overall smoothing efficiency and controls the sensitivity of the process to the edge contrast. A user has to define the conductance value and the effective width of the Gaussian filter mask itself. Anisotropic diffusion filtering includes terms of nonlinear partial differential equations that can be solved on a discrete grid using finite differences. Thus, the smoothed image is obtained by an iterative process. The efficiency of using anisotropic diffusion filtering for biological imaging has been shown in recent works [145, 146, 147].

1.3.4 Segmentation

To obtain meaningful quantitative data of pre-processed images the correctly corresponding objects have to be segmented. The basic aim of segmentation is the division of the image into uniform and homogeneous parts that correlate with objects in the original image. Therefore segmentation is used in the extraction of relevant structures from images. Broadly two general strategies can be used to obtain these object correlations. The first is a complete image segmentation that aims to result in uniquely defined regions that directly correlate with objects of the input image, e.g. definition of small cells on a homogeneous background extracted with a global threshold (see Figures 1.17 and 3.6). The second approach is a partial segmentation of the image. With this strategy the image

is divided into defined regions which not necessarily correlate directly with the complete image objects. Therefore partial segmentation and later merging of the separate structures leads to the final (binarized) shape of the target object. An example is the segmentation of medical images of the brain where different physiological subregions can be defined by different gray-values. A combination of segmented subregions can be merged to a meaningful and functional unit, e.g. segmentation of the white and gray brain matter. Such partial regions can be defined by similar brightness, color, reflectivity and texture properties. Finally, higher-level knowledge of the global arrangements can lead to a meaningful result for partial segmented images.

Segmentation of medical and biological images is a challenging task. Hundreds of different methods have been developed and implemented in recent years. Though many promising approaches have been proposed no single method can generally solve the problem of segmentation for the large variety of image modalities existing today. Often, the most effective segmentation results can be obtained by carefully customizing combinations of algorithms components for solving an existing problem. The parameters for these components are tuned depending on the characteristics of the image modalities of the input images and the features of the anatomical and biological structures to be segmented.

In general, segmentation is the most important and also most tedious part in the general image processing workflow, but is necessary for later quantitative analysis.

1.3.5 Registration

Depending on the experimental setup image or object aligning is necessary. In biology, image alignment (image registration) is mostly used in live cell experiments (2D or 3D plus time) to suppress global object movements or shape deformations during acquisition, e.g. moving cells during the observation period.

Image registration is the process of determining a spatial transform that maps points from one image to homologous points in the second image. The basic input data to the registration process are two images: one is defined as the source image and the other as the target image. Registration is treated as an optimization problem with the goal of finding the spatial mapping that will bring the moving image into alignment with the fixed image (see Figure 1.18).

To represent the spatial mapping of points from the fixed image space to points in the moving image space a transform has to be defined. The transform

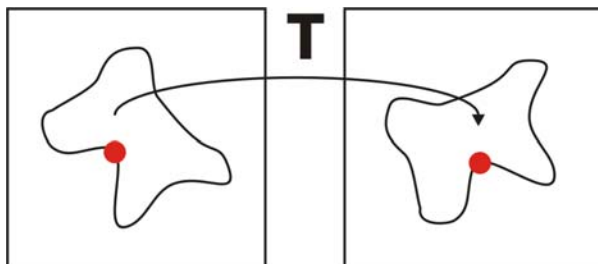


Figure 1.18: General concept of image registration. Image registration should map each point in one image onto the corresponding point in the second image.

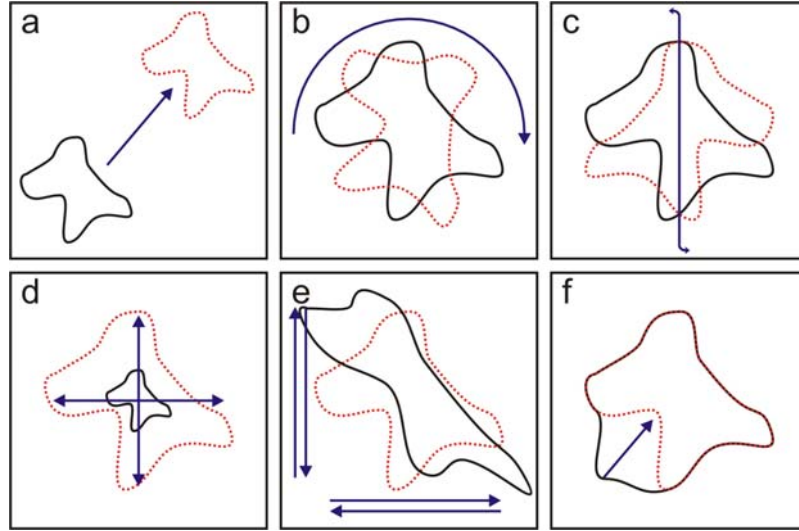


Figure 1.19: Representation of different forms of transformations in registration processes. The red dotted object represents the target structure, the black object is the source object. a) Rigid translational correction, b) rigid rotational correction, c) rigid transformation by mirroring the source object, d) affine scaling transformations, e) affine shearing and non-uniform scaling transformations, f) use of elastic transformations to correct for local deformations.

is shown and used inversely to avoid undefined values for mathematical solutions during the registration steps (which would lead to false and meaningless image registration results).

Rigid transformations including rotation, reflection and translation can be used to correct for simple object movements within the image. In addition to rigid transformations, affine transformations that include uniform and nonuniform scaling and shearing can be used to correct for area and volume changes over time. When local variations between the geometric structures are encountered elastic registration methods, e.g. thin-plate splines methods, can be applied, e.g. local cellular membrane changes can be corrected by these algorithms (see Figure 1.19).

To increase the registration effectivity for images certain assumptions have to be fulfilled. Such assumptions include that the transformation between the images of the different formats is isotropic. Further it is assumed that neither image is skewed and that pin cushion or barrel distortion for each image is negligible. With these assumptions the later described different approaches of image transformations are facilitated.

Common use of image registration for medical imaging applications

An area where image registration plays an important role is the early detection of cancers in medical imaging. Radiologists often have difficulties locating and accurately identifying cancer tissue. Even with the aid of structural information such as computer tomography images (CT) and magnetic resonance images

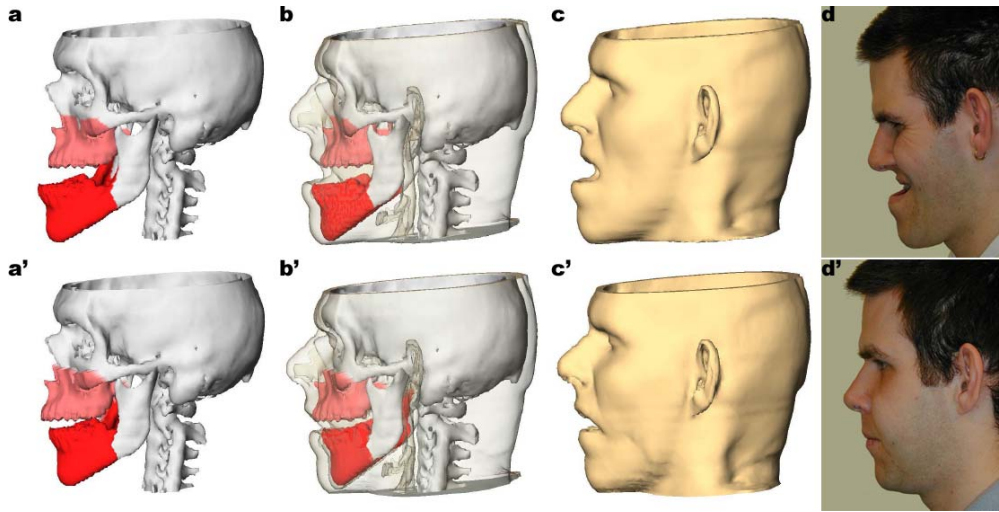


Figure 1.20: Simulation of bimaxillary osteotomy, including soft tissue prediction. The pre- and postoperative appearance of a patient with maxillary retrognathism and mandibular prognathism is simulated. a + a') Simulation of the corrective surgical impact (bimaxillary osteotomy), which consists in an advancement of the maxilla by 10mm and a set-back of the mandibula by 12mm (red). b + b') The resulting soft tissue deformation is simulated with linear and non-linear elastic registration methods. c + c') Result of the soft tissue deformations. The model shows predictive results of the patient's face prior and posterior the operation. d + d') Pre- and postoperative pictures of the patient showing the correction of the maxillary retrognathism and mandibular prognathism. (Image adapted from [148])

(MRI) the identification of abnormal structures is very difficult because of the low contrast between tumor and surrounding tissues in CT and MRI images [142]. Although improvements in detection with high contrast images can be obtained by using single photon emission computed tomography (SPECT) and radioactively labeled monoclonal antibodies, resolution and contrast problems might still be present. Sometimes it is difficult to determine the precise location of the high concentration of the radioactive isotope in SPECT or positron emission tomography (PET) images in relation to anatomic structures, such as vital organs and surrounding healthy tissue. For this purpose the patient images can be mapped or registered to each other or standard atlas images. The mapping procedure can significantly aid in the early detection of tumors and other diseases and improve the overall accuracy of medical diagnosis. Such applications of medical image registration have been used in the diagnosis of breast cancer, colon cancer, cardiac studies, wrist and other injuries, inflammatory diseases and different neurological disorders including brain tumors, Alzheimer's disease and schizophrenia. The method has also been utilized in radiotherapy, mostly for brain tumors, and by cranio-facial surgeons to prepare, predict and simulate complex surgical procedures (see Figure 1.20).

Image registration for biological applications

In biological applications image registration methods are needed when direct quantification of sub-compartment particles are performed, e.g. analysis of sub-nuclear particle velocity and diffusion properties within moving cell nuclei [145, 9]. With the aid of proper image registration methods the motion of the biological compartments can be corrected over long image acquisition times in 3D. Thus, direct quantitative data can be extracted from the local internal regions of the corrected images without distortion effects occurring from the global compartment movements.

In contrast to the abundant use of image registration for medical imaging sparse use is noted in the biological field. However, advances in registration methods for sodium-dodecyl-sulfate polyacrylamide gel electrophoresis (SDS-PAGE) and sucrose gel images have been made. On the other hand, image registration algorithms for microscopic images are rare and mostly restricted to manual or semi-automatic 2D registration (e.g. software packages such as ImageJ [149] or AutoAligner [150]). One major problem of microscopic image data is their diversity. Different microscopes use different formats, sizes and depths of storing their data, e.g. different image sizes, voxel sizes, image depths. Even the knowledge of the correct data format can sometimes not overcome the problem of comparing two datasets acquired on two different systems. Besides the problem of image modality another significant problem of using image registration algorithms in the biological field is the image quality. Often acquisitions are very noisy and might even show intensity fluctuations during the time series of the experiments, e.g. fluorescent bleaching can occur during the imaging period leading to a decrease of the SNR.

In biological as well as medical imaging the high voxel anisotropy in the z-direction compared to the x and y axis has to be taken into account for 3D image registration. The main sources of the poor z-resolutions are the physical and mechanical limits of the underlying microscope. These distortions can be partially reduced by using deconvolution algorithms to eliminate scattered light and increase the overall SNR of the image. The use of new 4 PI microscopic systems can significantly alter the image z-resolution although the overall acquisition time increases. One disadvantage is that fast biological processes can currently not be acquired with a 4 PI system within an appropriate time resolution, e.g. FRAP experiments for fast diffusion processes in the cell nucleus [151]. However, interpolation approaches for reducing anisotropy can be suggested to overcome limitations of the available imaging device. Further, a proper experimental planning and optimization is helpful to improve the image quality.

Registration using landmarks

A commonly used method for medical image registration is landmark-based registration. Landmarks are defined control points that are placed in the image and normally represent unique features (geometric properties). The placing of landmarks must be performed accurately and is the input for the following transformation. Control points themselves can be placed at internal structural

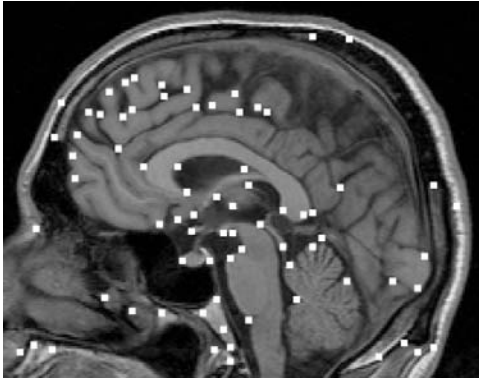


Figure 1.21: Automatic extraction of landmarks. The detected landmarks of the human brain are highlighted by the white squares (Image from [152]). The extracted points can be used to register this image to a reference target image, e.g. another image or an image atlas of the human brain (see also Figure 1.22)



Figure 1.22: Landmark-based registration of human MR images. a) The 2D section of a MR image of a human brain shall be mapped onto b) a reference image. For this purpose specific and clearly identifiable landmarks have been selected (numbers: 1-12). c) Registration results in an overlay of the source (as gray-value image) and target images (as outlines). Landmark-based registration is very efficient for medical images. Landmark-based registration in biological applications can be applied to gel and whole animal alignments. Registration of cell or cell nucleus images with this method is limited because of the lack of constant, meaningful and reproducible object features. (Image adapted from [153])

or external marker points (see Figure 1.21). In medical imaging clear anatomic landmarks can be found, e.g. rib cage, ventricles and bone surfaces. But the accurate placing of landmarks is very difficult for individual cells due to their morphological variety of structures. Therefore the use of landmark-based registration methods for microscopic imaging of cells is limited.

This is different for the medical image registration area where the transformation of control points of the first image to those on the second one yields satisfactory results. The definition of anatomical control points is not always an easy operation and the use of these internal landmarks requires considerable operator expertise. However, user provided control points usually lead to accurate, satisfactory and fast registration. Another advantage is that the *a priori* information from the user's knowledge is straightforwardly introduced in the registration process (see Figure 1.22).

Edge-based registration methods

The potential use of edge-based (contours-based) registration in medical imaging is significant. Often edges are the only common information found in these images. Though the method can be very powerful it is also very susceptible to image noise as contours are not easily extracted from noisy images. The extracted contour features must be representative and properly characterized for use with edge-based registration algorithms. For this purpose the pre-processing steps consists of discarding all image information except the edges for each individual image. In medical imaging such edge extraction steps can include active contours methods and edge detection algorithms, e.g. Canny or LoG zero crossing filters.

Poor image resolution and noise in the edge image can lead to registration problems because the minimum of the global matching function is missed. Instead of the absolute global minimum a local minimum of the fitting function is selected leading to a meaningless registration result. In order to overcome these artifacts and to ensure high reliability in the overall edge-based registration process, methods for systematic search and global optimization techniques have to be included.

Gray-value and moment-based registration

Another possible approach which works on similar methods as edge-based registration includes the comparison and matching of the intensity values of edge pixels in the source and target image [142]. The idea of gray-value-based registration is based on matching of voxel intensities. It can be combined with moment-based registration to improve the result. The extraction of common object information from images can be performed without or with minimal participation of the user. The properties for the moment-based registration are center of gravity, principal axis's and more complex features deriving from the gray-values. The parameters used to correct for object translation, rotation, scaling and shearing can be optimized using cost functions. The cost functions are based on the uniformity of the source to the target image. The minimum of these functions is found through iterative univariate or multivariate calculus-based minimization steps. The main feature of the extracted object moments is that they are invariant features of images.

Chapter 2

Objectives

In the following chapters I present the two main biological projects I worked on using the powerful features of my image processing platform Tikal. The Tikal image processing platform and the strategies and methods I used to analyze the huge multidimensional image datasets from both projects will be introduced in the Materials and Methods part.

Spatial aspects of X-chromosomal inactivation during embryonic stem cell differentiation

The major objectives of the first study was the determination of the Xic positioning within the cell nucleus and in respect to the nuclear membrane. I first investigated the changes of the Xic location upon differentiation and determined if a non-random spatial localization of the Xic locus in the nucleus at different days of differentiation exists. In a second part I analyzed different cell line types, such as multi / single copy transgenic and counting deficient ES cell lines to detect differences in Xic localization prior and after induction of X-inactivation. In respect to the data I further tested if and at which stage the counting event is dependent on the proximity of the two Xics in the different female and transgenic cell lines. Additionally I analyzed the implications of Xic localizations in cells carrying mutations in the regions responsible for counting. I described the quantitative localization analysis of the Xic in over 5000 individual cells during the initial phases of X-inactivation with the help of Tikal.

4D imaging and analysis of moving subcellular particles and chromatin dynamics

Using a combined computational and experimental approach I studied the dynamic behavior of nuclear body-like particles formed by GFP-NLS-vimentin [154]. As previously introduced the mobility of nuclear particles such as PML and Cajal bodies is a key aspect for understanding their biological function. For this purpose it is essential to observe those particles in their natural environment to understand the different global effects on their dynamics, e.g. the influence of chromatin structure and dynamics on those sub-nuclear particles. To understand those complex biological systems I investigated the functional

2. Objectives

effect of chromatin that influences the mobility behavior of nuclear particles. In this context I tested potential correlations between particle mobility and chromatin environment. Further I performed experiments to systematically measure the change of nuclear particle mobility in normal cells and in cells under stress conditions. Finally I investigated the overall suitability of vimentin as inert, small nuclear marker molecules for future chromatin accession experiments.

Chapter 3

Materials and Methods

3.1 Biological microscopy image processing methods

3.1.1 Image pre-processing

Definition of noise in microscopic images

For microscopic biological images the amount of noise is a very important factor for success or failure of the whole quantitative analysis (see Figure 3.1). The experimental setup and planning is very important in this aspect. The SNR has to be high. A proper calibration of the imaging device is crucial and significantly reduces noise in the images. Such mechanical adjustments include precise alignment of the laser lines and photodetectors but also the precautionary positioning of the microscope in a non-vibrant environment to avoid interference noise. Additionally, good SNRs can be obtained by optimizing the light intensity and exposure time of the sample. In this case the thickness of the specimen that can dramatically influence the SNR has to be taken into account. A thick and non-translucent object can absorb or even scatter light and therefore decrease the overall SNR in the image. On top of that impulsive noise is also introduced in confocal systems. Such high-pitch or impulsive noise means that the image is corrupted with individual noisy pixels whose brightness differs significantly from the others close by. These differences can have various sources such as different light absorptions properties, different emission efficiencies and light scattering effects of the fluorescent molecules.

Another significant source of impulsive noise are the CCD cameras. Often CCD cameras produce “salt and pepper” noise, a subtype of impulsive noise where the described pixels are fully saturated (“white” pixels). It is not always possible to avoid such saturated impulsive noise originating from CCD camera. However, an optimized setup of the microscope and the experiment itself can dramatically improve the image quality, e.g. optimized light intensities and photomultiplier parameters can reduce “salt and pepper” noise.

Smoothing noise reduction filters

To suppress the different types of occurring noise a variety of smoothing algorithms can be used. Generally, the calculation of new image intensity values is

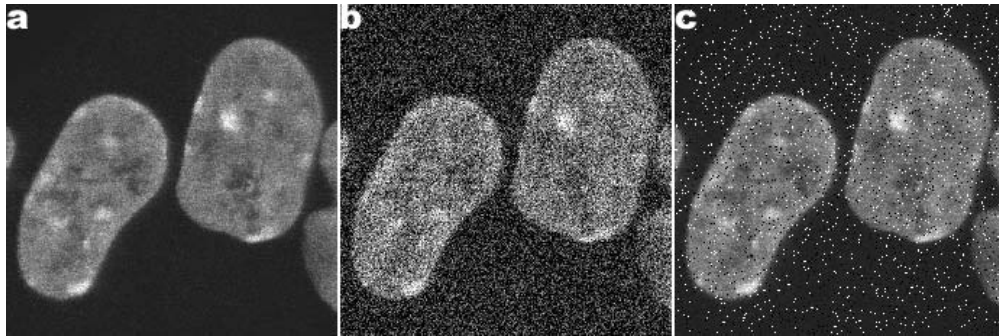


Figure 3.1: Different common types of noise in images originating from a laser scanning microscope. a) Original images with slight background noise. b) Noise (mostly Gaussian) originating of either faint fluorescent specimen signal or weak laser intensities resulting in a low SNR ratio. c) Typical "salt and pepper" or high pitch noise that emerges from the photo multiplier tubes (PMT) or CCD camera. It can be partially reduced depending on the experimental setup.

based on averaging of brightness values in a defined local neighborhood area. For example, Gaussian low-pass filtering computes a weighted average of pixel values in the neighborhood, in which the weights decrease with distance from the neighborhood center according to a Gauss function. In addition formal and quantitative explanations of this weight falloff can be given. The intuition is that images typically vary slowly over space, so near pixels are likely to have similar values, and it is therefore appropriate to average them together. The noise values that corrupt these nearby pixels are mutually less correlated than the signal values, so noise is averaged out. The assumption of slow spatial variations fails at edges, which are consequently blurred by such a kind of linear low-pass filtering.

The main problem of the smoothing process is the blurring of sharp edges in the image and therefore edge preserving methods, such as anisotropic diffusion, are the most effective choice to eliminate impulse noise or image degradations appearing as thin lines. However, extensive image degradations leading to large blobs or stripes can not be restored. Such severe image perturbances might occur because of ground vibrations carried forward to the imaging device or a flickering or partially interrupted laser or light source during the image acquisition (see Figure 3.2).

Gradient-based pre-processing filters

An important class of gradient-based operators are edge detectors, such as Sobel, Laplace or Canny edge detectors, which are very important in local image pre-processing methods to locate abrupt changes in the intensity functions (see Figure 3.3). Edges are often used for finding and defining region boundaries. Edges are defined as pixel boundaries of homogeneous regions where the image function varies. Thus, the ideal case of edges with or without noise consists of pixels with high edge magnitude.

Because of the high noise levels of biological microscopy images the overall

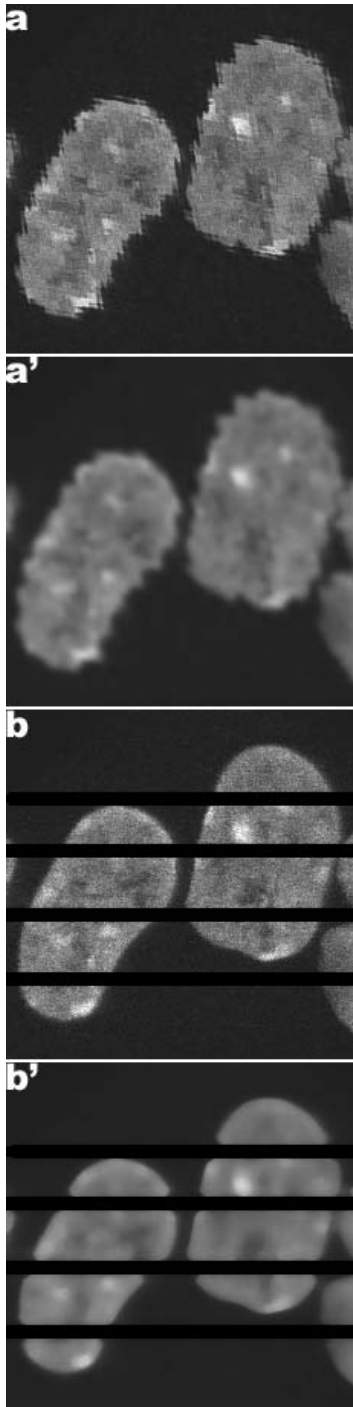


Figure 3.2: Severe distortion artifacts originating from laser scanning microscopes which cannot be restored by linear smoothing pre-processing algorithms. a) Image distortions from vibrations carried to the imaging device during image acquisition. The laser scans are severely different from their original scanning lines paths which results in ripple like internal and peripheral edge structures. a') Gaussian blurring of ripple noise results in general smoothing of the image. However, the edge contours are still distorted. b) Laser failure artifacts which occurred during the scanning process. Such a severe failure results in complete image information loss in the affected areas. b') Median filter restoration attempt resulting in an overall smoothed image with further image degradations and loss of edge information at transitions areas between the black stripes and the object borders.

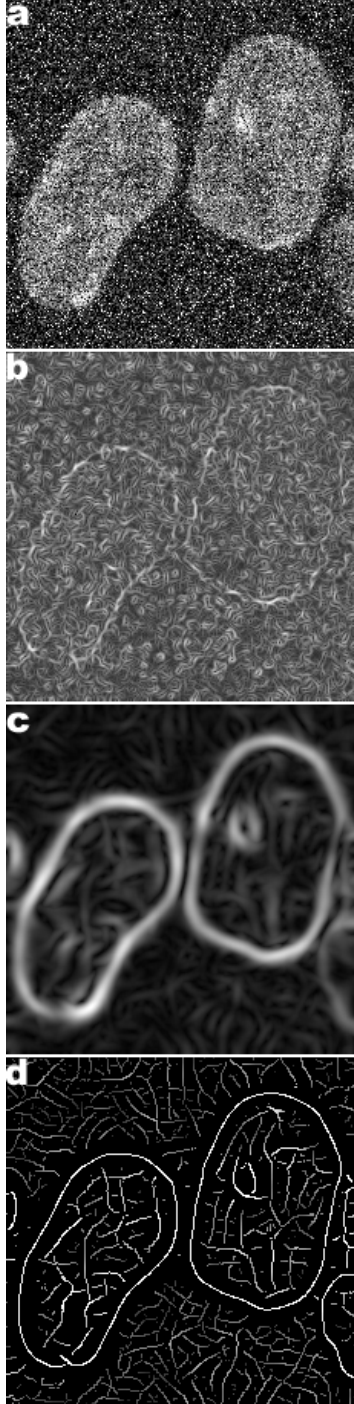


Figure 3.3: Gradient-based methods for object edge detection [155]. a) original noisy image b) Results of the Gaussian derivative edge detection from the original image (a). The objects itself are barely recognizable because no prior smoothing step has been performed to the image. c) Gaussian derivative of the original image. The image has been smoothed by Gaussian smoothing before edge detection has been performed. The image is heavily blurred and internal cellular structures are slightly distorted. d) Non maximum suppression of the edge image (c) which is also known as Canny edge detection. The object edges are clearly detected. However internal object structures and background noise is also detected.



Figure 3.4: Effects of smoothing filters. a) The original image was smoothed by b) Gaussian filtering and c) anisotropic filtering. Especially at the nuclear borders the clear advantage of the anisotropic diffusion algorithm is clearly visible because the image structures and edges remain preserved while the noise is strongly reduced. With Gaussian smoothing a diffusion of the overall contours is seen while the background noise is still visible.

noise has to be reduced while the object edges have to be preserved. Edges themselves are often fuzzy, blurred and hard to define. To overcome this problem edge preserving smoothing filters (e.g. anisotropic diffusion) can be applied prior the detection of the actual object boundaries. As already mentioned, the drawback of linear image denoising (smoothing) without including object and border features tends to blur away the sharp boundaries in the image that help to distinguish between the larger-scale structures. Such structures include either anatomical information in medical imaging or cellular or even subcellular features in biological imaging. Moreover even where smoothing does not erase the object boundaries it tends to distort the fine structures of the image. This can lead to subtle but essential changes in the overall properties of the anatomical or biological structures in question. For this purpose a new alternative to linear filtering was introduced. This new method is called anisotropic diffusion filtering (also called nonuniform or variable conductance diffusion) [141].

Anisotropic diffusion and bilateral filtering

Typically, the number of iterations required for anisotropic diffusion filtering is small, e.g. large 2D images can be processed in several tens of seconds. To obtain such an optimized performance it is essential that a carefully written code and the access to modern, general purpose, single-processor computers exists. The technique applies readily and effectively to 3D images, but requires more processing time. The output of the anisotropic diffusion filtering is an image or set of images with reduced noise while preserving edges (see Figure 3.4). Such images are useful for a variety of consecutive processes including segmentation, quantification and statistical analysis, visualization, and geometric feature extraction.

Another very efficient filter in this class is the bilateral image filter [156]. It combines gray levels on their geometric closeness and their photometric similarity, and prefers near values to distant values in both domain and range. Two pixels can be close to each other and occupy nearby spatial location, or they can be similar to one another meaning that they show nearby intensity values (possibly in a perceptually meaningful fashion). A discrete image is more than an array of values, it represents a regularly spaced set of samples over a contin-

uous two (or three) dimensional domain. One can think of the coordinates as a discrete realization of a function over the continuous two (or three) dimensional domain. The filter uses this information at pixels that are close to a pixel in the image domain and similar to a pixel in the intensity range to calculate the filtered value. Two Gaussian kernels (one in the image domain and one in the image range) are used to smooth the image. The result is an image that is smoothed in homogeneous regions but has preserved edges. The result is similar to anisotropic diffusion but the implementation, compared to anisotropic diffusion, is non-iterative and results in faster processing times for equivalent images. Another benefit to bilateral filtering is that any distance metric can be used for kernel smoothing of the image range. Bilateral filtering is capable of reducing the noise in an image by an order of magnitude while maintaining edges (see Figure 3.5).

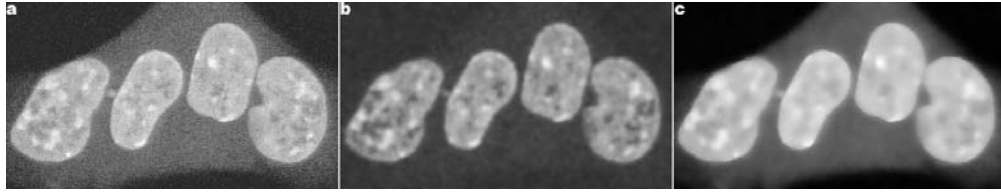


Figure 3.5: Two varieties of different edge preserving filters. a) An image containing cell nuclei with cytoplasmic derived background noise (also see Figure 3.4) was filtered by (b) anisotropic diffusion filtering [143] and bilateral filtering [156]. Both filters show their strength in preserving the object boundaries. Differences and the principle working concept of the two filters are noticed on structures within the nuclei. While the anisotropic filter preserves structural information within the object the bilateral filtering method results in more homogeneous and smoothed internal information. This can have a particular advantage in segmentation of the whole nucleus since the gray-value fluctuations are leveled out and improve the results of segmentation. If the segmentation of internal structures is needed the use of an anisotropic filter might be more advisable.

Summary

For my later work the introduced image pre-processing filters were crucial for the following quantification steps. Although the microscopic parameter settings were optimized, the image quality demanded the use of noise-reducing filtering. Basically every available smoothing algorithm could be used for pre-processing. However, for my work I found that the median, anisotropic diffusion and bilateral filters were essential for proper pre-processing. The former filter reduced “salt and pepper” noise originating from the CCD camera without blurring the edges. The two latter filters smoothed the image objects (and their histograms) while preserving their contours. The presented procedures optimally prepared the images for the preceding image segmentation steps.

3.1.2 Image segmentation

The simplest way of segmentation is global gray level thresholding. The conditions for effective segmentation are the proper definition and separation of the

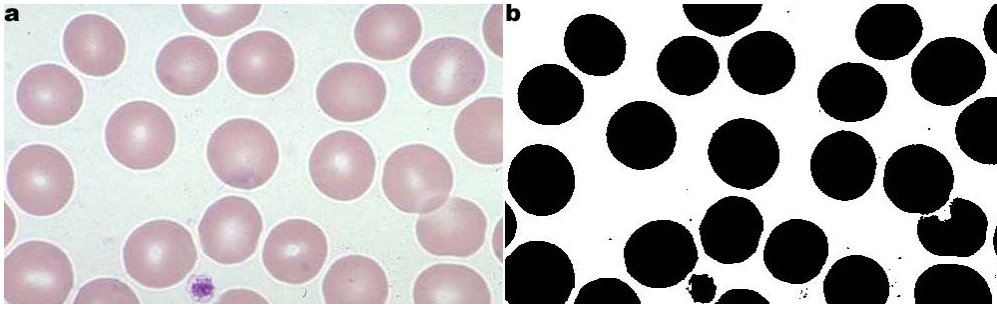


Figure 3.6: a) Red blood cell smear on a bright background glass cover slip. (Image adapted from [157]) b) Simple thresholding of the cells results in clearly segmented objects. Simple binarization is reasonable since no background noise is present and the individual cells often do not touch each other.

objects and background, e.g. by reflectivity or light absorption of their surface. Commonly, such images consist of contrasted objects located on a uniform background such as blood cells on a glass slide or black printed characters on white paper (see Figure 3.6). Gray level threshold filters are used to transform an image into a binary image by changing the pixel values according to two user defined values. These threshold values are an upper and a lower intensity value. For each pixel in the input image, its intensity value is compared with the lower and upper thresholds. If the intensity value is inside the range defined by the lower and upper limits the intensity value is set to 1. Otherwise the pixel intensity is treated as outside value and receives the value 0 (see Figure 3.6). Simple thresholding is computationally inexpensive and can be used in simple applications or at the end of an intensive pre-processing filter chain.

As long as objects do not touch each other and their gray-levels are clearly distinct from the background thresholding yields suitable results. However, microscopic images often do not show these optimal conditions to apply simple thresholding. Depending on the imaging device resolution, the specimen properties and the experimental setup the individual objects are not clearly separated and can show fuzzy edges. Furthermore, inhomogeneous background illumination complicates the finding of an optimal global threshold. An extension of simple thresholding by incorporating histogram based knowledge often fails. No bi-modal histogram curve is found due to the inhomogeneous distribution of the gray-values for the objects and the background (see Figure 3.7).

Although edge-based segmentation algorithms represent a large group of segmentation methods I found no effective use of this filter category for biological microscopic imaging. Edge-based segmentation relies on edge detecting operators such as the Sobel, Laplace, Canny methods. The edges normally mark image locations of abrupt changes in gray-level intensities, colors and textures. Again, the most common problems of edge-based segmentation algorithms are caused by image noise or unsuitable information in the image. This misleading noise can cause edge presence where no real border is detectable. In the opposite situation a skewing of information can result in non detectable edges where a real border should be existent. Such problems can especially occur in 3D microscopic image stacks. Due to the resolution limits of the micro-

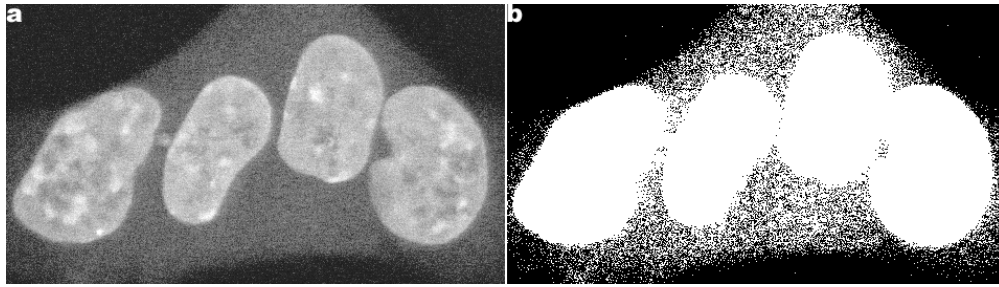


Figure 3.7: Simple thresholding. Simple thresholding of the image (a) by a global threshold often results in artifacts deriving from background noise (b). In this particular case edge preserving smoothing methods improve the result of the segmentation (for pre-processing examples see Figure 3.5) but simple binarization is not suitable for this example. Especially in regions where the cell nuclei are close to each other the method can not resolve the exact contours.

scope in z-axis compared to the x- and y-axes the edge information can be lost which leads to false segmentation of the object borders. Furthermore, fine object structure, textures, scattered light or experimental artifacts can also lead to misinterpretation of available edges and lead to an oversegmentation of the objects. Though not eliminated, such artifacts can be reduced by increasing the input image quality with deconvolution and pre-processing algorithms prior to segmentation, e.g. noise reductive pre-processing filters such as median, Gauss and edge preserving anisotropic diffusion filters (see Figure 3.8).

For the purpose of the later described projects of segmentation of 3D cell nuclei I obtained the best results by using region growing filters. Region growing techniques can be generally better for noisy images where borders are difficult to detect. Homogeneity is an important property of regions and is used as the main segmentation criterion for the algorithms. Again, the criteria for homogeneity can be based on image gray-levels, colors, textures and shape. Though strong intensity fluctuations may be noticed within microscopic images, extraction of homogeneous regions is possible by defining the correct segmentation intervals and parameters (see Figure 3.8). The use of region growing algorithms has proven to be an effective approach for image segmentation in the medical imaging field. The basic concept of a region growing algorithm is to start from a seed region (typically one or more pixels) that is considered to be inside the object to be segmented. The pixels neighboring this seed point region are evaluated to determine if they should also be considered part of the object. If so, they are added to the region and the process continues as long as new pixels are added to the growing region. Region growing algorithms vary depending on the criteria used to decide whether a pixel should be included in the region or not. These region growing criteria include the type of connectivity used to determine neighboring pixels and the strategy used to check neighboring pixels.

Since every biological experiment using microscopes produces images with tremendous differences in quality, size and extractable features no generally applicable segmentation method can be suggested. For my later experimental analyses region growing methods were the most efficient approaches in segment-

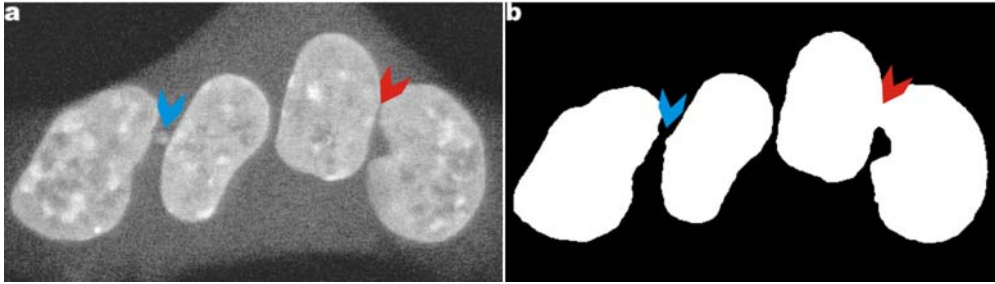


Figure 3.8: Segmentation of cell nuclei. a) The original image shows cell nuclei with cytoplasmic background noise. b) Segmentation of individual cell nuclei with the region growing method. Prior to segmentation the images were filtered by bilateral diffusion (see Figure 3.5). Segmentation is robust against small interfering noise regions and result in object separation (blue arrow). Because the cell nuclei are very close to each other in certain regions and the overall SNR is low segmentation artifacts (object fusions) can be observed (red arrow). Partially such fusion events might be avoided with template based segmentation algorithms. However due to the abundant morphological variety of cell nuclei shapes such an approach is limited.

ing nuclear shapes. Important is that the segmentation steps are carried out with the highest focus on the meaning and accuracy of the resulting segmented objects. Improper segmentation can result in difficulties in the further processing workflow (e.g. object registration or particle tracking) and even worse can lead to false and finally meaningless quantitative data. The overall success of image segmentation relies, besides the correct selection of available methods, on proper experimental planning and execution of the underlying experiment. Subsequent steps after successful segmentation could include image registration (see Section 3.1.3), object quantification by tracking algorithms (see Section 3.1.4) or visualization by isosurface rendering (see Figure 3.9 for isosurface rendering).

3.1.3 Image registration

Image registration can be performed prior or after the previously described segmentation procedure. In this section I will describe the strategies that I found the best applicable registration methods for biological microscopic images.

The use of standardized atlases known from the medical imaging field is almost not applicable in the biological field because of the huge morphological diversity of biological objects. Therefore, registration is mostly restricted to intra experimental applications, i.e. correcting the movements and shape deformation of single cells or cell nuclei over a given time series. But also the inter experimental registration is a challenging task. Because of the possible bleaching effects during the acquisition attention has to be paid to the light sensitivity of living biological specimens. This light sensitivity of living specimen is also known as phototoxicity. To avoid the harming effects of light on the object the light intensity or the exposure time has to be reduced. This again leads to a decrease of the SNR resulting in a possible decrease in the accuracy of the overall registration process. With proper experimental pre-planning and setup most of

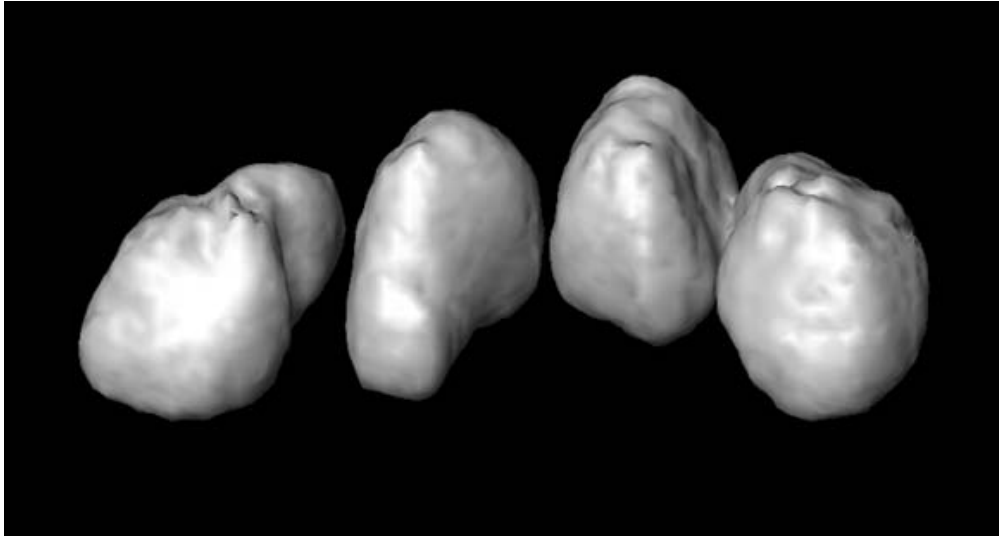


Figure 3.9: Isosurface rendering of cell nuclei. The technique is good to obtain a surface representation of the 3D scene of microscopic images and can be used to extract quantitative parameters.

the described problems can be avoided leading to good registration results.

There is no general approach to biological image registration. Several factors exist which influence the selection of the appropriate methods. Certainly, a high SNR is an influential point for accurate image registration. Spatial and temporal resolution and object morphology have additional impact on the selection for the most efficient algorithm. The final consideration of using a specific method are the experimental image dimensions. Single experimental datasets can be registered by selection of manual or semi-automatic registration methods. High-throughput image datasets such as complex time resolved images from live cell arrays need fully automated registration algorithms.

Registration using landmarks

A possible application for registration using landmarks for biological microscopic images might be the use of markers that reliably and repetitively define corresponding object features within the specimen, e.g. within a cell or a cell nucleus. Especially for registration of cells such markers could be DNA-FISH probes that always associate with two different chromatin sequences defining spots of known distance. Since chromatin or other cellular structures are deformable structures and underlie constant active and diffusible molecular processes, e.g. steady diffusional motion behavior of chromatin within the cell nucleus [158], the use of such a control point based application is restricted to a limited field of applications, e.g. short and highly temporal resolved (millisecond range) image series. Especially for long live cell experiments (minutes to hours) no constant rigid intra cellular structures suitable for representative landmark extraction and determination (i.e. euchromatin or heterochromatin regions) have been identified so far.

The process of landmark-based registration can be accomplished manually, semi-automatically or automatically. Though it is difficult to find appropriate marker points in biological live cell imaging data the method can be used in certain biological applications. Especially in the alignment of SDS-PAGE and polysaccharose gels control point based registration can be used. For gel alignments a semi to fully automated landmark-based registration approaches leads in most of the cases to considerably good results.

Edge-based registration methods

An important influencing factor for the quality of the results using edge-based registration methods is the detection and information extraction of object borders. For microscopically imaged biological specimen the edge extraction procedures do not always result in satisfactory results. Especially for big 4D cell experiments the deviation from physiological optimal acquisition parameters can lead to phototoxic reactions, e.g. apoptotic reactions and subsequent death of the investigated material. Taking this into account it is difficult to extract the edge information from the images. Even with sophisticated algorithms such as active contours methods the edge extraction is not always a task easy to perform because of high morphological changes of the different biological specimens. Especially during the analysis of living ES cells, one of the applications studied in this thesis, dramatic cellular and nuclear shape variations can be observed that make the use of active contours impossible.

On top of the morphological shape changes ES cells tend to grow in colonies and move in non uniform directions. This unpredictable growing behavior and low contrast makes it very difficult to extract clear and suitable contours for edge-based registration methods. A possible strategy to overcome some of the described problems is to acquire small ROIs that only include one single object, e.g. single cell or cell nucleus. Though the imaging of single cell nuclei is more laborious I achieved very remarkable edge extraction and rigid registration results (see Figure 3.10).

The edge-based registration processes can follow several methods. I achieved reasonably good results with an algorithm that tries to minimize the mean square error (MSE) of the control point mappings from the first image to the points extracted from the second image. For this purpose edge points originating from segmented and binarized images that represent the object shapes can be extracted. Registration is achieved by applying a parametrized deformation to the space containing the source point set and then adjusting the parameters in such a way that the shape of the target point set is most accurately matched [160, 159]. Using 3D image stacks the edge-based registration techniques match the images by minimizing the MSE distance between the surfaces of objects structure visible on both input and target images.

Gray-value and moment-based registration

Gray-value based methods are suitable for unsupervised or partially supervised image registration (see Figure 3.11). Therefore the gray-value based method is

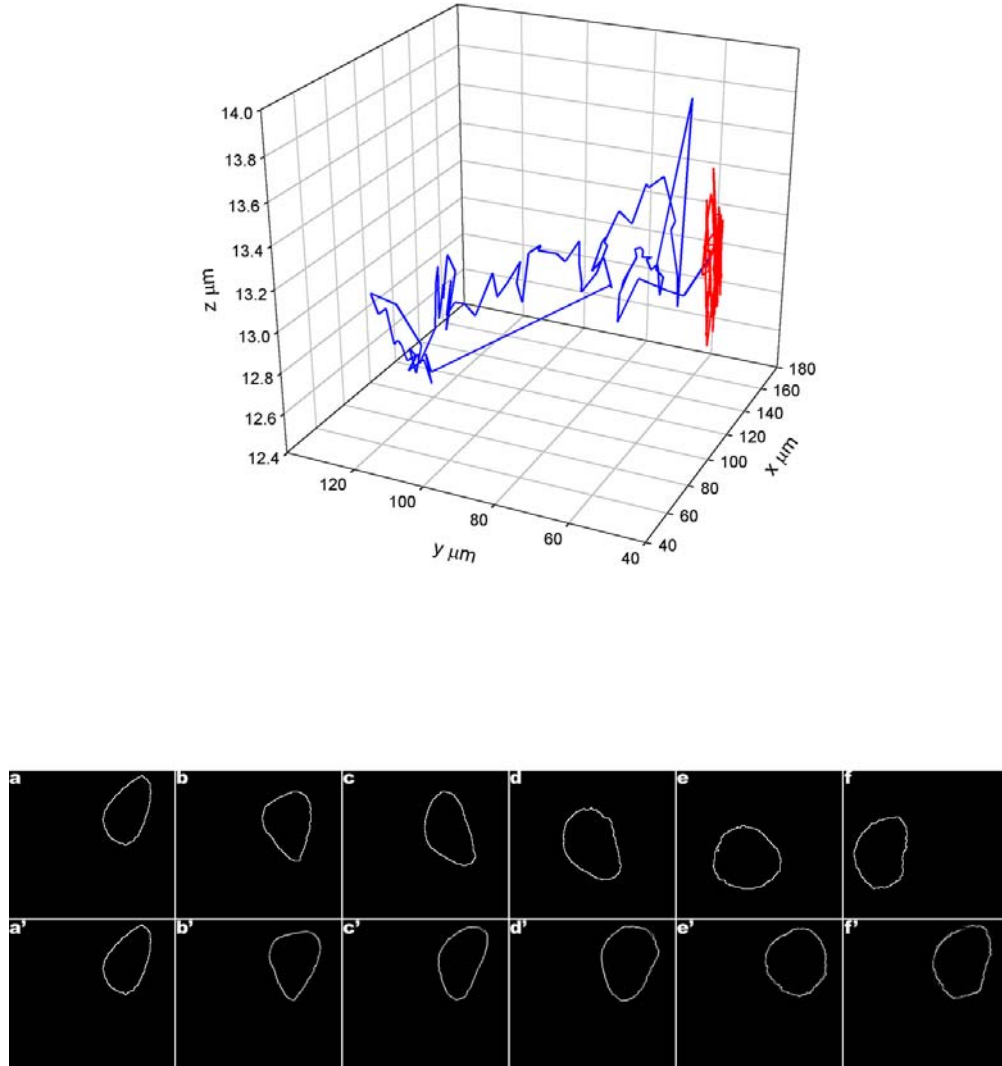


Figure 3.10: Edge-based registration for a cell nucleus. Top) Tracking of the center-of-mass (COM) of mass of the nucleus prior (blue) and after (red) rigid edge-based registration [159]. The oscillation of COM of the registered results in the z -direction is due to the fact that only a rigid correction of the objects was performed. Bottom) Time series of the original extracted edges of the cell nucleus over time (a-f). Results of the registration with the described edge-based methods (a'-f'). It shall be noted that the movements in the z -direction can not be seen.

also very suitable for registering large 3D datasets over time [145, 161]. However, as discussed previously, the method itself is very susceptible to noise as well. Proper pre-processing with edge preserving algorithms smoothing is advisable and increases the overall performance and results of the algorithm. Problems might occur if single cells are selected by defining ROIs and subsequent cropping of the images prior to registration. If wrong threshold parameters are set for the registration algorithms the result might show a perfect but meaningless matching of the image masks to each other. The actual problem of correcting the global movements and shapes of the target objects would be avoided.

3.1.4 Particle tracking

A special form of the previously described registration methods are single particle tracking algorithms. The goal is the quantitative extraction and tracking of particle features in a time resolved manner. Besides the matching of individual particles from two adjacent images that are temporal separated, object correlation networks, so called trajectories, have to be created. Due to the multitude of available tracking algorithms I will focus on two different methods that are suitable for biological tracking experiments. Possible approaches for particle tracking are the particle tracking velocimetry (PTV) method and the determination of the optical flow in image series (see Figure 3.12). In my thesis I used the PTV method for tracking small nuclear particles which will be discussed later (see Figure 3.13).

Particle tracking velocimetry and optical flow tracking

For the PTV process it is obligatory to determine individual object properties for each image. Such object properties include the volume, velocity and acceleration and are combined with physical assumptions such as the mass inertia law. This heuristic determination of the extracted object properties in time resolved image series leads to a construction of a trajectory network with the PTV approach. The discretization approach of the PTV method will link the spatial and temporal information during the trajectory construction. Additionally the particle velocity vector fields are extending the available information of the PTV. Compared to PTV the optical flow method does not need the parametrized object information from segmented images. Moreover, tracking based on optical flow determines the vector field shifts of two subsequent images on a per pixel base. Furthermore, a continuous formulation of the optical flow field for small time intervals is possible. This can lead to an increase in robustness of the optical flow field method to noise and artifacts for high resolution time intervals. It has been shown that the mean standard velocity distribution of particles is less error prone for the optical flow approach compared to the PTV-method using identical datasets [163]. Interestingly, the study showed that the mean velocity values were less depended on the SNR in the image using optical flow methods. In contrast, the PTV method showed a higher variability of the mean velocity values with changing SNR.

With the use of vector fields direct object motion correlations on a pixel

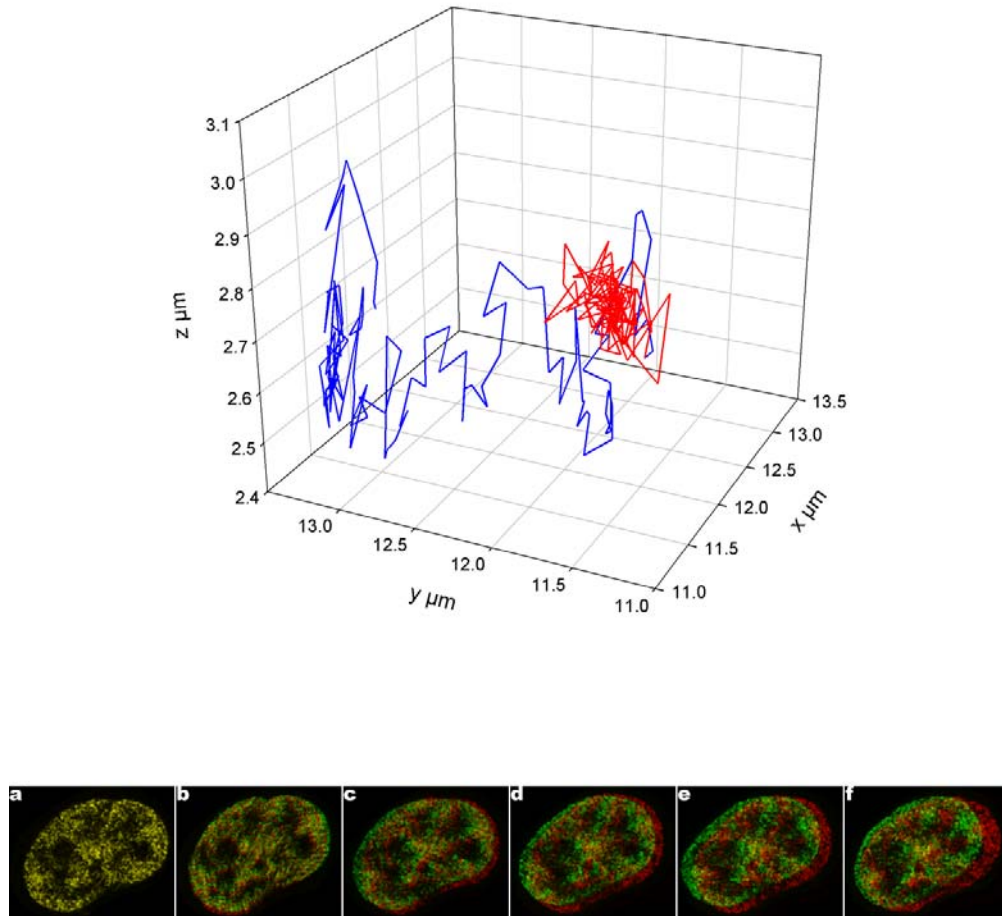


Figure 3.11: Intensity based registration for a cell nucleus. Top) Tracking of the center-of-mass of the nucleus prior (blue) and after (red) elastic gray-value-based registration with AIR [161]. A clear improvement especially for the translational and rotational movements can be observed. Bottom) Overlay of a single image planes of the original (red) and registered (green) cell nucleus over time (a-f). It shall be noted that the movements in the z -direction can not be seen.

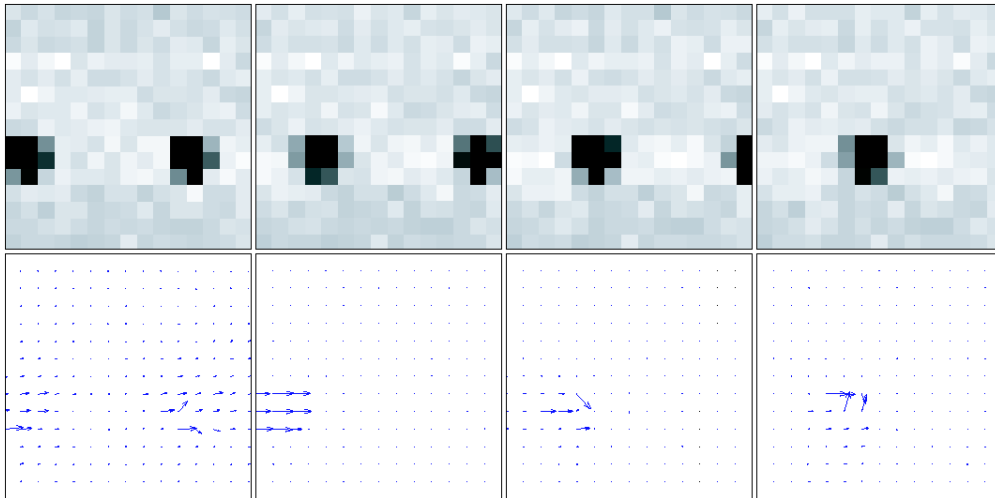


Figure 3.12: Tracking of particles with optical flow fields. Top) Small moving particles. Bottom) Optical flow vector fields of the respective moving particles. (Image adapted from [162])

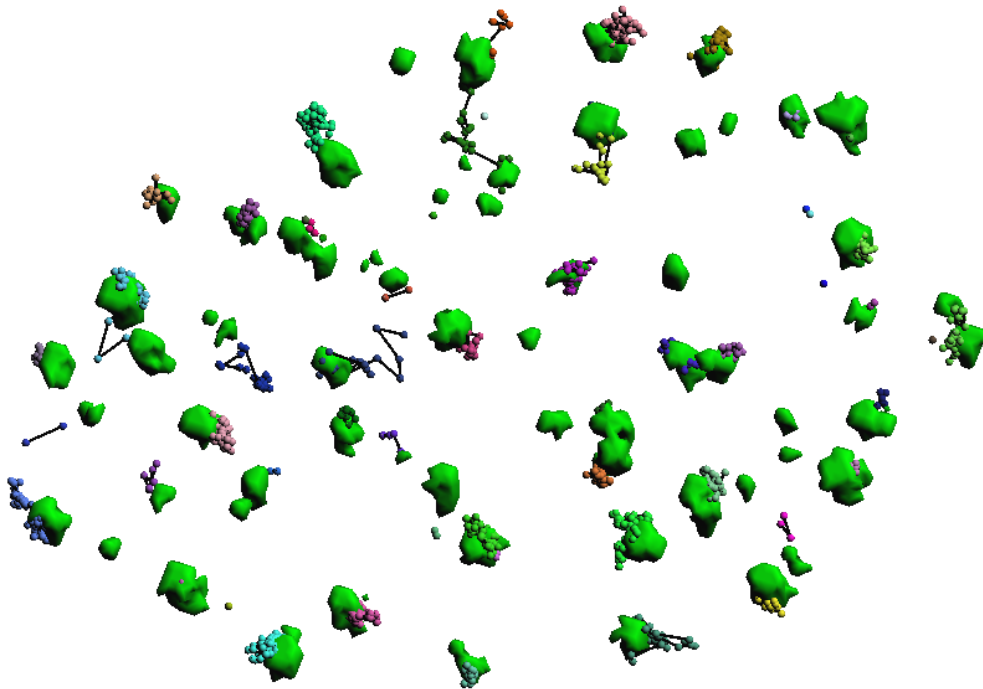


Figure 3.13: PTV tracking of segmented nuclear particles. The nuclear particles were binarized prior to tracking. Image information from the gray-value and the segmented images were used to perform the tracking over 70 timesteps. The trajectories are displayed as small colored dots interconnected with black lines. Short trajectory fragments are often originating from segmented noise particles and can be removed by setting thresholds for minimal trajectory lengths or manual correction.

bases can be extracted from the image. With optimal temporal image resolution the use of the optical flow method identifies regions that are slowly changing parameters, e.g. intensity shifts, pixel shifts, in space and over time. For this case the velocity vector field for a moving particle shows continuity for almost all data points. Normally, the unique assignment of a particle pixel for two subsequent particles is defined when using the optical flow tracking method.

Beside the direct correlation of vector fields to individual pixels segmentation is another way of extracting quantitative object properties from the image. In the case of PTV the correct pixel assignments in two or even more subsequent images has to be determined according to the segmented object parameters, e.g. mass, velocity, gray-value intensity. To obtain a correct trajectory linking with PTV, also for temporal low resolution image sequences, different interpolation models can improve the correct trajectory construction for objects over several time points. Possible interpolation models, such as B-splines interpolations, could be used for surface approximations and guarantee a continuous progression of the trajectories over time [164, 165].

Applications areas and limitations of automated particle tracking

Automated particle tracking bears several methodical problems leading to unwanted and artefactual results. The non-defined assignment of a pixel or object to another in the subsequent image is also known as correspondence problem (see Figure 3.14). The correspondence problem summarizes the fact that generally no method exists to uniquely link different correlating pixel or objects in an image sequence. To overcome the problem, a temporal higher resolved image acquisition has to be performed resulting in a significant decrease of the average displacement vector. If the average displacement vector is smaller than the average particle distance in a discrete time interval a meaningful result can be generated. A higher temporal resolution can facilitate the analysis of bigger and overlapping particles and would lead to better estimation of particle correspondence.

The use of microscopic images for certain biological applications might introduce other limitations for automated tracking approaches. Often fluorescent labeled particles are tracked over time which underlie, depending on the fluorescent dye, a decrease of intensity due to molecular bleaching effects. The decrease in intensity can be observed globally for the whole particle and leads to a decrease in the global tracking performance. The bleaching effect becomes especially severe at object boundaries where additional noise is observed. This again leads to the corresponding problem of pixel assignments in two adjacent images. The effect is even more intensified when a multitude of particles is present because of the illumination of numerous particles that influence the intensity of each individual particle. The single intensities could be even more skewed due to scattering light from the other objects.

The PTV tracking algorithms itself can be introduced by two different methods. The two-frame information method is used based on the extracted particle information from two subsequent images. An example of the two frame method is the appliance of the fuzzy-logic methods for calculating proper correspon-

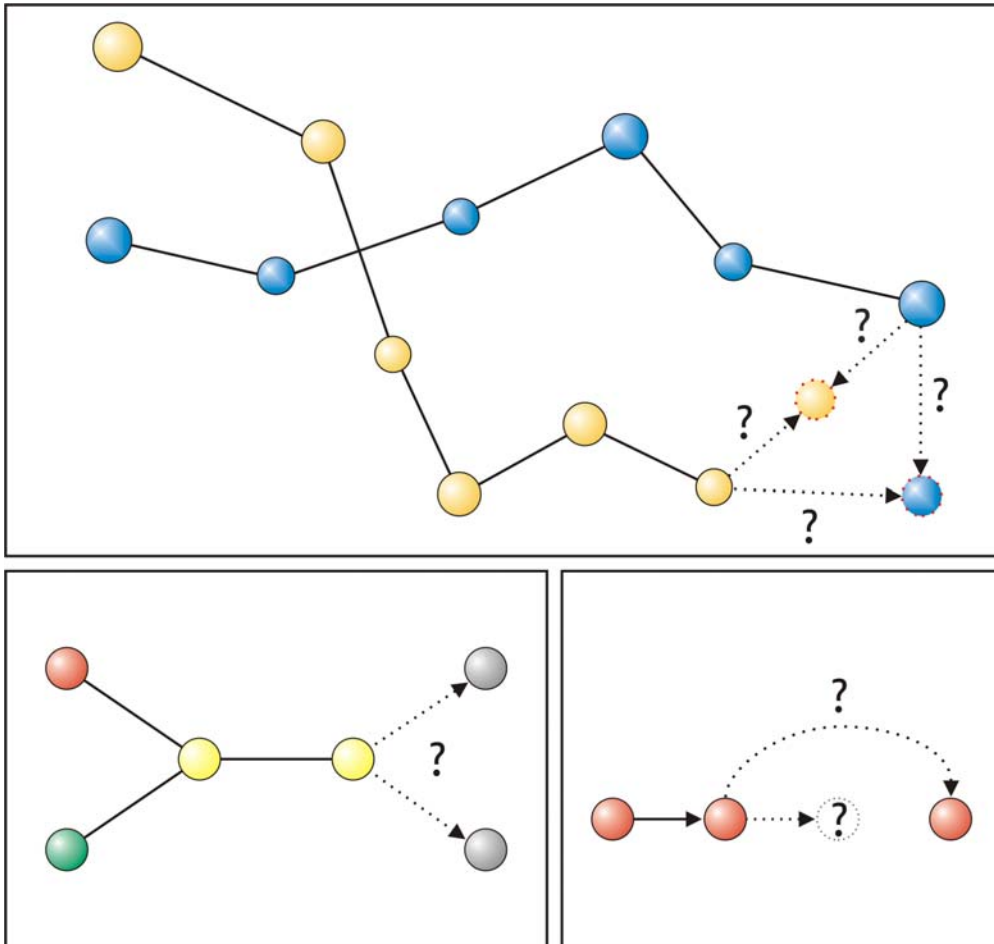


Figure 3.14: Possible correspondence problems for automated particle tracking. Top) The trajectories of two independently moving particles with similar physical properties are built. At the current position of the tracking process the two particles are in close proximity. For the prosecution of the yellow or the blue trajectory two possible mutually exclusive possibilities exist. The decision for the trajectory elongation is based on physical parameters, e.g. object mass, average gray-value intensity and velocities, from prior time steps. Bottom left) Missing correspondence to previously tracked particles can occur when particles merge and subsequently split again. Bottom right) Missing object information in one time step can also lead to problems in building trajectories. Interpolation methods using object properties from previous time steps can overcome the missing data and close the trajectory.

dences [164]. An extension of this method would be a three-frame method. This allows the calculation of the acceleration of a particle by incorporating its properties from three images in a sequence.

3.2 Tikal image processing platform

3.2.1 Introduction

New technologies such as multi-photon microscopes, improved confocal laser scanning microscopes, and cameras with higher resolution, speed, and sensitivity have enabled the acquisition of larger numbers of images in biology. These microscope technologies combined with fluorescent probes such as the Green Fluorescent Protein (GFP) allow the routine acquisition of very large datasets from live samples. Since many modern microscopes yield digital data, these large datasets require substantial computer resources, e.g. processor time for analysis, devices for data storage. This results in an increased need for computer hardware for the storage of huge amounts of image data but also for image processing, image analysis and visualization. To quantitatively approach such huge amounts of data, specialized, suitable and user friendly software tools have to be used. Although the current market shows some solutions for certain biological image processing problems, they are restricted to special application fields. The combined use of two or more programs is limited since data interchange between the different formats can be very difficult and time consuming. Furthermore image processing platforms are often proprietary and commercial products with high costs of purchases and restrictions of application programming interfaces (APIs) to include extensions of user needed modules. For the purpose of biological image processing I developed an image processing platform with the name Tikal to address and overcome some of the described software limitations, e.g. integration of the complete image processing workflow for processing and visualizing multidimensional data sets.

I created the Tikal image processing platform for facilitated and user friendly data processing for biological datasets. At the beginning of my work, at the end of 2002, I could not find suitable platforms that enabled the handling and processing of large multidimensional datasets in an easy and intuitive way. I tried to use programs with integrated image processing capabilities to approach quantitative measurements for various biological questions. Among the tested software packages were programs like ImageJ (<http://rsb.info.nih.gov/ij/>) [149], Heurisco (<http://www.heurisco.de>), Matlab (<http://www.mathworks.com>) image processing package and Imaris (<http://www.bitplane.ch>) [150]. Quickly the limits of these toolkits became visible for my work. Among other things the limitations included the lack of high-throughput capabilities, completely missing data handling, processing, and quantification of multidimensional datasets and poor visualization of the data and results in a multidimensional way. Another important aspect that I found missing was the lack of information for the underlying algorithms. Beside the often cryptic, program specific and non-intuitive parameter sets, the (proprietary) software documents did not describe the true underlying algorithms. Especially the use of

quantitative measurement algorithms showed large value differences in the results with only slight changes of the parameter sets, e.g. filter parameters, i.e. Imaris isosurface rendering and volume determination. The major drawback of the existing platforms was their lack of quantification routines and modules. I encountered severe problems extracting quantitative parameters from multidimensional microscopy data with the available pre-processing, segmentation and visualization algorithms, e.g. object surface and volumetric parameters, object velocities (by single particle tracking). Tikal was developed for this purpose.

The word Tikal has its origins in the ancient Mayan language and means "place of spirits". Today the name stands for the monumental Mayan temple ruins in the northern part of Guatemala. I have chosen this name because of the direct parallels to the construction methods of these ancient ruins. The Tikal temple area evolved step by step by the brilliant ideas of the former architects and great craftsmanship. So does the Tikal image processing platform: it grows by incorporating new image processing routines to facilitate the general workflow of image pre-processing, segmentation, quantification and visualization. Therefore Tikal is an easy, fast, reliable and extendable framework for the analysis of biological datasets.

3.2.2 Concept of Tikal

During the initial development stages I designed Tikal in a modular and extensible way. This modular concept means that the different parts can be run as stand-alone applications (see Figure 3.15). Tikal comes in two user accessible versions. A graphical user interface (GUI) that enables an intuitive and straightforward way of interaction with the program and its underlying routines. Another way of using the program is a command line interface that is suitable for high-throughput processing and repetitive tasks. The two interaction methods will be described in more detail later.

The most important core part of Tikal is the image processing library. The library is completely written in C/C++ and unifies the essential functions for data handling, memory allocation and handling, and data conversions. On top of these functions I included algorithms for image data import and export, processing and quantification. The import routines enable the opening of original Leica and Deltavision files and additional Tiff or raw files of different formats. To facilitate the import of huge multidimensional data stacks from other microscopic systems (e.g. Zeiss data files) I included an import macro. The image data can be exported as tiff or raw images or saved as internal Tikal format for later use.

After successful loading of the multidimensional images the user is able to interactively work with the dataset. For this purpose I programmed a GUI using an open source API Fox Toolkit (<http://www.fox-toolkit.com/>). The use of a non-commercial GUI has several advantages such as the avoidance of licensing fees, light weighted structure of the GUI containing only the essential functions and continuous (almost daily) new version updates with code feature improvements. The most important aspect was the selection of a platform independent GUI which is capable of compiling on Linux, Windows and Macintosh systems.

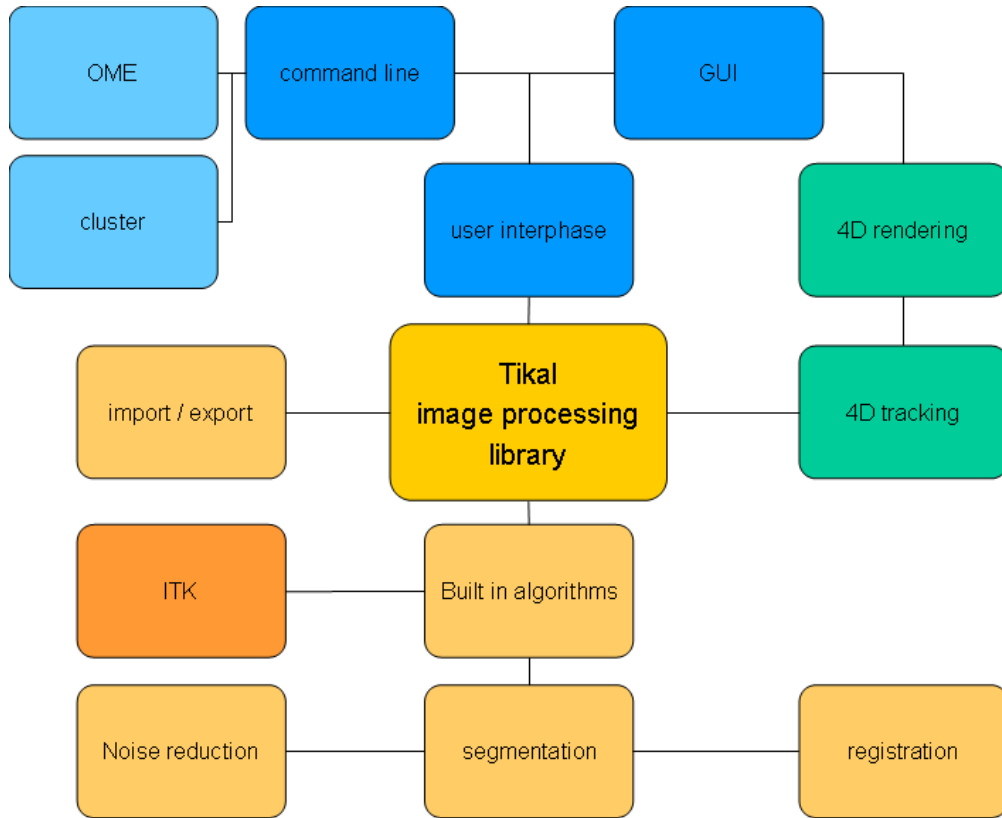


Figure 3.15: General conceptual overview of the Tikal image processing platform. The library is built around the fundamental core functions such as memory allocation and process coordination (yellow fields). Image processing functions can be called by a common interface, processed and returned (orange fields). Since also external libraries have been integrated special interface conversion functions have been written to enable flawless functioning of these foreign packages. On top of the core library function a user interface has been developed. The communication with the underlying routines can be either achieved by a GUI or a command line interface. The GUI features also enhanced visualization modules such as 4D isosurface rendering modes. Within the isosurface rendering scene tracking results can be displayed and manually manipulated (green fields). The command line interface gives capability to use the image processing libraries in conjunction with a Grid cluster computing environment. Further the Tikal library can be used with the open microscopy environment (OME) standard [166] to query large biological image databases, e.g. cell screening databases (blue fields).

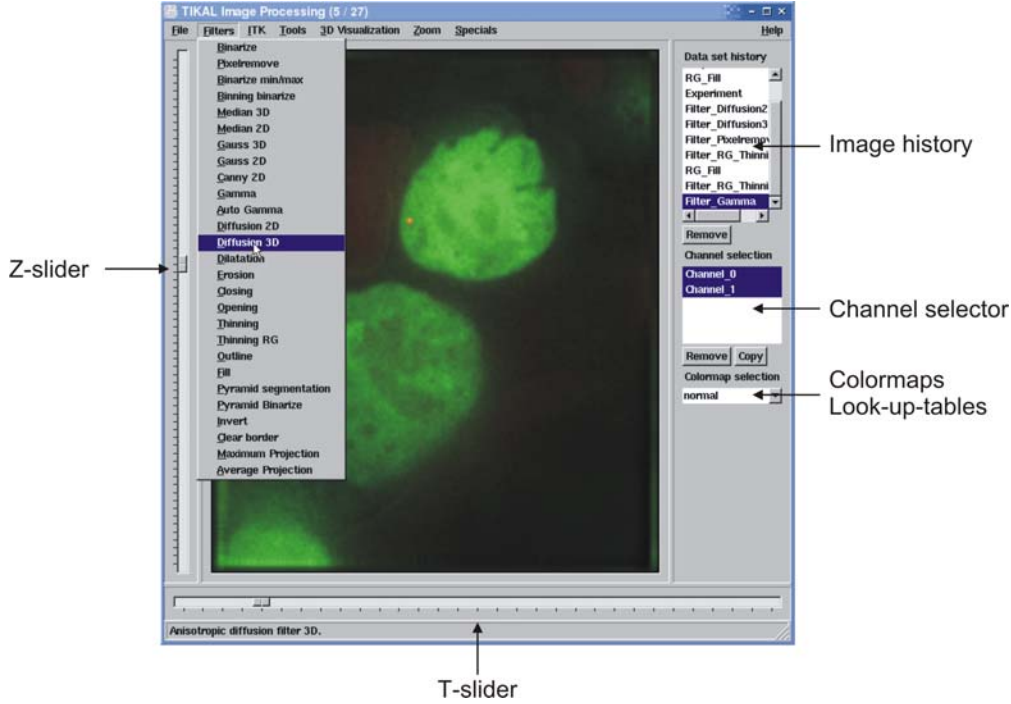


Figure 3.16: Overview of the working area of the Tikal image processing platform. The central element is the image display where the original and processed image can readily be seen. The interface enables the user to interactively browse through the complete datasets in all dimensions (z direction, time dimension and different colors) (sliders). The image history shows the already performed preprocessing steps and is identical to an extended undo function (image history). Additionally different channel and display modes can be selected (channel selector; colormaps). The pull-down menu shows a selection of applicable filters.

After extensive web-search I have chosen to use the open source GUI from Fox Toolkit (<http://www.fox-toolkit.com/>).

The user has an easy visual access to the multidimensional image dataset by using the GUI. I included a function for browsing and inspecting the multidimensional datasets in z direction, time dimension and different colors (channels) by using sliders, zooming and the use of color lookup tables (see Figure 3.16). To obtain a 3D representation of the data I programmed an isosurface extraction module. The isosurfaces are extracted by the marching cube algorithm approach [167] and improved by the iterative Taubin smoothing algorithm [168, 169] (see Figures 3.17, 3.18).

The extraction of information from segmented images by the marching cube algorithm [167] creates a polygonal surface representation of an isosurface through a 3D scalar field. A cube is considered to be eight neighboring pixels, where each pixel is either inside or outside the surface. There are 256 combinations of pixels in total. For every such cube, a combination of triangles is defined in a lookup table (zero to five triangles) that represents the part of the surface inside that particular cube (see Figure 3.17). The algorithm iterates over the whole 3D scalar field, forming a list of triangles in the process that represents

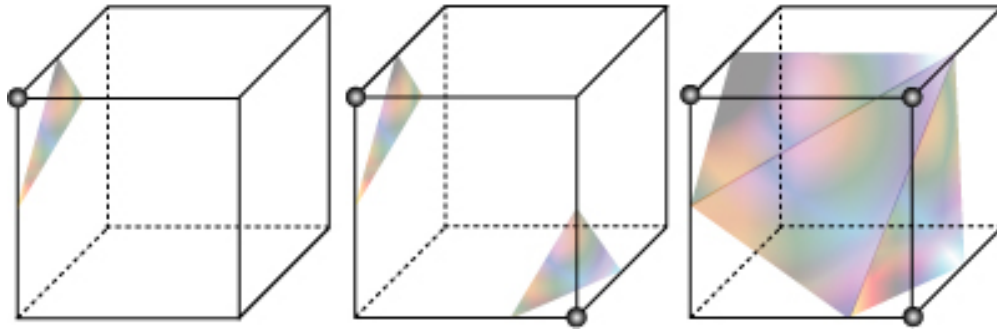


Figure 3.17: Schematic overview of the marching cube algorithm method for extraction of isosurfaces. The cube is rastered over the image and analyzes the individual corner pixels. If one of the checked pixels is within a user defined threshold a triangle is fitted within the corner of the cube (left cube). The same behavior is observed if two or more opposite corners are found (central cube). If adjacent pixels are detected the algorithm fits and optimizes the found triangles to result in a closed surface representation (right cube).

an isosurface.

After isosurface extraction the data can be inspected as a 4D scene with an integrated OpenGL scene viewer. A time slider enables again to easily and intuitively navigate through the data.

Visualization only allows qualitative statements about the datasets. Hence, I integrated an image processing filter module to the Tikal library that enables processing and quantification of the biological image data. The contribution of the image processing functions helps to define a seamless image processing workflow. Such a workflow can include noise reduction, registration, segmentation and final quantifications of the data, i.e. by 3D particle tracking over time. The variety of the available filters will be explained in the next chapter (see Chapter 3.2.3). To extend my image processing filter functions I integrated ITK (<http://www.itk.org/>), an open source image processing library, to Tikal, which offers major extension especially for image segmentation and registration processes. Furthermore the integration of this module proves the working modular concept of Tikal and the easy integration of additional features.

As already discussed one can use the vast amount of processing algorithms by accessing them with the graphical interface. Because findings in biological data have to be confirmed by repetition of the performed experiments manual evaluation of large and similar multidimensional image datasets can be very time-consuming and nerve-racking. Therefore I included a high-throughput processing procedure for these large and repetitive 4D datasets. The user is able to communicate and use all the importing, exporting and processing features of Tikal on the command line interface. This feature opens the option to run parallel batch jobs on its large datasets. To optimize the computational time I programmed a script to use the batch job capability of Tikal on a high performance Grid cluster.

Almost every physical object parameter, dependend on the underlying biological question, can be extracted with Tikal for data quantification, e.g. object

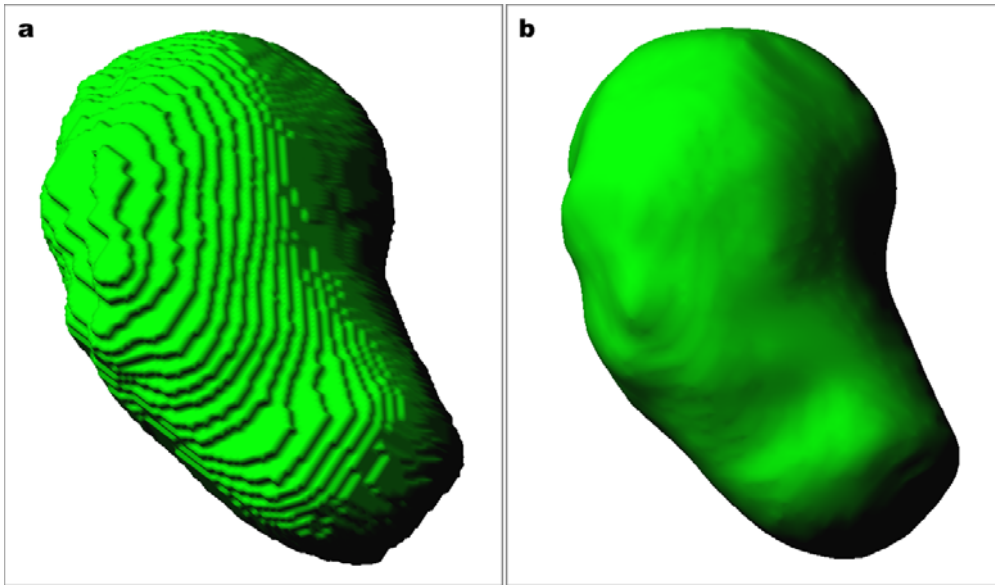


Figure 3.18: Effects of Taubin smoothing [168, 169]: Taubin smoothing is used for a number of computational purposes, including representative visualization and data extraction for biological data. The major problem in visualization is that smooth curves must be approximated by polygonal curves and surfaces by polyhedral surfaces. An inherent problem of these approximation algorithms is that the resulting curves and surfaces appear faceted. The algorithm optimizes the position of the polyhedral isosurface area corners which results in a real world representation of the processed object. During the iterative smoothing process the algorithm avoids shrinkage of the object. a) original and unprocessed cell nucleus extracted by the marching cube method. b) the same nucleus but processed with the iterative Taubin smoothing algorithm.

volumes, surfaces and velocities. Since I was interested in the timely resolved 3D positioning of particles in a cell or cell nucleus I included a 4D tracking module initially developed by Matthias Gebhard in our lab [164]. This module is capable of combining image features from binarized and gray-value images and tracks them in 3D over time. Physical object properties such as volume, center-of-mass (COM), gray-value distribution, speed and acceleration were taken into account to increase the accuracy of automated tracking. The trajectories are displayed within the previously described 4D isosurface rendering window in conjunction with the actual tracked objects (see Figures 3.13, 5.3). The visualization of the trajectories enables a visible approach to confirm the overall tracking result. To correct for possible tracking failures I added the capability of user defined manual tracking within the OpenGL isosurface rendering window. My manual tracking option greatly improves the tracking efficiency in two ways. First, by using the 4D trajectory visualization information the user is able to optimize the parameter sets for further automatic tracking. Second, the user can correct possible tracking artifacts or extend the trajectories in a manual way, by pointing and clicking with the mouse on the individual objects. The manual 4D tracking is especially powerful when the SNR ratio is very low resulting from a poor segmentation or from particle merging, dissolving or reappearing events [170].

Another common problem during the analysis of subcellular or subnuclear particles is the overall motion of the living biological specimens. These cellular or nuclear movements bias the tracking data. For this purpose I included an already implemented and tested registration scheme which was developed in our lab within the Tikal program [159, 171]. This module is capable of performing 4D registration based on a point-based matching method using already segmented image stacks. The advantage of this registration module are its various available transformation models. The incorporated registration algorithms include the option to perform simple rigid transformation, affine transformation and thin-plate splines transformation. However, for some applications this procedure led to misregistration due to the prior segmentation step and the resulting loss of gray-value information. To optimize the registration results I included another registration tool into Tikal. The second registration tool is an open source medical imaging registration library called AIR providing rigid and affine transformation models [161]. This package is capable of using gray-value images as starting points for registration. Due to the fact that the AIR library consists of self compiling stand-alone programs I decided not to take this third party registration library into Tikal. Moreover I added the option to transfer the 4D data in the correct format for registration with the AIR package. To use the AIR package on the computer cluster I wrote scripts which enabled an easy-to-use command line user interface to this abundant registration package. Beside the described registration modules, other registration algorithms are included in ITK. Because the registration algorithms of ITK have been added recently no tests for biological images have been performed so far.

3.2.3 Features of Tikal

I programmed Tikal in a modular way which enables an easy extension of the existing framework with new algorithms and available plug-ins. The main features of Tikal focus on image pre-processing, segmentation, registration, quantification and visualization. In this chapter I want to focus on specific features and algorithms of the Tikal image processing platform. More details will be given for the already introduced areas of pre-processing, segmentation and quantification methods in closer context with the underlying algorithms found in the program.

Data import, export and handling within Tikal

Data import routines for Leica and Deltavision files are incorporated as well as generic scripts to open standard multidimensional microscopic tiff images. To facilitate and obtain an overview of the working progress a “filter processing history” function has been included that is similar to an undo function. This function enables a precise reconstruction of the image processing workflow. Tikal further offers options to open and export this progress history from and to the hard disk at any time.

Image pre-processing routines

A large number of pre-processing algorithms is available within Tikal (see Table 3.1). Because of the modular concept of the Tikal image processing library further filter extensions can be integrated and made accessible very easy. Another advantage of Tikal compared to other image processing programs is that Tikal can make use of 3D capabilities of certain filters due to its internal data representation. Since there is no restriction to the filter types the user can choose the different modes according to the underlying dataset and problem, i.e. 2D or 3D images.

A variety of common usable generic pre-processing methods are implemented in Tikal. A good starting point for image noise suppression is the use of Gaussian or median filters. However, as already discussed, these filters can blur the image without taking object borders into account which subsequently can lead to unsatisfying segmentation and quantification results. Therefore edge preserving smoothing filters such as the introduced anisotropic diffusion filters are optimal in preserving edge information while preparing images for the following segmentation steps.

The gradient anisotropic diffusion filter represents a robust and good filter for the work with biological images. The filter is integrated in two optimized forms in Tikal. However, the smoothing results are similar and derive from an N-dimensional implementation of the classic Perona-Malik anisotropic diffusion approach for scalar-valued images [143, 147]. Similar to the anisotropic diffusion filter is the previously introduced bilateral image filter [156]. The bilateral filter is used from the ITK filter library and demonstrates besides its powerful processing function the seamless integration into the Tikal image processing library. The bilateral image filter is similar to anisotropic diffusion but is implemented

Pre-processing filters	Segmentation filters
2D/3D Gauss filter	Simple binarization
2D/3D Median filter	Pyramid linking binarization
2D/3D Anisotropic diffusion	Connected threshold region growing
Bilateral diffusion	Connected neighborhood region growing
Gradient diffusion	Confidence connected region growing
Gradient magnitude	Otsu thresholding
Canny edge detection	Outline detection
Gamma correction	Object filling
Autogamma correction	Pixelremover
Dilatation	
Erosion	
Opening	
Closing	
Inversion	
Maximum intensity projection	
Average intensity projection	

Table 3.1: Overview of filters included in Tikal. The filter are categorized into two groups of pre-processing and segmentation methods, respectively. Explanation of the relevant pre-processing and segmentation filters are given in the text.

as non-iterative algorithm which shows slightly faster processing results than the classical anisotropic filter.

Certainly there are more approaches available for image pre-processing but I obtained remarkable results applying the above described filters to my raw image datasets. Especially very noisy images that were distorted by high pitch noise or scattered light artifacts in the object or background areas were optimally prepared for the subsequent processing workflow.

Selection of segmentation methods for pre-processed data within Tikal

After pre-processing the images, e.g. with an anisotropic diffusion filter, the data had to be segmented for quantitative analysis. Due to the high variability of different structures within the images and the large amount of filters I decided to use segmentation filters that have shown suitable results in the medical imaging field. Beside different simple binarization methods such as simple thresholding and image pyramid linking thresholding I included more advanced filters such as region growing segmentation filters. The region growing filter category consists of several different methods that are implemented in Tikal (see Table 3.1).

The region growing filter, as defined earlier, tries to identify homogeneous regions within an image which fully or partially describe objects of interest. For this, a simple criterion for including pixels in a region is to evaluate the intensity value inside a specific gray-value interval. An example is the “connected threshold region growing filter” that uses a threshold interval criteria provided by the users. The region growing algorithm includes those pixels to the region

of interest whose intensities are inside the defined interval. Present noise in the image can reduce the efficiency of this filter to grow for large regions. When faced with noisy images, it is usually convenient to pre-process the image by using an edge preserving smoothing filter.

The “neighborhood connected threshold region growing filter” is an extension of the “connected threshold region growing filter” which accepts a pixel in the region if its intensity is in the interval that was again defined by two user-provided threshold values. The difference is that the extended filter will only accept a pixel if all its neighbors have intensities that are within the defined interval. The size of the neighborhood (defined by the user) to be considered around each pixel is defined by a variable filter mask. The reason for considering the neighborhood intensities instead of only the current pixel intensity is that small structures are less likely to be accepted in the region and might get lost.

Another criterion for dividing pixels into discrete regions is to minimize the error of misclassifications under the histogram. A way to look at the problem is that two groups of pixels exist within the image histogram, one with one range of values and one with another interval. The problem is that these two ranges usually overlap what makes thresholding difficult. The goal is to find a threshold that classifies the image into two clusters. The difficulty is that only the histogram for the combined regions exists but the separated histograms for each individual region is not available. The solution is to minimize the area under the histogram for one cluster that lies on the other cluster’s side of the threshold. This should result in the minimization of the error of classifying a background pixel as a foreground one or *vice versa*. The Otsu threshold selection algorithm can also be described by the minimization of the within class variance or equivalently maximization of the between class variance. The segmentation with the Otsu approach is very suitable for large 4D imaging experiments because it can automatically calculate without user interference an optimal threshold for each individual 3D stack. However, if the number of objects is too high, the SNR too low or the objects are touching each other the performance of the Otsu approach decreases and oversegmentation can occur.

Another interesting segmentation approach with minimal user interference is the “confidence connected threshold region growing filter”. The criterion used by this filter is based on simple statistics of the currently processed region. First, the algorithm computes the mean and standard deviation of intensity values for all the pixels included in the region. A user-defined variable factor is used to multiply the standard deviation and define a range around the mean for the actually scanned pixel. Neighboring pixels whose intensity values fall inside the range interval of the standard deviation are accepted and included in the region. When no more neighboring pixels are found that satisfy the criterion for region inclusion the algorithm is considered to have finished its first iteration. At that point, the mean and standard deviation of the intensity levels are recomputed using all the pixels included in the region. This new mean and standard deviation defines a new intensity range that is used to reprocess the region where the neighboring pixel are again evaluated whether their intensity fall inside the defined range. This iterative process is repeated until no more pixels are added or the maximum number of iterations is reached. Noise that is present in the im-

age can reduce the performance of this filter to form large regions. Though the selection of the correct number of iterations and the standard deviation might be very difficult the overall performance of the filter is very efficient, effective and robust for segmentation of biological images.

PTV tracking and quantification of image objects with Tikal

After successful segmentation the considered objects have to be quantified according to their size, movement and other descriptive parameters. One important aspect for quantification is the use of single particle tracking approaches. With these methods a network of connections of objects, so called trajectories, are built up in image series to describe their change in 3D localization over time.

The Tikal tracking module is a 3D particle tracking velocimetry (PTV) algorithm using a fuzzy-logic approach to enable weighted classifications of the relevant physical parameters, e.g. size, volume and gray-value distribution of objects. Prior to the determination of the relevant parameters a proper pre-processing and segmentation has to be performed. With these segmented images a two-frame or three-frame particle tracking can be performed [164]. Two-frame particle tracking generally has to properly assign the individual COMs of the particle in the first image to the different particle positions in the subsequent image sequence. In the three-frame tracking method an additional parameter is introduced to compute properties such as particle accelerations. Such a parameter describes the acceleration of an object between three trajectory segments and can be used to optimize the tracking result (by properly defining threshold values).

The already discussed correspondence problem can be solved by introducing heuristic approaches. The Tikal tracking module takes advantage of some heuristics to perform PTV tracking. One can use the maximum particle velocity and small distance changes criteria to find trajectory correspondences of moving objects between two images within an interval Δt using the mass inertia law of physical bodies. A body has to be within a given physical limiting interval of possible values to solve the correspondence problem, e.g. the volume is not allowed to be larger than a defined value (also see Figure 3.14). The proper selection of heuristics is crucial to solve the correspondence problem. Therefore the commonalities of particle movements and particle properties such as object volumes or surfaces and gray-value distributions have to be linked and determined. A short time interval Δt between the subsequent images is needed to solve the correspondence problem and to improve the tracking result. Beside the two-frame velocity determination the particle acceleration is measured in a three-frame to refine the tracking process. Additionally a heuristic to determine the uniqueness of the trajectory has to be determined. In biological processes bodies or vesicles often tend to fuse or split during the experimental sequence. With these heuristics the particle correspondence problem can be solved for a local neighborhood.

An approach for a solution of the determined parameters is based on a hierarchical method that makes use of constructing a trajectory network involving a temporal linear defined working direction. The strategy to solve the correspon-

dence problem within the trajectory network is to use a fuzzy logic approach. The fuzzy logic strategy shows clear advantages compared to strong deterministic approaches. This means in theory that the use of the fuzzy logic approach does not require exact Boolean values for solution.

The trajectories resulting from the Tikal tracking algorithm can be shown in several modes. The results can be written as raw data in an ASCII file to the hard disk and exported to other programs for further evaluation. Another option is to directly visualize the trajectories with the internal 4D scene viewer. The direct visualization has several advantages compared to the text-file output. So the overall success and efficiency of the tracking process is instantly accessible in correspondence with the underlying 3D reconstructions of the experimental dataset. The tracking artifacts can be instantly identified and manually corrected. If the overall result is not satisfying at all another tracking process with an optimized parameter set can be initiated and directly visualized again.

Summary

The program Tikal has been written completely in C/C++ from ground up without using operating system bound classes. Therefore, the program can be easily compiled and deployed on computers running Windows or Linux. The program consists of two major parts. A GUI enables the user to communicate interactively with the image processing platform, e.g. importing data and optimizing filter settings. The second part is the actual image processing package which is completely independent from the GUI. This enables to run the algorithms on a command line based form in an optimized environment, e.g. parallel computer cluster. Additionally this abstraction and separation is further mandatory to include the library into other environments such as OME. Extension of the existing modules is very efficient since there is a general interface for handling the data. Even external libraries such as the ITK [172] have been recently integrated and the available procedures are now functionally fully available and usable. Data handling is mostly restricted to the memory. The images are completely loaded into the memory, which enables very fast data processing without time consuming I/O to the hard disk. However, a limiting factor might be the amount of memory, though this problem can be overcome with computers equipped with the appropriate amount of memory.

3.3 Experimental procedures

3.3.1 ES cell lines and culture

Female mouse embryonic fibroblasts (MEFs), prepared from 13.5 day embryos were cultured in Dulbecco's modified eagle medium (DMEM) with GlutMAX (Invitrogen, Karlsruhe, Germany) supplemented with 10% fetal bovine serum (FBS) (Invitrogen). Male and female ES cell lines were grown either on monolayers of mitomycin C treated feeder cells (in the case of HP310, D102, 53BL and 4B4) as previously described [173, 174]; or on gelatin-coated flasks or plates in the case of feeder-free PGK12.1 and HM1 cells, as previously described [112].

ES cells were maintained in an undifferentiated state in DMEM with GlutMAX, 15% fetal calf serum (Invitrogen), 10-4mM 2-mercaptoethanol (Sigma, Munich, Germany), and 1000 U/ml leukemia inhibitory factor (LIF) (Chemicon, Hampshire, UK). Differentiation of ES cells was induced by pre-adsorbing feeders (in the case of feeder-dependent ES cell lines) (see [88, 173]); removing LIF and using 100nM *all-trans* retinoic acid (ATRA)(Sigma) in DMEM supplemented with 10% FBS, and 10-4mM 2-mercaptoethanol. Differentiation medium was changed daily. All cells were grown at 37°C in 8% CO₂. Feeder-free male HM1 cells were a gift from E. Wagner; feeder-free female PGK12.1 cells were a gift from N. Brockdorff; 4B4 cells were derived by lipofection of the feeder-dependent CK35 ES cell lines (see [88, 173]) with a bacterial artificial chromosome (BAC) transgene (see Section 3.3.2).

3.3.2 ES cell transfections

Transient transfections were performed on undifferentiated or differentiating ES cells at 70-90% confluence. The medium was changed 2-3 hours prior to transfection and Lipofectamine 2000 (Invitrogen, Karlsruhe, Germany) was used under the manufacturer's conditions. Cells were left with the transfection mix overnight, the medium was changed the next day and cells were either fixed and treated or else used for live cell imaging several hours later. The 4B4 cell line was created as described [175] by transfecting the 399K20 BAC into CK35 ES cells and selecting in G418 at 750µg/ml 48h post-transfection (1mg/ml of G418 after establishment). The 4B4 LacI7 line was generated by applying Hygromycin (250µg/ml) selection 2 days after transfection of 4B4 cells with the p3'ss LacI-YFP plasmid [176].

3.3.3 SW13 cell culture and transfection

SW13 lacking endogenous vimentin [177] were usually grown in DMEM (Invitrogen, Karlsruhe, Germany) supplemented with 10% fetal calf serum (Seromed, Berlin, Germany), 20mM glutamine and 100µg/ml penicillin / streptomycin (Invitrogen) at 37°C and 5% CO₂. For live cell imaging purposes the cells were resuspended in complete DMEM without Phenol Red (Invitrogen) and grown in 2- or 4-well Lab-Tek® II chambers (Nalge Nunc International, Rochester, USA). Transient transfections were carried out using the FuGene 6 transfection reagent according to the manufacture's protocol (Roche, Mannheim, Germany).

Immediately before imaging, chromatin counter stain was obtained by incubating the cells with 1µg/ml Hoechst 33342 in complete DMEM without Phenol Red for 20 min followed by three times washing with DMEM without Phenol Red. Cells were then kept in complete DMEM supplemented with 20mM Hepes without Phenol Red. For tracking of nuclear particles I stably transfected SW13 cells with the expression plasmid encoding *Xenopus laevis* GFP-NLS-vimentin. To track vimentin particles in the cytoplasm, SW13 cells were transiently transfected with the *Xenopus laevis* GFP-vimentin cDNA construct described above.

3.3.4 GFP-NLS-vimentin constructs

The cloning of the *Xenopus laevis* GFP-NLS-vimentin expression plasmid has been described previously [154]. For the generation of the N-terminally tagged GFP-vimentin construct the vimentin cDNA was modified at the 5'-end to contain a BspE I-site followed by a Nde I-site containing the start methionine in frame subcloned into pBlueScript (Stratagene, La Jolla, USA). The BspE I / BspE I fragment was then subcloned into pEGFP-C1 and the orientation verified by DNA sequencing.

3.3.5 Microinjection of fluorescent polystyrene microspheres

SW13 cells were cultured in P35G-1.5-7-C-Grid cell locate culture dishes (Mat-Tek Corporation, Ashland, USA) in complete DMEM medium for 1 day after plating. Carboxylate-modified $0.1\mu\text{m}$ microspheres (FluoSpheres, #F8800, Molecular Probes, Leiden, Netherlands) were obtained as 2% solids in solution and further diluted to 0.04% solution in 1M BSA in PBS. Before microinjection, the microspheres were sonificated for 30 seconds to avoid aggregation. The AIS 2 system (Cell Biology Trading, Hamburg, Germany) was used for microinjection. Injection needles were drawn from borosilicate glass capillaries GC120TF-10 (Harvard Apparatus, Edenbridge, UK) using a Flaming Brown micropipette puller P-97 (Sutter Instruments, Novato, USA). The injection pressure was adjusted to 20-250 kPa in the different experiments. For evaluation of cell viability microinjected cells were grown at 37°C with 5% CO_2 overnight and examined the next day.

3.3.6 3D RNA and DNA FISH

Fibroblasts or ES cells cultured on gelatin-coated coverslips were fixed in 3% paraformaldehyde for 15 min at RT. Permeabilization of the cells was performed on ice in PBS containing 0.5% Triton X-100, and 2mM Vanadyl Ribonucleoside Complex (New England Biolabs, Ipswich, USA) for 3.5 min. The coverslips were rinsed twice and kept in 70% ethanol. Prior to FISH, the coverslips were dehydrated through an ethanol series (70%, 90%, 100%), air-dried and the washed in 2X SSC. The DNA was then denatured in 50% formamide, 2X SSC for 40 min at 80°C in an oven. The coverslips were then placed in ice cold 2X SSC, rinsed once and RNA/DNA FISH performed. The *Xist* probe used was a 19 kb genomic fragment derived from a lambda clone (510) which covers most of the *Xist* gene (see [88]). The Xic probe (YAC PA-2) has been described previously [88]. Probes were labelled by nick translation (Vysis, Downers Grove, USA) with spectrum green or red-dUTP (Vysis). Hybridization involved $0.1\mu\text{g}$ of probe (per coverslip) precipitated with $10\mu\text{g}$ of salmon sperm and resuspended in 50% formamide, 2X SSC, 20% dextran sulfate, 1mg/ml BSA (New England Biolabs), 200 mM VRC, overnight at 37°C . After 3 washes in 50% formamide / 2X SSC and 3 washes in 2X SSC at 42°C , DNA was counterstained for 2 min in 0.2mg/ml 4'-6-diamidino-2-phenylindole (DAPI), followed by a final wash in 2X SSC. Samples were mounted in 90% glycerol, 0.1X PBS, 0.1% p-phenylenediamine (Aldrich, Munich, Germany) (pH 9). A Leica DMR

fluorescence microscope with a Cool SNAP FX camera (Photometrics, Tucson, USA) and Metamorph software (Photometrics) were used for image acquisition.

3.3.7 Immunofluorescence of RNA and DNA FISH

Cells were fixed and permeabilized as described for RNA and DNA FISH (see Section 3.3.6). Following permeabilization coverslips were rinsed in PBS and preparations were blocked in 1% BSA (Invitrogen, Karlsruhe, Germany), and $0.4U/\mu l$ RNAsguard (Amersham, Buckinghamshire, UK) in PBS for 15 min, incubated with primary antibody (diluted in blocking buffer) for 40 min, then washed in PBS four times for 5 min each and incubated with secondary antibody (Alexa Fluor 568 goat anti-rabbit IgG, Interchim, in blocking buffer, Montlucon Cedex, France) for 40 min at RT. After washing in PBS, preparations were postfixed in 3% paraformaldehyde for 10 min at RT and rinsed in 2X SSC. RNA FISH was then performed as described in Section 3.3.6 (without a denaturation step).

3.3.8 Drug treatment of SW13 cells

Before drug treatment, I acquired 3D time series of cells with a time-lapse of $\Delta t = 10$ seconds for 10 minutes. Immediately afterwards the medium was exchanged for one of the following solutions: i) 600mM sorbitol; ii) 20mM azide / 50mM deoxyglucose; iii) $0.04\mu g/ml$ nocodazole; and iv) $1\mu g/ml$ cytochalasin D - all in complete DMEM without Phenol Red except for ii), which was applied in PBS [178]. After change of medium, I immediately acquired further 3D time series images for another 10 min. Thereafter, the drug containing medium was replaced by complete DMEM without Phenol Red. In order to document the recovery and viability of cells, images were acquired for another 10 minutes with the same microscope settings.

3.4 Data acquisition and analysis

3.4.1 4D live cell imaging

Live cell imaging was carried out on a confocal laser scanning microscope TCS SP2 AOBS (Leica Microsystems, Wetzlar, Germany) using a 63x oil immersion objective with 1.4 optical aperture (HCX PL APO lbd.BL 63x / 1.4, #506192, Leica Microsystems). The microscope was further equipped with a 29 mm objective heater (#0280.010, Leica Microsystems) with temperature-controlled device (#0504.000, Leica Microsystems) and a temperature-controlled fan (ASI 400E, Nevtek, Burnsville, USA). A diode laser ($\lambda = 405nm$) was used for excitation of Hoechst 33342. An argon ($\lambda = 488nm$) and a helium / neon laser ($\lambda = 543nm$) was used for EGFP and fluorescent microsphere excitation, respectively. 3D image stacks, each consisting of 17 2D-images, of GFP-vimentin particles and Hoechst 33342 stained chromatin were acquired in parallel at the maximum scanning speed of 1400 Hz (i.e. scan lines per second) with a constant $\Delta t = 10$ seconds. Imaging format was set to 256 x 256 pixel, voxel sizes were generally

between $0.093\mu m \times 0.093\mu m \times 0.325\mu m$ and $0.093\mu m \times 0.093\mu m \times 0.450\mu m$. The laser intensity was adjusted to a minimum to avoid photodamage during imaging. For this purpose the acousto-optical beam splitter (AOBS) were set between 2-5% for both lasers with photo multiplier (PMT) settings of 715.7 Volt for the diode laser and 717.4 Volt for the argon and helium / neon lasers. All the image processing steps were carried out in Tikal.

3.4.2 3D fixed cell imaging

Fixed cell imaging was carried out on a confocal laser scanning microscope TCS SP2 AOBS (Leica Microsystems, Wetzlar, Germany) using a 63x oil immersion objective with 1.4 optical aperture (HCX PL APO lbd.BL 63x / 1.4, #506192, Leica Microsystems). A diode laser ($\lambda = 405nm$) was used for excitation of DAPI counterstain. An argon ($\lambda = 488nm$) and a helium/neon laser ($\lambda = 543nm$) was used for Spectrum Green *Xist* RNA probe and Spectrum Red XIC DNA probe excitation, respectively. 3-D image stacks with an image format of 1024×1024 pixel and constant voxel sizes of $0,058\mu m \times 0,058\mu m \times 0,204\mu m$ where acquired. The number of z-stacks was adjusted according to the heights of the cell nuclei resulting in an average amount of 40 2D-images for each cell nucleus. The DAPI stained chromatin, the *Xist* probes and the Xic-DNA probes were acquired in parallel at constant scanning speed of 800 Hz (i.e. scan lines per second). The laser intensities were adjusted to an optimal signal to noise ratio and kept constant for all imaged slides. For this purpose the AOBS were set to 35% for the diode laser and to 40% for the argon and helium/neon laser. The PMT settings where adjusted to 499.7 Volt for the diode laser, 650.3 Volt for the argon and 628.6 Volt for the helium/neon lasers.

3.4.3 Segmentation of cell nuclei

Image processing was carried out using my image analysis platform Tikal running on a high-performance computing cluster. Segmentation of cell nuclei based on DAPI staining was performed automatically and the results were manually checked and confirmed for each individual cell nucleus. This manual step was necessary a) to elucidate and avoid false segmentation due to hybridization artifacts b) to eliminate oversegmented cells. This oversegmentation occurred because of the tendency of ES cells to grow in closed colonies and the insufficient resolution of the microscope to resolve the nuclei borders in the nanometer scale.

To achieve optimal segmentation results the image analysis process was broken down into two subsequent parts (see Figure 3.19). The first part included the finding of a ROI including a cell nucleus. The second subsequent analysis performed the segmentation of the nucleus in the ROI.

The ROI selection was performed fully automated by reducing image noise by 2D median filter followed by maximum intensity projection of the whole image stack. The obtained 2D image was segmented using a neighborhood connected threshold region growing filter (NCTRG) integrated into Tikal. Region growing algorithms have proven to be an effective approach for image segmen-

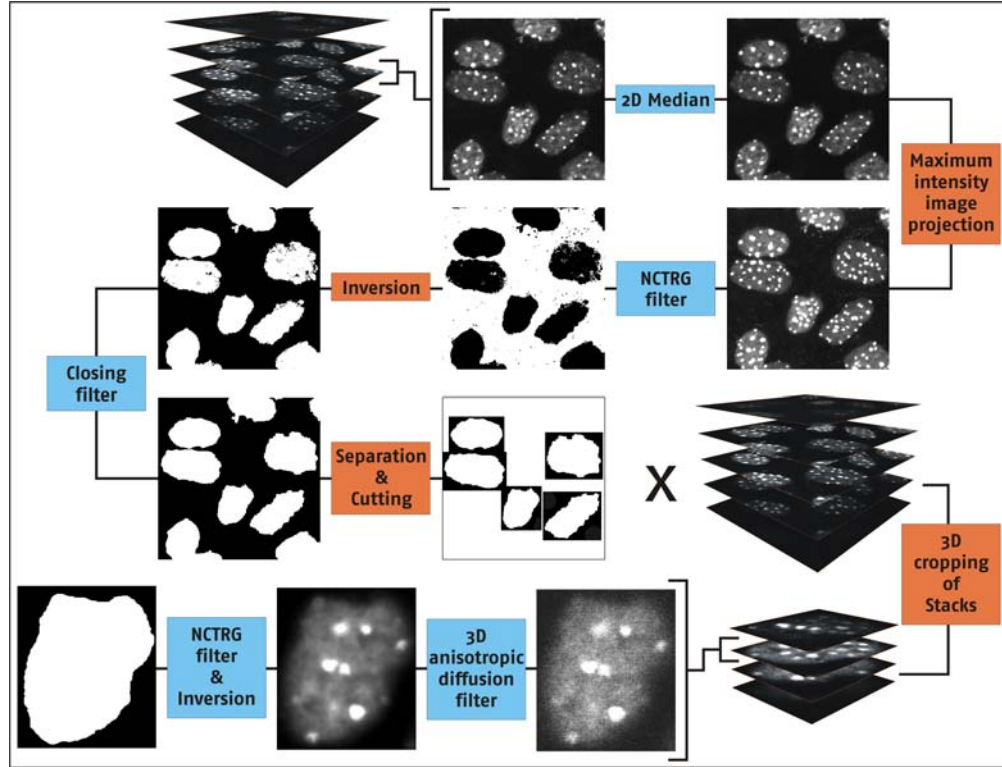


Figure 3.19: Data analysis workflow for segmenting 3D ES cell nuclei based on DAPI staining. 3D image stacks of populations of cell nuclei will be acquired by confocal laser microscopy. The different processing steps that are applied to the complete 3D data will be representatively visualized by a single 2D section. In a first step high pitch noise (such as "salt and pepper" noise) will be reduced by a 2D median filter followed by a maximum intensity projection of the whole 3D image stack. A neighborhood connected threshold region growing (NCTRG) filter will be applied to the image background area in the projection image. This leads to a complete segmentation of the background areas which needs to be inverted to obtain the corresponding cell nuclei. The segmented cell nuclei will be separated and individually used as regions of interests (ROI) to cut out single 3D stacks from the original data. These cropped 3D image stacks contain information to a single cell nucleus. The individual image stacks will be processed one by one by edge preserving 3D anisotropic diffusion filtering followed by a 3D NCTRG filtering of the background and subsequent inversion to obtain a representative segmented 3D cell nucleus.

tation. The NCTRG filter is an extension of the standard connected region growing filter using mathematical morphology erosion. The reason for considering the neighborhood intensities in the erosion process instead of only the current pixel intensity is that small structures are more likely to be segmented. The basic approach of the NCTRG algorithm is to start from a seed region that is considered to be inside the object to be segmented.

For our automated segmentation I used an inverted approach. That means I segmented regions not belonging to objects (background) and finally inverted the resulting image to obtain the binary nuclei regions. Following such a strategy has several advantages such as the selection of a seed point is independent of the actual position of the cell nucleus in the image, i.e. selection of the seed point can be always in the left upper corner of the image. Another advantage to segment the background are low intensity fluctuations within the background areas resulting in smooth object borders. High reliability of this inverted segmentation approach was crucial for application in a fully automated high throughput setting.

After obtaining a segmented 2D representation of the whole image area individual binary cell nuclei will be selected and used as template to define ROIs in each individual image of the 3D stack. The ROI is then processed by contour preserving and noise reducing 3D anisotropic diffusion filtering [147] followed by NCTRG in 3D using the same background segmentation strategy as described above. As a result I obtained accurately segmented cell nuclei in 3D.

3.4.4 4D Image registration

4D image registration [159, 161] of consecutively captured three-dimensional images of cell nuclei counterstained with Hoechst 33342 was performed for correcting for global movement of cell nuclei. In order to reduce alignment artifacts due to acquisition noise all three-dimensional image stacks were preprocessed using a 3D median filter and a 3D automatic gamma correction for maximum gray-value range. Image registration was then performed using an implementation of an automated image registration algorithm [161] running on a high-performance computing cluster. In this study, I only applied rigid and affine transformation since I did not observe drastic local deformations in cellular shape which would require correction by our non-rigid transformation method [171]. Rigid and affine transformation matrices were computed in a two-step process for optimal 4D object alignment. First, objects at time point $t + 1$ were consecutively aligned with 3D objects at time point t providing a pre-registered image stack at each time point. Secondly, each pre-registered image stack was aligned with respect to the initial image stack at time point $t = 0$. Transformation matrices calculated for the chromatin stained images were applied to all corresponding image stacks in the other color channels.

3.4.5 4D Tracking of fluorescent beads and vimentin particles

Image processing was carried out using the image analysis platform Tikal. The analysis chain consisted of three major modules: image pre-processing and segmentation, 4D tracking and quantification of dynamics, 4D visualization and user interaction with 4D datasets. To reduce noise in the vimentin channel, images were subjected to 3D diffusion filtering [147] followed by segmentation with a pyramid linking algorithm [179]. Particle tracking was performed by extending our already implemented single particle tracking algorithm from 2D + time to 3D + time [164, 146]. The tracking algorithm uses parameters such as the individual COMs, volumes, total gray-value intensities, velocities and accelerations. To control possible tracking and segmentation artifacts I visualized 4D tracks of beads and vimentin particles, respectively, together with their isosurface reconstruction at each time point.

3.4.6 Measurements of FISH signals

An automated segmentation of the Xic FISH signals was not possible owing to their variable intensity and size. Manual selection and segmentation of the Xic signal was therefore performed after segmentation of cell nuclei. This also enabled detection and correction of possible segmentation artifacts in the DAPI channel, e.g. caused by overlapping nuclei. To estimate the distance of the *Xist*/Xic region to the periphery and the inter *Xist*/Xic distance I implemented a new module in Tikal. This module is capable to find the closest distance of two segmented objects in different channels. For this purpose the Xic signal was automatically preprocessed by reducing noise by 2D median filtering followed by 3D anisotropic diffusion filtering. Segmentation was obtained by using NCTRG with a seed point in a background region. The segmentation results were manually cross validated against the original raw *Xist*/Xic data and if necessary corrected to avoid false segmentation. After this data validation the COM of each segmented signal was automatically obtained. The shortest Euclidian distances of the COM to the closest segmented nuclear periphery voxel (segmentation procedure described in Section 3.4.3) were calculated. The inter Xic distance was obtained by measuring the Euclidian 3D distance of the two segmented *Xist*/Xic COM within the cell nucleus.

3.4.7 Correlation analysis of chromatin density and tracked nuclear particles

Chromatin images were preprocessed by a 2D Gaussian smoothing filter to reduce noise. Additionally a gamma filter was applied to use the full gray-value range of 8 bits. For additional noise reduction the 256 different gray-values were divided into eight gray-value classes ranging from 0-32, 33-65, etc. The COMs for each individual polystyrene bead or nuclear vimentin body was calculated and tracked in 3D over time. For each time point the corresponding binned mean gray-value intensities of a 9 x 9 pixel area around the COM was determined.

3.4.8 Calculation of mean squared displacements and anomalous diffusion coefficients

The mean square displacement (MSD) was calculated for each particle and time point of the dataset according to

$$\langle d^2 \rangle = \langle [d(t) - d(t + \Delta t)]^2 \rangle$$

and plotted as $\langle d^2 \rangle$ (μm^2) versus $\Delta t(s)$ using Matlab (The MathWorks, Inc., Novi, MI). Further evaluation of anomalous diffusion (α) [180, 181] was determined by using the regression curve fitting functions implemented in Matlab.

3.4.9 Statistical analyses, simulations and plots for Xic locations

Significance analyses for Xic distributions were performed in R-Project (<http://www.r-project.org/>). For coherence the distributions were compared with two non-parametric tests, namely Wilcoxon and Kolmogorov-Smirnov tests [182, 183]. Both tests showed similar results for the analysis. Cut of threshold for similar distribution was the 95% quantile.

Simulation of random data points and q-q-plots generation were performed in R and are described in more detail below. Live cell line plots and barplots were generated with Sigmaplot. For data simulation random points with equal density distribution in a unit sphere were generated. For this purpose the volumes of all segmented nuclei were combined and the mean volume calculated which resulted in a approximation of a hypothetical cell nucleus with a radius of $7.2\mu m$. To simulate the Xic distance from the NE 1000 random spots within this sphere were generated by individually selecting the x, y, z, coordinate from a random uniform distribution number generator provided by R. Finally the shortest distances to the nuclear periphery were calculated by correlating the obtained 3D points to the previously determined simulated nuclear radius.

Similar procedures were chosen for the simulation of the distances in-between two hypothetical Xic signals. Two times 1000 individual uniformly distributed x, y, z coordinates were generated followed by the calculation of the Euclidian distance between two 3D coordinates resulting in 1000 simulated inter Xic distances.

The q-q (quantile-quantile) plot is a graphical technique for determining if two data sets come from populations with a common distribution. The method plots the quantiles of the first data set against the quantiles of the second data set. If the two sets come from a population with the same distribution, the points should fall approximately on a line with slope 1. The greater the departure from this reference line, the greater the evidence for the conclusion that the two data sets have come from populations with different distributions [184].

Chapter 4

Transient co-localization of Xics during the initiation of X-inactivation

4.1 Introduction

As previously introduced, one of the most intriguing features of the X-inactivation process is the differential treatment of two identical chromosomes within the same nucleoplasm. How does one X-chromosome become impervious to the same transcriptional machinery driving genetic activity of the second X-chromosome?

Initiation of this process is regulated by a master control locus, the X-inactivation center (Xic). Cells must register the presence of at least two Xics for X-inactivation to occur [104, 185] and only a single X-chromosome will remain active in a diploid cell. All supernumerary X-chromosomes become inactivated. The Xic is also the site from which inactivation spreads across the X-chromosome in *cis*, or even across an autosome, in X-autosome translocations. *Xist* RNA is essential for the initiation of X-inactivation and is thought to mediate spreading in *cis* [72, 75]. However, *Xist* is not involved in the counting function of the Xic [73]. A complex combination of antisense transcription to *Xist* (in the form of *Tsix*) and *cis*-regulatory sequences located in the region 3' to *Xist* appear to be involved in the choice and counting functions of the Xic (for reviews see [186, 95]). Several studies involving transgenesis have been performed for the Xic with the aim of defining the minimal region sufficient for Xic function at an ectopic (autosomal) site [86, 87]. Such experiments are a stringent test for assessing the sequences that are not only necessary, but sufficient, for the function of a locus. In transgenic ES cells and mice, such transgenes are able to act as ectopic Xics (when they included the *Xist* gene). However, they can only do so when present as multicopy arrays. Single copy *Xist* transgenes, up to 460 kb long (covering 130 kb of sequence 5' and 300 kb of sequence 3' to *Xist*) are unable to induce *Xist* RNA coating in *cis* or even to trigger inactivation of the endogenous X-chromosome (counting) [88]. Critical elements for autonomous Xic function must therefore still be lacking from these large single copy trans-

4. Transient co-localization of Xics during the initiation of X-inactivation

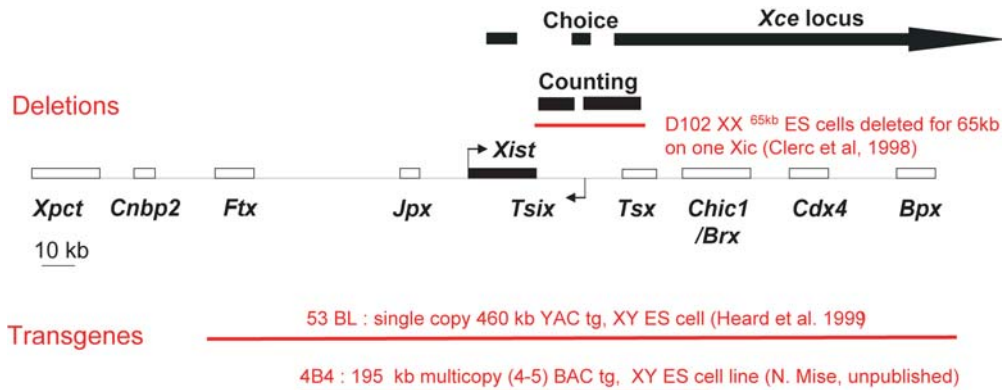


Figure 4.1: The mouse Xic region. The *wt* mouse Xic region with different X-inactivation specific gene loci (boxes) and their proposed functions (black arrows). The different lengths and sites of transgene regions or sequence deletions are indicated by red bars for the various cell lines. Bar: 10kb.

genes and multicopy arrays must compensate for this lack in some way. Given that the region involved in counting [174] lies intact within the large genomic transgenes tested so far [88], one hypothesis that has been proposed for the lack of counting and choice is that single copy transgenes may not be appropriately positioned within the nucleus, or relative to the X-chromosome. Such a mislocalization might prevent a single copy transgene from being "sensed" as a supplementary Xic and thus X-inactivation (of the endogenous X-chromosome) will not be triggered.

It is increasingly recognized that the localization of genes within specific nuclear compartments may be an important means of regulating gene expression [42, 187, 188]. Sub-nuclear domains enriched in factors specialized in particular functions may provide a nuclear context, beyond that provided by flanking sequence, that influences chromatin architecture and gene expression. Nuclear compartmentalization, mediated by binding of one X-chromosome to a single entity per nucleus, was one of the earliest models proposed to explain the differential treatment of the two X-chromosomes during X-inactivation [93]. In this context, one hypothesis for "counting" could be that the Xic on the remaining active X-chromosome is sequestered in a particular nuclear region (for example the nuclear envelope (NE)) and is therefore prevented from exposure to factors involved in triggering X-inactivation. Another, not mutually exclusive hypothesis proposes transient co-localization, or "cross-talk", between Xics [189]. Such cross-talk might help the cell to count or "sense" the number of X-chromosomes present and ensure that only a single X-chromosome remains active. This hypothesis is particularly attractive in the light of the incapacity of single copy transgenes to function as ectopic Xics and more specifically their inability to induce counting [88]. An absence of long range elements involved in directing the correct nuclear position of the Xic could result in these transgenes not being correctly "sensed" as supernumerary Xics due to their aberrant localization in the nucleus, or with respect to the other Xic.

Even though nuclear compartmentalization was one of the earliest mod-

Name	Genotype	Counting	Choice	<i>Cis</i> -inactiv.	References
HM1	XY	Yes	NA	NA	
PGK1	XX	Yes	Yes	Yes	[69]
HP310	XX	Yes	Yes	Yes	[174]
D102	XX ^{$\Delta 65kb$}	No	No	Yes	[174]
53BL	XY (Tgn=1)	No	No	No	[190, 173]
4B4LacI7	XY (Tgn=4)	Yes	Yes	Yes	this study

Table 4.1: List of the analyzed cell lines including their genotypes and observed phenotypes during early X-inactivation (see also Figure 4.1). Tgn: Transgene repeat inserts.

els proposed to explain the control of X-chromosome inactivation, surprisingly few studies have actually addressed this possibility. In this project I assessed whether the Xic locus shows any signs of non-random spatial distribution in the nucleus that might reflect - or underlie - its specific functions in controlling the onset of monoallelic gene expression of the X-chromosome. In particular I determined whether the Xic shows any particular association with the NE. I also addressed the possibility that cross-talk occurs between the Xics. To evaluate the functional significance of these Xic interactions, I analyzed a variety of wild type (*wt*), transgenic and mutant ES cell lines using 3D FISH analysis of thousands of nuclei (see Table 4.1 and Figure 4.1). Due to the vast amount of data, manual analysis was impossible and advanced computational and statistical tools had to be developed. Pre-processing, segmentation and analysis of over 5000 single cells were performed with Tikal (see Section 3.2 and [145]). Live cell imaging of Lac operator-tagged Xic transgenes in ES cells was also developed, in order to examine the *in vivo* dynamics of the Xic locus. Based on such analyses, I show that the Xic preferentially occupies a peripheral localization in early stages of ES cell differentiation. In female ES cells I reveal the existence of a transient co-localization between the two Xic during the initiation of X-inactivation, which I propose could be part of a “sensing” mechanism implicated in the counting and choice functions of the Xic.

4.2 Results

4.2.1 Peripheral nuclear localization of the Xic in undifferentiated and differentiating male ES cells

Using a 3D FISH approach, and my previously described image analysis tool Tikal (see Section 3.2), I set out to assess whether (i) the location of the Xic within the nucleus might be non-random (ii) the position of the Xic changes during ES cell differentiation, in particular during early differentiation, which is when the initiation of X-inactivation occurs and Xic function is important (iii) the location of the Xic in ES cells is comparable to that in fully differentiated cells, such as mouse embryonic fibroblasts (MEFs). I analyzed male (HM1) ES cells, grown on gelatinized coverslips and differentiated over a 4 day period, by

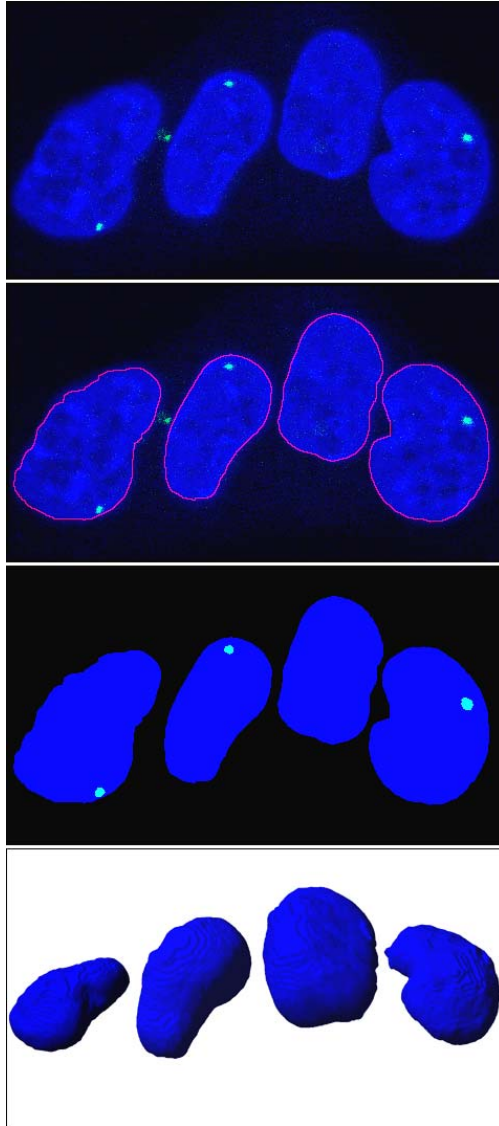


Figure 4.2: Illustrative visualization of the image processing workflow on a single confocal image plane to prepare the data for the later quantification process. In a first step the cell nuclei have to be pre-processed by noise reducing and edge preserving filters followed by detection of the nuclear edges that lead to a full segmentation of the cell nuclei. In a second step the Xic signals get segmented. Binarization of both signals in separate channels enables subsequent automated measurements of the various distances (see Figure 4.3). Blue = cell nuclei stained with DAPI; green = Xic-FISH signals; red line = outlines of detected cell nuclei.

LIF withdrawal and ATRA treatment. Male MEFs were used as fully differentiated controls. In order to preserve 3D nuclear structure, cells were fixed first and then permeabilized prior to DNA FISH (see Sections 3.3.6 and 3.3.7). Confocal laser scanning microscopy was used to acquire 3D stacks on large numbers of nuclei (≥ 80) per coverslip and advanced image analysis tools were used to perform semi-automated segmentation of the nucleus defined by DAPI staining (see Figures 4.2 and 3.19). The FISH signal corresponding to the Xic was segmented manually and the shortest distance (D_p) of the Xic from the NE, as defined by DAPI staining, was computed automatically (see Figure 4.3 and Section 3.4.6).

The distributions of Xic distances from the NE in MEFs and ES cells at different stages of differentiation were examined (see Figure 4.4). To assess whether these distributions were random or not, I compared each data set with a simulated data set of 1000 randomly distributed points in a hypothetical spherical

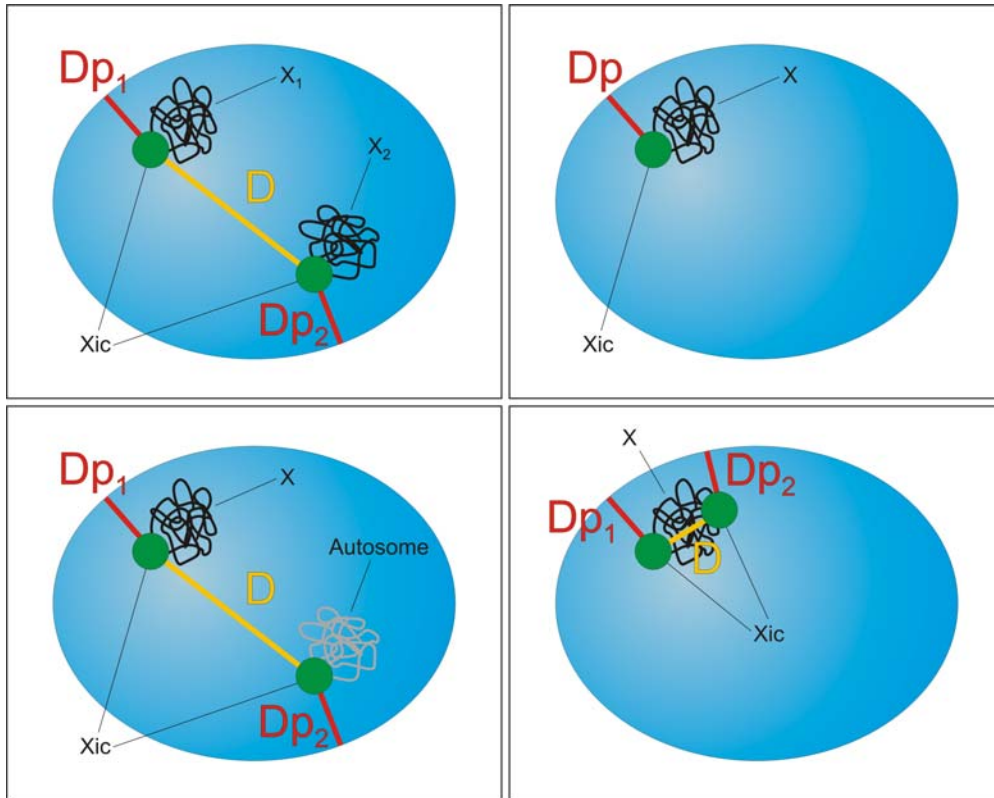


Figure 4.3: Different possibilities of distance measurements in ES cell nuclei according to the analyzed cell lines. DP_1 , DP_2 = shortest distances to the nuclear periphery; D = distance between two Xic loci; X = X-chromosome. Top left) representative female cell line nucleus with two X's and their corresponding Xic locus signal. Different parameters such as the two shortest distances of the Xic's to the nuclear periphery (DP_1 and DP_2) and the Xic inter distance (D) can be measured. Top right) representative *wt* male ES cell nucleus where only one X is present. In this case only the distance of the locus to the nuclear periphery (Dp) can be measured. Lower left) Transgenic male cell line with a *wt* Xic on the X-chromosome and a single or tandem repeat Xic insert on an autosomal chromosome. The parameters from data extraction are the same as compared to *wt* female ES cell lines. Lower right) Special case for male transgenic ES cell lines. The Xic LacO tandem repeat has been stably inserted into the *wt* X. Again, three possible parameters can be extracted, although they are distinctively different to the *wt* since Xic insertion on the only X-chromosome occurred. This integration shows limits in the spatial localizations of the Xics in respect to the nuclear periphery and in-between Xic distances.

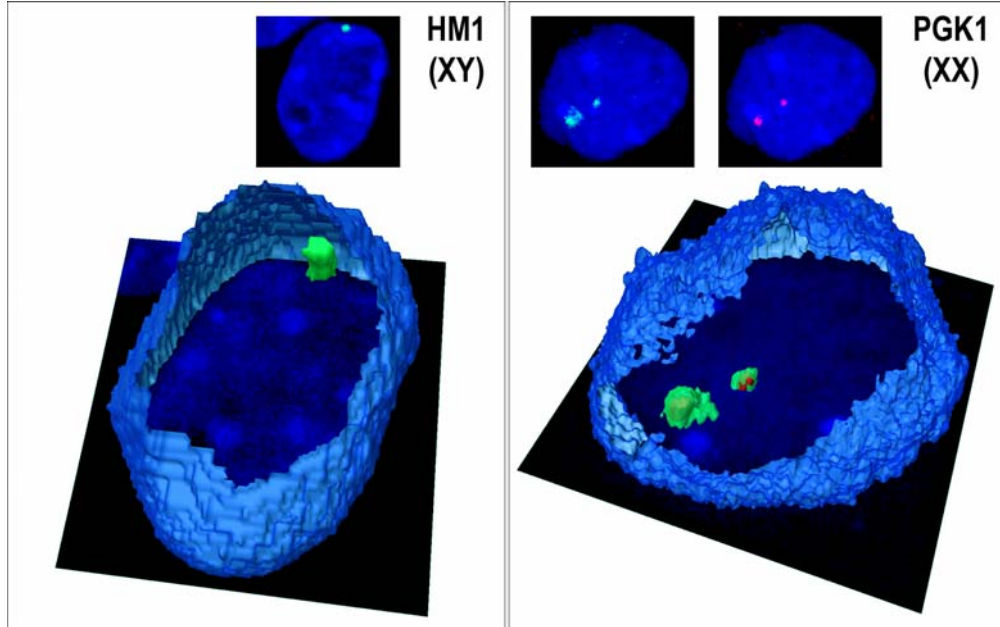


Figure 4.4: 3D isosurface visualization of male (HM1) and female (PGK1) ES cell nuclei. Prior to visualization the DAPI (blue) stained nuclei have been pre-processed and segmented to enable isosurface extraction. The nuclei are cut open to give sight on the *Xist*/*Xic* signals (green/red). A peripheral nuclear localization of the *Xic* in the male ES cells can be observed whereas in female ES cells a more internal nuclear localization of the *Xic* is detected.

cell nucleus with a radius of $7.2\mu m$, which corresponded to the average nuclear radius obtained from all of the acquired data. The mean distance of the *Xic* locus from the NE in male ES cells (ranging from $0.05 - 0.57\mu m$, depending on stage of differentiation) was significantly different ($p < 0.0001$; using the Kolmogorov-Smirnov and Wilcoxon tests, see Section 3.4.9) to that for the hypothetical cell nucleus ($1.6\mu m$) and also to the mean distance for male MEFs ($1.2\mu m$) (see Figure 4.5). The peripheral localization of the *Xic* was particularly striking in male ES cells, at 1.5 days of differentiation, where the mean distance was found to be just $\sim 0.05\mu m$ (compared to $0.52\mu m$ in undifferentiated ES cells and $\sim 0.6\mu m$ at other time points). Results obtained from two independent differentiations were similar. Statistical analysis of the HM1 data sets demonstrated that the localization of the *Xic* close to the NE, prior to and during differentiation, was highly non-random and that this skewed distribution was highly significant ($p < 0.0001$) (see Figure 4.6).

4.2.2 More internal nuclear localization of the *Xic* in undifferentiated and differentiating female ES cells

A similar analysis was performed on two different female ES cell lines (PGK and HP310) as well as on female MEFs. In this case simultaneous *Xist* RNA / *Xic* DNA FISH were performed, in order to identify the X-chromosome undergoing inactivation. The kinetics of *Xist* RNA accumulation and X-inactivation during

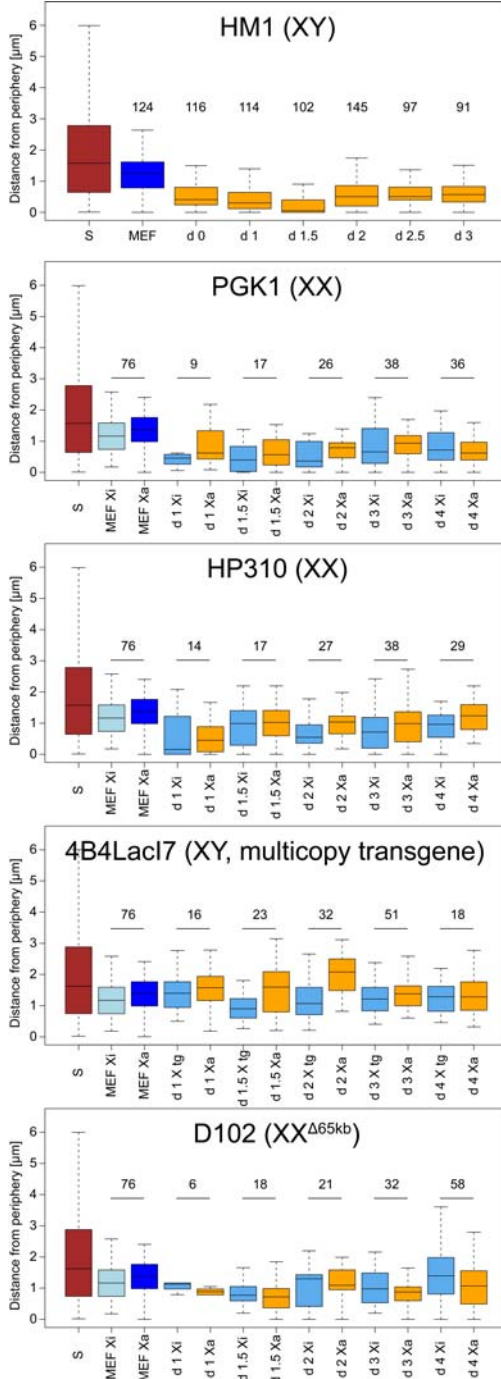


Figure 4.5: Visualization of Xic distance distributions to the nuclear periphery with box plots for male (HM1) and two female (PGK1, HP310) *wt* ES cell lines. The individual bars represent the combination of the peripheral distance distributions for the respective experimental classes. The number of data points for each class is shown on top of the corresponding bar. The average distance to the nuclear periphery is indicated by a horizontal line within the boxes. The solid boxes contain all values falling into the 95% quantile confidence level. For male ES cells a close association of the Xic to the nuclear periphery can be observed. Female ES cells show a more internal nuclear localization of the Xic. Strikingly, a significant shift of the Xic towards the nuclear periphery can be observed for HM1 cells on day 1.5 after induction of differentiation. In both female ES cells no significant changes in the distances of the Xic to the nuclear border can be observed. In female cells the Xics were linked to either the Xi and the Xa according to detectable or absent Xist accumulation, respectively. S = simulated distribution class consistent of 1000 randomly placed spots within an artificially simulated nucleus; C = Control experiment consisting of male or female MEF populations; dx = days after start of inactivation, where x indicates the actual time point in days from the initiation of X-inactivation.

4. Transient co-localization of Xics during the initiation of X-inactivation

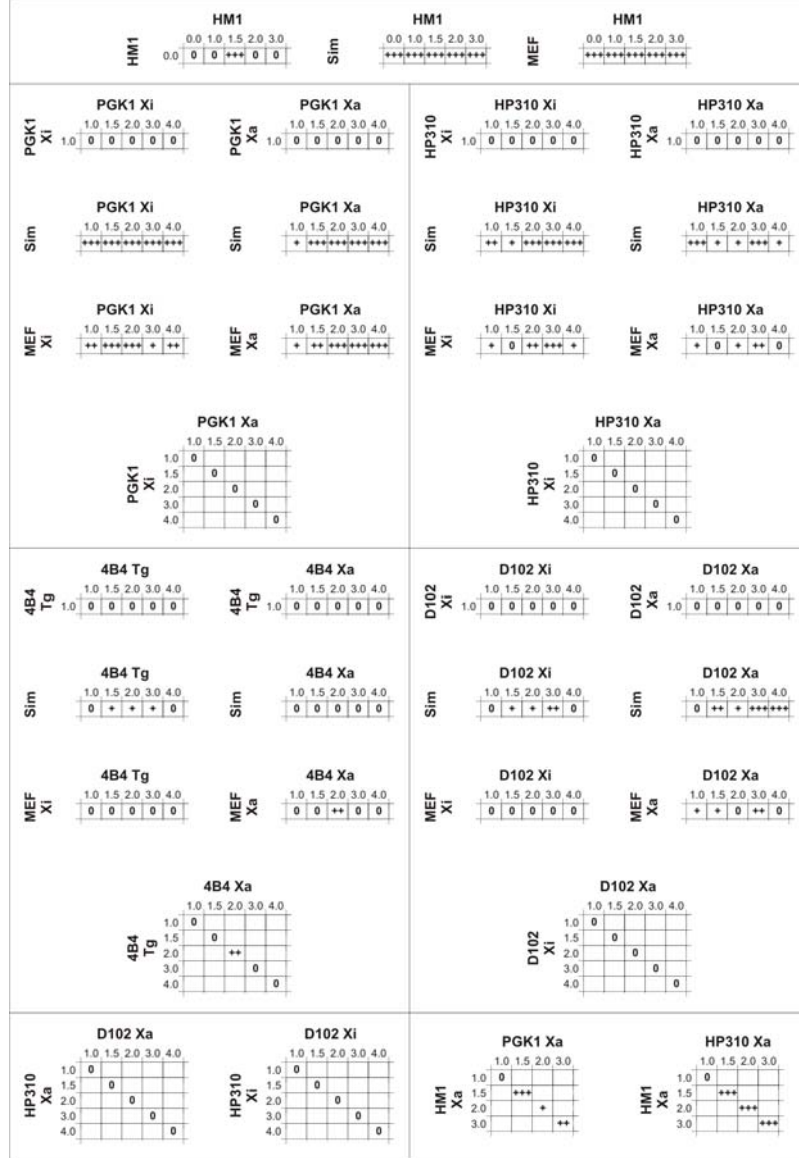


Figure 4.6: Significance determination with the Kolmogorov-Smirnov test of the Xic distance to the nuclear periphery in the analyzed cell lines for the different time points of X-inactivation. The labels of the compared cell lines are found at the top and on the left hand side of each matrix. The numbers indicate the time points of the respective day of inactivation. 0 = $p > 0.05$; + = $0.05 \leq p < 0.01$; ++ = $0.01 \leq p < 0.0001$; +++ = $p \leq 0.0001$; Xa = Active X-chromosome; Xi = inactive X-chromosome; Sim = Simulated data points (see Section 3.4.9); MEF = mouse embryonic fibroblasts.

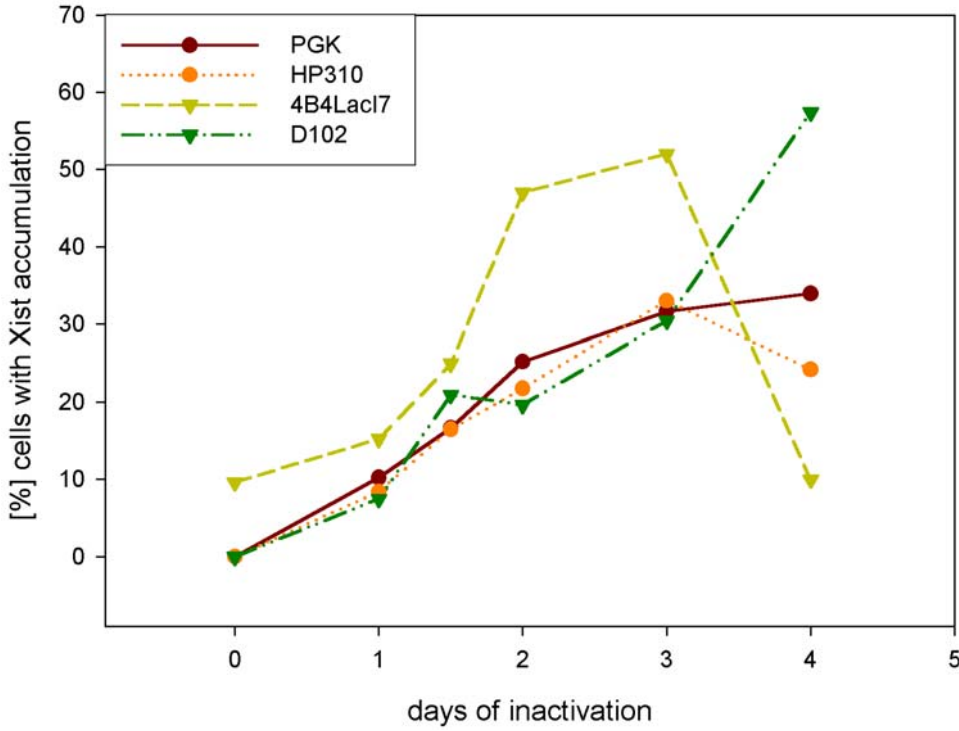


Figure 4.7: X-inactivation kinetics of early differentiating female mouse ES cells. The plots show the ratio in % between cells with detectable *Xist* accumulation (on the Xi) versus the total number of analyzed Xics.

the differentiation of female ES cells are shown in Figure 4.7. In female cells, the distance of each of the two Xic loci (DP_1 and DP_2) relative to the NE was evaluated using identical procedures to those described above. In undifferentiated female ES cells, the mean distance of Xic loci from the NE was found to be significantly shorter than that for the simulated random distribution (see Figures 4.5 and 4.6) but very similar to that in male ES cells (see Figure 4.5). The Xic on the active X (Xa) or inactive X (Xi) during female ES cell differentiation was identified based on the absence or presence of *Xist* RNA accumulation (see Figure 4.4). No significant differences between the Xa and Xi in Xic distance from the NE were found (p -values > 0.1). However, the mean distance of the Xic on the Xa from the NE in a differentiating female ES cell, was significantly larger ($0.4 - 0.9\mu m$ for PGK cells; $0.2 - 0.99\mu m$ for HP310) than the mean distance for the Xic in a differentiating male ES cells (ranging from $0.05 - 0.57\mu m$) (see Figure 4.6). Furthermore, the distributions of both the Xa- and Xi-linked Xics in ES cells were found, in general, to be significantly different to those in female MEFs (see Figure 4.6).

In summary, the Xic locus is closely associated with the NE in undifferentiated and early differentiating ES cells. However, neither the Xa nor Xi associated Xic loci in female cells are found to be as frequently close to the NE

as the single Xic in male ES cells. Thus, the spatial distribution of the Xic on the Xa in female ES cells appears not to be equivalent to that of the Xic on the Xa in male ES cells. Importantly, the distribution of the Xic locus in a fully differentiated male or female MEF (whether on the Xa or Xi), although peripheral, resembles a random distribution. This suggests that the specific distribution of the Xic observed in male and female ES cells may be linked to the central role that this locus plays in the initiation of X-inactivation.

4.2.3 Association of the Xic region with the nuclear periphery and constrained motion in living cells.

As the previously performed fixed cell analysis, I wished to confirm that the generally peripheral nuclear localization of the Xic locus could also be seen in living ES cells. For this reason transgenic male ES cell lines using a BAC (399K20) that covers 195 kb centered around the *Xist* gene were generated [102]. Multicopy *Xist* transgenes can function as ectopic arrays when integrated into autosomes [88, 86, 98]. A Neo-resistant gene cassette and a 256-mer LacO tandem array were serially inserted into the end of the insert 3' to the *Xist* gene with a RecA shuttle vector system [175]. A number of transgenic clones were isolated following transfection of this BAC into male ES cells. These were characterized for their copy number (data not shown) and their capacity to correctly induce *Xist* RNA coating and chromatin changes in *cis* (see Figure 4.8).

One line (4B4) with 2-4 copies of this BAC integrated into an autosome, showed efficient induction of *Xist* RNA coating in *cis* (see Figures 4.1, 4.8b and 4.4), associated chromatin changes (see Figure 4.8b) and transcriptional silencing (data not shown). In early stages of differentiation a small proportion of cells also showed the accumulation of *Xist* RNA on the endogenous X-chromosome, a sign of counting (see Figure 4.8b). It should be noted that cells showing accumulations on the endogenous X are rapidly lost because of the resulting X-chromosome nullisomy [88].

A second line (4B2) containing 4-5 copies of the BAC integrated onto the X-chromosome was also analyzed. Upon differentiation a *Xist* RNA domain could be seen in a proportion of cells (up to 20%) but this proportion rapidly decreased to 0%, again presumably as a result of cell lethality due to X-chromosome nullisomy (data not shown).

The distances of the transgenic and endogenous Xic loci from the nuclear periphery in fixed cells were measured according to the *Xist* RNA / Xic DNA FISH measurement procedure described in Section 4.2.1 (see Figure 4.3). Although a generally peripheral localization was found for both loci (mean distance from the NE ranging from 0.9 - 2 μ m), the mean distances were significantly greater ($p > 0.0001$) than those of the Xic in differentiating male ES cells but were similar to those of differentiating female ES cells.

To examine the nuclear localization of the Xic and its dynamics in living cells, live cell imaging was performed on the 4B4 cell line. One concern using *in vivo* microscopy is the degree to which phototoxicity might alter the biological process being investigated. We therefore established appropriate conditions for live cell

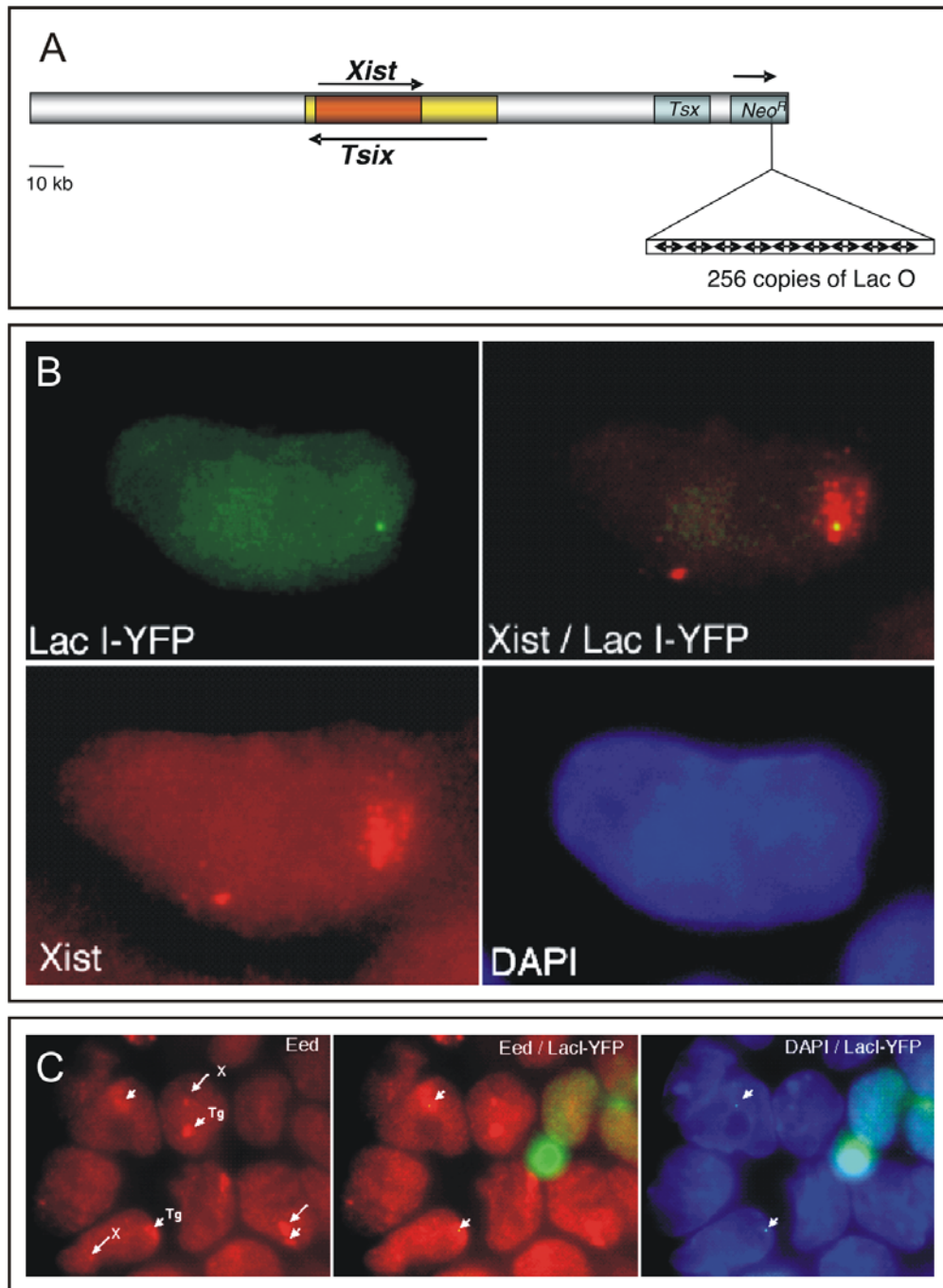


Figure 4.8: Principles of the Xic transgene constructs. A) Schematic overview of the modified Xic insertion cassette. The 256-LacO repeats are integrated within the Xic region downstream from *Xist*. B) Visualization of the autosomal transgene integration by LacI-YFP and *Xist* RNA FISH. C) Visualization of the native Xic and the autosomal integrated transgene by Eed and LacI-YFP in a ES cell colony.

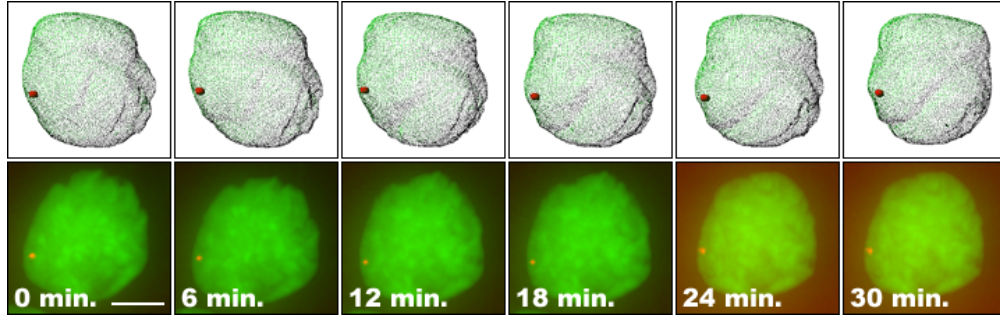


Figure 4.9: 4D Live cell imaging of the Xic locus in 4B4 cells (lower row). Snapshots of one image plane of the original 4B4 live cell data with merged fluorescent signals. Upper row: 3D isosurface reconstruction display of the acquired signals. Green = H2B-mRFP histone marker, red = LacO tagged Xic transgene detected via LacI-YFP. Bar $5\mu m$.

imaging on ES cells that minimize phototoxicity based on the appearance of the cells using phase contrast light microscopy at the end of the movie, and the capacity to detect mitoses (see Section 3.4.1). In order to visualize the LacO tagged transgenes, stably transfected clones of 4B4 cells expressing the Lac repressor protein fused to YFP were generated. Live cell imaging on these cells revealed that ES cells are highly motile and that dramatic changes in the shape and location of nuclei occur over short periods of time. This rendered the tracking of the Xic locus relative to nuclear periphery very difficult. To overcome this, we transiently transfected these cells with a plasmid expressing H2B-mRFP. In this way the LacO tagged Xic transgene could be detected via LacI-YFP and the nucleus could be visualized via H2B-mRFP. Imaging was performed on 4B4 cells in the undifferentiated state, or following differentiation after 1.5 days. To evaluate the movies, the two fluorescent signals were pre-processed, segmented and quantified in 3D over time (see Figure 4.9).

In most cases only a single LacI-YFP spot could be detected, although in some case 2 or 3 signals could be found. The fact that the 2-4 copies of the LacO (separated by 195 kb intervals if inserted as a tandem array) are not detected suggests that either these transgenes are unusually condensed at interphase, although in fixed cells this did not appear to be the case (data not shown). Alternatively, occupancy of the LacO array in each copy of the BAC may not be complete. Distances to the nuclear periphery for the LacO transgene in the individual 4B4 cells imaged are plotted against time (see Figure 4.10). This analysis revealed that the Xic transgene is located fairly close to the NE ($0.24 - 1.0\mu m$) in most (16 cells out of 24 cells), but not all, cells and that it shows relatively constrained mobility. In fact, in those cells where the transgene shows a more internal location (8 cells out of 24 cells), it appears to be associated with the nucleolar periphery. In differentiating ES cells, the Xi is the transgenic one in a minimum of 90% of cases ([88] and data not shown). The mobility of the transgene was similarly constrained in differentiating cells and its location was also peripheral. It is noteworthy that a 3D analysis was crucial for the evaluation of time resolved spatial analyses: evaluation of the same data sets

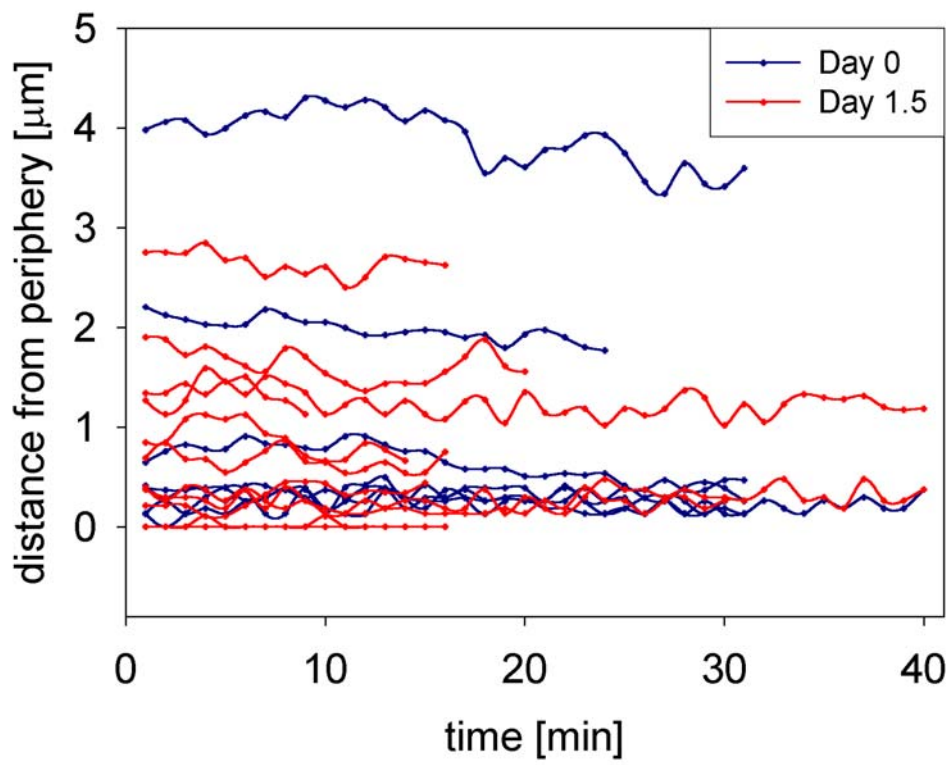


Figure 4.10: Tracking of the Xic locus and its distance from the nuclear periphery in 4B4 4D live cell experiments. The Xic distance from the nuclear periphery is plotted for 24 independently acquired cell nuclei with a time interval of one stack per minute (highlighted in different colors).

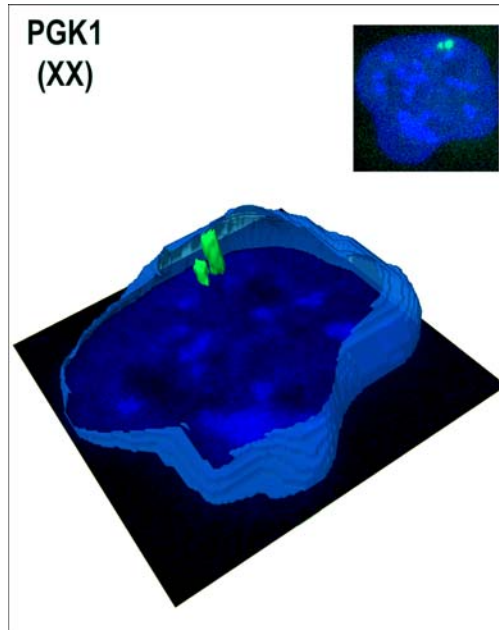


Figure 4.11: 3D isosurface visualization of Xic cross-talk event in a female (PGK1) ES cell nuclei. Prior to visualization the DAPI (blue) stained nuclei have been pre-processed and segmented to enable isosurface extraction. The nuclei are cut open to give sight on the *Xist*/Xic signals (green/red).

using maximum intensity projections often showed what appeared to be dramatic movements of the LacO transgene within the nucleus (data not shown) but these were in fact due to changes in nuclear orientation (rolling or rotating).

In summary, live cell imaging confirms that the Xic locus tends to be more peripheral in its location and further reveals that this locus is fairly constrained in its motion.

4.2.4 Spatial Xic cross-talk in female ES cells and male ES cells with multicopy transgenes

The above results show that the Xic tends to be located close to the nuclear periphery. However, I noted that in differentiating female ES cells, or male ES cells with multicopy Xic transgenes, the two Xics in fact exhibit a more internal nuclear location than the Xic in male ES cells, particularly at around 1.5 days of differentiation. One possible explanation for this could be that in cells with more than one Xic, where counting, choice and initiation of inactivation must occur, the Xics may have to associate with a common nuclear compartment, or interact transiently, in order to exchange information and/or to coordinate the ensuing X-inactivation process (see Figure 4.11).

To address this possibility, I used the 3D DNA FISH images described previously, to measure the distances between the two Xic loci, in the two female ES cells (PGK and HP310) as well as in the male line with a multicopy transgene (4B4). Close proximity of the two Xics (within a 0 - 3 μ m interval) could be detected in a small population of cells, particularly at day 1.5 of differentiation (see Figure 4.12). This is precisely the time when in male ES cells, where X-inactivation does not take place, the Xic is at its most peripheral, suggesting that when two or more Xics are present, their transient co-localization may be linked to the onset of X-inactivation. Nevertheless, the significance of the

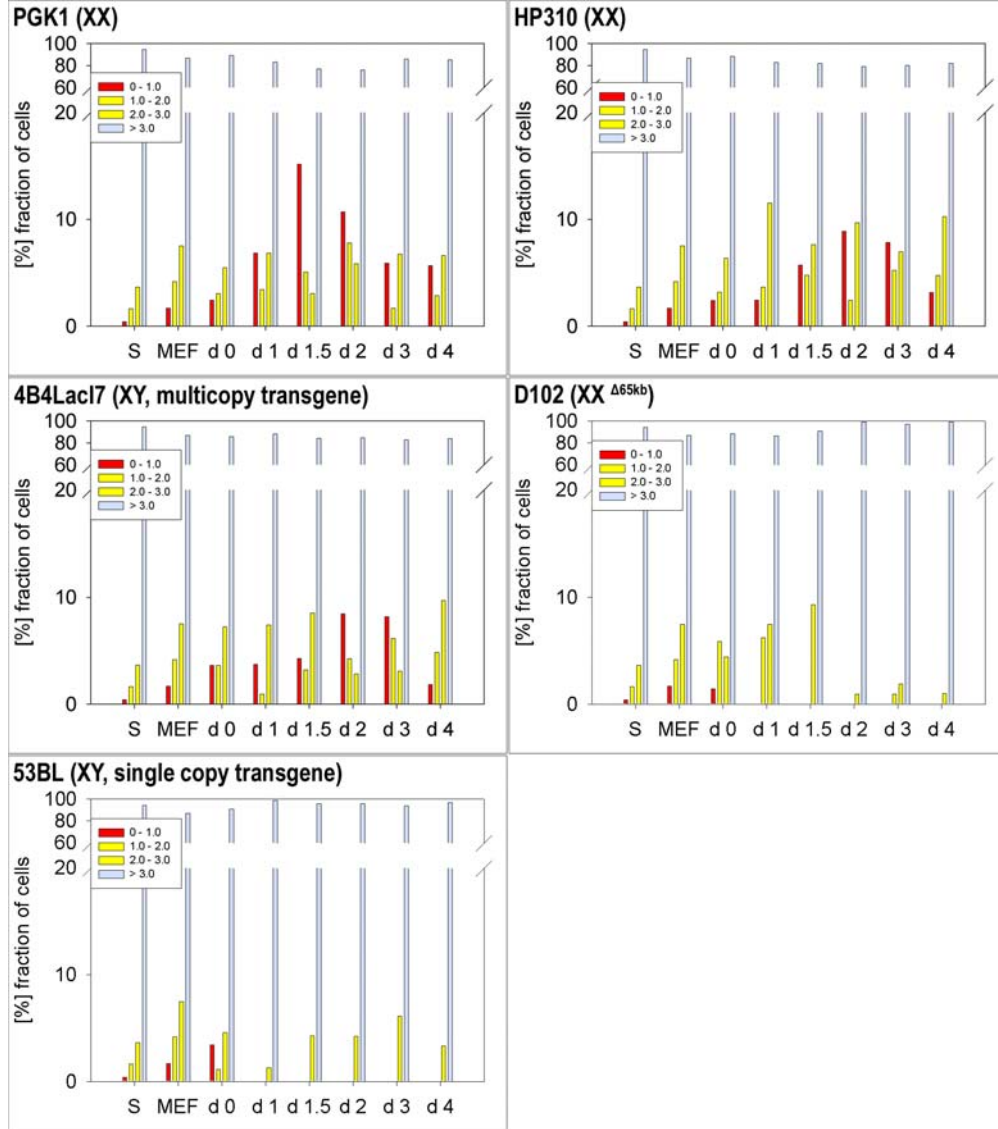


Figure 4.12: Detection of cross-talk events in wildtype female (PGK1, HP310), transgenic male (4B4, 53BL) and female counting deficient ES cells. A striking increase of Xic cross-talk events can be observed for PGK1, HP310 and 4B4 cell lines between day 1.5 and day 2.0 after induction of X-chromosomal inactivation. A general decrease of cross-talk events and no detectable Xic approximation events within a distance range of 0 - 2.0 μm were seen for 53BL and D102 cells. S = simulated distribution class consistent of 1000 calculated Xic distances from a random and uniform distribution within a simulated cell nucleus; MEF = Control experiments consisting of male or female MEF populations; dx = days after start of inactivation, where x indicates the actual time point in days from the initiation of X-inactivation.

co-localization being detected was unclear, given the very small proportion of cells in which it could be seen. To test for significance, I compared my data sets with a simulated distribution of two randomly positioned points within a sphere (see Section 3.4.9). The Xic intervals in female MEFs were also examined and found to be very similar to the simulated data set. From a statistical point of view, the overall Xic distances differences showed no obvious significant differences because of the global non-parametric analyses of the statistical tests. These global tests can fail to show any significance when the important events (in this case Xic co-localization or intervals $< 1.5\mu m$) are transient, or occur in a small fraction of cells. I therefore analyzed my data using quantile quantile (qq) plots (see Figure 4.13) and bar plots (see Figure 4.12) to give us some idea of differences in distributions. As a control group for the qq-plots, the Xic distances of the female MEFs were plotted against a random point population of simulated points in a virtual cell. The qq-plots (performed by running each data set against the random point simulation) reveal a shift to shorter than expected inter Xic distances for the female PGK and HP310 ES cells, as well as for the male transgenic 4B4 cells, compared to the female MEF control group (see Figure 4.13). This shift is most pronounced at 1.5 - 2 days of differentiation. The bar plots also reveal a higher proportion of short (0 - $1.5\mu m$) inter Xic distances in female PGK and HP310 cells, and in male transgenic 4B4 cells, compared to the female MEF control group (see Figures 4.12 and 4.13).

In order to test whether this transient co-localization of Xics has any functional significance that could be relevant to the known role of the Xic in counting and choice, I analyzed two female ES cell lines thought to be mutant for these functions (see Figure 4.1). One of these (the D102 cell line) was derived from HP310 by the creation of a 65 kb deletion within the Xic region [174]. Upon differentiation, the deleted $X^{\Delta 65kb}$ chromosome is always chosen for inactivation. Furthermore, this deletion is known to abolish counting function as in $X^{\Delta 65kb}O$ or $X^{\Delta 65kb}Y$ ES cells, the single $X^{\Delta 65kb}$ chromosome undergoes inactivation upon differentiation. This implies that the part of the Xic that is normally "blocked" to maintain one X-chromosome active per diploid cell is missing. I performed *Xist* RNA / Xic DNA FISH on D102 cells under identical conditions to those used for the other cell lines described above. The inter Xic distances were calculated and plotted using qq-plots. This revealed a dramatic absence of Xic co-localization (i.e. distances between 0 - $1.5\mu m$) and a shift from the statistically expected distribution of inter Xic distances (see Figures 4.12, 4.13 and 4.15).

The second ES cell line I used to test the functional significance of this Xic-Xic co-localization, was a male ES cell line, carrying a 460kb, single copy Xic transgene integrated on chromosome 13 (53BL). This transgene, which includes *Xist* as well as the "counting" region that is absent in the $X^{\Delta 65kb}$ allele in D102, has previously been extensively characterized and shown to be incapable of inducing counting, choice and *cis*-inactivation during ES cell differentiation [190, 173]. DNA FISH was performed to detect the endogenous Xic and the single copy transgene and inter Xic distances were calculated, as described above. No sign of proximity or co-localization (0 - $1.5\mu m$) was found between the two Xic signals at any stage of differentiation. The qq-plot analysis revealed a dramatic

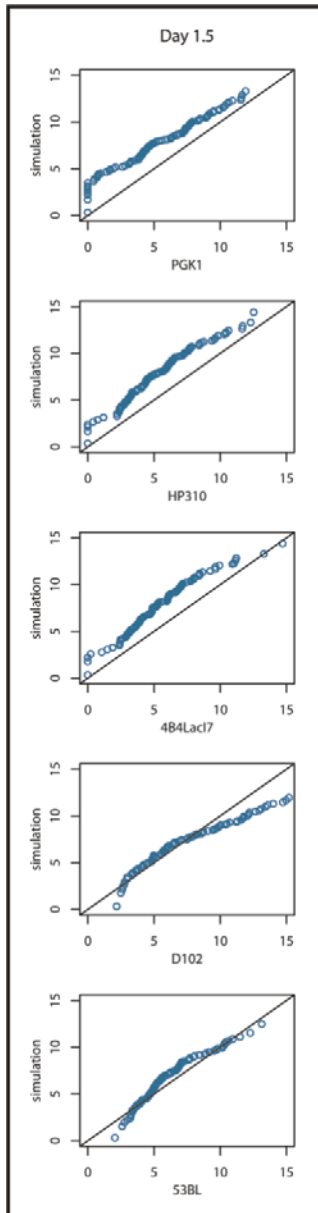


Figure 4.13: Analysis of inter Xic distance distributions with qq-plots. Visualization of the Xic distance distributions with qq-plots for all analyzed cell lines against a simulation of 1000 randomly determined Xic distance distribution at day 1.5 after differentiation. An approximation of the two Xic can be seen for PGK1, HP310 and 4B4 cell lines whereas a complete lack of the short Xic inter distance population can be detected for the 53BL and D102 cell lines.

4. Transient co-localization of Xics during the initiation of X-inactivation

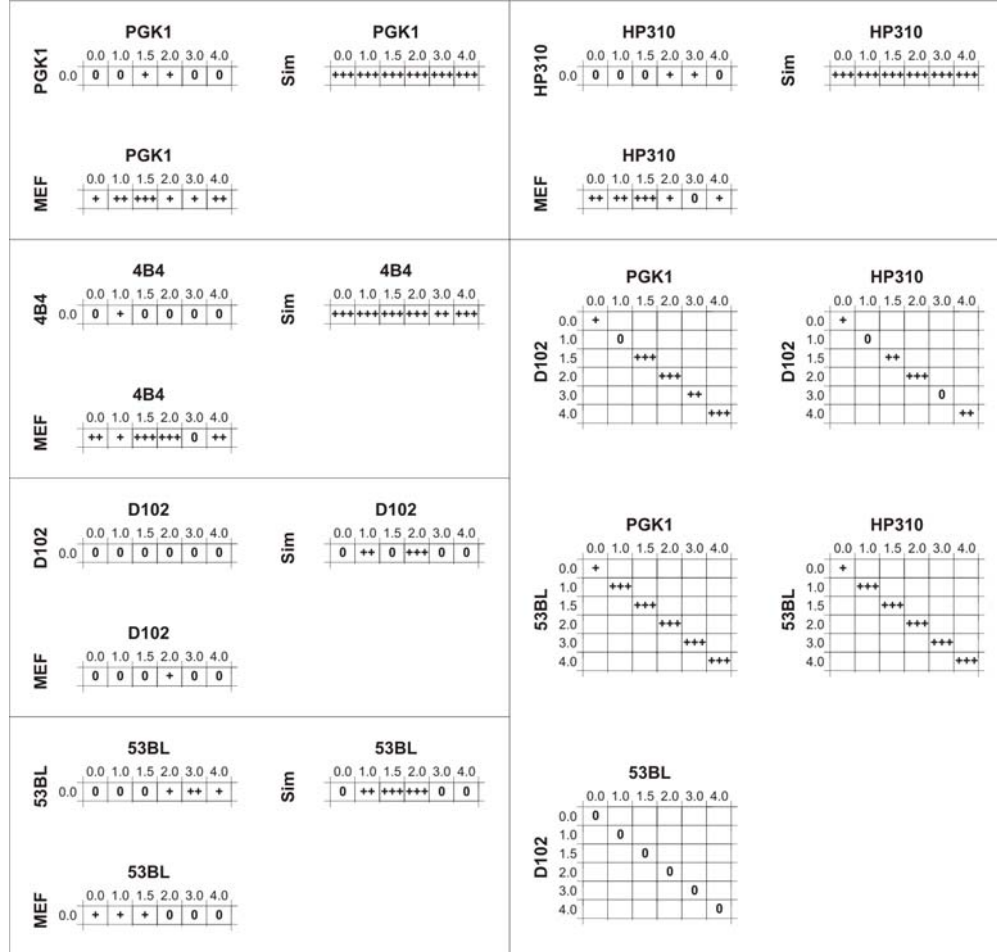


Figure 4.14: Significance determination with the Kolmogorov-Smirnov test of the Xic inter distances in the analyzed cell lines for the different time points of X-inactivation. The labels of the compared cell lines are found at the top and on the left hand side of each matrix. The numbers indicate the time points of the respective day of inactivation. 0 = $p > 0.05$; + = $0.05 \leq p < 0.01$; ++ = $0.01 \leq p < 0.0001$; +++ = $p \leq 0.0001$; Xa = Active X-chromosome; Xi = inactive X-chromosome; Sim = Simulated data points (see Section 3.4.9); MEF = mouse embryonic fibroblasts.

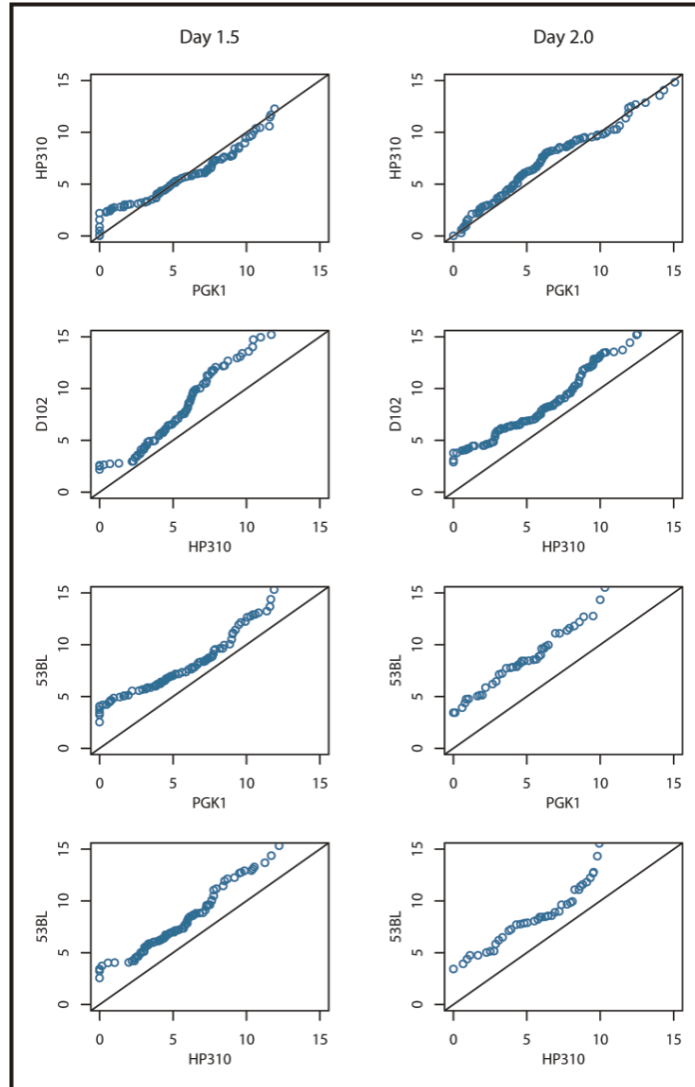


Figure 4.15: Analysis of inter Xic distance distributions with qq-plots Comparison of the wildtype female cell lines against the inactivation and counting deficient 53BL and D102 cell lines at day 1.5 and day 2.0 after induction of X-chromosomal inactivation. The qq-plotting of PGK1 against HP310 distribution at the respective days fall in the approximate line with slope 1 meaning similar distributions. The slight shift towards shorter inter Xic distances for PGK1 cells at day 1.5 after induction of differentiation can be explained by the slightly slower inactivation kinetics observed in HP310 cells. Again dramatic abolishment of short distances between the two Xic loci can be seen when female wildtype cells are compared to 53BL and D102 cells.

shift from the expected distribution of inter Xic distances, similar to that seen in the D102 line (see Figures 4.12, 4.13 and 4.15). This contrasts with the multicopy transgenic 4B4 cell line, which shows Xic co-localization and which is capable of inducing X-inactivation and some degree of counting.

In conclusion, the above results suggest that the co-localization between Xic loci observed in female ES cells, and in male ES cells with multicopy transgenes, may be functionally relevant, given that two ES cell lines in which counting and choice are abolished show Xic-Xic co-localization.

4.3 Discussion

During early mammalian development, inactivation of all X- chromosomes but one is triggered if a diploid nucleus contains more than one X-chromosome, or more specifically more than one Xic. The mechanism underlying this sensing and differential treatment, of multiple genetically identical Xics within the same nucleoplasm is fundamental to the understanding of X-inactivation and possibly to monoallelic gene regulation in general. In my study I have analyzed the nuclear localization of the Xic in fixed and living cells. I determined that the Xic locus shows a non-random spatial distribution in the nucleus that might reflect its specific functions in controlling the initiation of X-inactivation. Such a nuclear compartmentalization was one of the earliest models proposed to explain X-chromosome inactivation [93]. It stated that the binding of an X-chromosome to a single entity per nucleus, such as the nuclear envelope, could mediate X-inactivation. In particular the counting process, where one Xic is blocked from triggering X-inactivation (per diploid autosome set), could be explained by a single nuclear binding site that is able to block the signals that trigger up-regulation of *Xist* expression from a single Xic during development. This would ensure that the X-chromosome carrying the binding site would therefore remain active and ensuing in correct X-linked gene dosage compensation.

My high throughput, semi-automated 3D analysis on fixed cells has revealed that the Xic locus occupies a significantly peripheral location in nuclei of ES cells, which stands in contrast to fully differentiated fibroblasts. This peripheral location is most pronounced in male ES cells at early differentiation stages (minimal distance is seen at day 1.5) and could correspond, as proposed by Comings (1968) [93], to the sequestration of the Xic as a mean of preventing the initiation of X-inactivation on the single X-chromosome. In female cells, or in male cells with a multicopy Xic transgene, the Xic also shows a tendency to be peripheral in its location, whether it is on the active or inactive chromosome. However, the location of the Xic in these cells is less peripheral on average compared to the Xics detected in male cells during early differentiation stages. This more internal location may be linked to the co-localization of the Xics I observed in a small population of female cells and could reflect their movement towards each other (see below). However, the fact that a less peripheral location for the Xic, compared to male ES cells, was found not only in wild type female cells but also in D102 cells, in which counting is abolished and no Xic co-localization is seen, suggests that the internalization of the Xic occurs regardless

of whether or not the two Xics actually come into close contact with each other. Thus, an alternative explanation for this difference in peripheral location is that sequences required for the association of the Xic with the nuclear periphery are distinct from the sequences required for Xic co-localization. Indeed, if the hypothesis that suggests a single nuclear site per diploid cell for the Xic locus to bind is correct, then this unique site should only be occupied by a single Xic locus at any time. In cells with multiple Xics, they would "compete" with each other for binding to this unique site. Therefore the average distance of any Xic locus from the nuclear periphery would thus be greater in a female cell than in a male cell, where the single Xic can remain in residency of this site. Certainly, the definition of the nature of this unique binding site, assuming it exists, will clearly be an important challenge for the future. However, the importance of the Xic location could be determined by parallel labeling of the Xic locus and the X-chromosome territory with the subsequent comparison of the mean distance of the Xic in cells with a peripherally associated X-chromosome relative to the distance of other regions of the X-chromosome. Further the effect of the inhomogeneous DNA distributions on the Xic location could be tested by correlation of the Xic position to the underlying chromatin density (see Chapter General Conclusion and Section 3.4.7).

I also examined the location of the Xic in living cells, using a LacO tagged Xic locus which was visualized because of the fusion of the Lac repressor fused to YFP or GFP. As expected from the fixed cell analysis, the LacO tagged Xic was found to have a peripheral location in the majority of undifferentiated and early differentiating ES cells. In a few cases, the Xic showed a more internal location, which appeared to correspond to the nucleolar periphery (see also Chapter General Conclusion). In none of the live cell imaging experiments a dramatic movement of the Xic relative to the rest of the nucleus was observed. Indeed, the Xic appeared fairly constrained in its motion. However, I cannot exclude that the small variations in position that I observed over short time intervals corresponded to exchanges in Xic occupancy between the transgene and the endogenous Xic. The answer to this will have to await the tagging of both Xics for live cell imaging.

Another hypothesis that has been proposed to explain counting and choice in X-inactivation involved interactions or "cross-talk" (used as the equivalent for spatial approximation of two Xic in the following sections) between the two Xics during the initiation of X-inactivation. Both inter- and intrachromosomal interactions between loci are known to occur in several organisms including *Drosophila*, where transvection* and Polycomb associated interactions have been reported to occur at high frequencies. For a long time it was believed that such trans-interactions were rare or non-existent in mammalian systems, but recent findings have shown that such 3D communications do exist and may even be common in certain situations. For example, inter-chromosomal interactions were recently described for T-helper cell 1 and 2 loci [133]. Additionally, there is evidence that such inter-chromosomal interactions occur at sites of recurring translocation in mammalian cells [191]. Because such homologous,

*homologous chromosome pairing that influences gene expression

inter-chromosomal interactions, other than during meiosis, are of transient nature and therefore hard to detect, I performed my study on thousands of cells using automated 3D analysis. This allowed me to show that the two Xic loci in female ES cells or in male cells with multicopy Xic transgenes come into very close proximity of each other during ES cell differentiation. Although the population of cells in which this cross-talk happens is small, it reaches a peak at day 1.5 of differentiation, which is exactly the time window when counting and choice during the initiation of X-inactivation are expected to occur.

Most important, I found that the Xic co-localization is abolished in two ES cell lines that are disrupted in their counting and choice functions. The functional significance of the Xic co-localization is of great interest with respect to the regulation of X-inactivation and several possible explanations can be given.

One is that this co-localization reflects a nuclear targeting process, which allows correct initiation of X-inactivation to occur by placing all of the Xics in the same nuclear compartment. The fact that such a co-localization can be dissociated from *Xist* up-regulation, as the D102 mutant does not show cross-talk but does show *Xist* up-regulation and *cis*-inactivation of the deleted X-chromosome, suggests that Xic cross-talk is not required for up-regulation of one of the two *Xist* genes. Furthermore, *Xist* RNA itself does not appear to be responsible for this cross-talk (but Tsix might be, because it is missing in the deletion of the D102 line). On the other hand, the absence of co-localization in the D102 cell line may be linked to its known defects in counting and choice [174]. One hypothesis would be that bringing together the two Xics is necessary for one of them to be randomly chosen for blocking or *Xist* up-regulation (see model in Figure 4.16).

Obviously an important question is whether this Xic cross-talk is a cause or consequence of initiation of X-inactivation. The 53BL* cell line does not trigger inactivation of either the autosome that carries the transgene or of the endogenous X-chromosome. This fact would argue that Xic cross-talk is upstream of the initiation of X-inactivation and may be required in order for the cell to recognize the number of Xics it contains and to trigger X-inactivation.

What sequences might mediate co-localization of the Xics? Based on the lack of Xic cross-talk in D102 cells, an obvious candidate would be the 65 kb region, which is deleted on one allele in D102 cells. However, the fact that the single copy 53BL transgene contains this 65 kb region, would argue that this region cannot be sufficient for co-localization to occur given that no cross-talk is observed in 53BL cells. It should be noted that providing this transgene with a potential pairing partner on the homologous autosome is not sufficient, as ES cells homozygous for the 53 transgene were tested previously and found to be incapable of triggering inactivation in *cis*, or of the endogenous X [173]. Taken together, the data from the D102 and 53BL cell lines suggest that more than one region may be important for pairing of the Xic loci and / or for accurate positioning of the Xic in the nucleus (see Figure 4.16). This would be consistent

*single copy transgene line containing all of the known elements required for X-inactivation (as defined by deletion at least)

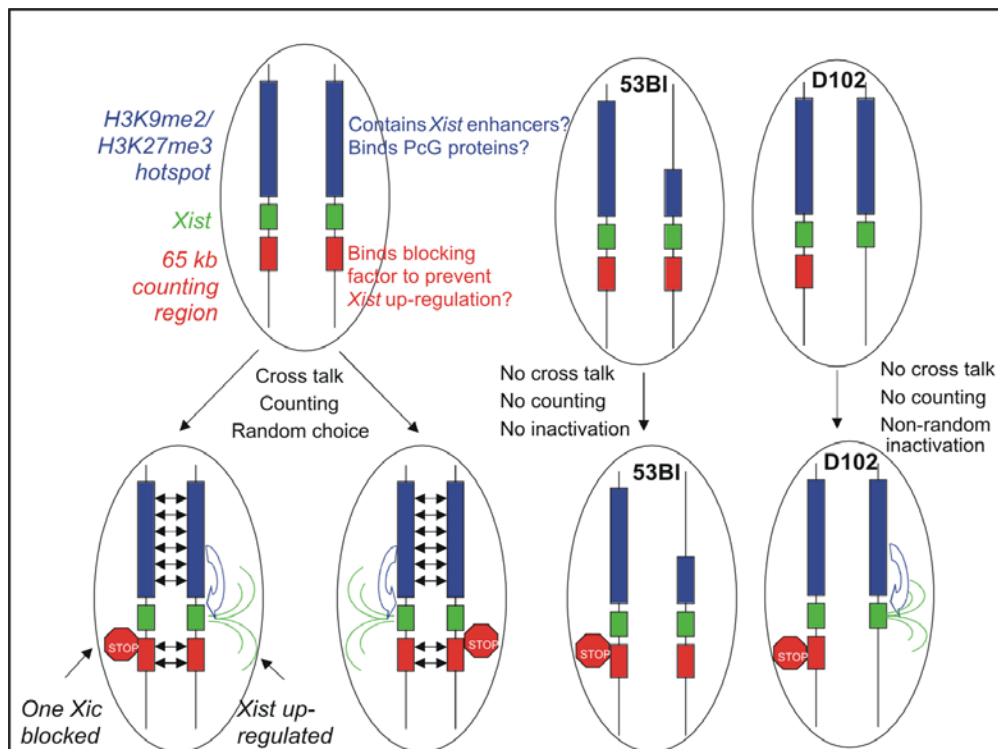


Figure 4.16: Possible models for the cross-talk mechanism during X-chromosomal inactivation. Several regions within the Xic sequence might be responsible for the coordination of this cross-talk process. In native ES cells, the overall process includes complex involvements of hypothetical blocking or competence factors, histone modification regions and expression controls mechanisms by transvection events. An imbalance in those regulating regions could lead to a skewing in X-chromosomal choice or even a complete loss of the inactivation capability.

with the fact that when two or more copies of a *Xist* transgene (equivalent to that in 53BL cells) are present in a tandem array, they are able to function as an ectopic Xic [173]. This suggests that multiple redundant sequences may be required to allow proper co-localization.

What other region, missing in the single copy transgene line could be involved? It was previously reported that the single copy transgene in line 53BL is missing a large part (> 150 kb) of a 250 kb hotspot of H3K9 di-methylation [110] and H3K27 tri-methylation [112] lying 5' to the *Xist* gene. The exact role of this region remains unclear, but given its unusual chromatin characteristics, one possibility is that it binds Polycomb group proteins which may help to mediate trans-interactions such as the ones described here. The H3K9 methyl hotspot could thus play a role in enabling the "kissing" between the two Xic regions, in a manner analogous to the transvection of homologous chromosomes seen in *Drosophila melanogaster* [192, 193, 194]. This could facilitate the interactions between Xics at the region 3' to *Xist*, involved in counting and choice and missing in the D102 mutant.

In conclusion, I have shown for the first time that in ES cells with multiple Xics, these loci undergo transient co-localization in ES cells that are competent for the counting and choice functions of X-inactivation. The functional significance of this co-localization is illustrated by the fact that in ES cell lines that cannot induce counting and choice, such co-localization is abolished. The exact nature of the Xic-Xic interactions and the molecular mechanisms that are likely to enable correct differential regulation of the Xic, has to be elucidated in future studies.

Chapter 5

4D single particle tracking of nuclear particles

5.1 Introduction

Interphase nuclei are structurally highly organized with chromosomes restricted to defined territories [37]. The movement of large complexes or nuclear bodies such as Cajal or PML bodies in the nucleus has been described by various groups [195, 13, 10]. This type of organization of interphase chromosomes indicates that the resulting interchromatin compartment provides a so-called interchromosomal domain (ICD) space that differs significantly from that occupied by chromatin [196]. It was shown that nuclear bodies as well as specific RNA are excluded from the chromosome territories but reside in an interchromatin compartment [54, 78, 196]. Investigation of the diffusional accessibility of the nucleus for microinjected DNA and dextrans of varying molecular weight by fluorescence recovery after photobleaching (FRAP) methods revealed significant differences in mobility according to size. FITC-dextrans of molecular sizes up to 580 kDa were demonstrated to be fully mobile, whereas DNA fragments were nearly immobile [197]. Furthermore, a size- and electrical charge-dependent exclusion for macromolecules is encountered for chromatin regions [198]. In contrast, poly(A) RNA has been shown to move freely throughout the interchromatin space of the nucleus with properties characteristic of diffusion [199]. Moreover, the large ribosomal subunits seem to exhibit a random movement in a Gaussian manner without evidence for any direct path on their way from the nucleolus to the nuclear pores [200]. Recently, microinjection of fluorescent nanospheres has been used to track the movement of such particles under distinct experimental conditions [201]. The authors employed a silicon-intensifier target camera coupled to an epifluorescence microscope in combination with a 2D particle-nanotracking routine implemented in the Metamorph / Metaview image processing system [202, 203]. In particular, tracking of nanospheres within the nucleus revealed that the particles diffused freely in restricted "cages", eventually translocating into another "cage". These studies, however, did not reveal any information on the 3D movement of particles in comparison with local chromatin density. Such a study requires recording of simultaneous time-lapse recording of three-

dimensional image stacks of particles and chromatin using a confocal laser scanning microscope as described in the present study.

Kinetic analysis of nuclear bodies requires spatio-temporal microscopic imaging of live cells generating a huge amount of data that is only difficult or impossible to analyze in a standardized way without computational support. The present developments of an Open Microscopy Environment (OME) aims at providing a standardized informatics solution for the storage, management and analysis of light microscopic image data [166]. For quantitative analysis of complex data from live cell experiments a variety of systems have been developed (for review see [135]). An integrated image analysis solution should include tools for all steps in the image processing chain, i.e. image pre-processing and segmentation of objects, registration of moving and deforming cells, tracking of objects over time, and multi-dimensional visualization and kinetic analyses of dynamic objects. Only with the availability of quantitative kinetic data it is possible to obtain insight into the underlying mechanisms of biological processes such as those involved in the functional and spatial organization of the cell nucleus.

In the present study I describe a combined computational and experimental approach to study the dynamic behavior of nuclear body-like particles formed by GFP-NLS-vimentin [154] in response to different cellular inhibitors and, most importantly, in relation to the chromatin structure of the nucleus. This has been compared with the motion of polystyrene particles of similar size. Since both kinds of "bodies" display identical movement, the vimentin bodies can be regarded and hence employed as entities supposedly "biologically inert" for the nucleus. Using my novel image processing platform Tikal I show that the kinetics of nuclear particles are influenced by various cellular inhibitors. Furthermore I show that the kinetics of nuclear bodies is directly influenced by local restructuring of chromatin domains.

5.2 Results

5.2.1 An experimental system for probing particle kinetics in the cell

I used fast 3D time-lapse confocal laser scanning microscopy to analyze the mobility of *Xenopus laevis* GFP-NLS-vimentin and synthetic particles (polystyrene microspheres) within the nucleoplasm. GFP-NLS-vimentin is deposited at 37°C within the nucleus of stably transfected SW13 cells in multiple discrete bodies (8-40). On average the cells contain bodies that are nearly 1 μ m in diameter as observed in the light microscope (see Figure 5.1a). This corresponds to a particle diameter of about 200-500nm in fixed cells as prepared for conventional electron microscopy (data not shown). From correlative light and electron microscopy studies I know that nuclear vimentin particles are excluded from dense chromatin regions [204]. In contrast, transfection of human vimentin-free SW13 cells with an expression plasmid encoding GFP-vimentin without the engineered NLS sequence leads to the formation of many cytoplasmic particles (> 100) of very similar size (see Figure 5.1c).

To study the nucleoplasmic mobility of particles of a defined size I microinjected unloaded polystyrene beads into the nucleus of living cells. I used orange fluorescent 100nm-beads that resemble in size authentic nuclear bodies such as PML- or Cajal bodies [158, 205, 13, 8] on the light microscopic level. Thereby I attempted to find out how the mobility of the ectopically expressed nuclear vimentin particles related to polystyrene particles [206, 154]. In the course of these studies I found that a system based on an ectopically expressed protein has several clear advantages compared to the microinjection of beads. First, the expression efficiency of the GFP-vimentin construct is very high. More than 50% of the cell nuclei show formation of nuclear vimentin bodies. Since the cells are stably transfected they reflect a normal physiological state. In contrast, for microinjection only approximately 10-20% of injected the cells survived over night culture ($n = 300$). Additionally, the artificial microspheres have to undergo tedious processing steps such as sonification and centrifugation prior to injection to avoid the formation of aggregates.

5.2.2 A computational system for tracking nuclear particles on the background of moving cells

For the analysis of complex data derived from spatio-temporal imaging of trafficking particles I used Tikal (see Section 3.2). As described previously, the platform allows to directly and easily handle complex microscopic data and to dynamically interact with the dataset throughout the whole quantitative data analysis steps. The image processing pipeline is initiated by image pre-processing steps including noise reduction followed by object segmentation. In many cases, cells move and also change their morphology during the observation period. Global movements include translocation and rotation, whereas morphological changes are either caused by global changes in size (affine transformation) or by local deformations. Since any of these transformations overlay the actual movement of nuclear particles within the cell, I corrected for them by rigid transformations (translocation and rotation), affine transformations (scaling) and by thin-plate spline models (local deformations; [159, 171]). These transformations allow a direct measurement of nuclear particle movements without any bias induced by external forces and cellular movements. For quantitative evaluation of kinetics of moving particles I extended our single particle tracking approach formerly developed for two-dimensional time series [147] to automatically track objects in 3D time series. The automatically computed 4D tracks are visualized together with a surface rendered 3D reconstruction of segmented nuclear particles in a multi-dimensional scene viewer (see Figure 5.2). By interacting with the automatically computed trajectories the user is able to interactively control and correct for possible artifacts during the tracking procedure, e.g. deriving from noisy images. Applying Tikal, I rapidly reconstructed, visualized and analyzed the trajectories of 1131 particles in more than 50 cells.

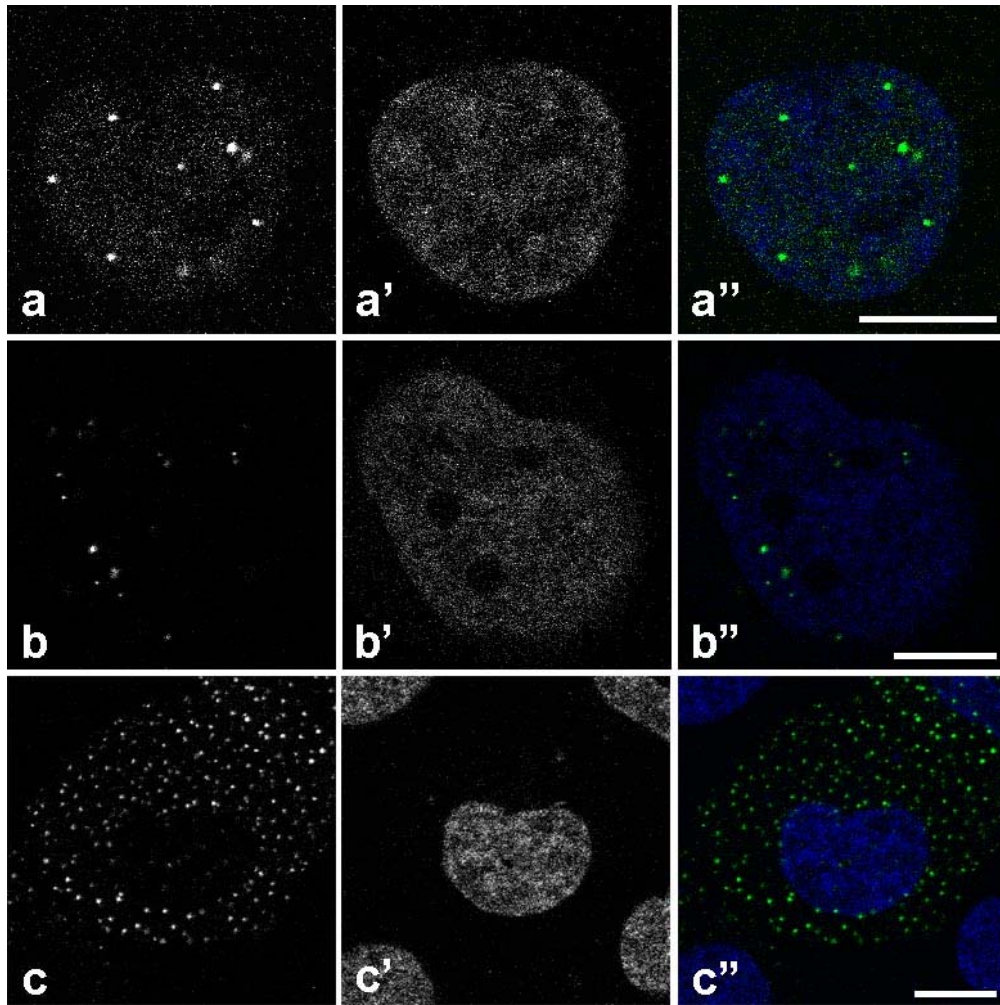


Figure 5.1: A) Nucleus of a SW13 cell stably transfected with an expression plasmid encoding for GFP-NLS-vimentin. B) SW13 cell nucleus containing microinjected 100nm-microspheres. C) SW13 cell transfected with GFP-vimentin showing cytoplasmic particle formation. A', B', C'): Corresponding Hoechst 33342 chromatin stain, A'', B'', C'') superimposed images.

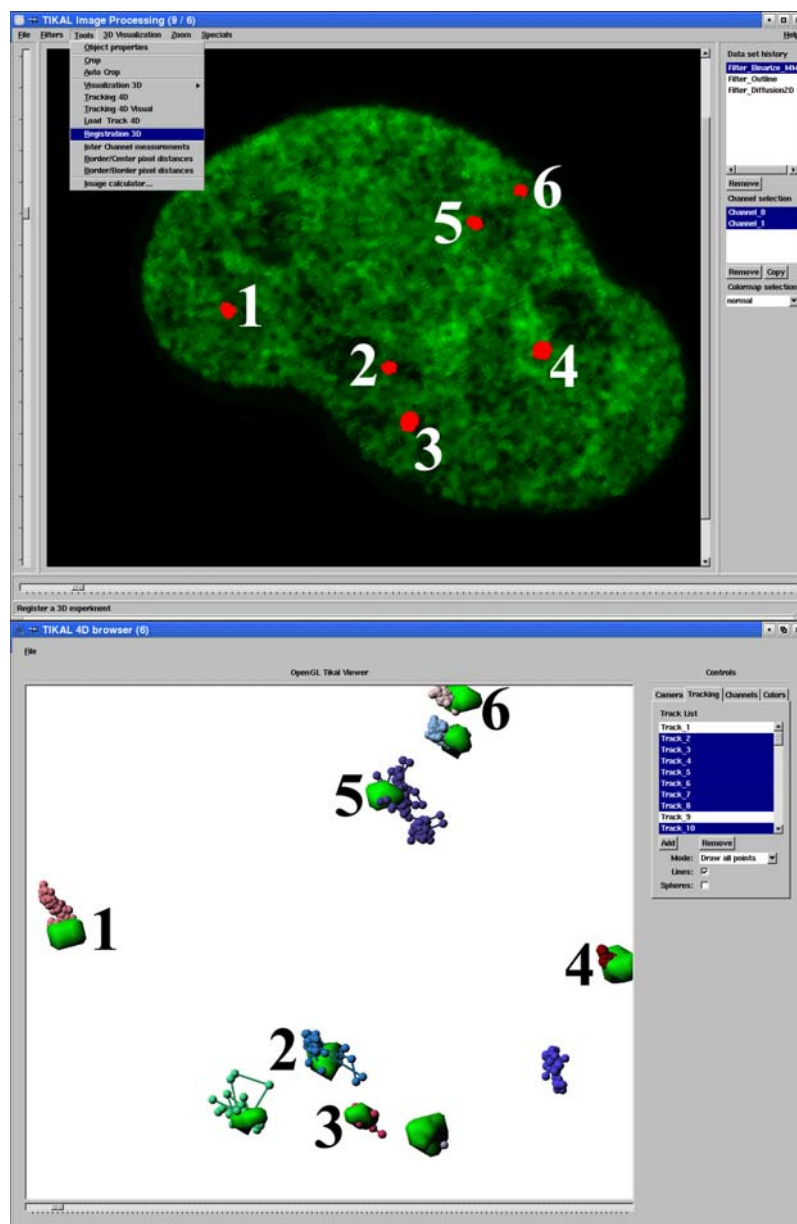


Figure 5.2: Screen shot of the image processing platform TIKAL. (top) Image shows a sample two-dimensional section through a nucleus with binarized nuclear particles (red) counterstained with Hoechst 33342 stain (green). Pull down menu exemplifies different tools for quantitative analysis integrated into TIKAL. Numbers indicate different nuclear particles reconstructed by 3D isosurface reconstruction (bottom). Computed tracks of nuclear bodies over time are displayed as spheres on a string in the multi-dimensional scene viewer.

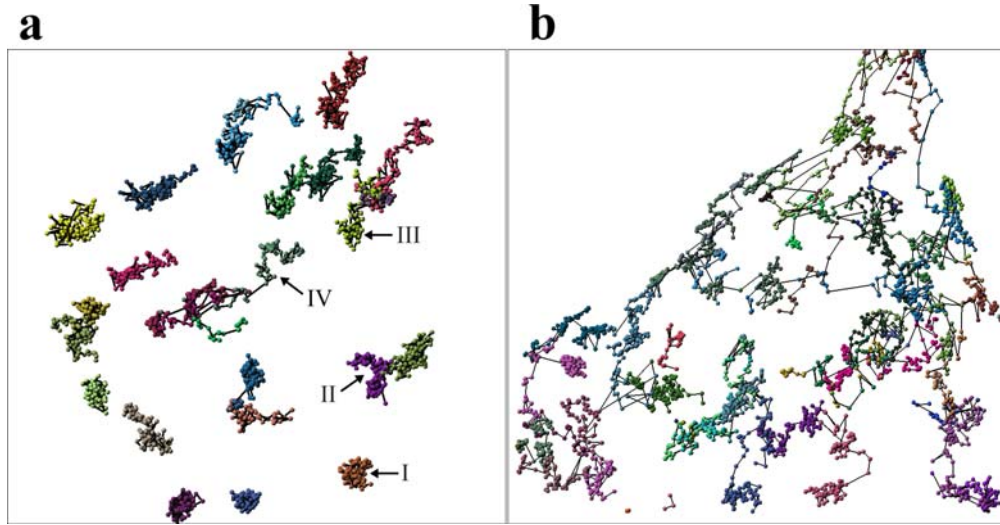


Figure 5.3: 4-D visualization of vimentin particle trajectories a) in the nucleus and b) the cytoplasm. Each color represents an individual vimentin body. The respective centers of masses are indicated as spheres. Tracks are symbolized by interconnecting lines. Arrows indicate the different kinds of diffusion (see Figure 5.4). Major types of movement are indicated: I) confined diffusion; II) obstructed diffusion; III) normal diffusion; IV) directed motion.

5.2.3 *In vivo* observation of microspheres

I imaged the microinjected microspheres and the GFP-NLS-vimentin particles in SW13 cells over a time interval of 20 min (see Figure 5.1a and 5.1b). After image processing a qualitative analysis of the trajectories of 154 microspheres visualized in 12 cells suggested the same kind of mobility for both the 100nm-beads and the GFP-NLS-vimentin bodies (see Figure 5.3).

For a more rigorous quantitative comparison the mean square displacement (MSD) was calculated for each individual particle as well as its anomalous diffusion coefficient α . Based on α , the analyzed particles were classified into four arbitrary groups of mobility using the theoretical framework from previous studies [180, 181]: (i) confined diffusion ($\alpha < 0.1$), (ii) obstructed diffusion ($0.1 \leq \alpha < 0.9$), (iii) simple diffusion ($0.9 \leq \alpha < 1.1$) and (iv) directed motion ($\alpha \geq 1.1$) (for sample trajectories see Figure 5.4). The comparison of the calculated anomalous diffusion coefficients of the GFP-NLS-vimentin bodies with those of the 100nm-microspheres revealed no significant changes in the distribution ($p = 0.126$; compare Figure 5.5a and 5.5b. For statistical significance of interexperimental differences of distribution patterns for anomalous diffusion coefficients refer to Table 5.1).

Next, I was interested in the differences of the kinetic behavior of the *Xenopus* GFP-vimentin particles in the nucleoplasm as compared to that in the cytoplasm. Transfected SW13 cells lack endogenous vimentin and therefore do not have intermediate filaments. Instead, only small spherical aggregates of the temperature-sensitive amphibian protein were deposited throughout the cytoplasm (see Figure 5.1c; [177, 207]). When directly comparing the particle trajec-

Experiment 1	Experiment 2	p-value
control	beads	0.1264
control	cytoplasm	$p < 0.0001$
beads	cytoplasm	$p < 0.0001$
control	azide / deoxyglucose	0.1453
control	cytochalasin D	0.01643
control	nocodazole	$p < 0.0001$
control	sorbitol	$p < 0.0001$
azide / deoxyglucose	cytochalasin D	0.1095
azide / deoxyglucose	nocodazole	0.0048
azide / deoxyglucose	sorbitol	$p < 0.0001$
cytochalasin D	nocodazole	0.7306
cytochalasin D	sorbitol	$p < 0.0001$
nocodazole	sorbitol	$p < 0.0001$

Table 5.1: Significance analysis of interexperimental differences in distribution of anomalous diffusion coefficients by Kolmogorov-Smirnov test: Statistical significance analysis for interexperimental differences in cumulative distribution of anomalous diffusion coefficients (for corresponding distribution plots see Figure 5.5 and Figure 9) was performed by the Kolmogorov-Smirnov test [182]. The different experiments are depicted as followed: control = vimentin particles in the nucleus; beads = sepharose microspheres (100nm) in the nucleus; cytoplasm = vimentin particles in the cytoplasm; Vimentin particles in the nucleus with drug treatment: azide / deoxyglucose (10mM / 50mM); cytochalasin D (1 μ g/ml); nocodazole (0.04 μ g/ml); sorbitol (600mM).

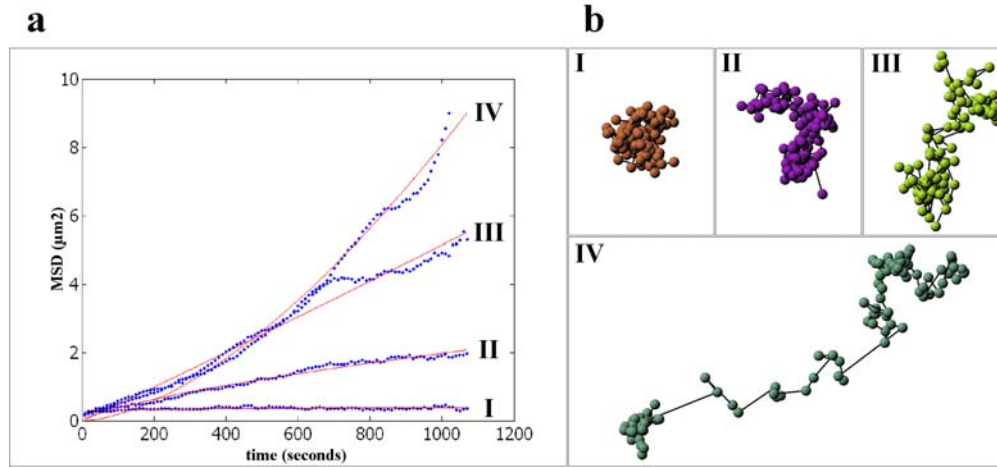


Figure 5.4: Different classes of mean square displacement of tracked nuclear vimentin particles. a) Mean squared displacement (MSD) of four representative modes of particle mobility (x-axis: acquisition time in seconds; y-axis: MSD). Roman numbers: I) confined diffusion; II) obstructed diffusion; III) normal diffusion; IV) directed motion (The numeration refers to indicated trajectories in Figure 5.3a). b) The four different mobility classes are represented by particle trajectories. The trajectories correlate to the numbers indicated by arrows in Figure 5.3.

tories of the nucleoplasmic vimentin bodies to the cytoplasmic vimentin bodies striking differences were found. Nuclear-targeted vimentin particles displayed a spatially restricted movement within distinct corrals. However, on occasion they were able to move spontaneously to an adjacent corral (see Figure 5.3a). The maximum distance that a NLS-vimentin particle moved was $4\mu\text{m}$ within the observation time of 20 min. This corresponds on average to a speed of $0.2\mu\text{m}/\text{min}$. Most strikingly, I never encountered crossing nuclear trajectories. In contrast, cytoplasmic vimentin particles moved along more extended trajectories and did hardly ever exhibit corralling events (see Figure 5.3b). Moreover, the cytoplasmic bodies moved three times as fast, i.e. up to $12\mu\text{m}$ in distance within 20 minutes.

A comparison of the overall kinetic characteristics of nuclear vimentin bodies versus sepharose beads revealed that in the nucleus obstructed diffusion is the major type of movement whereas in the cytoplasm directed motion is observed to a similar extent, both accounting for approximately 40%. Notably, confined diffusion is very rarely found in the cytoplasm whereas in the nucleus 11.4% of the movement can be accounted for it (see Figure 5.5, Table 5.1).

5.2.4 Chromatin remodeling directly effects mobility of nuclear particles

In the next step I analyzed the influence of chromatin density on mobility of nuclear particles. Upon inspection of corralled versus highly mobile nuclear particles (see Figure 5.6) I frequently observed a correlation between chromatin density in the neighborhood of particles and their degree of motility.

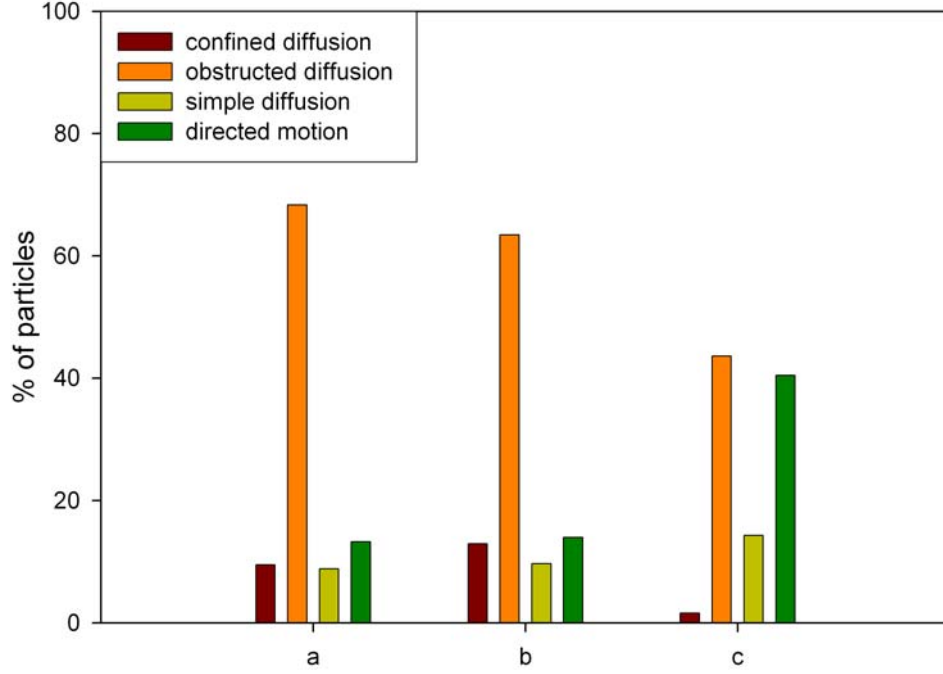


Figure 5.5: Classification of particles into four groups of diffusional motion according to cellular localization and their calculated anomalous diffusion coefficient. a) nuclear vimentin particles, (b) microinjected nuclear 100nm microspheres, (c) cytoplasmic vimentin particles.

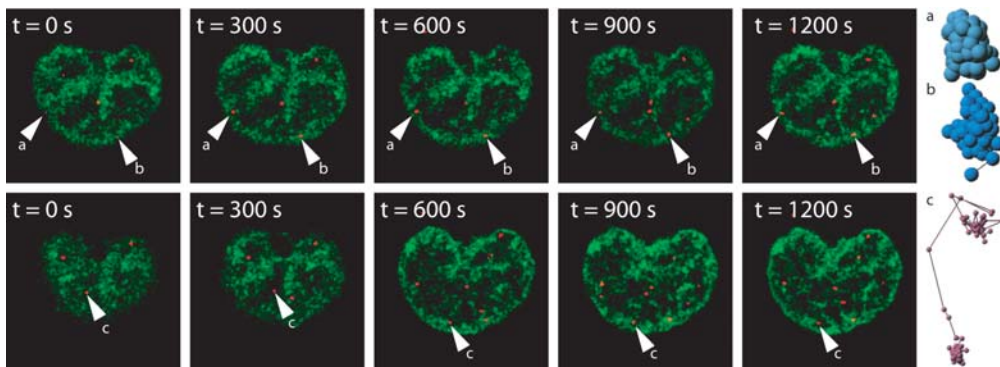


Figure 5.6: 4-D-tracking of vimentin particles in the nucleus. (a, b) particles with restricted movement (confined diffusion) c) corralled particle and corresponding trajectories. (red = vimentin bodies; green = Hoechst 33342 staining).

For a more rigorous quantitative analysis the mean gray-value in a neighborhood of 9 x 9 pixels was measured for each particle over an observation time of 20 min with a time-lapse of $\Delta t = 10$ seconds (see Figure 5.7).

Evidently, there is a strong correlation between chromatin density and particle velocity. Particles with high velocities were exclusively formed in areas of very low chromatin density. An increase in chromatin density directly led to a decrease of particle velocity (see Figure 5.8a and 5.8b). A similar reverse effect was detected in cases where particles had very low velocities. After release of a body from a dense chromatin cluster a sudden increase of its mobility could be observed. In this case a high chromatin density was measured during the resting phase of the body, whereas a decrease of chromatin density was detected before the particle started to increase its velocity (see Figure 5.8c). This phenomenon was prominently encountered with particles showing a high frequency of changes in corralled and more directed movement (see Figure 5.8a-c). For particles with minimal changes in distance and velocities, a constant chromatin density with low fluctuation in measured gray-values was observed (see Figure 5.8d).

5.2.5 Influence of inhibitors on the mobility of nuclear vimentin bodies

In order to investigate the contribution of structural elements of the cytoplasm to nuclear body mobility in living cells, inhibitors of cellular energy as well as drugs that lead to the depolymerization of cytoskeletal systems were employed. In particular, I inhibited cellular ATP production and incubated cells with agents that depolymerize microtubules or microfilaments, both of which are tracks for molecular motors in the cytoplasm. Cells were imaged prior to addition of the inhibiting substance for 10 minutes with image stacks acquired every $\Delta t = 10$ seconds. In a first step, the dependency of nuclear vimentin particles on energy-dependent mechanisms as investigated by depletion of ATP through incubation with 10mM azide and 50mM deoxyglucose followed by live cell imaging over a time interval of another 10 minutes. For more than 140 bodies in eight cells the diffusion coefficients were calculated. Compared to the control group (see Figure 5.5a, 5.9a and Table 5.1) an absolute increase of 5.7% for confined diffusion, an absolute increase of 0.6% for obstructed diffusion, an absolute decrease of 1.7% for simple diffusion and an absolute decrease of 4.6% for directed motion were observed (see Figure 5.9b, Table 5.1). Interestingly, after addition of azide / deoxyglucose a rapid condensation of chromatin was observed. Chromatin condensation was reversed after removal of the inhibitor as also reported recently [80].

Secondly, the impact of the presence of a functional actin cytoskeleton on vimentin body movement was tested using the actin polymerization inhibitor cytochalasin D at $1\mu g/ml$ (Figure 5.9c, Table 5.1). Five cells were imaged after addition of cytochalasin D every $\Delta t = 10$ seconds for 10 minutes. A quantitative analysis of 121 bodies revealed an absolute increase of 5.3% and 8.6% for confined and obstructed diffusion, respectively, and an absolute decrease of 3.9% for simple diffusion and a decrease of 10.0% for directed motion compared to the control group.

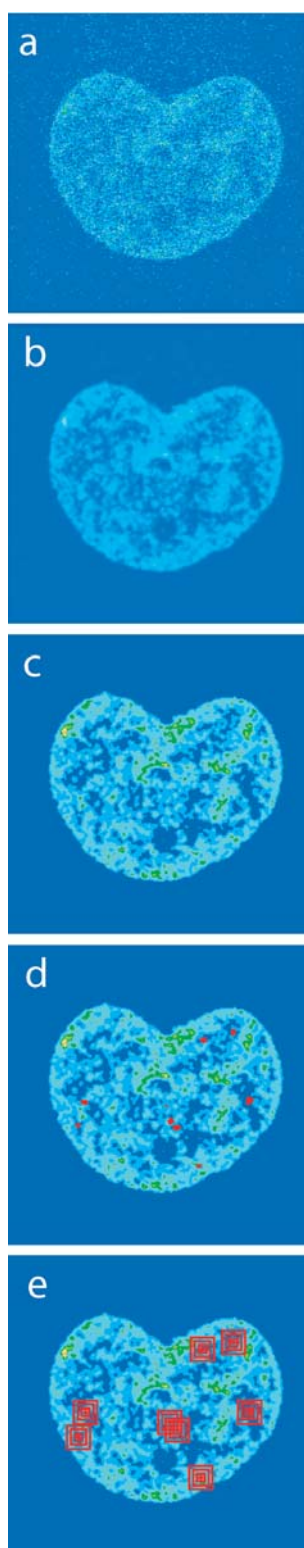


Figure 5.7: Chromatin intensity analysis showing the preprocessing steps for the Hoechst 33342 images: a) unprocessed original image; b) Gaussian smoothing; c) image classified into 8 regions of gray-values; d) localization of particles in the cell nucleus (red); e) measuring the mean gray-value intensity around the COM for each individual vimentin particle (see Section 3.4.7 for a complete description).

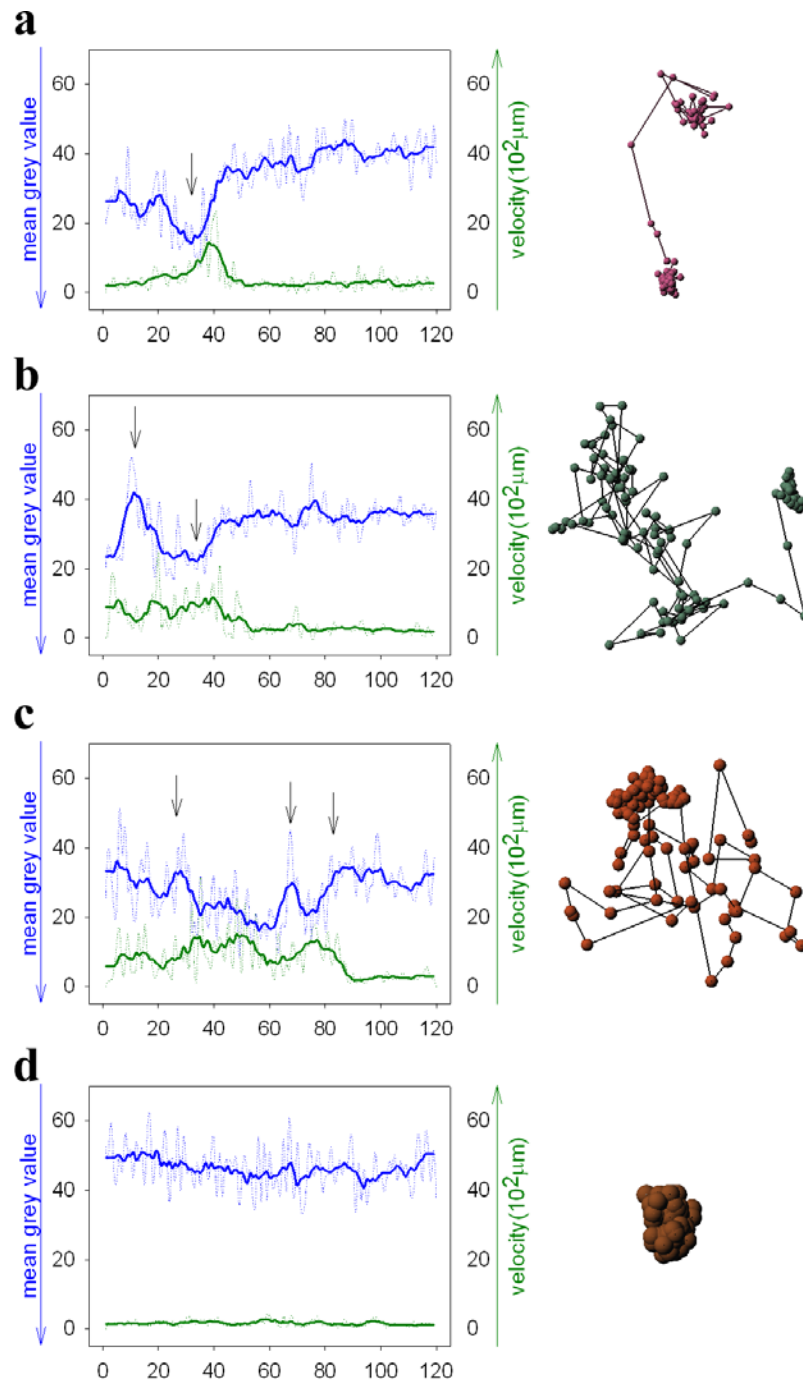


Figure 5.8: Correlation plots between mean gray-values (green line) of chromatin densities and particle velocity (blue line) over a time range of 20 minutes. Arrows indicate significant changes in intensity and particle velocity. Red: NLS-GFP-vimentin; green: Hoechst 33342 stain.

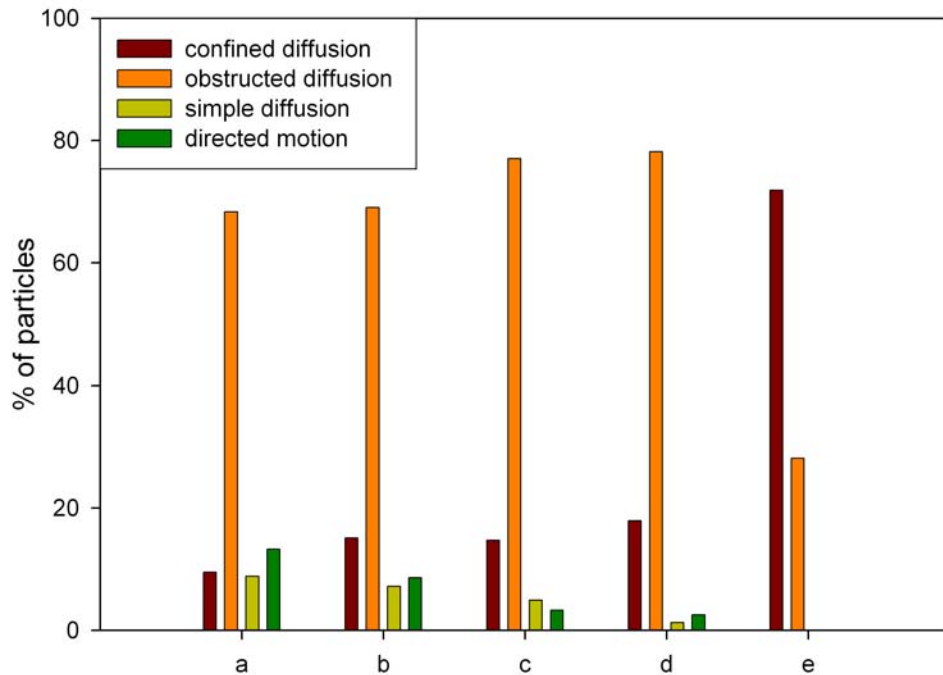


Figure 5.9: Mobility of nuclear vimentin bodies under the influence of inhibitors. Classification was performed according to the diffusion coefficient. a) control; b) azide / deoxyglucose (10mM / 50mM); c) cytochalasin D ($1\mu\text{g}/\text{ml}$); d) nocodazole ($0.04\mu\text{g}/\text{ml}$); e) sorbitol (600mM).

To study the role for microtubule structures on particle mobility I used the microtubule polymerization inhibitor nocodazole (see Figure 5.9d, Table 5.1). The effect of nocodazole treatment ($0.04\mu\text{g}/\text{ml}$) was also imaged in 5 cells with image stacks every $\Delta t = 10$ seconds for 10 minutes. By analyzing 119 bodies, an absolute increase of 8.7% and 9.9% was detected for confined and obstructed diffusion while an absolute decrease of 7.7% and 10.9% compared to the control groups was observed for simple diffusion and directed motion, respectively.

5.2.6 Particle movement in dehydrated cells

Finally the dependency of the GFP-NLS-vimentin mobility on availability of water in the nucleus was tested by treating the cells with sorbitol (600mM) [208] (Figure 5.9e, Table 5.1). In contrast to the previous inhibitors, I observed a dramatic change in particle mobility. Calculation of diffusion coefficients for 101 particles in five cells revealed the total loss of simple diffusion and directed motion activities. Accordingly, 79.1% of all particles were found in the confined diffusion and 20.9% in the obstructed diffusion group.

In summary kinetic changes were most prominent for the directed motion mode. ATP depletion decreased directed motion about 30% relative to the control group. Treatments with cytochalasin D and nocodazole even showed a 70% decrease in directed motion relative to the control group. The most striking

effect was encountered by treating the cells with sorbitol. Simple diffusion and directed motion were totally abolished whereas the number of particles exhibiting confined diffusion increased by a factor of 7 relative to the control group.

5.3 Discussion

In this study I developed comprehensive bioinformatics tools to analyze the kinetic behavior of small particles in the cell nucleus. For this purpose, fast time-lapse confocal laser scanning microscopy was used to record fluorescent particles in their chromatin environment. Automated image processing algorithms such as image registration and single particle tracking were instrumental to analyze the resulting complex datasets in a most efficient way. Usually, sophisticated image processing methods are widely not accessible for cell biology laboratories working with multi-dimensional datasets. A qualitative, interactive analysis of complex processes in living cells can yield interesting results. However, a quantitative insight into the underlying mechanisms can only be achieved by a rigorous computational analysis. While computational systems have been provided for estimating diffusion and binding constants based on photobleaching experiments of populations of small proteins [171, 209, 210, 211], integrated software packages for single particle tracking of nuclear bodies on the background of moving and shape changing objects have not been provided yet to the community. Here, my system Tikal closes an important gap. For an automated analysis of even larger sets of spatio-temporal data as in this study any software system needs to be adapted to data storage systems that are devoted for handling such huge datasets [166]. At the same time image analysis workflows have to be deployed onto computing clusters or the GRID ([212], accepted). Both developments are underway in our laboratory.

I visualized the different kinetic behaviors of nucleus-injected 100nm polystyrene microspheres. Furthermore, a stably transfected cell line expressing GFP-NLS-vimentin, which forms nuclear particles in the same size range as microspheres, was used. The majority of nuclear particles moved with obstructed diffusion within distinct corralled regions. This kind of movement was essentially found also for microinjected polystyrene beads. The obstructed diffusion behavior supports the notion that these particles can diffuse within corrals restricted by dense chromatin regions. Upon chromatin remodeling distinct less dense chromatin regions are formed and enable the particle to move to an adjacent corralled region. I was able to quantitatively assess this phenomenon by measuring the chromatin intensity around an individual particle. My data show that chromatin intensity decreases prior to a global velocity increase of the particle. Therefore I conclude that the particles do not actively push their way through the chromatin. Moreover, the chromatin itself is able to support or induce the movement of individual particles. The ability of the particle to move from one corral to the next is restricted and regulated by the surrounding chromatin remodeling activities. However, whether local chromatin regions can actively influence the destination of small nuclear particle movement has to be resolved in future investigations. With the present assay I cannot discern

whether changes in the velocity of a body simply correlate with the entry of a body into a domain or whether the changes are caused by interaction between a body and the surrounding chromatin domain surfaces.

The addition of cellular inhibitors caused significant changes in the diffusional behavior of nuclear particles. In all treatments a reduction of active transport processes was observed. This suggests that the coordination of nuclear processes such as chromatin remodeling is not solely dependent on single factors such as ATP, i.e. ATP consuming enzymes. Moreover, chromatin regions in interphase nuclei apparently move in a diffusional way [158], while other factors such as cytoplasmic microtubules and actin filaments attached to the NE possibly account for large-scale spatial chromatin rearrangements [47].

The phenomenon of energy dependent nuclear body movement has been also described in other studies where an anomalous diffusion behavior and an ATP- and transcription-dependent association of CBs with chromatin was reported [10]. Further, upon ATP depletion in BHK cells rapid and large-scale movement of PML bodies stopped, whereas small localized movements of PML bodies were still observed [13]. A recent examination of the dynamic behavior of PML nuclear bodies showed their fission to microstructures after different physiological stresses, and their fusion upon recovery [213]. Moreover it has been shown that movements of PML and other nuclear bodies can be described by diffusion of the individual body within a chromatin corral and its translocation resulting from chromatin diffusion [9]. However, future systematic studies will help to reveal the influence of drug treatments and cellular inhibitors on the dynamic behavior of those and other nuclear bodies.

A further interesting observation was the reversible formation of chromatin dense regions upon energy depletion. The general effect of this reorganization seems to influence the mobility distribution pattern of the particles only slightly. However, I could observe a significant decrease in directed motion of up to 30% upon inhibition of energy-depended processes.

Furthermore, in order to evaluate the degree of nuclear particle movement with respect to cytoplasmic dynamics, I used the vimentin system to analyze cytoplasmic particle mobility. Mostly active transport processes were observed. Two possible explanations for this phenomenon are suitable. Vimentin, which belongs to the group of intermediate filaments, forms crossbridges to other cellular structures. Since the SW13 cells lack endogenous expression of intermediate filament proteins such as cytokeratins and vimentin, possible interactions with these cytoplasmic intermediate filaments can be omitted. Specific interactions with dynein have been described [214, 215]. Hence, newly synthesized vimentin is subjected to active transport processes and "guided" to cellular locations for the establishment of vimentin networks. Another explanation could assume that the filaments do not bind any cytoplasmic structure. In this less likely scenario the active transport of vimentin particles would result from the densely packed cytoplasm and the resulting pushing and pulling of adjacent actively transported molecules.

From my data I conclude that the NLS-vimentin system is very suitable for further studies of nuclear architecture. Though I obtained the same results with microinjection assays, the GFP-NLS-vimentin system has significant advantages

5. 4D single particle tracking of nuclear particles

such as the higher expression efficiency and the fact that the experiments can be performed in a cell system with normal proliferation characteristics.

General Conclusion & Outlook

In this thesis I pursued two biological projects focusing on quantitative image analysis of biological processes. I used the image processing platform Tikal to perform the various pre-processing, quantification and visualization tasks.

The first project covered the spatial analysis of the Xic in various mouse ES cell line nuclei where I found a spatial Xic cross-talk event that is essential for the X-inactivation process. Fractions of the cells were fixed at discrete time points for subsequent confocal laser microscopy analysis. I had to acquire hundreds of multicolor 3D stacks for the different cell lines during the sequence of the differentiation process that resulted in the quantification of over 5000 analyzed cell nuclei.

In the second project I could show the correlation of movement of small sub-nuclear particles with the underlying chromatin density [145]. For this purpose large multicolor 4D image sequences were acquired, followed by extensive data pre-processing, segmentation and analysis with Tikal.

Additionally I could show the methodological proof of concept for Tikal in several other studies. Tikal was successfully used for the high throughput 3D segmentation of cell nuclei [216], the 3D segmentation and determination of physical properties for small nuclear particles [9] and the 3D segmentation, reconstruction, 4D tracking and visualization of starfish chromosomes during mitosis [170].

So what is the overall benefit and message of this thesis? I could give essential information about chromatin organization and show the importance of transient chromosome rearrangements (and cross-talk events) occurring during the early differentiation phases of mouse ES cells. With the analyzed data I could help to clarify the generally accepted Xic cross-talk theory that was suggested almost 40 years ago [93, 189]. My results will help to explain and understand the complex processes of X-inactivation and will help to initiate new ideas of research areas.

The arrangements of chromosomal territories and the presence of the nuclear ICD has been suggested and proved by several studies [196, 217, 54, 37, 204]. With the help of 3D FISH techniques and filamentous vimentin the ICD could be defined as a region with less chromatin in-between chromosome territories [54, 154, 204]. The function of these regions with less chromatin could be seen as chromatin open domains creating an environment that facilitates transcriptional activation and keeps clusters of genes together [53]. Often nuclear particles are found within the ICD although the physiological importance of this localization is still an open question [204]. An important aspect in defining the ICD function

is to understand the movement of nuclear particles within the chromatin environment. With the help of vimentin and inert sepharose beads I could measure the correlation between chromatin density and subnuclear particle movements and could conclude that alteration in chromatin density directly influences the mobility of protein assemblies within the nucleus [145, 9].

From these results it is clear that the chromatin confirmation and rearrangements are essential for coordination of nuclear processes. Taking this into account, how can the transient cross-talk event be explained by conformational changes of chromatin?

Two different but mutually not exclusive models for chromosome distribution exist. One model suggests a gene density dependent distribution of chromosomes within the nucleus, whereas in other studies a chromosome size depended distribution is observed [218, 34, 219, 220]. It seems that different cell states show different chromosomal arrangements. It has been shown that in quiescent fibroblasts a shift of chromosome 18 to the nuclear center is observed, whereas cycling fibroblasts show a peripheral localization of the same chromosome [45, 44]. In terminally differentiated myoblasts compared to cycling myoblasts such a positional change of specific chromosome loci has also been observed [221]. Could such a chromosomal shift be also responsible in the case of the Xic cross-talk? And if so, what nuclear factors might be included?

A major difference between the discussed data and my project on the Xic distribution are the cell types and their respective differentiation state. The previous analyses were performed in differentiated cells such as fibroblasts and myoblasts whereas I used undifferentiated mouse ES cells [222]. It is clear that those cells and their chromatin conformation are substantially different and it remains questionable if the existing models can be simply merged to ES cell line systems. In ES cells major chromatin rearrangements occur during the early lineage decisions that correspond exactly to the phase where I found that the Xic cross-talk events take place [222]. In this respect I could show by specific counting deletions, that the spatial Xic cross-talk is essential for X-inactivation and the subsequent differentiation steps. The approximation of specific chromosome regions must be of vital importance as shown by a recent study where interferon loci come into close spatial location and play a regulatory role during T-cell maturation [133]. This suggests that portions from different chromosomes communicate with each other, and bring related genes together in the nucleus to coordinate their expression (kissing chromosomes) [223]. But the main mechanistic process still remains unclear. What are the mechanisms that bring two functionally related genes on two different chromosomes together?

Since the Xic cross-talk events are very coordinated, precise and transient, an explanation only by chromatin diffusion models is unlikely [158]. Therefore, active nuclear processes might be involved in these chromosomal kissing events. That energy dependent processes can influence the movement of nuclear particles has been shown in several studies [145, 9, 13, 10, 8]. However, it is still controversially discussed how these energy dependent particle movements are coordinated. The subnuclear structures could either bind directly to transport molecules, e.g. myosin, or could be passively pushed through the nucleus by actively remodeled chromatin. Although some of the nuclear particles actively

bind to chromatin [10], it remains to be elucidated which molecular mechanisms are responsible for the Xic cross-talk event and if it can be explained with the knowledge about nuclear particle movement.

Certainly live cell imaging of two fluorescent labeled Xic regions would shed more light on the questions of the mechanism of Xic cross-talk. It could for example show at what cell cycle stages this transient Xic co-localization occurs. The transient co-localization could possibly take place shortly prior or after mitosis. Although it has been shown that global chromosome positioning is mainly inherited during mitosis [224], local conformational changes of the chromatin state could initiate the approximation of the Xics. These studies were again performed in fully differentiated cells. However, the FRAP technique on double labeled H2B chromatin with two different fluorophores could readily be performed in mouse ES cells. This could give a clear model of the timely coordinated extend of chromatin rearrangement in differentiating ES cells. A combination of the H2B staining with the information from the labeled Xic regions would maximize the explanatory power and give meaningful insights in the Xic cross-talk process.

Furthermore, an investigation of the Xic processes in different cell types would be interesting. Since the two analyzed female mouse ES cell lines derive from the same species I could not find any significant differences in spatial and temporal resolution during the Xic cross-talk. Therefore an extension of the fixed cell analysis to other mammalian cell lines such as human or monkey ES cells could reveal how conserved the Xic cross-talk is. New insights of human X-inactivation would be gained, although experimental planning and setup would be more complex from an ethical point of view.

In context with the extended fixed cell analysis other nuclear structures important for the possible coordination of X-inactivation could be investigated. Especially the importance of the nucleolus could be approached. Manual evaluation of internal Xic locations suggested that the Xic is closely associated to the nucleolus. An association to nuclear membrane structures would substantiate that the Xic has to be located in a heterochromatic region to get properly sensed and regulated for later inactivation processes. An interesting question would be to evaluate the importance of the Xic location to the nucleolus but also the influence of defined chromosome positions during the X-inactivation process.

At later stages different hypotheses could be validated by computer models. During my project, I introduced simple computer simulations to test whether or not the nuclear Xic positioning is random. However, to obtain meaningful information from such simulations a vast amount of data had to be acquired initially. For my projects thousands of microscopic cell images have been taken into account and it becomes obvious that a manual performed analysis of such huge datasets would have been impossible within the given time. For this reason, I developed an integrative data analysis platform that harbors the complete data analysis workflow. Prior to the programming of Tikal I tested several available data analysis programs.

A multitude of commercial and non-commercial image analysis packages is available on the market. Each individual package has its own strengths and weaknesses in specific fields of application. Because of the recent upturn of bio-

logical image analysis many of the nowadays available image software packages have a specific focus on medical image analysis. Between the various application fields, such as medical and biological image analysis, the programs have to be adapted to suit the differential needs of analysis due to the previously discussed differences in image quality but also different image features. For this reason the available and ready to use software packages for biological image analysis are limited.

Generally software suppliers follow two different strategies for their products, namely a commercial or a non-commercial way of distribution. Because of these two distribution channels software features often substantially differ from each other. For commercial packages I noted strong emphasis in the optimization of data visualization and rendering (Imaris, Bitplane). Indeed, data visualization is an important step in performing proper quantitative data analysis. But frequently this feature is a major drawback of such platforms because commercial platforms lack suitable modules for pre-processing and noise reduction filters. Often only simple filters such as median filters and Gauss smoothing algorithms are integrated. Beside those facts, it then appears controversial that data analysis is integrated in some of those programs, e.g. co-localization analysis, object quantification tools and rudimentary tracking algorithms. In this context it seems interesting that some commercial programs (such as Amira) feature extensive processing and quantification algorithms. However, these platforms often lack a substantial amount of capability to be used for higher dimensional biologic image sequences.

One solution would be the use of several different software packages. However, splitting of processing tasks amongst different programs is time consuming and inefficient in every way. Common problems occurring due to the use of multiple platforms might involve data conversion problems, but also hardware limitations such as storage problems. The latter aspect seems to have lost importance, since storage space has faced decreasing prices on the market over the last years. But in this respect the cost of data storage is not the main problem. The management of the abundant number of data files is becoming more and more the focus of central interest, e.g. like millions of files have to be stored in a retrievable way. Therefore the proper extraction, storage and filing of image meta data is essential for the coordinate functioning of future large scale screening projects, e.g. large scale phenotyping with cell arrays [225]. Although some of the surveyed analysis platforms showed attempts to integrate image data bases to their environment, none showed real high-throughput capabilities.

Another possibility is the use of non-commercial and open source programs. Compared to commercial packages, their focus often lies more on image processing and analysis but frequently shows a lack of visualization capabilities (especially for displaying multidimensional image sequences). A major advantage of open source platforms is their constant program updating and capability to integrate external extensions. Open source strategies give a transparent and easy way to implement virtually any kind of analysis modules. The only drawback of the existing open source solutions are their initial programming and data handling frameworks. ImageJ can be seen as such an example which was initially developed as a powerful tool for 2D microscopic image series. An exten-

sion to 4D multicolor datasets is almost impossible at the current software state and needs a total revision of the code. Also the previously discussed feature for high-throughput processing is lacking completely (although some kind of batch scripts have been integrated to ImageJ). But directions towards high throughput database platforms have been made. One of the most promising database developments for microscopic platforms is the formerly introduced OME open source image data base [166].

To avoid these various presented draw-backs of existing platforms I developed Tikal. With the data analysis methods used in the previously presented projects I was able to show the powerful features of my program. I could introduce the complete processing workflow from raw to quantitative data into my program. I added supplementary features such as the capabilities of 4D image registration and 4D single particle tracking to my software. Such features are in other programs either completely missing or only in basic versions available, e.g. lacking 3D registration capabilities of TurboReg (<http://www.epfl.ch/thevenaz/turboreg/>) and AutoAligner (<http://www.bitplane.ch>). Especially the 4D single particle tracking module is seamlessly integrated to the 4D isosurface visualization window which enables the user to survey and, if necessary, correct possible trajectory artifacts. A major additional advantage compared to all available programs is the capability of running Tikal on a high performance cluster. Only this high-throughput module made it possible to process the vast amount of my generated datasets. To close the open gap of lacking communication interfaces of various software packages to image databases (such as OME) new methods enabling the combination of the high-throughput capabilities of Tikal with such databases are currently integrated.

Future work definitely needs to focus on automatic and unsupervised analysis of biological microscopy images. Problems such as the reliable data storage and retrieval have been discussed in the previous section. Additional focus needs to be put on the extraction of meaningful and relevant cellular features from these images. Only with the help of such parameters clear biological conclusions can be drawn fully automated by computer algorithms. An example for such approaches is the already described cellular phenotyping by machine-learning-based classification methods [225]. Other projects are using similar methods to identify abnormalities during the cell cycle and especially during mitosis (see MitoCheck (<http://www.mitocheck.org>)). The identification of representative and reproducible features or markers for classification in living cells is difficult. Compared to higher animals single cells lack an anatomical map of their structure. Currently approaches are taken to identify the accurate 3D spatial localization of genes within the cell nucleus (see 3DGenome (<http://3dgenome.science.uva.nl/>)). Such information could be used to create an “anatomical” map of the cell.

To achieve these future goals one has also to focus on the constant development but also adaption of existing analysis algorithms to extract quantitative parameters from the cellular and subcellular imaging of biological samples. Especially the object segmentation methods but also the quantification by tracking algorithms have to be more robust and reliable to be usable for unsupervised

image analysis. For the segmentation of cells or cell nuclei algorithms using active contours or level sets might be a promising solution. Tracking could be optimized by combining the presented methods of PTV and optical flow to obtain a maximum of accuracy. Noticeable is, that whatever new algorithm or method is developed it can be easily deployed as a module to Tikal.

In conclusion, my platform is improving the overall analysis accuracy and performance for biological images compared to existing platforms. Due to the modular framework concept, it can easily be expanded with new modules and methods. Further the framework shows no limitation in image dimensionality and has shown its proof of concept on the performed biological data analysis projects. With the help of Tikal I was able to master the challenging amount of thousands of images and extract biological meaningful quantitative parameters.

Appendix A

Tikal Manual

A.1 General Functions

The GUI front-end can be divided into several parts:

- The “Canvas area” in the center of the GUI. 2D images of multi-dimensional datasets will be displayed.
- A menubar to select functions for file I/O, filter selection, quantification, and zooming can be found at the top of the working area
- Browsing through image stacks in the z (left slider) and time dimension (bottom slider). This function is only activated if the loaded images have multi-dimensional properties. The actual position in the dataset is displayed in the window bar (top): time / z-position.
- The “Data set history” window for displaying the already performed image processing results
- The “Channel selection” window for selection and display of all or individual channels in multi-channel images
- The “Colormap selection” drop-down menu for data visualization with color-maps.
- The “Console window” displays important messages and progress information during the data analysis. Besides a taskbar (bottom) will display short descriptions of the selected functions.
- The “Isosurface rendering” window renders extracted isosurfaces in 4D with OpenGL. Beside visualization it enables displaying of tracking trajectories and their manual modification.
- The “Experiment cropping” window allows the definition of areas for image cropping for complete 4D data sets.

A.1.1 The “Canvas area”

The “Canvas area” displays 2D image slices of multi-dimensional datasets. *Left mouse* click on the image area will display in the “Console window” the complete coordinates and grey-value information of the selected pixel. For mouse assisted navigation and manipulation see Section A.5.7 on page 147.

A.1.2 The “Data set history” window

The “data set history” window displays the current image processing history. Whenever a manipulation on an image is performed a new entry will be made. Such an entry will be called an “experiment” in the following.

Normally the selected entry will be used for data processing. With a selection of multiple entries (by pressing *Ctrl + left mouse*) the last selected entry will be used for processing.

Right mouse click on the menu entry enables renaming of the corresponding entry.

Deletion of one or multiple entries can be achieved by selection followed by pressing the *Remove* button.

A.1.3 The “Channel selection” window

The channel selection window enables selection, duplication and removal of individual channels. At least one and a maximum of 256 channels are available for an experiment.

Multiple channels can be selected and visualized by pressing *Ctrl + left mouse*. Processing filters will only be applied to the selected channels.

If no colormaps are selected the channels will be display according to RGB rules, e.g. first channel R = red, second channel G = green.

Deletion of a single channel can be performed by *left mouse* followed by clicking on the *Remove* button.

Duplication of a single channel can be performed by *left mouse* followed by clicking on the *Copy* button.

The channel removals and duplications are only working on single selected channels.

A.1.4 The “Colormap selection” window

The drop-down menu enables visualization of the data sets by pseudo colors. Standard selection is “*normal*” displaying the images in RGB mode.

New colormaps can be added by creating a 256 color look-up table with the ending “.act” in the folder “*color_maps*”. The name of the colormap has to be added in the file “*color_maps.lst*”. To load the colormap Tikal has to be restarted. The folder needs to be located in the same directory as the Tikal main executable.

A.1.5 The “Experiment cropping” window

The window displays a 4D maximum intensity projection of a complete data set. A region-of-interest (ROI) in the shape of a polygon can be drawn. The corners of the area can be defined by single selections in the projection area with the *left mouse*. The two following cropping modes are available: i) polygon region definition (red line), ii) rectangular region definition (yellow line). The selections have to be stored by selection the *Save Poly Mask* button or the *Save Rec Mask*, respectively. The cropping algorithm can be started by clicking on the *Apply* button. The window can be closed without cropping by selecting the *Cancel* button.

Resetting of the selection can be achieved by the use of the *middle mouse*. The selected area covered by the polygon can be visualized by the *right mouse*.

A.1.6 The “Isosurface rendering” window

The window appears after creation or loading of isosurfaces (see Section A.6). The dialog shows similar structure and components as the main Tikal GUI front-end:

- The “OpenGL canvas” area in the center of the GUI. 3D isosurface rendering of multi-dimensional datasets will be displayed.
- Browsing through the 3D isosurface scenes in the time dimension (bottom slider). The mouse can also be used for the slider control. The *d + left mouse* on the “OpenGL canvas” shifts the time slider $t + 1$. The *a + left mouse* on the “OpenGL canvas” shifts the time slider $t - 1$.
- A menubar to select functions for file I/O. This includes saving of isosurfaces (for isosurface loading see Section A.6.2 on page 153), trajectory export functions (object coordinates, object properties, mean squared displacements, changes in distance), trajectory saving and loading routines.
- A “controls” sections for camera positioning, trajectory handling (and visualization) (see Section A.5.5 on page 146), channel / display modes and color controls

The 3D objects in the “OpenGL canvas” area can be controlled with the mouse. With the *left mouse* pressed the object can be rotated, with the *middle mouse* pressed the scene can be zoomed and with the *right mouse* pressed the objects can be moved.

Export Mean Square Distance to Excel

Exports a *tab*-character delimited text with information for each individual trajectory:

Column 1: Trajectory index

Column 2-4: Scaled Trajectory COMs for the x, y, z coordinates

Column 5: Sum of all grey values found within a tracked binarized object

Column 6: Scaled volume in μm^3

Column 7: Total number of voxel for a binarized object

Column 8: Change in distance of an object

Column 9: Mean squared displacement (MSD) for a trajectory

A.2 The “File” menu

A.2.1 Open 4D desktop

Opens a complete Tikal Desktop. This is a proprietary file format which enables to save and restore the complete “Data set history” entries (for saving of Tikal Desktop see Section A.2.2).

A.2.2 Save 4D desktop

Saves the complete entries from the “Data set history” window into the Tikal file format. All image properties (such as voxel sizes) are saved as well.

A.2.3 Open 4D stack

Enables to open large 4D experiments of 8 bit grey-value *raw* and *tiff* files. Normally these file derive from other programs by exporting the image files. To open this single files a “listfile” containing the file paths has to be either automatically or manually created (see Section A.2.5). If *raw*-images are imported the correct extension and image sizes has to be provided. Loading of *Tiff*-files does not depend on provided image sizes since Tikal is obtaining those values directly from the dataset.

A.2.4 Save 4D stack

Writes a whole experiment with all its channels to the selected folder with the named “listfile” for later reimport to Tikal (see Section A.2.3). The data format is a 8 bit grey-value *raw* image without headers. The filenames are created according the following rules: “*tt_c_zzz.raw*” where *t* = time, *c* = channel, *z* = z-slice. Any leading space will be filled by “0”.

A.2.5 Create listfile

To facilitate opening of whole experimental datasets that consist of individual image files a “listfile” has to be created. For the automatic creation of the “listfile” the data need to be in the appropriate format (either 8 bit grey-value *raw* or 8 bit grey-value *tiff*) and with the correct naming. The file naming should be the following:

“*prefix_tt_c_zzz.raw*” where *prefix* = user defined value, *t* = time, *c* = channel, *z* = z-slice. Any leading space will be filled by a “0”. The files need to reside in the same directory.

In the “Create imagelist file” dialog the directory containing the images has to be selected (left). The other fields define the size, length and format of the

data set. Please note that the filenames are saved as absolute paths. If files are moved or renamed a new “listfile” has to be created.

If a manual creation of the “listfile” is needed it must be in the following structure to achieve successful loading of the dataset:

1. A new stack will be defined by a “!!” at the beginning of the line
2. A new channel will be defined by a “>>” at the beginning of the line
3. Each image must have a index number “1, 2, 3, ...” at the beginning of the line followed by the filename which includes the absolute path. The arrangement of the filenames also designate the positioning of the files in the image stack (first file = top image in the stack, last image = bottom image in the stack).

Example:

```
!! new image stack: 1
>> Image Channel 1
1 /path_to_file/filename_stack_1_channel_1
2 /path_to_file/filename_stack_1_channel_1
.
.
.
>> Image Channel 2
1 /path_to_file/filename_stack_1_channel_2
2 /path_to_file/filename_stack_1_channel_2
.
.
.
!! new image stack: 2
>> Image Channel 1
1 /path_to_file/filename_stack_2_channel_1
2 /path_to_file/filename_stack_2_channel_1
.
.
.
```

A.2.6 Create listfile Leica

Normally multi-dimensional data deriving from a Leica microscope should be opened with the “Open 4D Leica” (see section A.2.8). If the files with extension “.lei” are missing a “listfile” can be generated. The files have to be named according to the convention of the Leica format: “*prefix_ttt_zzzz_chcc.tif*” where *prefix* = user defined value, *tt* = time, *cc* = channel, *zzz* = z-slice.

A.2.7 Create listfile DeltaVision

Deprecated. For importing Deltavision files refer to Section A.2.10.

A.2.8 Open 4D Leica

Opens original Leica files with the extension “*.lei*” (Leica Microsystems). After opening a selection of available sub-experiments will be provided.

A.2.9 Open 3D Leica

Opens files without and available file with “*.lei*”-extension. However, the naming of the file has to follow the conventions from Leica: “*prefix_ttt_zzzz_chcc.tif*” where *prefix* = user defined value, *tt* = time, *cc* = channel, *zzz* = z-slice. The import filter strips all information except the prefix and loads the 3D stack.

A.2.10 Open DeltaVision

Opens original Metamorph files with the extension “*.dv*” (Deltavision / Applied Precision).

A.2.11 Open Metamorph

Opens original Metamorph files with the extension “*.stk*” (Molecular Devices).

A.2.12 Image properties

Displays properties of the selected image data sets e.g. image sizes, number of images in a stack. Further it enables a changing of the voxel size parameters (in μm). After changing the parameters the *Set* button has to be pressed to save the current settings. If changes should be discarded without saving or only the dialog window be closed the *Close* button has to be pressed.

A.2.13 Batch

The “Batch” processing is only accessible in the developer version of Tikal.

A.2.14 Quit

Closes the Tikal Software. All unsaved data will be lost.

A.3 The “Filters” menu

Normally all filters display a dialog window to set the processing parameters which will be used to initialize the filter itself. Prior to filter application the experiment for processing and the desired channels have to be selected, respectively. The filter will always be applied to the whole 3D stack for each individual time point (if available). It can be defined if only a certain time range of the experiment should be processed (default value is always the complete dataset). Filtering will be started by pressing the *OK* button.

A.3.1 Binarize

Global thresholding of an image. All pixel with grey-values \geq the threshold will be set to 255. Pixel grey-values $<$ the threshold will be set to 0.

- Binarize threshold = sets the global threshold

The other parameter fields are not used and do not influence the results of the filter.

A.3.2 Pixelremove

Removes pixels with defined size / volume from the image stack. Either by defining limits a range of object volumes (in voxel) can be selected or a precise object volume (in voxel) can be defined for removal. To obtain the object volumes a object property extraction on the binary image can be performed (see Section A.5.1).

Prior to apply this filter the images have to be segmented (a global threshold method is provided (see Section A.3.1)).

Remove a range of volumes:

- Binarize threshold = sets the global threshold (see Section A.3.1)
- Minimum voxel count = sets the lower range in voxel counts to remove objects
- Maximum voxel count = sets the upper range in voxel counts to remove objects
- Exact voxel counts = 0

Remove objects by defining their exact volume:

- Binarize threshold = Sets the global threshold (see Section A.3.1)
- Minimum voxel count = Not used
- Maximum voxel count = Not used
- Exact voxel counts = Exact volume in voxel of object to be removed

A.3.3 Binarize min/max

Global thresholding of an image within a threshold range. All pixel within the range of lower and upper threshold will be set to 255. All other pixel not fulfilling the conditions will be set set to 0.

- Binarize threshold low = Sets the lower threshold
- Binarize threshold high = Sets the upper threshold

A.3.4 Binning binarize

Classifies a image into 8 defined grey-value intensity ranges (bins) according to their pixel values. The first bin contains grey-value ranges between 0-32, the second 33-65, etc. Prior to binning the images get smoothed by a 2D Median (see Section A.3.8) and 2D Gauss filter (see Section A.3.8).

A.3.5 Median 3D

The median filter is a non-linear spatial filter used to remove noise spikes from an image. The 3D implementation is using a 3x3x3 kernel and is applied on the whole image stack.

A.3.6 Median 2D

The median filter is a non-linear spatial filter used to remove noise spikes from an image. The 2D implementation is using a 3x3 kernel and is applied on each single image plane.

A.3.7 Gauss 3D

The Gauss 3D filter computes the convolution of the input image with a 3x3x3 Gaussian kernel. The 3D filter is applied on the whole image stack.

A.3.8 Gauss 2D

The Gauss 2D filter computes the convolution of the input image with a 3x3 Gaussian kernel. The 2D implementation is using a 3x3 kernel and is applied on each single image plane.

A.3.9 Canny 2D

The Canny edge detection algorithm is an implementation of a Canny edge detector based on a publication by John Canny [226]. Six major steps are used in the edge-detection scheme:

1. Smoothing of the input image with a Gaussian filter. The larger the width (standard deviation) of the Gaussian mask, the lower is the detector's sensitivity to noise.
2. Calculation of the second directional derivatives of the smoothed image. The gradient of the image is taken by 2D Sobel operator. The Sobel operator uses a pair of 3x3 convolution masks, one estimating the gradient in the x-direction and the other estimating the gradient in the y-direction.
3. Finding of the edge direction.
4. Tracing of edges

5. Non-maximum suppression is used to trace along the edge in the edge direction and suppress any pixel value (sets it equal to 0) that is not considered to be an edge. This will give a thin line in the output image.
6. Use of hysteresis is a mean of eliminating streaking. Streaking is the breaking up of an edge contour caused by the operator output fluctuating above and below the threshold.

The filter is a 2D implementation and is applied on each single image plane.

- Lower edge tracker threshold = Lower threshold used for hysteresis (example value = 25)
- Upper edge tracker threshold = Upper threshold used for hysteresis (example value = 35)
- Standard deviation = Kernel size for Gaussian smoothing (example value = 4.0)

A.3.10 Gamma

Gamma correction is a method for controlling how mid-tones are displayed in an image. It is used to control the brightness of pixel according to equation:

$$p_{out} = \left(\frac{p_{in} - i_{low}}{i_{high} - i_{low}} \right)^{\gamma} * (o_{high} - o_{low})$$

- Input lower value = i_{low}
- Input higher value = i_{high}
- Output lower value = o_{low}
- Output higher value = o_{high}
- Gamma value = γ

A.3.11 Auto Gamma

Auto gamma correction uses the whole image stack to determine i_{low} and i_{high} by scanning each individual pixel. According to the found values gamma correction with $\gamma = 1$ is will be performed (see Section A.3.10).

A.3.12 Diffusion 3D

Perona and Malik formulate the anisotropic diffusion filter as a diffusion process that encourages intraregion smoothing while inhibiting interregion smoothing. The 3D filter is applied on the whole image stack using the voxel size values (see Section A.2.12 for viewing and setting the “image properties”).

- Tau factor = Not used

- Sigma factor = Kernel size (example value = 4)
- Lambda factor = Stopping factor (example value = 0.1)
- Times filter application = Sets the iterative steps performed on the image (example value = 50)

A.3.13 Diffusion 2D

Anisotropic diffusion filter according to Perona and Malik (see Section A.3.12). The filter is a 2D implementation and is applied on each single image plane.

- Tau factor = Timesteps of diffusion (example value = 0.01 - 0.001)
- Sigma factor = Kernel size (example value = 0.0001)
- Lambda factor = Stopping factor (example value = 2 (for small objects))
- Times filter application = Sets the iterative steps performed on the image (example value = 50)

A.3.14 Dilatation

Dilates an image using grey-scale morphology. The dilatation filter takes the maximum of all the pixels identified by the 3x3 structuring element. The structuring element is assumed to be composed of binary values (zero or one). Only elements of the structuring element having values > 0 are candidates that affect the center pixel. To avoid that object borders come in contact with image boundaries the image size will be increased linearly by each iterative step of the filter.

- Binarize threshold = Not used
- Number of iterations = Sets the iterative steps performed on the image

A.3.15 Erosion

Erodes an image using grey-scale morphology. The erosion filter takes the minimum of all the pixels identified by the 3x3 structuring element. The structuring element is assumed to be composed of binary values (zero or one). Only elements of the structuring element having values > 0 are candidates for affecting the center pixel. The image size will be decreased linearly by each iterative step of the filter.

- Binarize threshold = Not used
- Number of iterations = Sets the iterative steps performed on the image

A.3.16 Closing

The morphological closing operation is a sequential connection of the “Dilatation filter” (see Section A.3.14) followed by the “Erosion” filter (see Section A.3.15). The filter uses a 3x3 structuring element and can be used to separate interconnected objects.

- Binarize threshold = Not used
- Number of iterations = Sets the iterative steps performed on the image

A.3.17 Opening

The morphological opening operation is a sequential connection of the “Erosion” filter (see Section A.3.15) followed by the “Dilatation filter” (see Section A.3.14). The filter uses a 3x3 structuring element and can be used to separate interconnected objects.

- Binarize threshold = Not used
- Number of iterations = Sets the iterative steps performed on the image

A.3.18 Thinning

The morphological thinning algorithm (or skeletonization) removes gradually pixel from the borders of binary objects until the object skeleton remains. The filter is a 2D implementation and is applied on each single image plane.

No parameters influence the results of this filter. To return meaningful results a binary image must be provided to the filter.

A.3.19 Thinning RG

The filter detects single 3D binary objects and places a mark at the geometrical center of mass. The 3D filter is applied on the whole image stack.

- Binarize threshold = Sets the global threshold (see Section A.3.1)
- Minimum voxel count = Sets the lower range in voxel counts to remove objects
- Maximum voxel count = Sets the upper range in voxel counts to remove objects
- Exact voxel counts = Not used

A.3.20 Outline

Detects edges of binary objects in images. The filter is a 2D implementation and is applied on each single image plane. To return meaningful results a binary image must be provided to the filter. If edge detection in grey-value images is need then refer to the “Canny 2D” filter (see Section A.3.9).

A.3.21 Fill

Uses iterative dilatation followed by the same iterative number of erosions on single 3D binary objects. The advantage compared to the morphological applications on the whole image is the detection of binary objects and individual processing. This avoids that objects “fuse” with each other. Although the filter detects 3D object in the whole 3D stack the morphological processing is performed on the 2D images.

- Binarize threshold = Sets the global threshold (see Section A.3.1)
- Number of iterations = Sets the iterative steps performed on the image (first: x dilatations, second: x erosions)

A.3.22 Pyramid Segmentation

Pyramid-linking is a region based segmentation approach [227]. The algorithm consists of 3 steps:

1. Calculation of the Gauss pyramid
2. Segmentation with pyramid-linking
3. Averaging of the connected image points

The steps 2 + 3 are iteratively repeated until a stable result is obtained. The 2D implementation is applied on each single image plane. This filter works very good with small image structures and low background noise.

A.3.23 Pyramid Binarize

Uses the pyramid-linking approach to binarize the obtained areas (see Section A.3.22).

A.3.24 Inversion

Returns the inverse of a grey value image.

A.3.25 Clear Border

Removes 3 pixel at the borders of images. A common use this filter is after the use of the “Canny 2D” filter (see Section A.3.9) which could result in detection of the image boundaries as a edges.

A.3.26 Maximum Projection

Creates a maximum intensity projection of a 3D image stack in the z-direction. The output image is a grey-value 2D image with displaying the maximum of the detected grey-value intensity in the z-direction.

A.3.27 Average Projection

Creates an average intensity projection of a 3D image stack in the z-direction. The output image is a grey-value 2D image with the average of pixel values found in the z-direction.

A.4 The “ITK” menu

There is a seamless two-sided communication interface of the Tikal data structures to the open source ITK (Insight segmentation and registration toolkit [172]) library. With the correct parameters every ITK function can be called within Tikal and will return on success an experiment to the “Data set history” window (see Section A.1).

A.4.1 Binarize

Deprecated. For global thresholding refer to Section A.3.1.

A.4.2 Watershed

Segments images based on the watershed algorithm. Watershed segmentation gets its name from the manner in which the algorithm segments regions into catchment basins. If a continuous height function is defined over an image domain, then a catchment basin is defined as the set of points whose paths of steepest descent terminate at the same local minimum of the function. The filter is a 2D implementation and is applied on each single image plane. To filter contains two pre-processing steps consisting of “gradient anisotropic filtering” (see Section A.4.3) followed by “gradient magnitude filtering” (see Section A.4.5).

- Anisotropic Time Step = Effective width of the filter kernel (example value = 0.25)
- Anisotropic Conductance = Controls the sensitivity of the process to edge contrast (example value = 3)
- Anisotropic Iterations = Sets the iterative steps performed on the image (example value = 50)
- Watershed threshold = Controls oversegmentation of the image. Raising the threshold will generally reduce computation time and produce output with fewer and larger regions. (example value = 0.05)
- Watershed level = Controls watershed depth (example value = 0.1)

A.4.3 Gradient Diffusion

Perona and Malik formulate the anisotropic diffusion filter as a diffusion process that encourages intraregion smoothing while inhibiting interregion smoothing (see Sections A.3.12 and A.3.13) . The 3D filter is applied on the whole image stack according to equation:

$$C(x) = e^{-\left(\frac{|\nabla U(x)|}{K}\right)^2}$$

- Anisotropic Time Step = Effective width of the filter kernel (example value = 0.125)
- Anisotropic Conductance = Controls the sensitivity of the process to edge contrast (example value = 3)
- Anisotropic Iterations = Sets the iterative steps performed on the image (example value = 50)
- Watershed threshold = Not used
- Watershed level = Not used

A.4.4 Bilateral Diffusion

Bilateral filtering smooths images while preserving edges, by means of a nonlinear combination of nearby image values.

- Tau factor = Not used
- Sigma factor = Kernel size 1; defines how close pixel neighbors (spatially) should be in order to be considered for the computation of the output value (example value = 5)
- Lambda factor = Kernel size 2; defines how close pixel neighbors intensity should be in order to be considered for the computation of the output value (example value = 6)
- Times filter application = Not used

A.4.5 Gradient Magnitude

The magnitude of the image gradient is used to determine the separation of object contours and homogeneous regions. In the case of 2D images the computation is equivalent to convolving the image with masks of type

$$\begin{bmatrix} -1 & 0 & 1 \end{bmatrix} \begin{bmatrix} -1 \\ 0 \\ 1 \end{bmatrix}$$

then adding the sum of their squares and computing the square root of the sum. The 2D implementation is applied on each single image plane.

A.4.6 Connected Thresholding

The connected thresholding segmentation labels pixels that are connected to a seed point and lie within a specific range defined by a upper and lower threshold. The pixel intensities that are inside the interval are set to 255. All other pixel intensities are set to 0. The 3D filter is applied on the whole image stack.

Prior to use a seed point has to be defined. For this purpose a *Left mouse* click on the image in the “Canvas area” stores the coordinates (see Section A.1.1). On time series the seed point has to be set for each individual timestep.

- Lower edge tracker threshold = Lower range threshold (example value = 0)
- Upper edge tracker threshold = Upper range threshold (example value = 200)
- Standard deviation = Not used

A.4.7 Neighborhood Thresholding

The neighborhood connected thresholding segmentation is similar to the connected thresholding segmentation (see Section A.4.6) but also uses a mathematical morphology erosion using a structuring element with equivalent size and shape as provided for the region growing. To initialize the filter a seed point and a upper and lower threshold has to be defined. The pixel intensities that are inside the interval are set to 255. All other pixel intensities are set to 0. The 3D filter is applied on the whole image stack.

Prior to use a seed point has to be defined. For this purpose a *Left mouse* click on the image in the “Canvas area” stores the coordinates (see Section A.1.1). On time series the seed point has to be set for each individual timestep.

- Lower edge tracker threshold = Lower range threshold (example value = 0)
- Upper edge tracker threshold = Upper range threshold (example value = 200)
- Standard deviation = Kernel size (example value = 1.0)

A.4.8 Confidence Thresholding

This filter extracts a connected set of pixels whose pixel intensities are consistent with the pixel statistics of a seed point. The mean and variance across a neighborhood (8-connected, 26-connected, etc.) are calculated for a seed point. Then pixels connected to this seed point whose values are within the confidence interval for the seed point are grouped.

Prior to use a seed point has to be defined. For this purpose a *Left mouse* click on the image in the “Canvas area” stores the coordinates (see Section A.1.1). On time series the seed point has to be set for each individual timestep.

- Tau factor = Not used
- Sigma factor = Variance multiplier. Small values of the multiplier will restrict the inclusion to the current region. Larger values of the multiplier will relax the accepting condition and will result in more generous growth of the region. Values that are too large will cause the region to grow into neighboring regions that may actually belong to separate anatomical structures. (example value = 2.5)
- Lambda factor = Kernel size; rectangular region in 3D according to $2*\lambda+1$ pixel for each dimension (example value = 2)
- Times filter application = Sets the iterative steps performed on the image (example value = 5 - 6)

A.4.9 Distance Mapping

Watershed segmentation is a way of automatically separating or cutting apart particles that touch. It requires a binary image containing black particles on a white background. It first calculates the Euclidean distance map (EDM) and finds the ultimate eroded points (UEPs). It then dilates each of the UEPs (the peaks or local maxima of the EDM) as far as possible - either until the edge of the particle is reached, or the edge of the region of another (growing) UEP. Watershed segmentation works best for smooth convex objects that don't overlap too much. The filter is a 2D implementation and is applied on each single image plane.

A.4.10 Otsu Thresholding

The Otsu thresholding filter creates a binary thresholded image that separates an image into foreground and background components. A criterion for this classification of pixel is to minimize the error of misclassification. The goal is to find a threshold that classifies the image into the two desired clusters (foreground and background) in such a way that the area under the histogram for one cluster that lies on the other cluster's side of the threshold is minimized. This is equivalent to minimizing the within class variance or equivalently maximizing the between class variance. The 3D filter is applied on the whole image stack.

- Lower edge tracker threshold = Grey-value for foreground pixel (example value = 255)
- Upper edge tracker threshold = Grey-value for foreground pixel (example value = 0)
- Standard deviation = Grey-values contained within one histogram bin (example value = 128)

A.5 The “Tools” menu

A.5.1 Object properties

Performs a region growing approach on 3D binary image stacks and extracts the single object information, e.g. such as volumes, center-of-mass coordinates, etc. to a text file. Each line represents a detected object. Each entry is delimited by *tab*-characters in the following format:

Particle number, voxel size X (see also A.2.12), voxel size Y, voxel size Z, unscaled geometrical center-of-mass (COM) X, unscaled geometrical COM Y, unscaled geometrical COM Z, scaled geometrical COM X, scaled geometrical COM Y, scaled geometrical COM Z, unscaled grey-value COM X, unscaled grey-value COM Y, unscaled grey-value COM Z, scaled grey-value COM X, scaled grey-value COM Y, scaled grey-value COM Z, total number of voxel, scaled volume, unscaled volume

A.5.2 Crop

Enables cropping of regions of interests in complete 4D images. The dialog displays a maximum intensity projection of the complete selected 4D experiment. The use of the cropping dialog can be found in Section A.1.5 on page 131.

A.5.3 Visualization 3D

Equivalent to menu entry “3D Visualization” (see Section A.6).

A.5.4 Tracking 4D

Performs 4D particle tracking velocimetry (PTV) on a combination of binary and grey-value based image stacks [164, 13]. The measurements always require a binarized image for measurements (see Section A.3.1). A grey-value experiment with equal image property parameters (see Section A.2.12) compared to the binary input experiment can be supplied for additional information extractions and refining of the tracking process. The output will be written to a text file containing the coordinates for all trajectories.

- Maximum distance = Maximum distance an object is allowed to move between two subsequent time intervals. The distance is supplied as real world values (μm) (see also Section A.2.12).
- Maximum Acceleration = Maximum acceleration value allowed for an object between two subsequent time intervals. The acceleration is supplied as real world values ($\frac{\mu m}{s^2}$) (see also Section A.2.12).
- Volume Change = Maximum volume change an object is allowed to show between two subsequent time intervals. The change in volume is supplied as real world values (μm^3) (see also Section A.2.12).
- Grey Value Change = Maximum volume change an object is allowed to show between two subsequent time intervals. The grey-value change is the

sum of all grey-values for voxel in the volume defined by the binary image stack.

- Maximum Volume = Maximum volume for an object to be considered valid for tracking. The maximum volume is supplied as real world values (μm^3) (see also Section A.2.12).
- Minimum Volume = Minimum volume for an object to be considered valid for tracking. The minimum volume is supplied as real world values (μm^3) (see also Section A.2.12).
- Maximum Grey Value = Maximum sum of grey-values for an object to be considered valid for tracking. The maximum grey-values sum can only be calculated correctly if a grey-value stack was provided.
- Minimum Grey Value = Minimum sum of grey-values for an object to be considered valid for tracking. The maximum grey-values sum can only be calculated correctly if a grey-value stack was provided.
- Correlation Threshold = Not used
- Distance Correlation Weight = Weighting option for the distance correlation parameters to fine tune the tracking process.
- Greyvalue Correlation Weight = Weighting option for the grey-value correlation parameters to fine tune the tracking process.
- Volume Correlation Weight = Weighting option for the volume correlation parameters to fine tune the tracking process.
- Grey value experiment = Sets the input grey-value experiment for additional information extraction. If no grey-value experiment is available the this entry must point to the entry of the binary experiment.
- Binary value experiment = Sets the input binary experiment for data extraction and tracking

A.5.5 Tracking 4D Visual

Performs an equivalent 4D PTV tracking approach as described in Section A.5.4 on the preceding page. The tracking results will be displayed with an isosurface reconstruction (see Section A.6) in the “Isosurface rendering” window (see Section A.1). The rendering allows interactive manual manipulation and correction of the trajectories in the “OpenGL canvas”. For this purpose single trajectories have to be selected in the “controls” section. A new trajectory point will be placed by pressing *w + left mouse* on an object. A placing of a trajectory point followed by time shift ($t+1$) will be achieved by pressing *t + left mouse*. A trajectory point will be removed by pressing *r + left mouse* on an object.

A.5.6 Load track 4D

Performs an equivalent 4D PTV tracking approach as described in Section A.5.4 on page 145. The tracking results will be displayed with a loaded isosurface reconstruction (see Section A.6) in the “Isosurface rendering” window (see Section A.1). After successful tracking a previously generated and saved isosurface has to be provided. The rendering allows interactive manual manipulation and correction of the trajectories in the “OpenGL canvas” (see Section A.5.5).

A.5.7 Enable / Disable manual tracking in image

Enables manual drawing functions on the “Canvas area”. These single points can be later tracked with the help of the automated PTV method (see Sections A.5.4 and A.5.5). By default the selection results are placed in the last channel, therefore this function needs to be used with great care to avoid any data loss. A good strategy before enabling the manual tracking feature is to copy the experiment channel (see Section A.1.3).

The following drawing modes and shortcuts are available:

- $q + \textit{left mouse}$ = draws a single spot in the last channel of an experiment
- $e + \textit{left mouse}$ = deletes last channel and draws a single spot; a second click adds another single spot in the last channel; a third click restarts the overall procedure
- $c + \textit{left mouse}$ = clears the last channel of an experiment
- $t + \textit{left mouse}$ = click on a single spot generates an empty channel in an experiment and moves the spot to this new channel
- $a + \textit{left mouse}$ = shifts the time slider $t - 1$
- $d + \textit{left mouse}$ = shifts the time slider $t + 1$
- $w + \textit{left mouse}$ = shifts the z-slider $z - 1$
- $s + \textit{left mouse}$ = shifts the z-slider $z + 1$

A.5.8 Registration 3D

Performs iterative rigid 4D edge-based registration on the selected experiment [160, 159]. The registration procedure always requires binarized outline images (see Sections A.3.1, A.3.20) to obtain meaningful results. The function is applied on all 3D image stacks. Before the menu entry is selected an experiment and one (and only one) channel containing the binarized object outlines has to be chosen.

- Threshold = Sets the global threshold (see Section A.3.1)

- Downsample = Defines the pixel resolution interval for point extraction extraction for each dimension. (The higher the value the less information is used, the faster the algorithm returns the results)
- Octree resolution = Defines the octree resolution (Default value = -1 = automatic selection)
- Match threshold = Sets the maximum standard error for overlapping objects (if this value is too small the algorithm will not find an appropriate solution and escapes after the number of iterative steps defined with “Max epochs”)
- Regularization threshold = Defines the discretization interval for the matching approximation
- Max epochs = Sets maximum iterative steps until the algorithm escapes without solution
- Sphere radius = Not used

A.5.9 Inter Channel measurements

Measures the distances of binary image objects within an experiment and a selected channel and saves the found distances in a text file. The 3D method is applied on the whole image stack. The measurements always require a binarized image for measurements (see Section A.3.1). The different distances will be measured from the center-of-masses of the detected objects. A grey-value experiment with equal image property parameters (see Section A.2.12) compared to the binary input experiment can be supplied for additional information extractions. However, it is not necessary for the final distance results and can be omitted.

- Minimum volume = Sets the lower range in voxel counts for an object to be included for calculation
- Maximum volume = Sets the upper range in voxel counts for an object to be included for calculation
- Minimum distance = Sets the lower distance limits in pixel for objects that are spatially located to each other (can not be > 0)
- Maximum distance = Sets the upper distance limits in pixel for objects that are spatially located to each other
- Grey-value experiment = Sets the input grey-value experiment for additional information extraction. If no grey-value experiment is available the this entry must point to the entry of the binary experiment.
- Binary experiment = Sets the input binary experiment for data extraction and distance measurement

- Measure distances in = Sets the channel with binary images for the distance measurements
- to channel (e.g. DAPI) = Not used

A.5.10 Border/Center pixel distances

Measures the distances of binary image objects within an experiment and in two selected channels and saves the found distances in a text file. The 3D method is applied on the whole image stack. The measurements always require a binarized image for measurements (see Section A.3.1). The different distances will be measured from the center-of-masses of objects in channel 1 to objects in channel 2. A grey-value experiment with equal image property parameters (see Section A.2.12) compared to the binary input experiment can be supplied for additional information extractions. However, it is not necessary for the final distance results and can be omitted.

- Minimum volume = Sets the lower range in voxel counts for an object to be included for calculation
- Maximum volume = Sets the upper range in voxel counts for an object to be included for calculation
- Minimum distance = Sets the lower distance limits in pixel for objects that are spatially located to each other (can not be > 0)
- Maximum distance = Sets the upper distance limits in pixel for objects that are spatially located to each other
- Grey-value experiment = Sets the input grey-value experiment for additional information extraction. If no grey-value experiment is available the this entry must point to the entry of the binary experiment.
- Binary experiment = Sets the input binary experiment for data extraction and distance measurement
- Measure distances in = Sets channel 1 with binary images for the distance measurements
- to channel (e.g. DAPI) = Sets channel 2 with binary images for the distance measurements

A.5.11 Border/Border pixel distances

Measures the shortest distances of the edges of binary image objects within an experiment and in two selected channels and saves the found distances in a text file. The 3D method is applied on the whole image stack. The measurements always require a binarized image for measurements (see Section A.3.1). The different distances will be measured from the edges of objects in channel 1 to objects in channel 2. Objects in channel 1 must located in the volumes

of objects in channel 2 (to measure the shortest border to border distances). A grey-value experiment with equal image property parameters (see Section A.2.12) compared to the binary input experiment can be supplied for additional information extractions. However, it is not necessary for the final distance results and can be omitted.

- Minimum volume = Sets the lower range in voxel counts for an object to be included for calculation
- Maximum volume = Sets the upper range in voxel counts for an object to be included for calculation
- Minimum distance = Sets the lower distance limits in pixel for objects that are spatially located to each other (can not be > 0)
- Maximum distance = Sets the upper distance limits in pixel for objects that are spatially located to each other
- Grey-value experiment = Sets the input grey-value experiment for additional information extraction. If no grey-value experiment is available the this entry must point to the entry of the binary experiment.
- Binary experiment = Sets the input binary experiment for data extraction and distance measurement
- Measure distances in = Sets channel 1 with binary images for the distance measurements
- to channel (e.g. DAPI) = Sets channel 2 with binary images for the distance measurements

A.5.12 Border/Border pixel localization distances

Measures the shortest distances of the center-of-masses of binary image objects within an experiment and in two selected channels and saves the found distances in a text file. The 3D method is applied on the whole image stack. The measurements always require a binarized image for measurements (see Section A.3.1). The different distances will be measured from the edges of objects in channel 1 to objects in channel 2. The relative localization of objects in channel 1 compared to objects in channel 2 are provided in the following way:

1. inside = Object from channel 1 lies completely within the volume of object in channel 2
2. periphery = Object from channel 1 touches the edges of object in channel 2
3. outside = Object from channel 1 does not correlate with the volume of object in channel 2 at all

A grey-value experiment with equal image property parameters (see Section A.2.12) compared to the binary input experiment can be supplied for additional information extractions. However, it is not necessary for the final distance `resmanual_section_ults` and can be omitted.

- Minimum volume = Sets the lower range in voxel counts for an object to be included for calculation
- Maximum volume = Sets the upper range in voxel counts for an object to be included for calculation
- Minimum distance = Sets the lower distance limits in pixel for objects that are spatially located to each other (can not be > 0)
- Maximum distance = Sets the upper distance limits in pixel for objects that are spatially located to each other
- Grey-value experiment = Sets the input grey-value experiment for additional information extraction. If no grey-value experiment is available the this entry must point to the entry of the binary experiment.
- Binary experiment = Sets the input binary experiment for data extraction and distance measurement
- Measure distances in = Sets channel 1 with binary images for the distance measurements
- to channel (e.g. DAPI) = Sets channel 2 with binary images for the distance measurements

A.5.13 Image calculator

Performs simple image calculations on two selected channels of an experiment. The result will be returned as an additional channel. The calculations will be performed on the whole experiment.

- Experiment = Sets the input experiment for channel arithmetic.
- Choose channel = Set the input channels for calculation and the arithmetic calculation (addition (+), subtraction (-)).

A.5.14 Convolve image with mask

Convolve a grey-value with a binary 2D image. Every pixel co-localizing with the segmented area remain unchanged, all other pixel are set to a grey-value = 0. The filter is a 2D implementation and is applied on each single image plane. The binary image must be a 2D image (see Sections A.3.26, A.3.27 for projections and A.3.1 for binarization).

- Minimum volume = Not used

- Maximum volume = Not used
- Minimum distance = Not used
- Maximum distance = Not used
- Grey-value experiment = Sets the input grey-value experiment which will be convolved with the 2D binary image
- Binary experiment = Sets the 2D binary image
- Measure distances in = Not used
- to channel (e.g. DAPI) = Not used

A.5.15 Crop with mask

Crops a grey-value into single 3D sub-stacks using a binary 2D image as a template. The bounding boxes of the detected 2D binary areas are used as cropping templates on the original grey-value stack. The filter is a 3D implementation and is applied on the whole image stack. The binary image must be a 2D image (see Sections A.3.26, A.3.27 for projections and A.3.1 for binarization).

- Minimum volume = Not used
- Maximum volume = Not used
- Minimum distance = Not used
- Maximum distance = Not used
- Grey-value experiment = Sets the input grey-value experiment which will be convolved with the 2D binary image
- Binary experiment = Sets the 2D binary image
- Measure distances in = Not used
- to channel (e.g. DAPI) = Not used

A.6 The “3D Visualization” menu

A.6.1 Extract new isosurface

Extracts optimized isosurfaces from binary objects with marching cubes algorithm [167] and Taubin smoothing [168, 169] and displays them in the “Isosurface rendering” window (see Section A.1). The extraction is performed on the whole 3D image stacks and the displaying is dependent on the voxel size values (see Section A.2.12 for viewing and setting the “image properties”). To return meaningful results the images need to be binarized.

- Binarize threshold = sets the global threshold (see Section A.3.1)

- Downscale X = Defines the pixel resolution interval for extraction (the higher the number the lower the extractable information). (example value = 1 (= kernel size of 3 in X direction))
- Downscale Y = Defines the pixel resolution interval for extraction (the higher the number the lower the extractable information). (example value = 1 (= kernel size of 3 in Y direction))
- Downscale Z = Defines the pixel resolution interval for extraction (the higher the number the lower the extractable information). (example value = 1 (= kernel size of 3 in Z direction))
- Smoothing iterations = number of Taubin smoothing iterations (the higher the number the smoother the resulting objects). (example value = 100)
- Smoothing lambda factor = regulates the weighted shift of extracted triangles for each iterative step (example value = 0.33)
- Smoothing mu factor = regulates the weighted shift of extracted triangles for each iterative step (example value = -0.34)

A.6.2 Load isosurface

Loads a previously saved isosurface file.

A.6.3 Import old isosurface

Loads old versions of isosurface files. Depreciated; use “Load isosurface” (see Section A.6.2).

A.7 The “Zoom” menu

Enables image zooming (original size - 7x zoom) of the “Canvas area” (see Section A.2.12). If the displayed images is large than the “Canvas area” scrollbars will provide help for navigation.

A.8 The “Specials” menu

This section covers highly experimental procedures for image manipulating and are a beta release from the developer version of Tikal. Wrong values can lead to a memory leaks, termination of the program and to undesired loss of data.

A.8.1 Combine Experiments

Combines two experiments in a sequential order (The second experiment will be added to the first which results in an increase of the time dimension). The two experiments must have the exact properties (see Section A.2.12), e.g. equal number of channels, equal number of z-slices.

- Experiment 1 = Original experiment
- Experiment 2 = Second experiment will be added to Experiment 1

A.8.2 Split Experiments

Splits an experiment in the time dimension. The break point has to be entered in the “Console window” (see Section A.1) followed by confirmation with the *Enter*-key on the keyboard.

A.8.3 Remove current time step

Removes the current time step of the selected experiment

A.8.4 Add empty layers at top and bottom of Experiment

Adds empty 2D images at the top and the bottom of single 3D stacks. The number of slices has to be entered in the “Console window” (see Section A.1) followed by confirmation with the *Enter*-key on the keyboard.

A.8.5 Remove top layers

Removes empty 2D images at the top of single 3D stacks. The number of slices to be removed has to be entered in the “Console window” (see Section A.1) followed by confirmation with the *Enter*-key on the keyboard.

A.8.6 Remove bottom layers

Removes empty 2D images at the bottom of single 3D stacks. The number of slices to be removed has to be entered in the “Console window” (see Section A.1) followed by confirmation with the *Enter*-key on the keyboard.

A.8.7 Split Objects

Uses a binary image channel to automatically split a complete 3D stack into smaller sub-stacks according to the found objects. This filter discards all objects smaller than 5'000 voxel and bigger than 500'000 voxel. The single sub-stacks will be added to the “Data set history” window. Only 3D stacks can be splitted.

A.8.8 Colormap test data

Generates a new experiment named “Colormap test” where different colormaps (see Section A.1) can be visualized and tested.

A.9 The “Help” menu

A.9.1 About Tikal

Displays the Tikal program version number, build number and build date.

Acknowledgments

At this point I want to thank Prof. Dr. Roland Eils for offering me the possibility to write my PhD thesis in a great and interdisciplinary work environment at a renowned German research institute, the DKFZ. During that time Prof. Eils assisted me to find my way through the various parts of my thesis, but always left enough room for my own decisions. As a mentor, doctoral adviser and friend I could learn a lot from Prof. Eils and refine my biological but also personal skills.

I also want to thank Dr. Edith Heard, Curie Institute, Paris for the fruitful cooperative project on the interesting and “hot-topic” of mammalian X-inactivation. Dr. Heard always had time for my questions and guided me to the successful finishing of this particular part of my work.

Special thanks go also to my second adviser Prof. Dr. Peter Lichter for his help in successful planning and performing my experiments during the time of the thesis.

I also want to acknowledge Dr. Harald Herrmann for the successful cooperation project. Dr. Herrmann always had time for fruitful but also critical discussions about biological questions.

In this context I also want to thank Dr. Michaela Reichenzeller for her constantly provided knowledge, thoughts and help in all possible situations.

Certainly without the support of my girlfriend Dr. Barbara Nau I would not have been able to pursue this work. She lifted me up from the depths of backstrokes, helped me navigate through the fields of all kinds of pitfalls and celebrated with me the highs of scientific returns.

Certainly I also want to thank my parents for their advises and their endeavors to lighten the load for all imaginable situations.

Many people advised and helped me during the time of my PhD thesis. Without their help I would not have been able to keep on moving and to complete my work. Therefore, I especially want to thank Dr. Benedikt Brors, Dr. Joël Beaudouin, Dr. Jan Ellenberg, Dr. Sabine Görisch, Dr. Patricia Le Baccon, Sébastien Huart, Julie Chaumeil, Macha Guggiari and certainly all members of the TBI group at the DKFZ, Heidelberg.

Bibliography

- [1] M. J. Hendzel, M. J. Kruhlak, N. A. MacLean, F. Boisvert, M. A. Lever, and D. P. Bazett-Jones. Compartmentalization of regulatory proteins in the cell nucleus. *J Steroid Biochem Mol Biol*, 76(1-5):9–21, Jan-Mar 2001. 0960-0760 Journal Article Review Review, Academic.
- [2] D. L. Spector. Nuclear domains. *J Cell Sci*, 114(Pt 16):2891–3, Aug 2001. 0021-9533 Journal Article.
- [3] I. F. Wang, N. M. Reddy, and C. K. Shen. Higher order arrangement of the eukaryotic nuclear bodies. *Proc Natl Acad Sci U S A*, 99(21):13583–8, Oct 15 2002. 0027-8424 Journal Article.
- [4] M. Dundr, U. Hoffmann-Rohrer, Q. Hu, I. Grummt, L. I. Rothblum, R. D. Phair, and T. Misteli. A kinetic framework for a mammalian RNA polymerase in vivo. *Science*, 298(5598):1623–6, Nov 22 2002. 1095-9203 Journal Article.
- [5] A. G. Matera. Nuclear bodies: multifaceted subdomains of the interchromatin space. *Trends Cell Biol*, 9(8):302–9, Aug 1999. 0962-8924 Journal Article Review Review, Tutorial.
- [6] X. Darzacq, B. E. Jady, C. Verheggen, A. M. Kiss, E. Bertrand, and T. Kiss. Cajal body-specific small nuclear RNAs: a novel class of 2'-O-methylation and pseudouridylation guide RNAs. *Embo J*, 21(11):2746–56, Jun 3 2002. 0261-4189 Journal Article.
- [7] M. Cioce and A. I. Lamond. Cajal bodies: A long history of discovery. *Annu Rev Cell Dev Biol*, Oct 7 2004. 1081-0706 Journal article.
- [8] M. Platani, I. Goldberg, J. R. Swedlow, and A. I. Lamond. In vivo analysis of Cajal body movement, separation, and joining in live human cells. *J Cell Biol*, 151(7):1561–74, Dec 25 2000. 0021-9525 Journal Article.
- [9] S. M. Gorisch, M. Wachsmuth, C. Ittrich, C. P. Bacher, K. Rippe, and P. Lichter. Nuclear body movement is determined by chromatin accessibility and dynamics. *Proc Natl Acad Sci U S A*, 101(36):13221–6, Sep 7 2004. 0027-8424 Journal Article.
- [10] M. Platani, I. Goldberg, A. I. Lamond, and J. R. Swedlow. Cajal body dynamics and association with chromatin are ATP-dependent. *Nat Cell Biol*, 4(7):502–8, Jul 2002. 1465-7392 Journal Article.

- [11] K. L. Borden. Pondering the promyelocytic leukemia protein (PML) puzzle: Possible functions for PML nuclear bodies. *Mol Cell Biol*, 22(15):5259–69, Aug 2002. 0270-7306 Journal Article Review Review, Tutorial.
- [12] G. G. Maul. Nuclear domain 10, the site of DNA virus transcription and replication. *Bioessays*, 20(8):660–7, Aug 1998. 0265-9247 Journal Article Review Review, Tutorial.
- [13] M. Muratani, D. Gerlich, S. M. Janicki, M. Gebhard, R. Eils, and D. L. Spector. Metabolic-energy-dependent movement of PML bodies within the mammalian cell nucleus. *Nat Cell Biol*, 4(2):106–10, Feb 2002. 1465-7392 Journal Article.
- [14] F. Almeida, R. Saffrich, W. Ansorge, and M. Carmo-Fonseca. Microinjection of anti-coilin antibodies affects the structure of coiled bodies. *J Cell Biol*, 142(4):899–912, Aug 24 1998. 0021-9525 Journal Article.
- [15] K. E. Tucker, M. T. Berciano, E. Y. Jacobs, D. F. LePage, K. B. Shpargel, J. J. Rossire, E. K. Chan, M. Lafarga, R. A. Conlon, and A. G. Matera. Residual Cajal bodies in coilin knockout mice fail to recruit Sm snRNPs and SMN, the spinal muscular atrophy gene product. *J Cell Biol*, 154(2):293–307, Jul 23 2001. 0021-9525 Journal Article.
- [16] R. Berezney, M. J. Mortillaro, H. Ma, X. Wei, and J. Samarabandu. The nuclear matrix: A structural milieu for genomic function. *Int Rev Cytol*, 162A:1–65, 1995. 0074-7696 Journal Article Review.
- [17] R. van Driel, D. G. Wansink, B. van Steensel, M. A. Grande, W. Schul, and L. de Jong. Nuclear domains and the nuclear matrix. *Int Rev Cytol*, 162A:151–89, 1995. 0074-7696 Journal Article Review.
- [18] M. A. Mancini, D. He, II Ouspenski, and B. R. Brinkley. Dynamic continuity of nuclear and mitotic matrix proteins in the cell cycle. *J Cell Biochem*, 62(2):158–64, Aug 1996. 0730-2312 Journal Article Review Review, Tutorial.
- [19] K. A. Mattern, B. M. Humbel, A. O. Muijsers, L. de Jong, and R. van Driel. hnRNP proteins and B23 are the major proteins of the internal nuclear matrix of HeLa s3 cells. *J Cell Biochem*, 62(2):275–89, Aug 1996. 0730-2312 Journal Article.
- [20] J. Nickerson. Experimental observations of a nuclear matrix. *J Cell Sci*, 114(Pt 3):463–74, Feb 2001. 0021-9533 Journal Article Review.
- [21] H. Romig, F. O. Fackelmayer, A. Renz, U. Ramsperger, and A. Richter. Characterization of SAF-A, a novel nuclear DNA binding protein from HeLa cells with high affinity for nuclear matrix/scaffold attachment DNA elements. *Embo J*, 11(9):3431–40, Sep 1992. 0261-4189 Journal Article.

-
- [22] R. Helbig and F. O. Fackelmayer. Scaffold attachment factor A (SAF-A) is concentrated in inactive X-chromosome territories through its RGG domain. *Chromosoma*, 112(4):173–82, Dec 2003. 0009-5915 Journal Article.
- [23] F. O. Fackelmayer. A stable proteinaceous structure in the territory of inactive X-chromosomes. *J Biol Chem*, 280(3):1720–3, Jan 21 2005. 0021-9258 Journal Article.
- [24] J. H. Martens, M. Verlaan, E. Kalkhoven, J. C. Dorsman, and A. Zantema. Scaffold/matrix attachment region elements interact with a p300-scaffold attachment factor A complex and are bound by acetylated nucleosomes. *Mol Cell Biol*, 22(8):2598–606, Apr 2002. 0270-7306 Journal Article.
- [25] W. H. Stratling and F. Yu. Origin and roles of nuclear matrix proteins. Specific functions of the MAR-binding protein MeCP2/ARBP. *Crit Rev Eukaryot Gene Expr*, 9(3-4):311–8, 1999. 1045-4403 Journal Article Review Review, Tutorial.
- [26] O. Nayler, W. Stratling, J. P. Bourquin, I. Stagljar, L. Lindemann, H. Jasper, A. M. Hartmann, F. O. Fackelmayer, A. Ullrich, and S. Stamm. SAF-B protein couples transcription and pre-mRNA splicing to SAR/MAR elements. *Nucleic Acids Res*, 26(15):3542–9, Aug 1 1998. 0305-1048 Journal Article.
- [27] S. Cai, H. J. Han, and T. Kohwi-Shigematsu. Tissue-specific nuclear architecture and gene expression regulated by SATB1. *Nat Genet*, 34(1):42–51, May 2003. 1061-4036 Journal Article.
- [28] J. M. Woynarowski. AT islands - their nature and potential for anticancer strategies. *Curr Cancer Drug Targets*, 4(2):219–34, Mar 2004. 1568-0096 Journal Article Review.
- [29] M. L. Barr and D. H. Carr. Correlations between sex-chromatin and sex-chromosomes. *Acta Cytol*, 6:34–45, Jan-Feb 1962. 0001-5547 Journal Article.
- [30] M.L. Baar and E.G. Bertram. A morphological distinction between neurones of the male and female, and the behavior of the nucleolar satellite during accelerated nucleoprotein synthesis. *Nature*, 163:676, 1949.
- [31] P. Lichter, T. Cremer, J. Borden, L. Manuelidis, and D. C. Ward. Delineation of individual human chromosomes in metaphase and interphase cells by in situ suppression hybridization using recombinant DNA libraries. *Hum Genet*, 80(3):224–34, Nov 1988. 0340-6717 Journal Article.
- [32] L. Manuelidis and J. Borden. Reproducible compartmentalization of individual chromosome domains in human CNS cells revealed by in situ hybridization and three-dimensional reconstruction. *Chromosoma*, 96(6):397–410, 1988. 0009-5915 Journal Article.

- [33] R. G. Nagele, T. Freeman, L. McMorrow, Z. Thomson, K. Kitson-Wind, and H. Lee. Chromosomes exhibit preferential positioning in nuclei of quiescent human cells. *J Cell Sci*, 112 (Pt 4):525–35, Feb 1999. 0021-9533 Journal Article.
- [34] M. Cremer, J. von Hase, T. Volm, A. Brero, G. Kreth, J. Walter, C. Fischer, I. Solovei, C. Cremer, and T. Cremer. Non-random radial higher-order chromatin arrangements in nuclei of diploid human cells. *Chromosome Res*, 9(7):541–67, 2001. 0967-3849 Journal Article.
- [35] F. A. Habermann, M. Cremer, J. Walter, G. Kreth, J. von Hase, K. Bauer, J. Wienberg, C. Cremer, T. Cremer, and I. Solovei. Arrangements of macro- and microchromosomes in chicken cells. *Chromosome Res*, 9(7):569–84, 2001. 0967-3849 Journal Article.
- [36] A. E. Visser, F. Jaunin, S. Fakan, and J. A. Aten. High resolution analysis of interphase chromosome domains. *J Cell Sci*, 113 (Pt 14):2585–93, Jul 2000. 0021-9533 Journal Article.
- [37] T. Cremer and C. Cremer. Chromosome territories, nuclear architecture and gene regulation in mammalian cells. *Nat Rev Genet*, 2(4):292–301, Apr 2001. 1471-0056 Journal Article Review Review, Tutorial.
- [38] J. A. Croft, J. M. Bridger, S. Boyle, P. Perry, P. Teague, and W. A. Bickmore. Differences in the localization and morphology of chromosomes in the human nucleus. *J Cell Biol*, 145(6):1119–31, Jun 14 1999. 0021-9525 Journal Article.
- [39] H. Tanabe, S. Muller, M. Neusser, J. von Hase, E. Calcagno, M. Cremer, I. Solovei, C. Cremer, and T. Cremer. Evolutionary conservation of chromosome territory arrangements in cell nuclei from higher primates. *Proc Natl Acad Sci U S A*, 99(7):4424–9, Apr 2 2002. 0027-8424 Journal Article.
- [40] M. Nogami, O. Nogami, K. Kagotani, M. Okumura, H. Taguchi, T. Ike-mura, and K. Okumura. Intranuclear arrangement of human chromosome 12 correlates to large-scale replication domains. *Chromosoma*, 108(8):514–22, Mar 2000. 0009-5915 Journal Article.
- [41] C. Francastel, D. Schubeler, D. I. Martin, and M. Groudine. Nuclear compartmentalization and gene activity. *Nat Rev Mol Cell Biol*, 1(2):137–43, Nov 2000. 1471-0072 Journal Article Review.
- [42] K. E. Brown, S. S. Guest, S. T. Smale, K. Hahm, M. Merkenschlager, and A. G. FISHer. Association of transcriptionally silent genes with Ikaros complexes at centromeric heterochromatin. *Cell*, 91(6):845–54, Dec 12 1997. 0092-8674 Journal Article.
- [43] D. Zink, A. H. Fischer, and J. A. Nickerson. Nuclear structure in cancer cells. *Nat Rev Cancer*, 4(9):677–87, Sep 2004. 1474-175x Journal Article Review Review, Tutorial.

-
- [44] A. Bolzer, G. Kreth, I. Solovei, D. Koehler, K. Saracoglu, C. Fauth, S. Muller, R. Eils, C. Cremer, M. R. Speicher, and T. Cremer. Three-dimensional maps of all chromosomes in human male fibroblast nuclei and prometaphase rosettes. *PLoS Biol*, 3(5):e157, May 2005. 1545-7885 Journal Article.
- [45] J. M. Bridger, S. Boyle, I. R. Kill, and W. A. Bickmore. Re-modelling of nuclear architecture in quiescent and senescent human fibroblasts. *Curr Biol*, 10(3):149–52, Feb 10 2000. 0960-9822 Journal Article.
- [46] M. Ferguson and D. C. Ward. Cell cycle dependent chromosomal movement in pre-mitotic human T-lymphocyte nuclei. *Chromosoma*, 101(9):557–565, Aug 1992.
- [47] D. Gerlich and J. Ellenberg. Dynamics of chromosome positioning during the cell cycle. *Curr Opin Cell Biol*, 15(6):664–71, Dec 2003. 0955-0674 Journal Article.
- [48] E. M. Manders, A. E. Visser, A. Koppen, W. C. de Leeuw, R. van Liere, G. J. Brakenhoff, and R. van Driel. Four-dimensional imaging of chromatin dynamics during the assembly of the interphase nucleus. *Chromosome Res*, 11(5):537–47, 2003. 0967-3849 Journal Article.
- [49] N. L. Mahy, P. E. Perry, and W. A. Bickmore. Gene density and transcription influence the localization of chromatin outside of chromosome territories detectable by FISH. *J Cell Biol*, 159(5):753–63, Dec 9 2002. 0021-9525 Journal Article.
- [50] N. L. Mahy, P. E. Perry, S. Gilchrist, R. A. Baldock, and W. A. Bickmore. Spatial organization of active and inactive genes and noncoding DNA within chromosome territories. *J Cell Biol*, 157(4):579–89, May 13 2002. 0021-9525 Journal Article.
- [51] E. V. Volpi, E. Chevret, T. Jones, R. Vatcheva, J. Williamson, S. Beck, R. D. Campbell, M. Goldsworthy, S. H. Powis, J. Ragoussis, J. Trowsdale, and D. Sheer. Large-scale chromatin organization of the major histocompatibility complex and other regions of human chromosome 6 and its response to interferon in interphase nuclei. *J Cell Sci*, 113 (Pt 9):1565–76, May 2000. 0021-9533 Journal Article.
- [52] Markus O Scheuermann, Jian Tajbakhsh, Anette Kurz, Kaan Saracoglu, Roland Eils, and Peter Lichter. Topology of genes and nontranscribed sequences in human interphase nuclei. *Exp Cell Res*, 301(2):266–279, Dec 2004.
- [53] N. Gilbert, S. Boyle, H. Fiegler, K. Woodfine, N. P. Carter, and W. A. Bickmore. Chromatin architecture of the human genome: gene-rich domains are enriched in open chromatin fibers. *Cell*, 118(5):555–66, Sep 3 2004. 0092-8674 Journal Article.

- [54] J. M. Bridger, H. Herrmann, C. Munkel, and P. Lichter. Identification of an interchromosomal compartment by polymerization of nuclear-targeted vimentin. *J Cell Sci*, 111 (Pt 9):1241–53, May 1998. 0021-9533 Journal Article.
- [55] H. Caron, B. van Schaik, M. van der Mee, F. Baas, G. Riggins, P. van Sluis, M. C. Hermus, R. van Asperen, K. Boon, P. A. Voute, S. Heisterkamp, A. van Kampen, and R. Versteeg. The human transcriptome map: Clustering of highly expressed genes in chromosomal domains. *Science*, 291(5507):1289–92, Feb 16 2001. 0036-8075 Journal Article.
- [56] Jordi Surrallés, María J Ramírez, Ricard Marcos, Adayapalam T Natarajan, and Leon H F Mullenders. Clusters of transcription-coupled repair in the human genome. *Proc Natl Acad Sci U S A*, 99(16):10571–10574, Aug 2002.
- [57] R. Versteeg, B. D. van Schaik, M. F. van Batenburg, M. Roos, R. Monajemi, H. Caron, H. J. Bussemaker, and A. H. van Kampen. The human transcriptome map reveals extremes in gene density, intron length, GC content, and repeat pattern for domains of highly and weakly expressed genes. *Genome Res*, 13(9):1998–2004, Sep 2003. 1088-9051 Journal Article.
- [58] Markus O Scheuermann, Andrea E Murmann, Karsten Richter, Sabine M Görisch, Harald Herrmann, and Peter Lichter. Characterization of nuclear compartments identified by ectopic markers in mammalian cells with distinctly different karyotype. *Chromosoma*, 114(1):39–53, May 2005.
- [59] T. Tumbar, G. Sudlow, and A. S. Belmont. Large-scale chromatin unfolding and remodeling induced by VP16 acidic activation domain. *J Cell Biol*, 145(7):1341–54, Jun 28 1999. 0021-9525 Journal Article.
- [60] M. F. Lyon. Gene action in the X-chromosome of the mouse (*Mus musculus* L.). *Nature*, 190:372–3, Apr 22 1961. 1476-4687 Journal Article.
- [61] M. C. Simmler, B. M. Cattanaach, C. Rasberry, C. Rougeulle, and P. Avner. Mapping the murine Xce locus with (CA)_n repeats. *Mamm Genome*, 4(9):523–530, Sep 1993.
- [62] R. M. Plenge, B. D. Hendrich, C. Schwartz, J. F. Arena, A. Naumova, C. Sapienza, R. M. Winter, and H. F. Willard. A promoter mutation in the XIST gene in two unrelated families with skewed X-chromosome inactivation. *Nat Genet*, 17(3):353–356, Nov 1997.
- [63] E. Debrand, C. Chureau, D. Arnaud, P. Avner, and E. Heard. Functional analysis of the DXPas34 locus, a 3' regulator of Xist expression. *Mol Cell Biol*, 19(12):8513–25, Dec 1999. 0270-7306 Journal Article.
- [64] J. T. Lee and N. Lu. Targeted mutagenesis of Tsix leads to nonrandom X-inactivation. *Cell*, 99(1):47–57, Oct 1999.

-
- [65] G. D. Paterno and M. W. McBurney. X-chromosome inactivation during induced differentiation of a female mouse embryonal carcinoma cell line. *J Cell Sci*, 75:149–63, Apr 1985. 0021-9533 Journal Article.
- [66] E. Heard. Recent advances in X-chromosome inactivation. *Curr Opin Cell Biol*, 16(3):247–55, Jun 2004. 0955-0674 Journal Article Review Review, Tutorial.
- [67] P. Avner and E. Heard. X-chromosome inactivation: Counting, choice and initiation. *Nat Rev Genet*, 2(1):59–67, Jan 2001. 1471-0056 Journal Article Review.
- [68] G. Borsani, R. Tonlorenzi, M. C. Simmler, L. Dandolo, D. Arnaud, V. Capra, M. Grompe, A. Pizzuti, D. Muzny, C. Lawrence, and et al. Characterization of a murine gene expressed from the inactive X-chromosome. *Nature*, 351(6324):325–9, May 23 1991. 0028-0836 Journal Article.
- [69] N. Brockdorff, A. Ashworth, G. F. Kay, P. Cooper, S. Smith, V. M. McCabe, D. P. Norris, G. D. Penny, D. Patel, and S. Rastan. Conservation of position and exclusive expression of mouse Xist from the inactive X-chromosome. *Nature*, 351(6324):329–31, May 23 1991. 0028-0836 Journal Article.
- [70] N. Brockdorff, A. Ashworth, G. F. Kay, V. M. McCabe, D. P. Norris, P. J. Cooper, S. Swift, and S. Rastan. The product of the mouse Xist gene is a 15 kb inactive X-specific transcript containing no conserved ORF and located in the nucleus. *Cell*, 71(3):515–26, Oct 30 1992. 0092-8674 Journal Article.
- [71] Y. Marahrens, J. Loring, and R. Jaenisch. Role of the Xist gene in X-chromosome choosing. *Cell*, 92(5):657–64, Mar 6 1998. 0092-8674 Journal Article.
- [72] Y. Marahrens, B. Panning, J. Dausman, W. Strauss, and R. Jaenisch. Xist-deficient mice are defective in dosage compensation but not spermatogenesis. *Genes Dev*, 11(2):156–66, Jan 15 1997. 0890-9369 Journal Article.
- [73] G. D. Penny, G. F. Kay, S. A. Sheardown, S. Rastan, and N. Brockdorff. Requirement for Xist in X-chromosome inactivation. *Nature*, 379(6561):131–7, Jan 11 1996. 0028-0836 Journal Article.
- [74] C. J. Brown and H. F. Willard. The human X-inactivation centre is not required for maintenance of X-chromosome inactivation. *Nature*, 368(6467):154–6, Mar 10 1994. 0028-0836 Journal Article.
- [75] A. Wutz and R. Jaenisch. A shift from reversible to irreversible X-inactivation is triggered during ES cell differentiation. *Mol Cell*, 5(4):695–705, Apr 2000. 1097-2765 Journal Article.

- [76] E. Heard, J. Chaumeil, O. Masui, and I. Okamoto. Mammalian X-chromosome inactivation: An epigenetics paradigm. *Cold Spring Harb Symp Quant Biol*, LXIX, 2004.
- [77] C. J. Brown, B. D. Hendrich, J. L. Rupert, R. G. Lafreniere, Y. Xing, J. Lawrence, and H. F. Willard. The human XIST gene: analysis of a 17 kb inactive X-specific RNA that contains conserved repeats and is highly localized within the nucleus. *Cell*, 71(3):527–42, Oct 30 1992. 0092-8674 Journal Article.
- [78] C. M. Clemson and J. B. Lawrence. Multifunctional compartments in the nucleus: Insights from DNA and RNA localization. *J Cell Biochem*, 62(2):181–90, Aug 1996. 0730-2312 Journal Article Review Review, Tutorial.
- [79] A. Calapez, H. M. Pereira, A. Calado, J. Braga, J. Rino, C. Carvalho, J. P. Tavanetz, E. Wahle, A. C. Rosa, and M. Carmo-Fonseca. The intranuclear mobility of messenger RNA binding proteins is ATP dependent and temperature sensitive. *J Cell Biol*, 159(5):795–805, Dec 9 2002. 0021-9525 Journal Article.
- [80] Y. Shav-Tal, X. Darzacq, S. M. Shenoy, D. Fusco, S. M. Janicki, D. L. Spector, and R. H. Singer. Dynamics of single mRNPs in nuclei of living cells. *Science*, 304(5678):1797–800, Jun 18 2004. 1095-9203 Journal Article.
- [81] C. M. Clemson, J. A. McNeil, H. F. Willard, and J. B. Lawrence. XIST RNA paints the inactive X-chromosome at interphase: Evidence for a novel RNA involved in nuclear/chromosome structure. *J Cell Biol*, 132(3):259–75, Feb 1996. 0021-9525 Journal Article.
- [82] B. Panning and R. Jaenisch. DNA hypomethylation can activate Xist expression and silence X-linked genes. *Genes Dev*, 10(16):1991–2002, Aug 15 1996. 0890-9369 Journal Article.
- [83] B. Panning, J. Dausman, and R. Jaenisch. X-chromosome inactivation is mediated by Xist RNA stabilization. *Cell*, 90(5):907–16, Sep 5 1997. 0092-8674 Journal Article.
- [84] G. F. Kay, G. D. Penny, D. Patel, A. Ashworth, N. Brockdorff, and S. Rastan. Expression of Xist during mouse development suggests a role in the initiation of X-chromosome inactivation. *Cell*, 72(2):171–82, Jan 29 1993. 0092-8674 Journal Article.
- [85] S. A. Sheardown, S. M. Duthie, C. M. Johnston, A. E. Newall, E. J. Formstone, R. M. Arkell, T. B. Nesterova, G. C. Alghisi, S. Rastan, and N. Brockdorff. Stabilization of Xist RNA mediates initiation of X-chromosome inactivation. *Cell*, 91(1):99–107, Oct 3 1997. 0092-8674 Journal Article.

-
- [86] L. B. Herzing, J. T. Romer, J. M. Horn, and A. Ashworth. Xist has properties of the X-chromosome inactivation centre. *Nature*, 386(6622):272–5, Mar 20 1997. 0028-0836 Journal Article.
- [87] J. T. Lee, W. M. Strauss, J. A. Dausman, and R. Jaenisch. A 450 kb transgene displays properties of the mammalian X-inactivation center. *Cell*, 86(1):83–94, Jul 12 1996. 0092-8674 Journal Article.
- [88] E. Heard, F. Mongelard, D. Arnaud, and P. Avner. Xist yeast artificial chromosome transgenes function as X-inactivation centers only in multi-copy arrays and not as single copies. *Mol Cell Biol*, 19(4):3156–66, Apr 1999. 0270-7306 Journal Article.
- [89] A. D. Riggs, J. Singer-Sam, and D. H. Keith. Methylation of the PGK promoter region and an enhancer way-station model for X-chromosome inactivation. *Prog Clin Biol Res*, 198:211–22, 1985. 0361-7742 Journal Article.
- [90] F. Ye and E. R. Signer. RIGS (repeat-induced gene silencing) in Arabidopsis is transcriptional and alters chromatin configuration. *Proc Natl Acad Sci U S A*, 93(20):10881–6, Oct 1 1996. 0027-8424 Journal Article.
- [91] M. F. Lyon. X-chromosome inactivation: A repeat hypothesis. *Cytogenet Cell Genet*, 80(1-4):133–7, 1998. 0301-0171 Journal Article Review Review, Tutorial.
- [92] C. Morey, P. Navarro, E. Debrand, P. Avner, C. Rougeulle, and P. Clerc. The region 3' to Xist mediates X-chromosome counting and h3 Lys-4 dimethylation within the Xist gene. *Embo J*, 23(3):594–604, Feb 11 2004. 0261-4189 Journal Article.
- [93] D. E. Comings. The rationale for an ordered arrangement of chromatin in the interphase nucleus. *Am J Hum Genet*, 20(5):440–60, Sep 1968. 0002-9297 Journal Article.
- [94] J. M. LaSalle, R. J. Ritchie, H. Glatt, and M. Lalande. Clonal heterogeneity at allelic methylation sites diagnostic for Prader-Willi and Angelman syndromes. *Proc Natl Acad Sci U S A*, 95(4):1675–80, Feb 17 1998. 0027-8424 Journal Article.
- [95] P. Clerc and P. Avner. Multiple elements within the Xic regulate random X-inactivation in mice. *Semin Cell Dev Biol*, 14(1):85–92, Feb 2003. 1084-9521 Journal Article Review Review, Tutorial.
- [96] J. T. Lee, L. S. Davidow, and D. Warshawsky. Tsix, a gene antisense to Xist at the X-inactivation centre. *Nat Genet*, 21(4):400–4, Apr 1999. 1061-4036 Journal Article.
- [97] N. Mise, Y. Goto, N. Nakajima, and N. Takagi. Molecular cloning of antisense transcripts of the mouse Xist gene. *Biochem Biophys Res Commun*, 258(3):537–41, May 19 1999. 0006-291x Journal Article.

- [98] J. T. Lee, N. Lu, and Y. Han. Genetic analysis of the mouse X-inactivation center defines an 80-kb multifunction domain. *Proc Natl Acad Sci U S A*, 96(7):3836–41, Mar 30 1999. 0027-8424 Journal Article.
- [99] N. Stavropoulos, N. Lu, and J. T. Lee. A functional role for Tsix transcription in blocking Xist RNA accumulation but not in X-chromosome choice. *Proc Natl Acad Sci U S A*, 98(18):10232–7, Aug 28 2001. 0027-8424 Journal Article.
- [100] Jeannie T Lee. Regulation of X-chromosome counting by Tsix and Xite sequences. *Science*, 309(5735):768–771, Jul 2005.
- [101] Y. Ogawa and J. T. Lee. Xite, X-inactivation intergenic transcription elements that regulate the probability of choice. *Mol Cell*, 11(3):731–43, Mar 2003. 1097-2765 Journal Article.
- [102] C. Chureau, M. Prissette, A. Bourdet, V. Barbe, L. Cattolico, L. Jones, A. Eggen, P. Avner, and L. Duret. Comparative sequence analysis of the X-inactivation center region in mouse, human, and bovine. *Genome Res*, 12(6):894–908, Jun 2002. 1088-9051 Journal Article.
- [103] C. M. Johnston, A. E. Newall, N. Brockdorff, and T. B. Nesterova. Enox, a novel gene that maps 10 kb upstream of Xist and partially escapes X-inactivation. *Genomics*, 80(2):236–44, Aug 2002. 0888-7543 Journal Article.
- [104] S. Rastan. Non-random X-chromosome inactivation in mouse X-autosome translocation embryos—location of the inactivation centre. *J Embryol Exp Morphol*, 78:1–22, Dec 1983. 0022-0752 Journal Article.
- [105] J. T. Lee and N. Lu. Targeted mutagenesis of Tsix leads to nonrandom X-inactivation. *Cell*, 99(1):47–57, Oct 1999.
- [106] K. A. Rack, J. Chelly, R. J. Gibbons, S. Rider, D. Benjamin, R. G. Lafreniere, D. Oscier, R. W. Hendriks, I. W. Craig, H. F. Willard, and et al. Absence of the XIST gene from late-replicating isodicentric X-chromosomes in leukaemia. *Hum Mol Genet*, 3(7):1053–9, Jul 1994. 0964-6906 Journal Article.
- [107] T. Jenuwein and C. D. Allis. Translating the histone code. *Science*, 293(5532):1074–80, Aug 10 2001. 0036-8075 Journal Article Review Review, Tutorial.
- [108] Y. Zhang and D. Reinberg. Transcription regulation by histone methylation: Interplay between different covalent modifications of the core histone tails. *Genes Dev*, 15(18):2343–60, Sep 15 2001. 0890-9369 Journal Article Review.
- [109] A. M. Keohane, P. O’Neill L, N. D. Belyaev, J. S. Lavender, and B. M. Turner. X-inactivation and histone H4 acetylation in embryonic stem cells. *Dev Biol*, 180(2):618–30, Dec 15 1996. 0012-1606 Journal Article.

-
- [110] E. Heard, C. Rougeulle, D. Arnaud, P. Avner, C. D. Allis, and D. L. Spector. Methylation of histone H3 at Lys-9 is an early mark on the X-chromosome during X-inactivation. *Cell*, 107(6):727–38, Dec 14 2001. 0092-8674 Journal Article.
- [111] J. Chaumeil, I. Okamoto, M. Guggiari, and E. Heard. Integrated kinetics of X-chromosome inactivation in differentiating embryonic stem cells. *Cytogenet Genome Res*, 99(1-4):75–84, 2002. 1424-859x Journal Article.
- [112] C. Rougeulle, J. Chaumeil, K. Sarma, C. D. Allis, D. Reinberg, P. Avner, and E. Heard. Differential histone h3 Lys-9 and Lys-27 methylation profiles on the X-chromosome. *Mol Cell Biol*, 24(12):5475–84, Jun 2004. 0270-7306 Journal Article.
- [113] B. A. Boggs, B. Connors, R. E. Sobel, A. C. Chinault, and C. D. Allis. Reduced levels of histone H3 acetylation on the inactive X-chromosome in human females. *Chromosoma*, 105(5):303–9, Dec 1996. 0009-5915 Journal Article.
- [114] A. Kuzmichev, K. Nishioka, H. Erdjument-Bromage, P. Tempst, and D. Reinberg. Histone methyltransferase activity associated with a human multiprotein complex containing the enhancer of Zeste protein. *Genes Dev*, 16(22):2893–905, Nov 15 2002. 0890-9369 Journal Article.
- [115] A. Kohlmaier, F. Savarese, M. Lachner, J. Martens, T. Jenuwein, and A. Wutz. A chromosomal memory triggered by Xist regulates histone methylation in X-inactivation. *PLoS Biol*, 2(7):E171, Jul 2004. 1545-7885 Journal Article.
- [116] K. Plath, J. Fang, S. K. Mlynarczyk-Evans, R. Cao, K. A. Worringer, H. Wang, C. C. de la Cruz, A. P. Otte, B. Panning, and Y. Zhang. Role of histone H3 lysine 27 methylation in X-inactivation. *Science*, 300(5616):131–5, Apr 4 2003. 1095-9203 Journal Article.
- [117] I. Okamoto, A. P. Otte, C. D. Allis, D. Reinberg, and E. Heard. Epigenetic dynamics of imprinted X-inactivation during early mouse development. *Science*, 303(5658):644–9, Jan 30 2004. 1095-9203 Journal Article.
- [118] R. Cao and Y. Zhang. The functions of E(Z)/EZH2-mediated methylation of lysine 27 in histone H3. *Curr Opin Genet Dev*, 14(2):155–64, Apr 2004. 0959-437x Journal Article Review Review, Tutorial.
- [119] K. Tajul-Arifin, R. Teasdale, T. Ravasi, D. A. Hume, and J. S. Mattick. Identification and analysis of chromodomain-containing proteins encoded in the mouse transcriptome. *Genome Res*, 13(6B):1416–29, Jun 2003. 1088-9051 Journal Article.
- [120] B. J. Richardson, A. B. Czuppon, and G. B. Sharman. Inheritance of glucose-6-phosphate dehydrogenase variation in kangaroos. *Nat New Biol*, 230(13):154–5, Mar 31 1971. 0090-0028 Journal Article.

- [121] D. W. Cooper, J. L. VandeBerg, G. B. Sharman, and W. E. Poole. Phosphoglycerate kinase polymorphism in kangaroos provides further evidence for paternal X-inactivation. *Nat New Biol*, 230(13):155–7, Mar 31 1971. 0090-0028 Journal Article.
- [122] G. B. Sharman. Late DNA replication in the paternally derived X-chromosome of female kangaroos. *Nature*, 230(5291):231–2, Mar 26 1971. 0028-0836 Journal Article.
- [123] N. Takagi and M. Sasaki. Preferential inactivation of the paternally derived X-chromosome in the extraembryonic membranes of the mouse. *Nature*, 256(5519):640–2, Aug 21 1975. 0028-0836 Journal Article.
- [124] J. D. West, W. I. Frels, V. M. Chapman, and V. E. Papaioannou. Preferential expression of the maternally derived X-chromosome in the mouse yolk sac. *Cell*, 12(4):873–82, Dec 1977. 0092-8674 Journal Article.
- [125] L. Selwood. Mechanisms for pattern formation leading to axis formation and lineage allocation in mammals: a marsupial perspective. *Reproduction*, 121(5):677–83, May 2001. 1470-1626 Journal Article Review Review, Tutorial.
- [126] C. M. Watson, R. L. Hughes, D. W. Cooper, R. T. Gemmell, D. A. Loebel, and P. G. Johnston. Sexual development in marsupials: genetic characterization of bandicoot siblings with scrotal and testicular maldevelopment. *Mol Reprod Dev*, 57(2):127–34, Oct 2000. 1040-452x Journal Article.
- [127] J. A. Graves and M. Westerman. Marsupial genetics and genomics. *Trends Genet*, 18(10):517–21, Oct 2002. 0168-9525 Journal Article Review Review, Tutorial.
- [128] R. Ohlsson, A. Paldi, and J. A. Graves. Did genomic imprinting and X-chromosome inactivation arise from stochastic expression? *Trends Genet*, 17(3):136–41, Mar 2001. 0168-9525 Journal Article.
- [129] R. V. Jamieson, S. X. Zhou, S. S. Tan, and P. P. Tam. X-chromosome inactivation during the development of the male urogenital ridge of the mouse. *Int J Dev Biol*, 41(1):49–55, Feb 1997. 0214-6282 Journal Article.
- [130] E. Lifschytz and D. L. Lindsley. The role of X-chromosome inactivation during spermatogenesis (Drosophila-allocycly-chromosome evolution-male sterility-dosage compensation). *Proc Natl Acad Sci U S A*, 69(1):182–6, Jan 1972. 0027-8424 Journal Article Review.
- [131] E. Jablonka and M. J. Lamb. Meiotic pairing constraints and the activity of sex-chromosomes. *J Theor Biol*, 133(1):23–36, Jul 8 1988. 0022-5193 Journal Article.
- [132] K. D. Huynh and J. T. Lee. Inheritance of a pre-inactivated paternal X-chromosome in early mouse embryos. *Nature*, 426(6968):857–62, Dec 18 2003. 1476-4687 Journal Article.

-
- [133] C. G. Spilianakis, M. D. Lalioti, T. Town, G. R. Lee, and R. A. Flavell. Interchromosomal associations between alternatively expressed loci. *Nature*, 435(7042):637–45, Jun 2 2005. 1476-4687 Journal Article.
- [134] M. Sonka, V. Hlavac, and R. Boyle. *Image Processing, Analysis, and Machine Vision*. Brooks/Cole Publishing Company, 2nd edition edition, 1999.
- [135] R. Eils and C. Athale. Computational imaging in cell biology. *J Cell Biol*, 161(3):477–81, May 12 2003. 0021-9525 Journal Article Review Review, Tutorial.
- [136] A. Watt and M. Watt. *Advanced Animation and Rendering Techniques: Theory and Practice*. Addison-Wesley, 1992.
- [137] J. Beaudouin. *Dynamique structurale et moléculaire des protéines nucléaires révélée par microscopie de fluorescence*. Phd thesis, Université Paris 7 - Denis Diderot, June 2003.
- [138] E. R. Davies. *Machine Vision: Theory, Algorithms, Practicalities*. Academic Press, 1997.
- [139] T. Lehmann and E. Meyer zu Bexten. *Handbuch der Medizinischen Informatik*. Hanser, 2002.
- [140] B. Jähne, H. Haußecker, and P. Geißler. *Handbook on Computer Vision and Applications*, volume 2nd volume. Academic Press, 1999.
- [141] J. Weickert. *Handbook on Computer Vision and Applications*, volume Volume 2: Signal Processing and Pattern Recognition, chapter Nonlinear diffusion filtering, pages 423–450. Academic Press, 1999.
- [142] I.N. Bankman. *Handbook of medical imaging: Processing and analysis*. Academic Press, 2000.
- [143] P. Perona and J. Malik. Scale-space and edge detection using anisotropic diffusion. *IEEE Transactions on Pattern Analysis Machine Intelligence*, 12:629–639, 1990.
- [144] S. Grossberg. Neural dynamics of brightness perception: Features, boundaries, diffusion, and resonance. *Perception and Psychophysics*, 36(5):428–456, 1984.
- [145] C. P. Bacher, M. Reichenzeller, C. Athale, H. Herrmann, and R. Eils. 4-D single particle tracking of synthetic and proteinaceous microspheres reveals preferential movement of nuclear particles along chromatin - poor tracks. *BMC Cell Biol*, 5(1):45, Nov 23 2004. 1471-2121 Journal Article.
- [146] D. Gerlich, J. Beaudouin, M. Gebhard, J. Ellenberg, and R. Eils. Four-dimensional imaging and quantitative reconstruction to analyse complex spatiotemporal processes in live cells. *Nat Cell Biol*, 3(9):852–5, Sep 2001. 1465-7392 Journal Article.

- [147] W. Tvarusko, M. Bentele, T. Misteli, R. Rudolf, C. Kaether, D. L. Spector, H. H. Gerdes, and R. Eils. Time-resolved analysis and visualization of dynamic processes in living cells. *Proc Natl Acad Sci U S A*, 96(14):7950–5, Jul 6 1999. 0027-8424 Journal Article.
- [148] E. Gladilin. *Biomechanical Modeling of Soft Tissue and Facial Expressions for Craniofacial Surgery Planning*. Dissertation, Freie Universität Berlin, Berlin, 2003.
- [149] W.S. Rasband. *ImageJ*. U. S. National Institutes of Health, Bethesda, Maryland, USA, 1997 - 2005.
- [150] M. Messerli. *Imaris*. Bitplane AG, Zürich, Switzerland, 1993 - 2005.
- [151] R. D. Phair and T. Misteli. High mobility of proteins in the mammalian cell nucleus. *Nature*, 404(6778):604–9, Apr 6 2000. 0028-0836 Journal Article.
- [152] K. Rohr. On 3D differential operators for detecting point landmarks. *Image and Vision Computing*, 15(3):219 – 233, 1997.
- [153] K. Rohr, H. S. Stiehl, R. Sprengel, T. M. Buzug, J. Weese, and M. H. Kuhn. Landmark-based elastic registration using approximating thin-plate splines. *IEEE Trans Med Imaging*, 20(6):526–34, Jun 2001. 0278-0062 Journal Article.
- [154] M. Reichenzeller, A. Burzlaff, P. Lichter, and H. Herrmann. In vivo observation of a nuclear channel-like system: Evidence for a distinct interchromosomal domain compartment in interphase cells. *J Struct Biol*, 129(2-3):175–85, Apr 2000. 1047-8477 Journal Article.
- [155] M. Jacob and M. Unser. Design of steerable filters for feature detection using Canny-like criteria. *IEEE Transactions on Pattern Analysis and Machine Intelligence*, 26(8):1007 – 1019, August 2004.
- [156] C. Tomasi and R. Manduchi. Bilateral filtering for gray and color images. In *IEEE International Conference on Computer Vision*, Bombay, India, 1998.
- [157] R. Ohno. *Atlas of Hematology*. Nagoya University School of Medicine, 1996.
- [158] J. R. Chubb, S. Boyle, P. Perry, and W. A. Bickmore. Chromatin motion is constrained by association with nuclear compartments in human cells. *Curr Biol*, 12(6):439–45, Mar 19 2002. 0960-9822 Journal Article.
- [159] J. Fieres, J. Mattes, and R. Eils. A point set registration algorithm using a motion model based on thin-plate splines and point clustering. In S. Florczyk B. Radig, editor, *DAGM-Symposium*, volume 2191, pages 76–83. Springer Verlag, 2001.

-
- [160] J. Fieres. *A new point set registration algorithm*. Diploma thesis, Ruprecht-Karls-Universität, Heidelberg, 2001.
- [161] R. P. Woods, S. T. Grafton, J. D. Watson, N. L. Sicotte, and J. C. Mazziotta. Automated image registration: II. intersubject validation of linear and nonlinear models. *J Comput Assist Tomogr*, 22(1):153–65, Jan-Feb 1998. 0363-8715 Clinical Trial Journal Article.
- [162] A. Stocker and R. J. Douglas. Analog integrated 2-D optical flowsensor with programmable pixels. *ISCAS*, III:1–12, May 2004.
- [163] D. Uttenweiler, C. Veigel, R. Steubing, C. Gotz, S. Mann, H. Haussecker, B. Jahne, and R. H. Fink. Motion determination in actin filament fluorescence images with a spatio-temporal orientation analysis method. *Biophys J*, 78(5):2709–15, May 2000. 0006-3495 Journal Article.
- [164] M. Gebhard. *Multidimensionale Segmentierung in Bildfolgen und Quantifizierung dynamischer Prozesse*. PhD thesis, Ruprecht-Karls-Universität, Heidelberg, 2004.
- [165] M. Gebhard, J. Mattes, and R. Eils. An active contour model for segmentation based on cubic B-splines and gradient vector flow. *Lecture notes in computer science*, 2208:1373–1375, 2001 2001.
- [166] J. R. Swedlow, I. Goldberg, E. Brauner, and P. K. Sorger. Informatics and quantitative analysis in biological imaging. *Science*, 300(5616):100–2, Apr 4 2003. 1095-9203 Journal Article.
- [167] W. E. Lorensen and H. E. Cline. Marching cubes: A high resolution 3D surface construction algorithm. *Computer Graphics*, 21(4):163–169, 1987.
- [168] G. Taubin. Curve and surface smoothing without shrinkage. Technical report, IBM, September 1994.
- [169] A. Sabanas and Z. Tang. Enhancing Tikal: Development of visualization, tracking and networking integration. Internship project report, International University, 2004.
- [170] Péter Lénárt, Christian P Bacher, Nathalie Daigle, Arthur R Hand, Roland Eils, Mark Terasaki, and Jan Ellenberg. A contractile nuclear actin network drives chromosome congression in oocytes. *Nature*, 436:812–818, Jul 2005.
- [171] J. Mattes, J. Fieres, and R. Eils. A shape adapted motion model for non-rigid registration. In *SPIE Medical Imaging 2002: Image Processing*, volume Proceedings of SPIE 4684, pages 518–527, San Diego, 23.-28. Feb. 2002 2002.
- [172] Kitware. Insight segmentation and registration toolkit. Kitware Inc., New York, 1999 - 2005.

- [173] E. Heard, F. Mongelard, D. Arnaud, C. Chureau, C. Vourc'h, and P. Avner. Human XIST yeast artificial chromosome transgenes show partial X-inactivation center function in mouse embryonic stem cells. *Proc Natl Acad Sci U S A*, 96(12):6841–6, Jun 8 1999. 0027-8424 Journal Article.
- [174] P. Clerc and P. Avner. Role of the region 3' to Xist exon 6 in the counting process of X-chromosome inactivation. *Nat Genet*, 19(3):249–53, Jul 1998. 1061-4036 Journal Article.
- [175] N. Mise and P. Avner. BAC modification using a RecA expressing shuttle vector system. *Methods Mol Biol*, 256:77–87, 2004. 1064-3745 Journal Article.
- [176] C. C. Robinett, A. Straight, G. Li, C. Willhelm, G. Sudlow, A. Murray, and A. S. Belmont. In vivo localization of DNA sequences and visualization of large-scale chromatin organization using lac operator/repressor recognition. *J Cell Biol*, 135(6 Pt 2):1685–1700, Dec 1996.
- [177] K. K. Hedberg and L. B. Chen. Absence of intermediate filaments in a human adrenal cortex carcinoma-derived cell line. *Exp Cell Res*, 163(2):509–17, Apr 1986. 0014-4827 Journal Article.
- [178] T. M. Svitkina and G. G. Borisy. Arp2/3 complex and actin depolymerizing factor/cofilin in dendritic organization and treadmilling of actin filament array in lamellipodia. *J Cell Biol*, 145(5):1009–26, May 31 1999. 0021-9525 Journal Article.
- [179] P. J. Burt, T. Hong, and A. Rosenfeld. Segmentation and estimation of image region properties through cooperative hierarchical computation. *IEEE Trans on Systems Man and Cybernetics*, 12:802–809, Dec 1981.
- [180] M. J. Saxton. Lateral diffusion in an archipelago. Single-particle diffusion. *Biophys J*, 64(6):1766–80, Jun 1993. 0006-3495 Journal Article.
- [181] M. J. Saxton. Single-particle tracking: Effects of corrals. *Biophys J*, 69(2):389–98, Aug 1995. 0006-3495 Journal Article.
- [182] W. J. Conover. One-sample "Kolmogorov" test / Two-sample "Smirnov" test. In B. Wiley, editor, *Practical nonparametric statistics*, pages 295–301 / 309–314. John Wiley & Sons, New York, 1971.
- [183] M. Hollander and D. A. Wolfe. One-sample "Wilcoxon" test. In *Nonparametric statistical inference*, pages 27–33. John Wiley & Sons, New York, 1973.
- [184] R. A. Becker, J. M. Chambers, and A. R. Wilks. *The New S Language*. Wadsworth & Brooks/Cole, 1988.
- [185] S. Rastan and E. J. Robertson. X-chromosome deletions in embryo-derived (EK) cell lines associated with lack of X-chromosome inactivation. *J Embryol Exp Morphol*, 90:379–88, Dec 1985. 0022-0752 Journal Article.

-
- [186] R. M. Boumil and J. T. Lee. Forty years of decoding the silence in X-chromosome inactivation. *Hum Mol Genet*, 10(20):2225–32, Oct 1 2001. 0964-6906 Journal Article Review Review, Tutorial.
- [187] M. Cockell and S. M. Gasser. Nuclear compartments and gene regulation. *Curr Opin Genet Dev*, 9(2):199–205, Apr 1999. 0959-437x Journal Article Review Review, Tutorial.
- [188] D. L. Spector. The dynamics of chromosome organization and gene regulation. *Annu Rev Biochem*, 72:573–608, 2003. 0066-4154 Journal Article Review Review, Academic.
- [189] Y. Marahrens. X-inactivation by chromosomal pairing events. *Genes Dev*, 13(20):2624–32, Oct 1999.
- [190] E. Heard, C. Kress, F. Mongelard, B. Courtier, C. Rougeulle, A. Ashworth, C. Vourc'h, C. Babinet, and P. Avner. Transgenic mice carrying an Xist-containing YAC. *Hum Mol Genet*, 5(4):441–50, Apr 1996. 0964-6906 Journal Article.
- [191] Jeffrey J Roix, Philip G McQueen, Peter J Munson, Luis A Parada, and Tom Misteli. Spatial proximity of translocation-prone gene loci in human lymphomas. *Nat Genet*, 34(3):287–291, Jul 2003.
- [192] Alistair B Coulthard, Nadia Nolan, John B Bell, and Arthur J Hilliker. Transvection at the vestigial locus of *Drosophila melanogaster*. *Genetics*, Jun 2005.
- [193] Mikhail Savitsky, Tatyana Kahn, Ekaterina Pomerantseva, and Pavel Georgiev. Transvection at the end of the truncated chromosome in *Drosophila melanogaster*. *Genetics*, 163(4):1375–1387, Apr 2003.
- [194] James A Kennison and Jeffrey W Southworth. Transvection in *Drosophila*. *Adv Genet*, 46:399–420, 2002.
- [195] S. M. Janicki and D. L. Spector. Nuclear choreography: Interpretations from living cells. *Curr Opin Cell Biol*, 15(2):149–57, Apr 2003. 0955-0674 Journal Article Review Review, Tutorial.
- [196] R. M. Zirbel, U. R. Mathieu, A. Kurz, T. Cremer, and P. Lichter. Evidence for a nuclear compartment of transcription and splicing located at chromosome domain boundaries. *Chromosome Res*, 1(2):93–106, Jul 1993. 0967-3849 Journal Article.
- [197] G. L. Lukacs, P. Haggie, O. Seksek, D. Lechardeur, N. Freedman, and A. S. Verkman. Size-dependent DNA mobility in cytoplasm and nucleus. *J Biol Chem*, 275(3):1625–9, Jan 21 2000. 0021-9258 Journal Article.
- [198] S. M. Gorisch, K. Richter, M. O. Scheuermann, H. Herrmann, and P. Lichter. Diffusion-limited compartmentalization of mammalian cell nuclei assessed by microinjected macromolecules. *Exp Cell Res*, 289(2):282–94, Oct 1 2003. 0014-4827 Journal Article.

- [199] J. C. Politz. Use of caged fluorochromes to track macromolecular movement in living cells. *Trends Cell Biol*, 9(7):284–7, Jul 1999. 0962-8924 Journal Article Review Review, Tutorial.
- [200] J. C. Ritland Politz, R. A. Tuft, and T. Pederson. Diffusion-based transport of nascent ribosomes in the nucleus. *Mol Biol Cell*, 14(12):4805–12, Dec 2003. 1059-1524 Journal Article.
- [201] Y. Tseng, J. S. Lee, T. P. Kole, I. Jiang, and D. Wirtz. Micro-organization and visco-elasticity of the interphase nucleus revealed by particle nanotracking. *J Cell Sci*, 117(Pt 10):2159–67, Apr 15 2004. 0021-9533 Journal Article.
- [202] J. Apgar, Y. Tseng, E. Fedorov, M. B. Herwig, S. C. Almo, and D. Wirtz. Multiple-particle tracking measurements of heterogeneities in solutions of actin filaments and actin bundles. *Biophys J*, 79(2):1095–106, Aug 2000. 0006-3495 Journal Article.
- [203] Y. Tseng and D. Wirtz. Mechanics and multiple-particle tracking microheterogeneity of alpha-actinin-cross-linked actin filament networks. *Biophys J*, 81(3):1643–56, Sep 2001. 0006-3495 Journal Article.
- [204] Karsten Richter, Michaela Reichenzeller, Sabine M Görisch, Ute Schmidt, Markus O Scheuermann, Harald Herrmann, and Peter Lichter. Characterization of a nuclear compartment shared by nuclear bodies applying ectopic protein expression and correlative light and electron microscopy. *Exp Cell Res*, 303(1):128–137, Feb 2005.
- [205] P. Heun, T. Laroche, K. Shimada, P. Furrer, and S. M. Gasser. Chromosome dynamics in the yeast interphase nucleus. *Science*, 294(5549):2181–6, Dec 7 2001. 0036-8075 Journal Article.
- [206] H. Herrmann, A. Eckelt, M. Brettel, C. Grund, and W. W. Franke. Temperature-sensitive intermediate filament assembly. Alternative structures of *Xenopus laevis* vimentin in vitro and in vivo. *J Mol Biol*, 234(1):99–113, Nov 5 1993. 0022-2836 Journal Article.
- [207] H. Herrmann, T. Wedig, R. M. Porter, E. B. Lane, and U. Aebi. Characterization of early assembly intermediates of recombinant human keratins. *J Struct Biol*, 137(1-2):82–96, Jan-Feb 2002. 1047-8477 Journal Article.
- [208] G. Albrecht-Buehler and A. Bushnell. Reversible compression of cytoplasm. *Exp Cell Res*, 140(1):173–89, Jul 1982. 0014-4827 Journal Article.
- [209] R. D. Phair, P. Scaffidi, C. Elbi, J. Vecerova, A. Dey, K. Ozato, D. T. Brown, G. Hager, M. Bustin, and T. Misteli. Global nature of dynamic protein-chromatin interactions in vivo: three-dimensional genome scanning and dynamic interaction networks of chromatin proteins. *Mol Cell Biol*, 24(14):6393–402, Jul 2004. 0270-7306 Journal Article.

-
- [210] E. D. Siggia, J. Lippincott-Schwartz, and S. Bekiranov. Diffusion in inhomogeneous media: Theory and simulations applied to whole cell photobleach recovery. *Biophys J*, 79(4):1761–70, Oct 2000. 0006-3495 Journal Article.
- [211] B. L. Sprague, R. L. Pego, D. A. Stavreva, and J. G. McNally. Analysis of binding reactions by fluorescence recovery after photobleaching. *Biophys J*, 86(6):3473–95, Jun 2004. 0006-3495 Journal Article.
- [212] S. Frank, J. Moore, and R. Eils. A question of scale: Bringing an existing bio-science workflow engine to the grid. *Concurrency and Computation*, (Special Issue), 2004.
- [213] C. H. Eskiw, G. Dellaire, J. S. Mymryk, and D. P. Bazett-Jones. Size, position and dynamic behavior of PML nuclear bodies following cell stress as a paradigm for supramolecular trafficking and assembly. *J Cell Sci*, 116(Pt 21):4455–66, Nov 1 2003. 0021-9533 Journal Article.
- [214] B. T. Helfand, L. Chang, and R. D. Goldman. The dynamic and motile properties of intermediate filaments. *Annu Rev Cell Dev Biol*, 19:445–67, 2003. 1081-0706 Journal Article Review Review, Academic.
- [215] V. Prahlad, M. Yoon, R. D. Moir, R. D. Vale, and R. D. Goldman. Rapid movements of vimentin on microtubule tracks: Kinesin-dependent assembly of intermediate filament networks. *J Cell Biol*, 143(1):159–70, Oct 5 1998. 0021-9525 Journal Article.
- [216] Katalin Fejes Tóth, Tobias A Knoch, Malte Wachsmuth, Monika Frank-Stöhr, Michael Stöhr, Christian P Bacher, Gabriele Müller, and Karsten Rippe. Trichostatin A-induced histone acetylation causes decondensation of interphase chromatin. *J Cell Sci*, 117(Pt 18):4277–4287, Aug 2004.
- [217] T. Cremer, A. Kurz, R. Zirbel, S. Dietzel, B. Rinke, E. Schrock, M. R. Speicher, U. Mathieu, A. Jauch, P. Emmerich, H. Scherthan, T. Ried, C. Cremer, and P. Lichter. Role of chromosome territories in the functional compartmentalization of the cell nucleus. *Cold Spring Harb Symp Quant Biol*, 58:777–92, 1993. 0091-7451 Journal Article.
- [218] H. B. Sun, J. Shen, and H. Yokota. Size-dependent positioning of human chromosomes in interphase nuclei. *Biophys J*, 79(1):184–190, Jul 2000.
- [219] M. Cremer, K. Kupper, B. Wagler, L. Wizelman, J. von Hase, Y. Weiland, L. Kreja, J. Diebold, M. R. Speicher, and T. Cremer. Inheritance of gene density-related higher order chromatin arrangements in normal and tumor cell nuclei. *J Cell Biol*, 162(5):809–20, Sep 1 2003. 0021-9525 Journal Article.
- [220] S. Boyle, S. Gilchrist, J. M. Bridger, N. L. Mahy, J. A. Ellis, and W. A. Bickmore. The spatial organization of human chromosomes within the nuclei of normal and emerin-mutant cells. *Hum Mol Genet*, 10(3):211–9, Feb 1 2001. 0964-6906 Journal Article.

- [221] Phillip T Moen, Carol Villnave Johnson, Meg Byron, Lindsay S Shopland, Ivana L de la Serna, Anthony N Imbalzano, and Jeanne Bentley Lawrence. Repositioning of muscle-specific genes relative to the periphery of SC-35 domains during skeletal myogenesis. *Mol Biol Cell*, 15(1):197–206, Jan 2004.
- [222] Theodore P Rasmussen. Embryonic stem cell differentiation: A chromatin perspective. *Reprod Biol Endocrinol*, 1(1):100, Nov 2003.
- [223] Dimitris Kioussis. Gene regulation: Kissing chromosomes. *Nature*, 435(7042):579–580, Jun 2005.
- [224] Daniel Gerlich, Joël Beaudouin, Bernd Kalbfuss, Nathalie Daigle, Roland Eils, and Jan Ellenberg. Global chromosome positions are transmitted through mitosis in mammalian cells. *Cell*, 112(6):751–764, Mar 2003.
- [225] C. Conrad, H. Erfle, P. Warnat, N. Daigle, T. Lorch, J. Ellenberg, R. Pepperkok, and R. Eils. Automatic identification of subcellular phenotypes on human cell arrays. *Genome Res*, 14(6):1130–6, Jun 2004. 1088-9051 Journal Article.
- [226] J. Canny. A computational approach to edge detection. *IEEE Transactions on Pattern Analysis and Machine Intelligence*, 8(6):679–698, November 1986.
- [227] P.J. Burt. *The pyramid as a structure for efficient computation*, pages 6 – 35. Springer, New York, 1984.